LEABHARLANN CHOLÁISTE NA TRÍONÓIDE, BAILE ÁTHA CLIATH | TRINITY COLLEGE LIBRARY DUBLIN
Ollscoil Átha Cliath | The University of Dublin

Terms and Conditions of Use of Digitised Theses from Trinity College Library Dublin

Copyright statement

All material supplied by Trinity College Library is protected by copyright (under the Copyright and Related Rights Act, 2000 as amended) and other relevant Intellectual Property Rights. By accessing and using a Digitised Thesis from Trinity College Library you acknowledge that all Intellectual Property Rights in any Works supplied are the sole and exclusive property of the copyright and/or other IPR holder. Specific copyright holders may not be explicitly identified. Use of materials from other sources within a thesis should not be construed as a claim over them.

A non-exclusive, non-transferable licence is hereby granted to those using or reproducing, in whole or in part, the material for valid purposes, providing the copyright owners are acknowledged using the normal conventions. Where specific permission to use material is required, this is identified and such permission must be sought from the copyright holder or agency cited.

Liability statement

By using a Digitised Thesis, I accept that Trinity College Dublin bears no legal responsibility for the accuracy, legality or comprehensiveness of materials contained within the thesis, and that Trinity College Dublin accepts no liability for indirect, consequential, or incidental, damages or losses arising from use of the thesis for whatever reason. Information located in a thesis may be subject to specific use constraints, details of which may not be explicitly described. It is the responsibility of potential and actual users to be aware of such constraints and to abide by them. By making use of material from a digitised thesis, you accept these copyright and disclaimer provisions. Where it is brought to the attention of Trinity College Library that there may be a breach of copyright or other restraint, it is the policy to withdraw or take down access to a thesis while the issue is being resolved.

Access Agreement

By using a Digitised Thesis from Trinity College Library you are bound by the following Terms & Conditions. Please read them carefully.

I have read and I understand the following statement: All material supplied via a Digitised Thesis from Trinity College Library is protected by copyright and other intellectual property rights, and duplication or sale of all or part of any of a thesis is not permitted, except that material may be duplicated by you for your research use or for educational purposes in electronic or print form providing the copyright owners are acknowledged using the normal conventions. You must obtain permission for any other use. Electronic or print copies may not be offered, whether for sale or otherwise to anyone. This copy has been supplied on the understanding that it is copyright material and that no quotation from the thesis may be published without proper acknowledgement.

University of Dublin
Trinity College

Fabrication and Characterisation of Micro- and Nano- Structures with High Aspect Ratio

A thesis submitted to the University of Dublin in application for the degree
of Doctor of Philosophy

Joseph McCarthy
School of Chemistry
University of Dublin
March 2011

Declaration

This thesis is submitted by the undersigned to the University of Dublin, Trinity College for the examination of Doctorate of Philosophy. Except as otherwise stated, the author carried out the work described herein alone and has not submitted as an exercise for a degree to any other university. I hereby agree that the library may lend or copy the thesis upon request. This permission covers only single copies made for study purposes, subject to normal conditions of acknowledgement.

Summary:

The main aim of the work presented in this thesis was to develop novel high aspect ratio micro- and nano- structures by using metal alkoxide derived sol-gels and polymer solutions and infiltrating them into porous templates. These structures are expected to find a range of potential biomedical, photonic and photocatalytic applications.

Chapter 1 covers the introduction to properties of the various materials and describes main synthetic approaches used throughout the work.

Chapter 2 describes the work performed on the fabrication of optical microtubes. Outlined in the work is the fabrication process of infiltrating silica/aluminosilicate sol-gels into microchannel glass membranes and their annealing and release procedures. The microtubes have been produced with a high aspect ratio and diameters of ~8-25μm. Doping of the sol-gels has led to the microtubes being tailored to show characteristic emission from Eu^{3+} and CdTe QDs. Microtubes have also been fabricated to display broad visible defect emission. Some of the microtubes have been shown to have sufficient optical quality to display whispering gallery mode resonance. In addition some studies on the coupling of microtubes and optical microspheres and corresponding light energy transfer between the microcavities have been performed.

Chapter 3 explores the fabrication of silica/aluminosilicate nanowires by vacuum assisted infiltration into porous alumina membranes. These nanowires demonstrated high aspect ratios with diameters of ~230nm and lengths of several microns. Some of the nanowires have been processed to display defect luminescence after annealing treatment and demonstrated the capacity for high surface functionalisation for conjugation and coverage with gold nanoparticles. Magnetic nanowires have also been fabricated through the loading of the silica/aluminosilicate sol-gel with magnetic nanoparticles. Selected bio-functionalise magnetic nanowires have been successfully utilised as multiplexed immunoassays in flow cytometry, showing a unique detection fingerprint and distinct advantages over similar particles.

Chapter 4 describes the fabrication of polystyrene nanowires by infiltration into porous alumina membranes. The fabrication of new fluorescent and magnetic polystyrene nanowires was achieved by doping the polymer solution with dye and superparamagnetic magnetite NPs. These multimodal nanowires showed excellent ability to be manipulated by an external magnetic field and strong luminescence under UV excitation. The antibody functionalisation and the interaction with epithelial lung cancer cells of the nanowires has

also been explored. This section also demonstrates the fabrication of CdZnSe/ZnSe QD loaded PS nanowires. These nanowires have also demonstrated good emission under UV excitation.

Chapter 5 describes the development of novel TiO_2 based materials for photocatalytic applications. The work utilises various titanium alkoxide precursors to fabricate composite SiO_2-TiO_2 gels, pure TiO_2 nanowires and gold nanoparticle doped TiO_2 nanowires. Each of these has been characterised and tested for photocatalytic activity. All samples showed some activity in the degradation of methylene blue under UV radiation with the AuNP doped nanowires showing the highest activity. The coating of CdTe QDs with TiO_2 was also performed resulting in the formation of nanoparticles which retained good luminescence from the QDs after coating.

Chapter 6 contains details of all the experimental procedures and instrumentation relating to the materials synthesised and characterised in the work.

Chapter 7 gives conclusions of the research performed over all and highlights possible areas of future work and shows some preliminary results.

Finally the appendices contain supplemental work regarding results in the main text and also some results deemed surplus to requirement in the main body.

We believe that this work will contribute to further development of new photonic materials with a range of potential applications in materials science and biotechnology.

Acknowledgements

Firstly I would like to thank my supervisor Prof. Yurii Gun'ko for giving me the chance to work in his group in an area of research which really interests me. I also would like to thank him for the endless support through the years in everything work related and allowing me the opportunity to explore research topics I found interest in overtime and guiding me through any problems I had. It has been a great pleasure to work within the group and with you.

To all the members of the Gun'ko group come and gone I owe a huge thanks to all for various reasons. Amro, Rowan, Gemma, Mícheál, Ian, Renata, Anna, Joe 2, Valerie, Cormac, Áine, Serena, Stephen, Tim, Arunas, Sivakumar, Shane, Damien and Gosia. A special mention for Maciej, who was taken away from us all too soon, rest in peace my friend. To Michele who introduced me to work in the Gun'ko group I owe you a lot for starting me of on the path to research (I'm sure I'll appreciate it one day).

I'd also like to thank Prof. David Grayson, the Head of the School of Chemistry for use of the facilities. On no small note a thanks to all the technical staff who keep the place running, especially to; Patsy, Martin, Fred and Manuel. Another big thanks to Neal Leddy and all the staff in the CMA for assistance with all my electron microscopy needs.

I have been assisted no end in much of my work by people in other departments throughout the college (Physics, Electronic engineering and Crann). But a special thanks is owed to the following; Dr. Tanya Perova, Joanna, Vasily, Adriele, and Fiona.

I have been fortunate enough to make a lot of friends outside the group over my years in Trinity, and they have helped to keep me going and made all this worthwhile. So thanks to Dave, Dilwyn, Ger, Conn, Phil, Fiona, Denise, Ed, Dec and Grá!!! Also friends outside the college have always been there for banter and a bit of craic outside college and I thank them all; Rob, Conor, Nomo, Will, Macken, Col, Reilly and Vin.

Last but certainly not least my family. Eoin ya mad yoke, did you not learn anything from me in so far as following me into a PhD in nanomaterials chemistry! Only messing I'm sure you'll produce a far better one of these than I have in a couple years time. To my parents, I owe you everything I've achieved so far in life. Thanks for always supporting me in everyway in all my endeavours and never doubting me even when you probably had good reason to at times. Thank you too for raising me to think for myself and always appreciate how lucky I am to have the opportunities I have been given.

List of Abbreviations:

1D – One Dimensional

NWs – Nanowires

$Ti(OEt)_4$ – Titanium ethoxide

$Ti(OPr^i)_4$ – Titanium iso-propoxide

$Ti(OBt)_4$ – Titanium butoxide

WGM – Whispering Gallery Mode

CNTs – Carbon Nanotubes

NPs – Nanoparticles

APTES – 3-Aminopropyltriethoxysilane

UV – Ultraviolet

RE – Rare earth

AuNPs – Gold Nanoparticles

SPB – Surface Plasmon Band

QDs – Quantum Dots

AAO – Anodised Aluminium Oxide

MCG – Micro Channel Glass

PL – Photoluminescence

TGA – Thermo Gravimetric Analysis

PMMA – Poly (methyl methacrylate)

SEM – Scanning Electron Microscopy

TEM – Transmission Electron Microscopy

DMAP – 4-(Dimethylamino) Pyridine

MPS - 3-mercaptopropyltrimethoxysilane

VSM – Vibrating Sample Magnetometer

SQUID – Superconducting Quantum Interface Device

EDC - 1-ethyl-3-(3-dimethylaminopropyl) carbodiimide hydrochloride

THP1 – Human acute monocytic leukemia cell line

FITC – Fluorescein isothiocyanate

PSS – Polystyrene sulfonate

THF – Tetrahydrofuran

XRD – X-Ray Diffraction

MB – Methylene Blue

PC – Photocatalytic

TEOS – Tetraethoxysilane

PZC – Point of Zero Charge

List of Figures:

Contents

Chapter 1

Introduction

One-dimensional micro- and nano-structured materials have attracted much attention due to their unique photonic, electronic and magnetic properties, which lead to a number of technological applications. For example long aspect ratio and 1D nanostructures offers a unique substrate for the selective binding of biological species with the advantage of maximizing the functional binding of the nanomaterials along their principal axis. It has been demonstrated that anisotropically shaped nanostructures can avoid bio-elimination better than spherical nanoparticles and have an increased in vivo blood circulation time. For these reasons these materials can find a number of important applications in biology and medicine.

The use of porous membranes for fabrication of 1D micro- and nano-structures is well documented for many materials using various membranes such as porous alumina, porous silicon, micro-channel glass etc[1-4]. Our work is focused on the development of new micro- and nano-wire-like structures with high aspect ratio using template membranes.

1.1 Introduction to Sol-gel Processing

The sol-gel processing technique has been known for a long time, first appearing commonly in the 1930's. The sol-gel process generally involves the hydrolysis and condensation of metal alkoxides through reactivity of their functional groups. Tetraethoxysilane (TEOS) is one of the most common alkoxide precursors used in the production of silica sol-gels. TEOS can be easily hydrolysed using a mixture of water and ethanol and an acid or base as a catalyst according to Scheme 1.

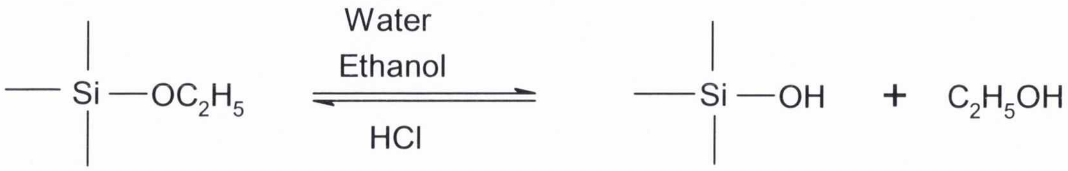

$$-\mathrm{Si}-OC_2H_5 \overset{\text{Water, Ethanol}}{\underset{\text{HCl}}{\rightleftharpoons}} -\mathrm{Si}-OH + C_2H_5OH$$

Scheme 1: Schematic of hydrolysis of TEOS

Alcohol is added as the common solvent as water and alkoxysilanes are immiscible. The mechanism of the hydrolysis is that the alkoxide group is rapidly protonated leaving it susceptible to attack from water[5]. Once complete it leaves the Si with a substituted hydroxyl group. This process repeats until completion or near completion as the reverse reaction also competes.[5]

A gel is formed as a result of the condensation reaction of the hydrolysed TEOS. This can proceed via alcohol condensation and water condensation usually in the presence of an acidic or basic catalyst as shown in Scheme 2.

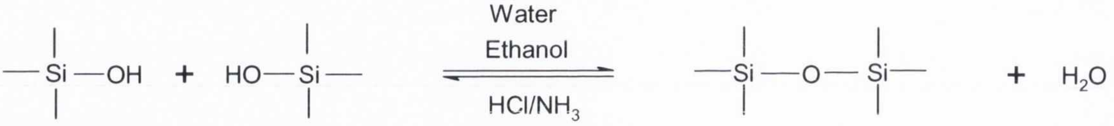

Scheme 2: Condensation reaction resulting in formation of Si-O-Si bonds

The condensation reaction proceeds by either producing water or an alcohol during condensation of the silanol groups to form siloxane bonds. Condensation usually starts before hydrolysis is complete and is in some competition with the reverse reactions however control of solvent water and precursor ratios can yield control over gelation times. For acid catalysis condensation gelation proceeds via progressive polymerisation from monomer to dimer to linear chain polymers which entangle with each other and randomly form branching bonds which eventually cause gelation. For base catalysed reactions clusters tend to form and reach a critical size which then branch together to form a gel as is schematically demonstrated in Figure 1.1[5]. In general acid catalysis is preferred for the hydrolysis step, however acid catalysis of the condensation step results in long gelation times, while basic conditions greatly reduce the gelation times in the condensation step if so desired[5-7] as shown in the work performed during this project. The sol-gel process is of course not strictly the realm of the silicates, it has found a large number of applications in many other metal oxides which are far more reactive than silicon alkoxides where the trend towards higher reactivity tends to go with decreasing electronegativity of the metal atom (while also noting the part the size of the alkoxy group attached plays in altering the hydrolysis and condensation rate of the metal alkoxides due to steric hindrance). One of the other most common applications of sol-gel chemistry is titania and titanate synthesis. Common titania precursors (such as

$Ti(OEt)_4$, $Ti(OPr^i)_4$ and $Ti(OBt)_4$) show a much higher reactivity then their silica analogues. This increased reactivity results in the attached alkoxy group playing a more significant role in the formation of titania sols due to their ability to change the reactivity and change the way the precursors behave with $Ti(OEt)_4$ showing preference to form oligomers and longer chain alkoxy groups to remain monomeric[7].

Once gelation has occurred ageing and drying of a gel occurs over time long after the gelation point by successive condensation reactions causing shrinkage and stiffening of the gel to produce a xerogel (a xerogel is defined as a gel dried under normal conditions that gives rise to capillary pressure that causes shrinkage of the gel network[5]). The properties of the gel change greatly during this stage from an easily morphed viscous liquid to solid glassy brittle substance. The time taken and degree of shrinkage can vary wildly depending on the process employed in gel formation or drying technique. During drying of a gel fracture can readily occur due to forces of the evaporating solvent moving through the porous structure. With care this can be avoided if required. Annealing of gels results in rapid drying and most often fracture (without due care), however it also has its uses as it can cause luminescence via carbon substitutional defect emission from the residual of the precursor[8] as will be discussed in more detail further on.

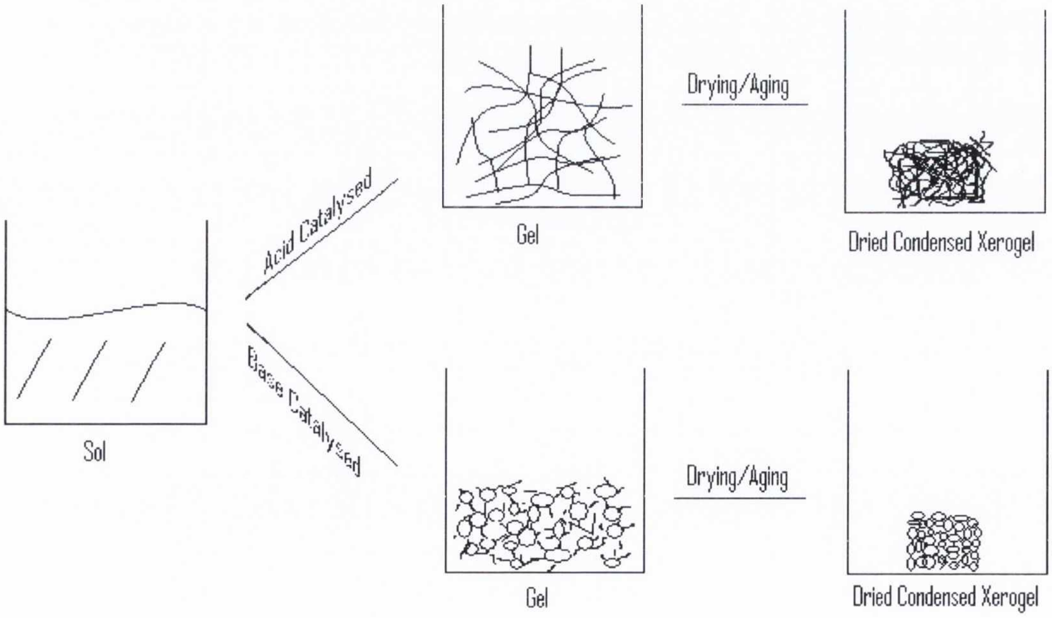

Figure 1.1: Representation showing the difference gelation and drying of acid catalysed and base catalysed sol-gels

1.1.1 Multi-Component Sol-gels

Multi component gels can also be formed usually by the addition of a suitable alkoxide precursor to an already partially hydrolysed sol (e.g. aluminium iso-propoxide to partially hydrolysed TEOS) resulting in a homogeneous mixture of the two partially hydrolysed precursors. Condensation carried out on the sol then results in the formation of a mixed component gel. However the degree of binding between the two different species can vary greatly depending on the species attempted to be mixed and on the degree of mixing desired (i.e. the ratio of the two or more components). Indeed for two common binary gels (Al_2O_3-SiO_2 and TiO_2-SiO_2) any level of binding between the two species (i.e. Ti-O-Si and Al-O-Si bonds) generally only occurs at low mol% (often <10mol%) additions of the secondary species[5,9-10]. However this phase separation can be beneficial as described in later sections for the europium co-doped gels.

1.2 Optical Microcavities and whispering gallery modes

Optical microcavities have become hugely important in the area of optics and photonics. They have a huge range of applications in optical communications and display associated with optical fibres. With the ability of microcavities to resonate electromagnetic waves within themselves in resonant modes called whispering gallery modes for relatively extended periods of time has also opened up many avenues of device application in sensing devices, micro-lasers[11], optical and photonic filters, photonic atoms and optical amplifiers which are generally reviewed in[12]. These optical microcavities come in a variety of designs including rings, toroids, spheres and cylinders.

The term whispering gallery mode (WGM) originally comes from Lord Rayleigh over a century ago who used it to describe sound waves propagating close to the surface of the gallery wall in St. Paul's cathedral in London[13], although the common usage today quite differs from its inspired name. Today WGM resonators describe a range of devices that trap electromagnetic waves in resonant modes within a microcavity via total internal reflection along its walls. The first observation of WGMs was in solid state lasers[14], however the first observations of their influence on fluorescence of spherical microcavities was by Brenner et al[15]. Since then WGMs have been characterised using various theories involving light scattering in microcavities such as Lorentz-Mie theory. This introduction is intended to give a relatively brief explanation of WGM properties in micro resonators to the reader, whereas a full treatment of WGM theory is beyond the scope of this work.

The first issue facing microcavities and the setting up of WGM resonances is the coupling of light into the device. There are a number of ways to couple to WGMs; critical coupling, evanescent field couplers, symmetry breaking techniques and free beam coupling. As free beam coupling is utilised in this work it is the only one examined here. The efficiency η of coupling continuous wave light into a ring resonator can be given by (1) where P_{in} is the power of light circulating inside the resonator, P is the external pump power and F is the finesse of the resonator[16] given by (2) which is a measure of the ability of the resonator to retain light energy (where ρ is the fraction of power left in the resonator after 1 round trip).

$$\eta = \frac{\pi}{F}\frac{P_{in}}{P} \text{ ------------- } (1) \qquad F = \frac{2\pi}{1-\rho} \text{ ------------ } (2)$$

The resonator is deemed to be under coupled if $\eta < 1$ and over coupled if $2 > \eta > 1$. Free beam coupling relies on the external beam coupling to the evanescent field of the WGM resonator which extends outside the device by a number of wavelengths. Coupling via this method tends to be quite inefficient however with sufficient beam power optimal positional excitement of the resonator coupling can be achieved. One of the limitations to coupling is an intrinsic property of WGM resonators (and indeed any optical system), that being loss due to light scattering and absorption of the material. This inherent issue due to the material properties and shape of the WGM resonator leads to one of the most important parameters, that of their Q-factor (or quality factor). It is a more accurate parameter for determining the quality of the device than the finesse that was discussed previously as it takes into account propagation effects within the cavity. The Q factor can be determined by $Q = \lambda_r/\delta\lambda_r$ where λ_r is the resonance wavelength (see Figure 1.3) and neatly indicates the resonators capacity to store light energy within it[17]. Q is also related to the photon lifetime within the cavity by $Q=\omega\tau$ where ω is the frequency of the mode and τ is the lifetime of the photon in that particular mode. Aspects such as surface roughness can play a large part in the ultimate Q factor which is why it is essential to have as smooth a surface as possible. Theoretical models of WGM resonators have placed upper limits of Q at around 10^{21} which are impossible to observe in the real world. Normally Q factors tend to range from 10^2 to 10^9 for amorphous resonators. Also material properties can have an effect for example absorption of water and formation of -OH groups on the surface of silica resonators has been shown to have an effect on Q factor[18].

If successfully coupled light propagates around the microcavity at the cavity boundary in concentric circles via total internal reflection as demonstrated in Figure 1.2. When an integer number of wavelengths in a WGM fit into the microcavity it is said to be in resonance for that particular mode. The WGM are characterised by their polarizations, transverse electric (TE) where the electric field is perpendicular to the direction of propagation and transverse magnetic (TM) where the magnetic field is perpendicular to the direction of propagation and three mode numbers n, l and m. Where n represents the radial number giving the number of peaks in the radial direction inside a sphere, l is the angular mode number giving the number of wavelengths that fit into the circumference and m is the azimuthal mode number equal to $-l......0......+l$. The identification and assignment of these modes requires the application of spherical Bessel and Henkel functions.

The WGM are shown in PL spectra by a series of repetitive sharp peaks as demonstrated in Figure 1.3 below due to the fact that at resonance the transition probability is increased when the emission wavelength couples to the spectral mode of the microcavity [1,19].

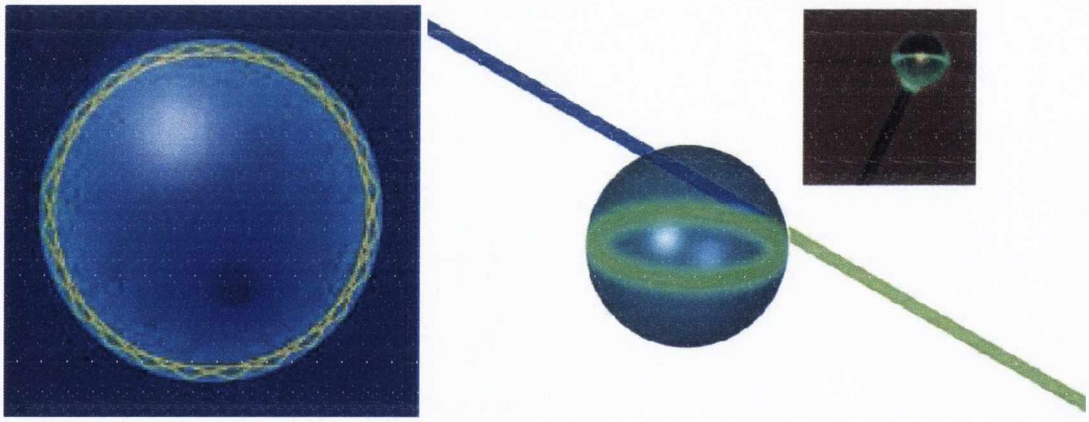

Figure 1.2: Schematic images representing WGM resonance in microcavities[17,19]

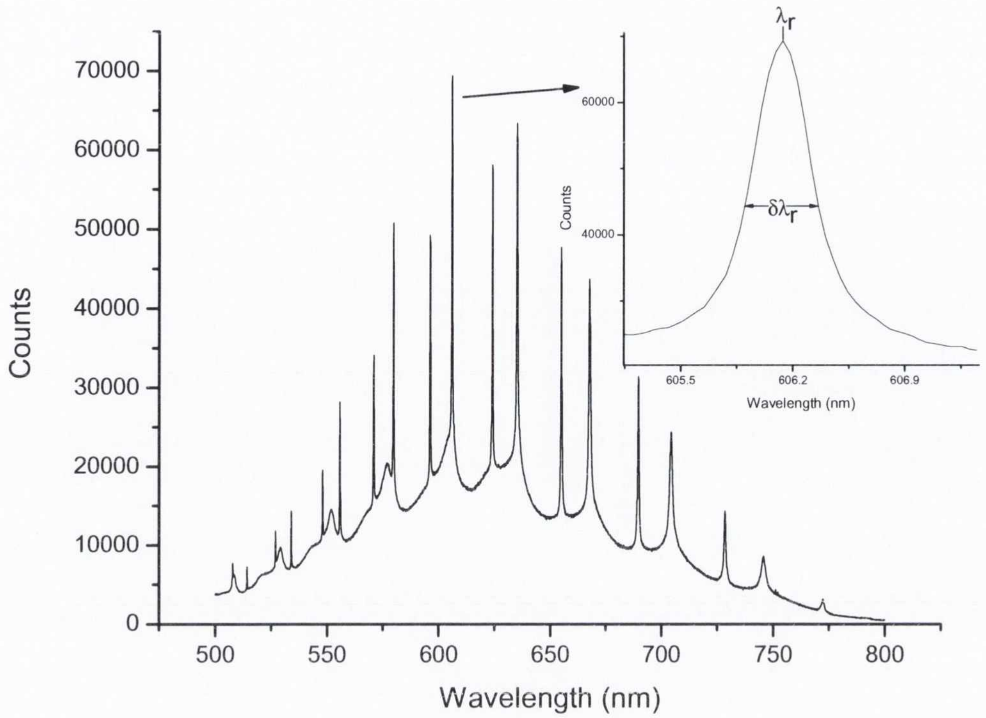

Figure 1.3: Solid state PL scan of dye coated microsphere displaying WGM resonance Inset; Close up of peak showing λ_r *and* $\delta\lambda_r$

1.3 Introduction to Nanowire Fabrication

In recent years the need for the relatively cheap production of uniform nano scale structures has been in great demand in all aspects of research, be it academic to industrial R&D to commercial product manufacture. The ready availability of nano sized porous templates (such as anodized alumina, macro-porous Si and PTFE membranes) has enabled such relatively cheap and easy production[3-4,20]. The use of templates to create 1D linear assemblies has been applied to produce various nanoparticle (NP) chains. Before this the chains were produced via NP interactions such as magnetic/electronic dipole moments, the use of couplers etc. However this method of formation was not always ideal and only certain materials possessed the correct properties of this self assembly growth. Structures such as DNA and carbon nanotubes (CNTs) were then employed as templates with great success in forming NP chains from a wide range of materials[21]. Electrodeposition techniques have been widely used to fabricate metallic nanowires such as gold, nickel and iron[22-25]. This is achieved by having a conductive back to the nanoporous template (often the aluminium back from which the alumina pores were grown from in the case of porous alumina templates) to act as an electrode and a counter electrode immersed in an appropriate electrolyte with a sufficient potential applied to grow the nanowire/tube structure within the pores. To further simplify 1D nano structure formation, infiltration into ordered hollow structures was the next obvious step and using easily manipulated and doped fluids such as sol-gels, polymer solutions and melts, NP properties can be utilised in this dimension with cost effective ease.

However, mastering the use of such membranes requires practise and knowledge of how solutions behave on this scale and how to subsequently manipulate them in order to produce a product useful for your purpose. At micron and large nano scales viscosity, surface tension and interfacial energies of the solutions dominate and their roles are very important in infiltration and structure fabrication when compared to macro-scale fabrication. Therefore the liquid must be of the right viscosity to infiltrate the pores of the membrane; this means for work with polymer solutions an appropriate concentration of polymer to solvent is required. For the purposes of this project polystyrene is used, which is easily soluble in THF which has a relatively low surface tension and should wet the walls of the membrane after a period of time as demonstrated by Steinhart et al (Figure 1.4)[4]. However to achieve complete filling of the pores vacuum assisted infiltration is required to break the surface tension and pull the solution into the pores. Removal of the nanowires structures from the porous membrane requires drying of the infiltrated membrane to remove any solvent from the structures within the pores via either heating or simply letting sit in a breathable atmosphere. Release can be achieved by dissolution of the membrane (in a basic solution for porous alumina for example) and subsequent washing of the 1D structures. The method of washing and membrane dissolution can be important to optimise for each type of 1D structure being fabricated for instance xerogel structures can be fragile and broken up with excessive treatment to the sample with methods such as sonication and polymer structures can deform from heating.

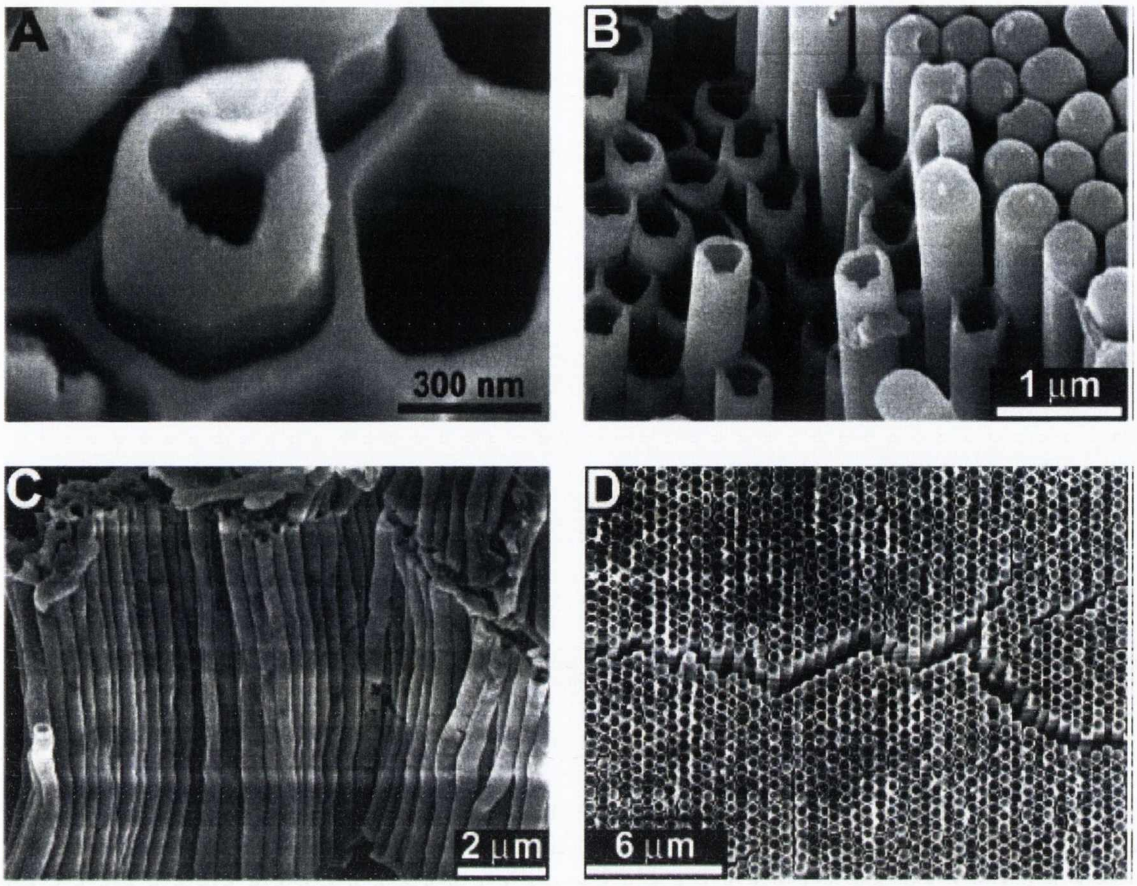

Figure 1.4: SEM images of polymer nanotubes formed by the wetting of porous alumina membranes[4]

1.4 Defect Emission in Silica

Currently there are increasing and wide ranging applications of silica based sol-gel technology in telecommunications, photonics, displays, sensors and numerous biological applications. In particular the fabrication for intrinsically highly luminescent silica devices in the visible region has great potential in current technologies. The phenomenon was first reported by Green et al[8] who observed intense broad visible luminescence from mainly TMOS (but also some APTES and TEOS) derived sol-gels catalysed by a variety of carboxylic acids. The origin of the luminescence was explained by the presence of carbon defects within the silica matrix, which have originated from the carboxylic acid catalyst trapped within the silica matrix and un-hydrolysed alkoxy groups (from the TMOS or TEOS precursors) which upon annealing cause carbon substitutional defects as shown in the scheme in Figure 1.5 below. Other investigations have demonstrated that SiC/C and SiOC groups implanted into silica can produce highly luminescent materials in the UV and visible region [26-28], these species could also occur during annealing of silica samples containing organic constituents and are considered a strong possible contributor to the emission.

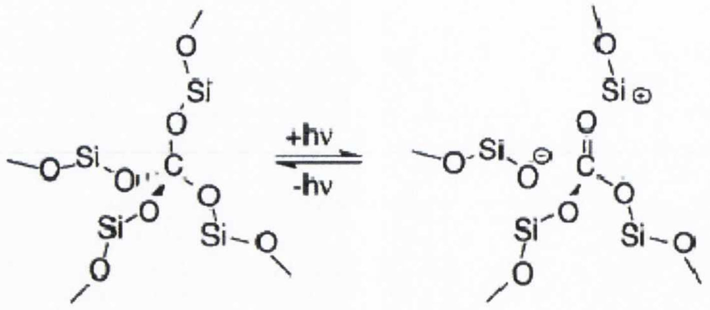

Figure 1.5: Scheme showing proposed mechanism for C substitutional defect emission in silica[8]

Other publications have suggested that non-bridging oxygen hole centres activated from silanol species in the matrix upon annealing could be responsible for some luminescence in silica in the UV region[29-30]. Further investigations by Glinka and co-workers into UV and green emission from annealed mesoporous silica samples also attributed emission to oxygen hole luminescent centres. They also state that emission was prominent from surface defects of the pores via hydrogen related species interacting with oxygen vacancies which were also proposed for luminescent nanoparticle silica composites[31-35]. Additional studies by Uchino et al with silicon and fumed silica nanoparticles[36] and using n-alkylhydroxysilanes[37] argued further that the UV and visible luminescence observed is caused by oxygen defects created after annealing up to ~400°C and not carbon related defects. They demonstrated this in Figure 1.6 below but did argue that the organic groups acted to stabilise the defect pair they claims responsible for emission going on further to say an ideal Si stoiciometric environment for luminescence was $R\text{-}SiO_{3/2}$ ($R=C_{18}H_{37}$) or $R\text{-}(CH_3)SiO_{2/2}$. It was demonstrated that annealing in an air atmosphere resulted in an increase of the blue visible emission and UV emission increased with vacuum annealing in fumed silica samples. This was attributed to differing dehydroxylation reactions taking place during the annealing process[38]. These defect emission processes have also been found in alumina and aluminosilicate materials. Similarly these reports also attribute the emission to oxygen vacancies and presence of carbon related defects within the matrix[1,39-41].

Thus despite the above mentioned reports on the origin of the emission from silica/siloxane species and /or carbon related defects, the issue is still not fully resolved and a definitive explanation remains incomplete on the source of the emission. Our work does not attempt to solve this but hopefully to add to the knowledge of the subject and venture possible explanations using the evidence presented above.

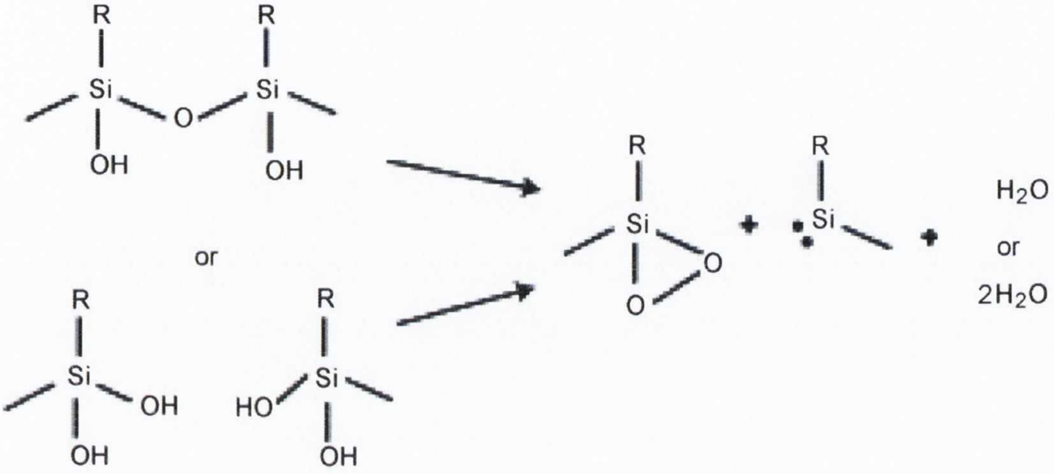

Figure 1.6: *Scheme for origin of species responsible for visible emission according to Uchino et al*[37]

1.5 Dopant Properties

As mentioned previously one of the most attractive properties of working with sol-gels is the relative ease of which they are doped either with molecules intrinsically bonded into the matrix or particles simply embedded within. In this section the properties and application potential of these dopants will be discussed.

1.5.1 Rare Earth Metals

With the huge demand in modern life for optical communication technologies RE metals have come to the fore as dopants in optical devices due to their visible and NIR emission profiles and the opportunities for up-conversion using various sensitising agents. Lanthanide ions electronic structure is generally described by the Russel-Saunders coupling (LS coupling) approach. This approach takes each electron's contribution of orbital angular momentum (L) and electronic spin angular momentum (S). The total atomic angular momentum given by the coupling of L and S is described by J. These 3 quantum numbers are used to describe the energy levels via the term symbol. This has the general form of ${}^{2S+1}L_J$ where each f electron (only considered due to the electrons in inner shells contributing a constant energy shift) contributes a spin of

±1/2 which is used to get the spin multiplicity 2S+1, the value of L is determined and assigned a letter corresponding to the series;

L	0 1 2 3 4 5 6 7
Symbol	S P D F G H J K

J is given values according to the equation;

$$J = L+S, L+S-1, \ldots L-S$$

The values are then assigned in accordance with Hund's rules and the term symbol assembled.

Trivalent lanthanides have unique spectral properties with sharp absorption profiles due to their confined f→f transitions. These transitions are forbidden in accordance with selection rules however the rules are relaxed via vibrational coupling which breaks the symmetry enough to allow transitions similarly as in transitions metals or though not to the same extent leading to the less intense transitions observed for lanthanide metals. Fluorescence in the Ln^{3+} ions is facilitated from UV excitation of a ligand based electron into an excited state, this is followed by a non-radiative relaxation to an excited triplet state (inter system crossing ISC), which when it relaxes to the ground vibrational level of the excited triplet under goes a further ISC to the excited level of the Ln^{3+} ion and radiative decay to the ground level via an f→f transition. This mechanism is highly favoured for Tb^{3+} and Eu^{3+} given their excited levels are only slightly lower than the triplet states of typical ligands. The Eu^{3+} ion having transitions of $^5D_0 \rightarrow {}^7F_{4\text{-}0}$ has a bright red emission making it useful in a number of applications such as biological detection probes[42] and dye dopants for visual optics. The incorporation of these RE ions into silica glasses has allowed them to be used for many optic and photonic applications. In addition due to the ease of the sol-gel process in producing silica glasses with optical quality this approach is also cost effective.

The tendency also for Ln^{3+} ions to act as sensitizing agents for one another in silica glasses has become a widely investigated area, not least in the telecommunications industry and in the area of micro-lasing[43-44] with Er^{3+} sharply emitting at 1.54μm[45]. This proceeds via photon absorption and excitation of a sensitising ion and energy transfer into the excited states of the target emitting ion causing an increase in fluorescence yield. One of the most common combinations in RE metals is that of Yb^{3+} and Er^{3+} [46]. Here the Yb^{3+} ion absorbs at 980nm and transfers energy to the Er^{3+} which emits at 1.54μm (telecommunications wavelength) a simple energy level diagram is shown below in Figure 1.7.

Other combinations also lead to cooperative up-conversion between Ln^{3+} ions. This is the process by which 2 ions undergoes photon absorption in the NIR range and cooperative energy transfer to a higher excited state in the host ion for emission in the visible region. One example of this is Yb^{3+} to Eu^{3+} leading to higher intensity fluorescence yield[47-48] as demonstrated in the simple energy level diagram shown in Figure 1.7 below.

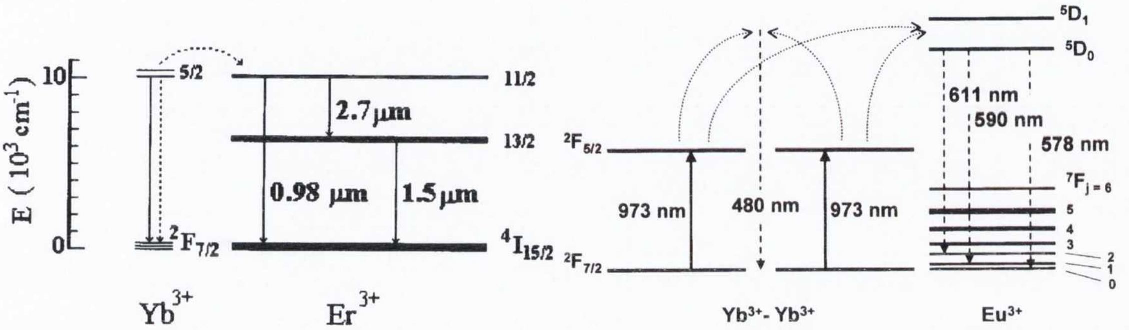

Figure 1.7: *Left; Energy level diagram showing energy transfer from* Yb^{3+} *to* Er^{3+} *ion* [46] *Right; Energy level diagram showing cooperative up-conversion from* Yb^{3+} *to* Eu^{3+} *ion* [47]

1.5.2 Gold Nanoparticles (AuNPs)

Gold has played a huge part in our development as a modern culture stretching back thousands of years through its aesthetic value in art and design through to its basis in helping shape our monetary systems. It has also long held a prominent position in research science and medicine dating back centuries in areas of alchemy and early medical theories (flawed basis as they may have been). Given metallic gold's prominence in society it is therefore unsurprising that it has played such a role in nearly all areas of modern culture, what is surprising is the role gold colloids and as an extension gold nanoparticles have played in everyday life and in the sciences from as far back as the 4th or 5th century BC. They were used to colour ceramics and create ruby glass, indeed the most famous example being the Lycurgus cup which contains Au colloids giving it its unique colour properties. Colloidal gold solutions have also historically been used for medicinal purposes for all manner of ailments.

In more recent times AuNPs have found application in a range of photonic, electronic and medical systems. This is largely due to their unique properties once they reach <20nm size range. Within this range quantum effects begin to dominate, where properties neither resemble exactly that of the bulk metal or molecular properties. One particular feature of metal nanoparticles within this size range is that of the plasmon resonance band which occurs when the de Broglie wavelength of the free electrons is greater than that of the nanoparticle, this allows the valence electrons (6s in the case of AuNPs) of the nanoparticle collectively oscillate at a given frequency (~520nm for 5-20nm range). The surface plasmon band (SPB) characterises the collective oscillation of the valence electrons at the surface of the nanoparticle which correlate to the incident exciting light. The SPB properties are well described by Mie theory, and it is known to be affected by the core size of the nanoparticle with decreasing intensity with decreasing size along with increasing bandwidth, it is also shifted due to the presence of surface ligands on the particle and the shape of the particle[49-50]. A typical absorbance spectrum of the SPB of AuNPs changing with changing pH causing a change to surface group alterations is shown in Figure 1.8. These properties enable a high degree and wide variety of application for AuNPs in electrochemistry, many areas of biology and especially bio-sensing (utilising the sensitivity of the SPB to detect changes and also as a body for resonant energy transfer to fluorescent markers[51]) and catalysis[49,52-54]. AuNPs hope to be utilised in this work for potential applications in improving immunoassays via better fluorescent marker signatures in antibody-antigen interactions and also in photo-catalysis by fabricating AuNP – TiO_2 composite nanostructures[55].

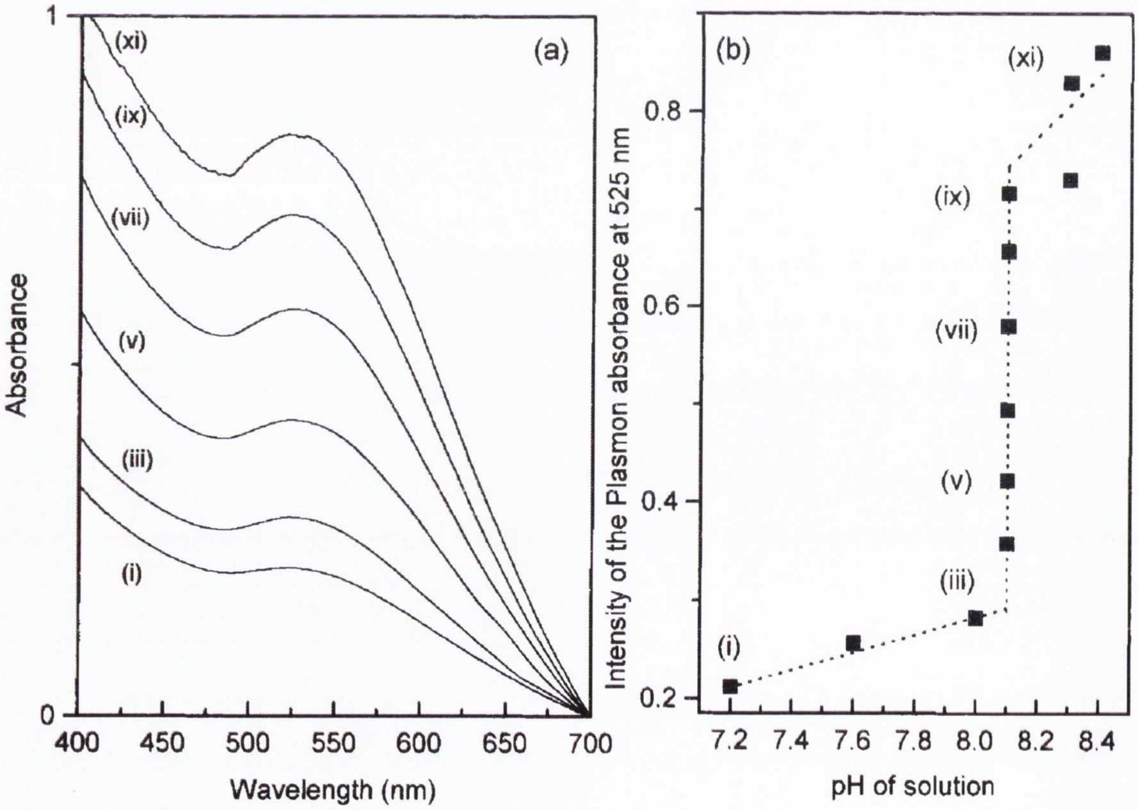

Figure 1.8: SPB of AuNPs changing with pH of solution (which causes the a change in the surface properties of the AuNPs)[50]

1.5.3 Magnetism and Magnetic Nanoparticles

Magnetic materials have long played a role in our society as a whole for many centuries and they have found countless applications in every aspect of our daily lives from the very large to sub-nanoscale devices which drive our world. Magnetisation originates most basically from the movement of electric charge either by electrons moving through atoms in a material or electrons spinning around an atomic nucleus, this movement induces a magnetic field. The magnetic field produced by a material can induce a field on other materials, the strength of which depends on the materials properties, it can also induce electric currents in materials. This relationship between electricity and magnetism referred to as electromagnetism is intrinsic to the study of magnetic materials and is generally well described by Maxwell's equations. A magnetic field has two main components; the *B-field* and the *H-field*. The relationship between the two fields changes depending on a number of factors. Generally the two fields are identical outside the magnetic material however internally the H-field is generally opposed to the B, this is due to the components that constitute the two fields, the B-field is concerned with the total current (both the external free currents and the internal bound currents) the H-field describes the external currents but treats the internal bound currents as magnetic charges, the relationship between the two is mathematically described by $H = \frac{B}{\mu_0} - M$ where μ_0 is the permeability of the material and M is the magnetisation. The magnetism M describes how strongly a region of the material is magnetised, the strength will largely depend of the type of material and the type of magnetisation it will undergo upon exposure to a magnetic field. The central type of magnetisation is termed *diamagnetism*, this is where an external magnetic field induces a force on the electrons orbital momentum in the material, this results in repulsion of the magnetic field. All materials undergo this type of interaction however only materials with no unpaired electrons can be diamagnetic; this effect is overwhelmed in materials with an unpaired electron in their electronic structure, which will be *paramagnetic* or *ferromagnetic* in nature. In such paramagnetic materials the unpaired electron is 'free' to align itself with the applied magnetic field (in orbitals with paired electrons the opposite spin (Pauli exclusion principle) ensures their respective magnetic contribution are cancelled out) resulting in a reinforcement of the field within the material. In ferromagnetism this effect is also observed however the aligned electrons also tend to align to each other. This result means that upon the removal of the external magnetic field the material will remain magnetised in its lower energy level with its electrons aligned parallel to each other. This effect can be undone by reaching the materials intrinsic Curie temperature (T_c), where the substance gains sufficient energy to overcome that gained by staying aligned and randomly re-orientates its electrons once more becoming demagnetised. Some materials also exhibit what is known as *anti-ferromagnetism* whereby the neighbouring spins of the unpaired electrons align anti-parallel to each other resulting in a net zero magnetisation, this can be overcome at the Néel temperature which is the temperature at which an anti-ferromagnetic material becomes paramagnetic). In certain substances both ferro and anti-ferro magnetism is observed, this phenomenon referred to as *ferrimagnetism* results when like in an anti-ferromagnetic material the spins align anti-parallel due to a mismatch within the material one alignment will be stronger than the other resulting in a net positive induced magnetism which behaves as a ferromagnet. This was first established by Louis Néel from 1936 onwards[56] where he proved the phenomenon was present in magnetite whereby the sub-lattices of Fe^{2+} and Fe^{3+} were the cause of the two differing strengths in alignments.

The formation of nanoparticles made of magnetic materials consisting of only a single magnetic domain can result in what is described as superparamagnetism. This type of magnetism results from when a nanocrystalline particle is small enough (usually <50nm depending on the material) to undergo reorientation of its magnetic alignment below the Curie temperature often at ambient temperatures meaning that generally the overall net magnetisation is zero[57]. This results in the material only becoming magnetic in the presence of an external magnetic field, once this field is removed it demagnetises. The time it takes to revert back to a demagnetised state depends on the average particle size and material properties. This superparamagnetism of magnetic nanoparticles (such as γ-Fe_2O_3, Fe_3O_4 and $CoFe_2O_4$) and ferro-fluids (liquid suspensions of superparamagnetic nanoparticles) along with their optimisation of production and ready functionalisation[58-60] to make them compatible with many media, make them attractive options in numerous bio-medical applications[61-73].

A common way to characterise ferromagnetic materials is a hysteresis loop carried out on a magnetometer, this maps the magnetisation of the sample with applied field. Most ferromagnetic materials show a trace pattern when the field is initially applied so that the reverse field when applied does not return along the same path due to the sample retaining magnetism hence the name hysteresis (typically demonstrated in Figure 1.9). The technique provides information such as the magnetisation saturation (M_s) which is the point at which the sample is fully magnetised (i.e. when nearly all the magnetic moments in the sample are aligned parallel to the external field). They also show the residual magnetism retained (M_r) in the sample after return to zero applied field and the coercivity (H_c) which is the force that would be needed to be applied to the sample to remove the remnant magnetisation. However as can be seen in Figure 1.9 (right), the 'hysteresis loop' for a superparamagnetic particle is quite different as it passes back through zero magnetisation at zero applied field showing that all magnetism is lost once the external field is removed as described above.

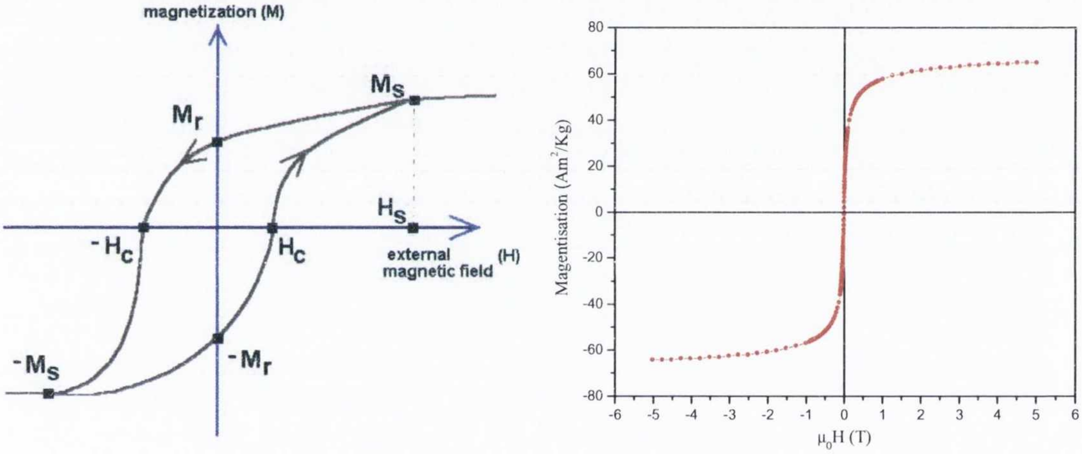

Figure 1.9: Left; Diagram of hysteresis loop showing main points of interest[74] *Right; Typical hysteresis loop of superparamagnetic NP*

1.5.4 Quantum Dots (QDs)

The properties of binary semiconductor alloys as with many materials can differ markedly between the bulk and nanosized regime in some of their properties. This is particularly true when it comes to the class of II-VI semiconductors (i.e. Cd,Zn-(S,Te,Se) among others) when fabricated as nanocrystals which can display interesting optical properties due to their size. In the bulk these materials behave similarly to many other direct bandgap semiconductors in their properties. Semiconductors as the name suggests are classed in between insulators and conductors. This means the gap between the valence and conduction band of the material is such that such that if raised to a certain temperature or biased sufficiently the valence electrons gain enough energy to be promoted to the conduction band of the material allowing it to act as a conductor (albeit a relatively poor one). Direct bandgap semiconductors have a band structure such that they do not require a phonon to assist in a transition from valence to conduction band. This allows them to undergo radiative recombination whereby an optically excited electron falls back down to the valence band (or electron hole recombination) resulting in the emission of a photon. Similarly to other semiconductors they can be doped to alter the band structure for desired results. As mentioned these semiconductors can also have their valence electrons promoted via absorbed incident radiation, a promotion of an electron into the conduction band results in what is commonly referred to as an exciton. An exciton is described as the entity that exists between the promoted electron and the positive 'hole' left in its wake. It is a loosely bound state in semiconductors which is bound over a lattice constant of the crystal (a so called Wannier exciton). It is often compared in state to that of a hydrogen atom held together by coulomb forces, however given the screening of these forces in the material over the longer length scale the binding energy is much lower than that of hydrogen (13.5eV compared to typically 0.01-0.05eV).

When the semiconductor is reduced in size to a nanocrystal such that its diameter is smaller than the Bohr radius of the exciton (typically ~7.3nm for CdTe and ~5.3nm in CdSe QDs) the continuous optical transitions become quantized and electronic structure of the crystal become size dependant, this semiconductor nanocrystal is now commonly referred to as a quantum dot. The size decrease results in an increase in the exciton energy and is observed as a blue shift in the optical absorption of the material this can be observed visually with a change in colour of the materials at nanocrystal size[75]. The absorption spectra of these materials are one of the most common forms of characterisation to visualise their transition to the region of quantized transitions. As mentioned the enlargement of the bandgap as the nanocrystal reduces in size is seen as a blue shift in the peak absorption wavelength of the material, however the discrete quantized states are not easily visible in normal conditions and the spectrum suffers from homogeneous and inhomogeneous line broadening due to exciton phonon coupling, differing size distribution, shape of the NP and surface defects. So far the radiative emission properties of the QDs have not been discussed, however it this aspect that makes them attractive entities in many areas. The PL emission is observed by exciting the QDs at a specific wavelength at or close to the absorption maxima as determined by UV-vis spectra. Once again information on the QDs other than their emission maxima can be determined from the scan such as probing the different size QDs by choosing different excitation wavelengths and giving information as to the degree of defects and nature of the radiative decay pathways in comparison with the absorption spectra. As mentioned previously absorption of radiation by a QD results in the promotion of an electron to the conduction band and the formation of an exciton, this exciton is not permanently stable in the QD and can recombine resulting in the emission of a photon corresponding to the bandgap energy required to drop back to the valence band (as simply demonstrated in the energy level diagram in Figure 1.10, however these transitions are generally quite complex depending on a number of factors within the QD and not all absorptions result in radiative recombinations.

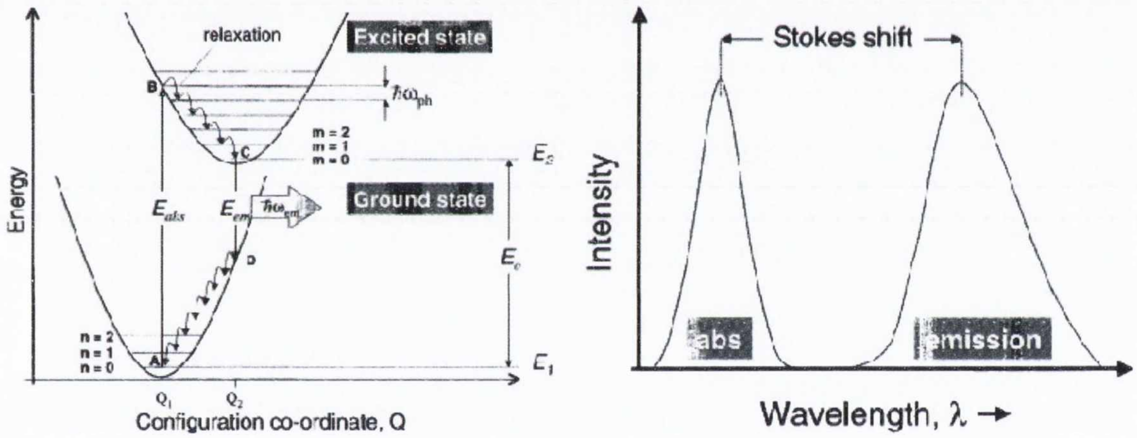

Figure 1.10: Simple diagrams of left; absorption and emission pathways in energy level diagram and right; demonstration of stokes shift between absorption and emission peaks[76]

The emissive character of the QDs results from differing radiation pathways, intrinsic luminescence whereby the emission is purely due to the dots themselves and have a very small Stokes shift (some shift is generally inevitable due to energy loss to the surroundings). However due to the small size of QDs and their high surface to volume ratio there are often defects on the surface of the QD which create 'trap sites' for the exciton which can result in longer lifetimes for the exciton and different decay pathways for it (both radiative and non-radiative) by altering the bandgap for recombination by introducing intermediate 'steps' lowering the energy of the gap and thus changing the emission profile of the QD, this results in a broad emission peak with larger stokes shift[77]. QDs with good surface passivation via care during fabrication can help correct this broad emission[78]. However this surface sensitivity can also lead to interesting applications by interacting with stabilizing agents[79-80] and driving research into core-shell structures[81]. With developments in the fabrication process and surface coatings of various types of QD it is possible to tune the emission wavelength to a desired maximum (demonstrated in Figure 1.11) essentially designing the optical and chemical properties of the NP for any desired application. Their intense and tuneable emission properties while having greater resistance to photo-bleaching compared to commercial dyes makes them attractive as fluorophores in solar cells[82-84] as sensitizers and in bio-medical applications (with surface protection to help toxicity) as fluorescent markers to assist biological imaging[85-86].

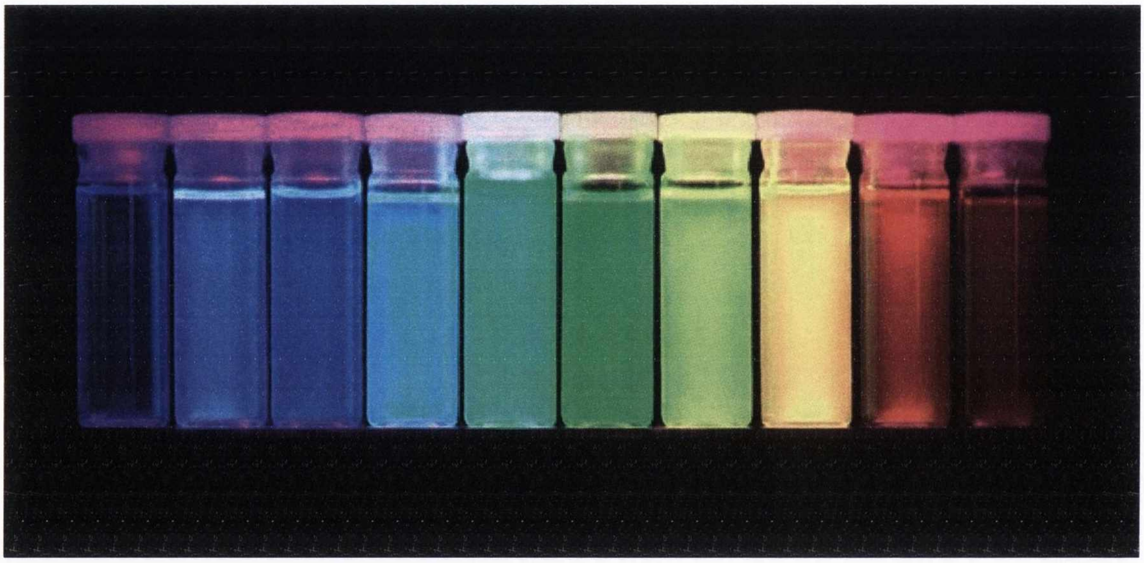

Figure 1.11: Photo showing QD solutions emitting at various wavelength under UV radiation[87]

1.6 Aims and Objectives of the Project

The main aim of this project is to develop new multifunctional "1D" micro- and nano- structures with high aspect ratio and investigate them using various instrumental techniques. These structures are expected to find a range of potential biomedical, photonic and photocatalytic applications.

One of the objectives is to prepare silica-based microfibres and microtubes using sol-gel processing and porous templates. We plan to develop optical quality silica/aluminosilicate microtubes via sol-gel infiltration into a porous membrane. Doping of tubes will consist of RE metals such as europium and also quantum dots. The work will also include photo-physical characterisation of the materials, design and fabrication of a prototype of a new micro-cylindrical emitting device for photonic applications. An incorporation of micro-spheres which can exhibit WGM into the tubes will also be performed. These structures are expected to demonstrate interesting optical effects due to their luminescence properties.

Another objective of the project is to produce fluorescent/magnetic silica and polystyrene nanowires. The fabrication of the nanowires will be achieved via infiltration and wetting of porous anodised aluminium oxide (AAO) membranes. Silica nanowires can be made using the sol-gel process in a similar style to the microtubes. These wires have been demonstrated to have potential in bio-medical applications such as biological tagging and sensors via functionalisation and surface manipulation. We plan to load silica or polystyrene nanowires with magnetic nanoparticles and/or a fluorescent material (e.g. RE, dye or quantum dots) and examine both their magnetic and fluorescence properties. Initial work on the nanowires will be concentrated on creating intrinsically emitting silica wires and using fluorescent dyes and then with quantum dots. These multimodal nanowires will then be functionalised with antibodies and used for biological testing in live cell cultures.

Finally we plan to prepare novel titania, silica/titania and titania/Au nanostructures and investigate their optical and photocatalytic properties. In overall we believe that this work will contribute to further development of new photonic materials with a range of potential applications in optics and biotechnology.

1.7 References:

1 Balakrishnan, S. *et al.* Confined optical modes and amplified spontaneous emission from a microtube cavity formed by vacuum assited filtration. *Appl. Phys. Lett.* **89**, 143113 (2006).

2 Suber, L., Imperatori, P., Ausanio, G., Fabbri, F. & Hofmeister, H. Synthesis, Morphology, and Magnetic Characterization of Iron Oxide Nanowires and Nanotubes. *J. Phys. Chem. B* **109**, 7103-7109 (2005).

3 Song, G., She, X., Fu, Z. & Li, J. Preparation of good mechanical property polystyrene nanotubes with array structure in anodic aluminum oxide template using simple physical techniques. *J. Mat. Res.* **19**, 3324-3328 (2004).

4 Steinhart, M., Wehrspohn, R. B., Gösele, U. & Wendorff, J. H. Nanotubes by Template Wetting: A Modular Assembly System. *Angewandte Chemie International Edition* **43**, 1334-1344 (2004).

5 Brinker, J. C. & Scherer, G. W. *The Physics and Chemistry of Sol-Gel Processing*. (Academic Press Limited, 1990).

6 Silva, C. R. & Airoldi, C. Acid and Base Catalysts in the Hybrid Silica Sol-Gel Process. *Journal of Colloid and Interface Science* **195**, 381-387 (1997).

7 Livage, J. & Sanchez, C. Sol-gel chemistry. *Journal of Non-Crystalline Solids* **145**, 11-19 (1992).

8 Green, W. H., Le, K. P., Grey, J., Au, T. T. & Sailor, M. J. White Phosphors from a Silicate-Carboxylate Sol-Gel Precursor That Lack Metal Activator Ions. *Science* **276**, 1826-1828, doi:10.1126/science.276.5320.1826 (1997).

9 Karthikeyan, A. & Almeida, R. M. Phase separation in SiO2-TiO2 gel and glassy films studied by AFM and TEM. *Journal of Materials Research* **16**, 1626-1631 (2001).

10 Karthikeyan, A. & Almeida, R. M. Crystallization of SiO2-TiO2 glassy films studied by atomic force microscopy. *Journal of Non-Crystalline Solids* **274**, 169-174 (2000).

11 Moon, H.-J., Chough, Y.-T. & An, K. Cylindrical Microcavity Laser Based on the Evanescent-Wave-Coupled Gain. *Phys. Rev. Lett.* **85**, 3161 (2000).

12 Ilchenko, V. S. & Matsko, A. B. Optical resonators with whispering-gallery modes-part II: applications. *Selected Topics in Quantum Electronics, IEEE Journal of* **12**, 15-32 (2006).

13 Rayleigh, L. The Problem of the Whispering Gallery *Philosophy Magazine* **20**, 1001-1004 (1910).

14 Garrett, C. G. B., Kaiser, W. & Bond, W. L. Stimulated Emission into Optical Whispering Modes of Spheres. *Physical Review* **124**, 1807 (1961).

15 Benner, R. E., Barber, P. W., Owen, J. F. & Chang, R. K. Observation of Structure Resonances in the Fluorescence Spectra from Microspheres. *Physical Review Letters* **44**, 475 (1980).

16 Matsko, A. B. & Ilchenko, V. S. Optical resonators with whispering-gallery modes-part I: basics. *Selected Topics in Quantum Electronics, IEEE Journal of* **12**, 3-14 (2006).

17 Vollmer, F. & Arnold, S. Whispering-gallery-mode biosensing: label-free detection down to single molecules. *Nat Meth* **5**, 591-596 (2008).

18 Gorodetsky, M. L., Savchenkov, A. A. & Ilchenko, V. S. Ultimate Q of optical microsphere resonators. *Opt. Lett.* **21**, 453-455 (1996).

19 Vahala, K. J. Optical microcavities. *Nature* **424**, 839-846 (2003).

20 Zhang, M., Bando, Y. & Wada, K. Silicon dioxide nanotubes prepared by anodic alumina as templates. *Journal of Materials Research* **15**, 387-392 (2000).

21 Tang, Z. & Kotov, N. A. One-Dimensional Assemblies of Nanoparticles: Preparation, Properties, and Promise. *Adv. Mat.* **17**, 951-962 (2005).

22 Borissov, D., Isik-Uppenkamp, S. & Rohwerder, M. Fabrication of Iron Nanowire Arrays by Electrodeposition into Porous Alumina. *The Journal of Physical Chemistry C* **113**, 3133-3138, doi:10.1021/jp809202h (2009).

23 Kato, S., Kitazawa, H. & Kido, G. Magnetic properties of Ni nanowires in porous alumina arrays. *Journal of Magnetism and Magnetic Materials* **272-276**, 1666-1667 (2004).

24 Phok, S. & et al. Copper indium diselenide nanowire arrays by electrodeposition in porous alumina templates. *Nanotechnology* **18**, 475601 (2007).

25 Zhang, X., Li, D., Bourgeois, L., Wang, H. & Webley, P. A. Direct Electrodeposition of Porous Gold Nanowire Arrays for Biosensing Applications. *ChemPhysChem* **10**, 436-441 (2009).

26 Li, G. *et al.* High-temperature photoluminescence in sol-gel silica containing SiC/C nanostructures. *Appl. Phys. Lett.* **76** (2000).

27 Zhao, J. *et al.* Intense short-wavelength photoluminescence from thermal SiO_2 films co-implanted with Si and C ions. *Appl. Phys. Lett.* **73** (1998).

28 Karakuscu, A., Guider, R., Pavesi, L. & Sorarù, G. D. White Luminescence from Sol–Gel-Derived SiOC Thin Films. *Journal of the American Ceramic Society* **92**, 2969-2974, doi:10.1111/j.1551-2916.2009.03343.x (2009).

29 Yao, B., Shi, H., Zhang, X. & Zhang, L. Ultraviolet photoluminescence from nonbridging oxygen hole centers in porous silica. *Appl. Phys. Lett.* **78**, 174 (2001).

30 Haiping, H., Yuxia, W. & Honggao, T. Intense ultraviolet and green photoluminescence from sol-gel derived silica containing hydrogenated carbon. *Journal of Physics: Condensed Matter*, 11867 (2002).

31 Glinka, Y. D. & Sheng-Hsien, L. The photoluminescence from hydrogen-related species in composites of SiO_2 nanoparticles. *Appl. Phys. Lett.* **75**, 778 (1999).

32 Glinka, Y. D., Lin, S. H., Hwang, L. P. & Chen, Y. T. Photoluminescence from mesoporous silica: Similarity of properties to porous silicon. *Appl. Phys. Lett.* **77** (2000).

33 Glinka, Y. D. *et al.* Photoluminescence from mesoporous silica akin to that from nanoscale silicon: the nature of light-emitters. *Chemical Physics Letters* **358**, 180-186 (2002).

34 Zyubin, A. S., Mebel, A. M., Lin, S. H. & Glinka, Y. D. Photoluminescence of silanone and dioxasilyrane groups in silicon oxides: A theoretical study. *Journal of Chemical Physics* **116**, 9889 (2002).

35 Glinka, Y. D., Lin, S.-H. & Chen, Y.-T. Time-resolved photoluminescence study of silica nanoparticles as compared to bulk type-III fused silica. *Physical Review B* **66**, 035404 (2002).

36 Uchino, T., Kurumoto, N. & Sagawa, N. Structure and formation mechanism of blue-light-emitting centers in silicon and silica-based nanostructured materials. *Physical Review B* **73**, 233203 (2006).

37 Nishimura, A., Sagawa, N. & Uchino, T. Structural Origin of Visible Luminescence from Silica Based Organic-Inorganic Hybrid Materials. *J. Phys. Chem. C* **113**, 4260-4262, doi:10.1021/jp900911v (2009).

38 Aboshi, A., Kurumoto, N., Yamada, T. & Uchino, T. Influence of Thermal Treatments on the Photoluminescence Characteristics of Nanometer-Sized Amorphous Silica Particles. *The Journal of Physical Chemistry C* **111**, 8483-8488, doi:10.1021/jp0718505 (2007).

39 Hayakawa, T., Hiramitsu, A. & Nogami, M. White light emission from radical carbonyl-terminations in Al_2O_3--SiO_2 porous glasses with high luminescence quantum efficiencies. *Appl. Phys. Lett.* **82**, 2975-2977 (2003).

40 Lin, C. *et al.* Bluish-White Emission from Radical Carbonyl Impurities in Amorphous Al2O3 Prepared via the Pechini-Type Sol−Gel Process. *Inorganic Chemistry* **47**, 49-55, doi:10.1021/ic700652v (2007).

41 Yoldas, B. E. Thermochemically induced photoluminescence in sol-gel-derived oxide networks. *Journal of Non-Crystalline Solids* **147-148**, 614-620 (1992).

42 Supkowski, R. M., Bolender, J. P., Smith, W. D., Reynolds, L. E. L. & Horrocks Jr, W. D. Lanthanide ions as redox probes of long-range electron transfer in proteins. *Coordination Chemistry Reviews* **185-186**, 307-319 (1999).

43 Hsu, H.-S., Cai, C. & Armani, A. M. Ultra-low-threshold Er:Yb sol-gel microlaser on silicon. *Opt. Express* **17**, 23265-23271 (2009).

44 Laporta, P., Taccheo, S., Longhi, S., Svelto, O. & Svelto, C. Erbium-ytterbium microlasers: optical properties and lasing characteristics. *Optical Materials* **11**, 269-288 (1999).

45 Benatsou, M., Capoen, B., Bouazaoui, M., Tchana, W. & Vilcot, J. P. Structural and Optical Properties of Sol-Gel Derived Aluminosilicate Planar Waveguides Doped with Er3+ Ions. *Journal of Sol-Gel Science and Technology* **13**, 529-533 (1998).

46 da Vila, L. D., Gomes, L., Tarelho, L. V. G., Ribeiro, S. J. L. & Messadeq, Y. Mechanism of the Yb–Er energy transfer in fluorozirconate glass. *Journal of Applied Physics* **93**, 3873 (2003).

47 Maciel, G. S., Biswas, A. & Prasad, P. N. Infrared-to-visible Eu3+ energy upconversion due to cooperative energy transfer from an Yb3+ ion pair in a sol-gel processed multi-component silica glass. *Optical Communications* **178**, 65-69 (2000).

48 Dwivedi, Y., Thakur, S. N. & Rai, S. B. Study of frequency upconversion in Yb3+/Eu3+ by cooperative energy transfer in oxyfluoroborate glass matrix. *Appl. Phys. B* **89**, 45-51 (2007).

49 Daniel, M.-C. & Astruc, D. Gold Nanoparticles: Assembly, Supramolecular Chemistry, Quantum-Size-Related Properties, and Applications toward Biology, Catalysis, and Nanotechnology. *Chemical Reviews* **104**, 293-346, doi:10.1021/cr030698+ (2003).

50 Johnson, S. R., Evans, S. D. & Brydson, R. Influence of a Terminal Functionality on the Physical Properties of Surfactant-Stabilized Gold Nanoparticles. *Langmuir* **14**, 6639-6647, doi:10.1021/la9711342 (1998).

51 Paresh Chandra, R. & et al. A gold-nanoparticle-based fluorescence resonance energy transfer probe for multiplexed hybridization detection: accurate identification of bio-agents DNA. *Nanotechnology* **18**, 375504 (2007).

52 Jain, P. K., Lee, K. S., El-Sayed, I. H. & El-Sayed, M. A. Calculated Absorption and Scattering Properties of Gold Nanoparticles of Different Size, Shape, and Composition: Applications in Biological Imaging and Biomedicine. *The Journal of Physical Chemistry B* **110**, 7238-7248, doi:10.1021/jp057170o (2006).

53 Schubert, M. M. *et al.* CO Oxidation over Supported Gold Catalysts--"Inert" and "Active" Support Materials and Their Role for the Oxygen Supply during Reaction. *Journal of Catalysis* **197**, 113-122 (2001).

54 Buso, D., Pacifico, J., Martucci, A. & Mulvaney, P. Gold-Nanoparticle-Doped TiO_2 Semiconductor Thin Films: Optical Characterization. *Advanced Functional Materials* **17**, 347-354 (2007).

55 Lidia, A. & et al. Photocatalytic and antibacterial activity of TiO 2 and Au/TiO 2 nanosystems. *Nanotechnology* **18**, 375709 (2007).

56 Coey, J. M. D. Louis Néel: Retrospective (invited). *Journal of Applied Physics* **93**, 8224-8229 (2003).

57 An-Hui, L., Salabas, E. L. & Ferdi, S. Magnetic Nanoparticles: Synthesis, Protection, Functionalization, and Application. *Angewandte Chemie International Edition* **46**, 1222-1244 (2007).

58 Mikhaylova, M. *et al.* Superparamagnetism of Magnetite Nanoparticles: Dependence on Surface Modification. *Langmuir* **20**, 2472-2477, doi:10.1021/la035648e (2004).

59 Zhang, M. & et al. Synthesis and characterization of monodisperse ultra-thin silica-coated magnetic nanoparticles. *Nanotechnology* **19**, 085601 (2008).

60 Santra, S. *et al.* Synthesis and Characterization of Silica-Coated Iron Oxide Nanoparticles in Microemulsion: The Effect of Nonionic Surfactants. *Langmuir* **17**, 2900-2906, doi:10.1021/la0008636 (2001).

61 Neuberger, T., Schöpf, B., Hofmann, H., Hofmann, M. & von Rechenberg, B. Superparamagnetic nanoparticles for biomedical applications: Possibilities and limitations of a new drug delivery system. *Journal of Magnetism and Magnetic Materials* **293**, 483-496 (2005).

62 Kückelhaus, S. *et al.* In vivo investigation of cobalt ferrite-based magnetic fluid and magnetoliposomes using morphological tests. *Journal of Magnetism and Magnetic Materials* **272-276**, 2402-2403 (2004).

63 Fortin, J.-P., Gazeau, F. & Wilhelm, C. Intracellular heating of living cells through Néel relaxation of magnetic nanoparticles. *European Biophysics Journal* **37**, 223-228 (2008).

64 Baldi, G. *et al.* Synthesis and Coating of Cobalt Ferrite Nanoparticles: A First Step toward the Obtainment of New Magnetic Nanocarriers. *Langmuir* **23**, 4026-4028, doi:10.1021/la063255k (2007).

65 Tartaj, P., Morales, M. P., Gonzalez-Carreno, T., Veintemillas-Verdaguer, S. & Serna, C. J. Advances in magnetic nanoparticles for biotechnology applications. *J Magn Magn Mater* **290**, 28 - 34 (2005).

66 Saiyed, Z. M., Telang, S. D. & Ramchand, C. N. Application of magnetic techniques in the field of drug discovery and biomedicine. *BioMagn Res Technol* **1**, 1 - 8 (2003).

67 Pankhurst, Q. A., Connolly, J., Jones, S. K. & Dobson, J. Applications of magnetic nanoparticles in biomedicine. *J Phys D Appl Phys* **36**, R167 - R181 (2003).

68 Salata, O. V. Applications of nanoparticles in biology and medicine. *J Nanobiotech* **2**, 1 - 6 (2004).

69 Berry, C. C., Wells, S., Charles, S., Aitchison, G. & Curtis, A. S. G. Cell response to dextran-derivatised iron oxide nanoparticles post internalisation. *Biomaterials* **25**, 5405 - 5413 (2004).

70 Lara, O., Tong, X., Zborowski, M. & Chalmers, J. J. Enrichment of rare cancer cells through depletion of normal cells using density and flow-through, immunomagnetic cell separation. *Experimental Hematology* **32**, 891-904 (2004).

71 Bulte, J. W. M. Magnetic nanoparticles as markers for cellular MR imaging. *J Magn Magn Mater* **289**, 423 - 427 (2005).

72 Dutz, S. *et al.* Magnetic nanoparticles for biomedical heating applications. *Z Phys Chem* **220**, 145 - 151 (2006).

73 Son, S. J., Reichel, J., He, B., Schuchman, M. & Lee, S. B. Magnetic Nanotubes for Magnetic-Field-Assisted Bioseparation, Biointeraction, and Drug Delivery. *J. Am. Chem. Soc.* **127**, 7316-7317 (2005).

74 Geerts, D. I. W. J. *http://uweb.txstate.edu/~wg06/manuals/kerrtracer/KerrHome.htm*.

75 Wang, Y. & Herron, N. Nanometer-sized semiconductor clusters: materials synthesis, quantum size effects, and photophysical properties. *The Journal of Physical Chemistry* **95**, 525-532, doi:10.1021/j100155a009 (1991).

76 Yoffe, A. D. Semiconductor quantum dots and related systems: electronic, optical, luminescence and related properties of low dimensional systems. *Advances in Physics* **50**, 1 - 208 (2001).

77 Burda, C., Chen, X., Narayanan, R. & El-Sayed, M. A. Chemistry and Properties of Nanocrystals of Different Shapes. *Chemical Reviews* **105**, 1025-1102, doi:10.1021/cr030063a (2005).

78 Murray, C. B., Norris, D. J. & Bawendi, M. G. Synthesis and characterization of nearly monodisperse CdE (E = sulfur, selenium, tellurium) semiconductor nanocrystallites. *Journal of the American Chemical Society* **115**, 8706-8715, doi:10.1021/ja00072a025 (1993).

79 Elliott, S. D., Moloney, M. c. l. P. & Gun'ko, Y. K. Chiral Shells and Achiral Cores in CdS Quantum Dots. *Nano Letters* **8**, 2452-2457, doi:10.1021/nl801453g (2008).

80 Lemon, B. I. & Crooks, R. M. Preparation and Characterization of Dendrimer-Encapsulated CdS Semiconductor Quantum Dots. *Journal of the American Chemical Society* **122**, 12886-12887, doi:10.1021/ja0031321 (2000).

81 Reiss, P., Bleuse, J. & Pron, A. Highly Luminescent CdSe/ZnSe Core/Shell Nanocrystals of Low Size Dispersion. *Nano Letters* **2**, 781-784, doi:10.1021/nl025596y (2002).

82 Ernst, K. *et al.* Contacts to a solar cell with extremely thin CdTe absorber. *Thin Solid Films* **387**, 26-28 (2001).

83 Larramona, G. *et al.* Nanostructured Photovoltaic Cell of the Type Titanium Dioxide, Cadmium Sulfide Thin Coating, and Copper Thiocyanate Showing High Quantum Efficiency. *Chem. Mater.* **18**, 1688-1696 (2006).

84 Seabold, J. A. *et al.* Photoelectrochemical Properties of Heterojunction CdTe/TiO2 Electrodes Constructed Using Highly Ordered TiO2 Nanotube Arrays. *Chem. Mater.* **20**, 5266-5273 (2008).

85 Byrne, S. J. *et al.* Optimisation of the synthesis and modification of CdTe quantum dots for enhanced live cell imaging. *Journal of Materials Chemistry* **16**, 2896-2902 (2006).

86 Wolcott, A. *et al.* Silica-Coated CdTe Quantum Dots Functionalized with Thiols for Bioconjugation to IgG Proteins. *The Journal of Physical Chemistry B* **110**, 5779-5789, doi:10.1021/jp057435z (2006).

87 Hickey, H. & Gao, X. http://uwnews.org/uweek/article.aspx?id=42599, 2008).

Chapter 2

Preparation and characterisation of silica / aluminosilicate microtubes

2.1 Introduction

Porous materials as described previously can serve as perfect hosts for one dimensional (high aspect ratio) materials. Microchannel glass is potentially a suitable material for developing optical quality silica/aluminosilicate microtubes due to their micrometre pore diameter, high aspect ratio and highly ordered smooth walls[1-2]. Cylindrical optical microcavities are of particular interest due to their potential application as microcavity resonators in photonics. Microcavity resonators that can store and recirculate electromagnetic energy at optical frequencies have many uses, including lasing, optical amplification, high-precision spectroscopy, sensing, signal processing and filtering[3]. Optical microcavity resonators have quality factors (Qs) that are higher by several orders of magnitude compared to other electromagnetic devices. Today, commercially available devices typically have Qs ranging from 102 to 104 approximately. The highest Q resonances encountered in these microcavities are due to optical whispering-gallery-modes (WGM) that are supported within the microcavities. The utility of WGM-based devices depends on accurate engineering of the optical cavity and on the feasibility for integration in optical communication networks. While traditional lasers built from discrete components use macroscopic spherical mirrors, microcavity lasers do not. Non planar quantum well microcavity lasers have been actively studied and can show low threshold operation[4] but their progress has been delayed by the fabrication limitations. Another approach for the optical design is the fabrication of photonic crystals which however involves complex and expensive fabrication strategies. Other methods of production of high Q WGM resonators include photolithography based micro-fabrication[5-6] and fusing the tip of a silica fibre to create a fused silica microsphere[7-8], however these methods tend to only produce 1 or few ideal devices and/or tend to be expensive. Thus new methods for the cost effective fabrication of microcavity light emitting devices structurally compatible with telecommunication optical fibres would have tremendous commercial potential.

In this project the microtubes were fabricated using a vacuum assisted infiltration method of sol-gel into microchannel glass membranes Figure 2.1 as previously described in reports by our research group[9-10]. Microchannel glass provided a highly suitable environment for the formation of microtubes within the pores due to its high pore regularity and smooth pore walls. The process of infiltration is complicated as the viscosity of the sol is constantly changing as the reaction proceeds therefore the reaction must be carefully monitored and checked until the right viscosity is achieved for filling of the pores and also to check that the reaction has proceeded sufficiently to ensure the gel will form a thick enough coating once infiltrated. The sol should be infiltrated shortly before gelation point therefore the very viscous sol must be pulled through the pores under vacuum. This results in a coating of the pore walls with sol-gel which dries slowly over time becoming a xerogel. The formation of silica/aluminosilicate microtubes by vacuum filtration of the gel can be explained by the fact that the cohesive driving forces for complete microchannel filling are substantially weaker than the adhesive forces to the pore walls. Similar phenomena have been reported for the formation of polymer nanotubes by wetting of ordered porous templates using a polymer melt[11]. The infiltrated membrane is then annealed at a given temperature to shrink the tubes of the pore walls so that upon breakage of the membrane the tubes fall easily from the pores. The microtubes can be released over a suitable substrate to be examined in situ.

The ease of doping sol-gels via addition of alkoxide precursors and various nanoparticles allows the microtubes to be tailored for various applications. The following sections will build on previous work done in the group in regards to microtube fabrication and emission properties and explore the properties of RE metal and CdTe QD doped microtubes and also intrinsically luminescent microtubes due to defect emission. The interaction of the doped microtubes and of microspheres will also be examined using solid state PL.

Figure 2.1: Optical images of MCG membranes with different pore diameters

2.2 Preparation and characterisation of europium doped aluminosilicate microtubes

The aluminosilicate microtubes were prepared by a 2-step acid catalysed reaction using TEOS as the silica precursor. Firstly partial hydrolysis of the TEOS is preformed with an alcohol, water and HCl solution. Aluminium iso-propoxide is then added as an alumina co-doping precursor along with europium acetate hydrate. Secondly the 3 partially hydrolysed constituents are then condensed into a gel by addition of a second solution of alcohol, water and HCl. The sol is infiltrated under vacuum assist into MCG membranes as discussed above. Annealing the MCG membrane at 500 °C for 1 hour results in the shrinking of the tubes off the pore walls easing their release from the MCG.

The ratios of Si:Al:Eu^{3+} can be altered to desired specification by simply changing precursor quantities. The addition of Al^{3+} into the silica matrix has been shown to act as a network modifier and to facilitate the separation of Eu^{3+} species by preferentially binding to them by the Al forming a solvating sphere around the rare earth ion[12] and to thus prevent quenching of the luminescence due to Eu^{3+} clustering in the matrix[13-14] as shown in Figure 2.2 below. Previous studies have shown the optimum ratio for this system is around 10:1 (Al:Eu)[13,15-16]. Aluminosilicate gels have also been shown to have a smaller pore size and enhanced condensation time[17-18] which is preferable when working with gels to infiltrate into porous materials as the viscosity (as mentioned previously) needs to be right for the tube to form within the MCG pores.

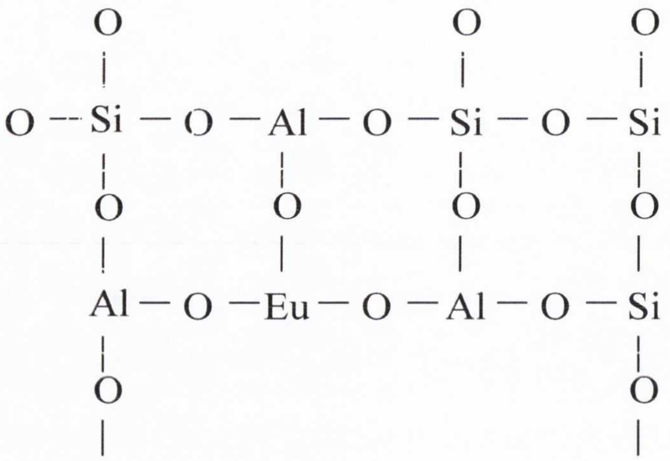

Figure 2.2: Schematic of silica matrix showing Al^{3+} and Eu^{3+} dopants

The bulk xerogel samples were annealed and tested to ascertain if they exhibited Eu^{3+} emission and to compare it to that of the corresponding microtube samples. The solid state PL spectra (procedure for obtaining solid state PL spectra is explained in Section 6.2.2) in Figure 2.3 of an annealed Eu doped gel at 1000 °C showed characteristic Eu^{3+} broad emission peaks. These peaks correspond to transitions of trivalent Eu namely; $^5D_0$ - $^7F_0$ at 572 nm, $^5D_0$ - $^7F_1$ at 599 nm, $^5D_0$ - $^7F_2$ at 621 nm, $^5D_0$ - $^7F_3$ at 656 nm and $^5D_0$ - $^7F_4$ at 703 nm. A high annealing temperature is necessary to observe strong Eu^{3+} emission due to the fact that un-annealed sol-gel glasses have large amounts of hydroxyl group defects within the matrix cause quenching of the emission of Eu[19]. Annealing of the gels results in the condensation of silanols to form siloxane bonds[20] thus removing hydroxyl groups from the matrix, resulting in the decrease of quenching of the Eu^{3+} species. The intense peak at 621 nm is most likely attributed to this transition being hypersensitive[19] which may account for its increased intensity due to its surroundings. However there are also some reports that it might be due to an energy transfer from some Eu^{2+} and Eu^{3+} [21-24]. The peaks demonstrated significant line broadening when compared to that of the precursor (black spectra in Figure 2.3) and typically of rare earths in crystalline samples. This effect is commonly observed in glass doped with RE metals[19]. It is due to two effects, the first; homogenous broadening which results from lifetime broadening between stark components in different J multiplets, which is due to phonon induced transitions between stark levels within a multiplet[25]. This broadening process and its components are heavily influenced by temperature effects. The second is inhomogenous broadening which results from the difference in the individual ions environment in the glass so that the exciting wavelength interacts slightly differently with each ion[25].

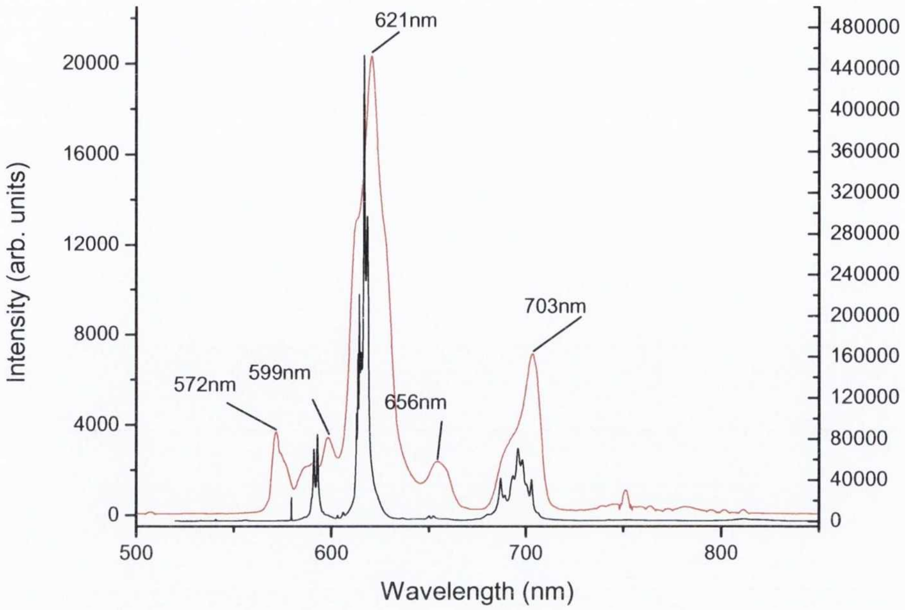

Figure 2.3: PL spectra of bulk aluminosilicate gel showing characteristic Eu^{3+} peaks (Red) and of Eu(III) acetate hydrate (black) (excitation at 457 nm)

2.2.1 Characterisation of microtubes by microscopy

The microtubes shown in the following section were prepared as above with an Si:Al of 8.8:1.2 and a 0.73 mol% of Eu. The MCG membrane had a pore diameter of 10 µm. Subsequent to annealing of the infiltrated matrix it was examined under optical microscopy to ascertain if tubes could be observed in the pores. Upon inspection and shown in Figure 2.4 and Figure 2.5 it can be clearly seen that microtubes occupy the pores and seemed to have shrunk off the pore walls upon annealing.

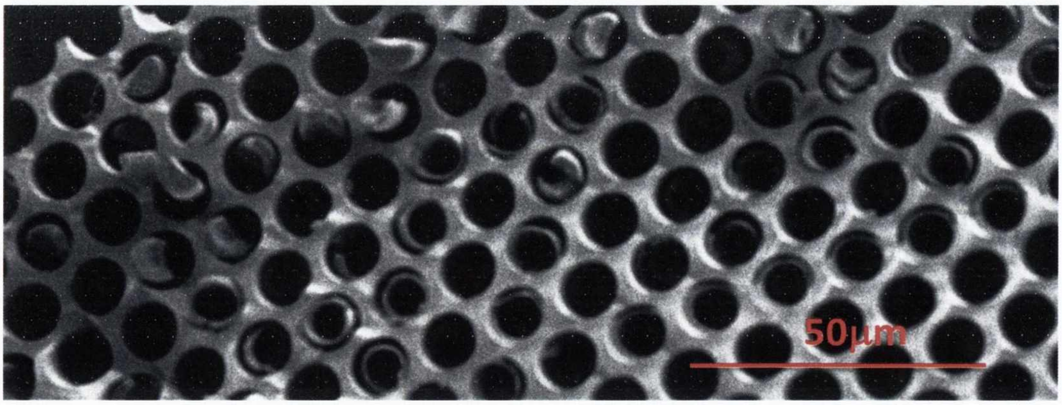

Figure 2.4: SEM image of microtubes inside MCG membrane

The tubes can be released over any suitable substrate for examination. Figure 2.6 below shows the tubes after release over a Si wafer. As can be seen from Figure 2.6 below the tubes are quite regularly shaped with high aspect ratio and reasonably high quality. The tubes are generally in the length scale of 70-100 μm and have an inner diameter of ~8 μm. The varying range of length sizes of the microtubes may be the result of breakage during the fracturing of the MCG to release the tubes or if the vacuum infiltration was not exactly even over the surface of the membrane the sol-gel will infiltrate and coat the walls fully in some areas (highest suction) and less in the areas where the sol-gel would not have been pulled as strong.

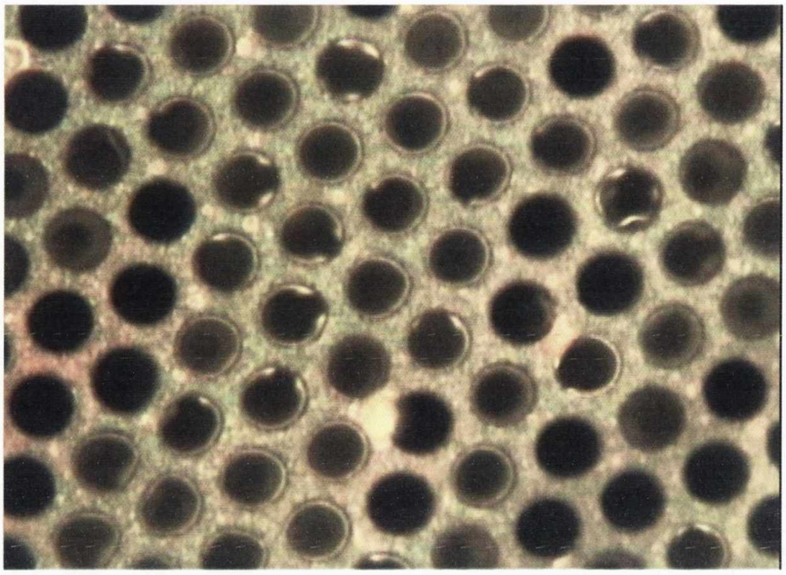

Figure 2.5: Optical image of tubes in MCG matrix

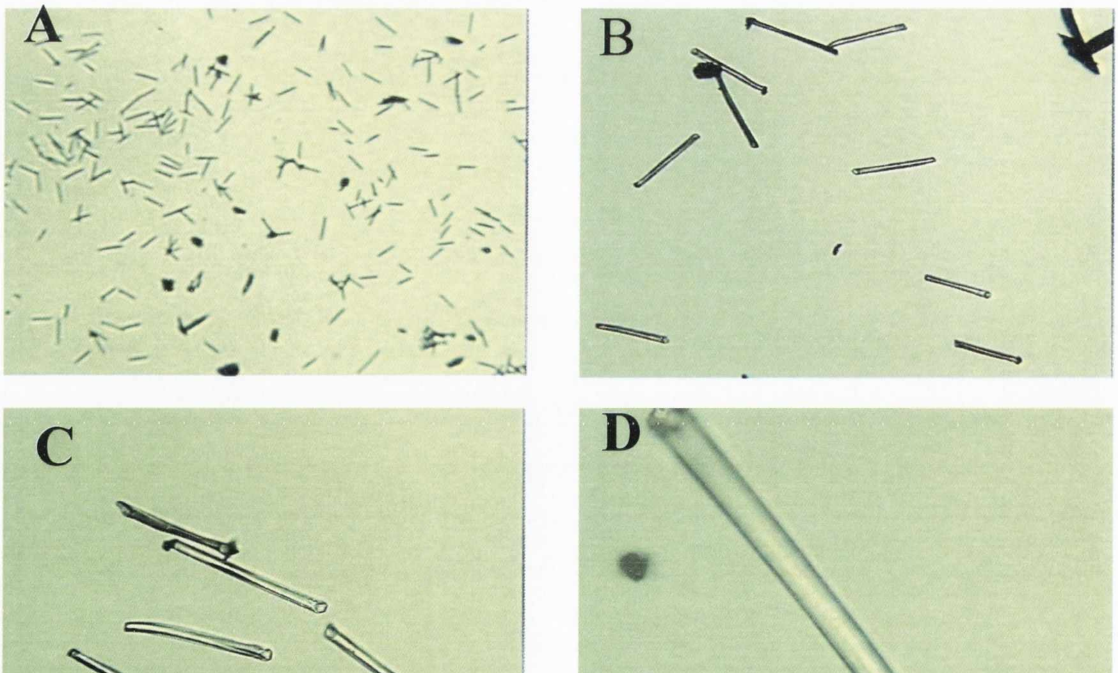

Figure 2.6: A-D; Optical images of aluminosilicate tubes on a Si wafer

The uniform luminescence of the microtubes emitting primarily in the red (Eu^{3+} region) was examined using a confocal microscope shown below in Figure 2.7. The figure shows a series of overlapped images (3 channels blue, green and red (details in Section 6.2.11) showing emission from the microtube under radiation at different height levels up through the tube. The image on the right in Figure 2.7 is roughly at the mid-point (cross-section) of the tube and as can be seen the emission is quite uniform throughout the tube. The uniform emission from the tubes is further indicated in the intensity graphs in Figure 2.8. These intensity graphs show that the emission is of a relative uniform intensity along the length of the tube (a distance of ~95 μm) with each intensity line (red, green and blue) being relatively flat. The region from ~75-95 μm shows some slight error, this is due to the tube being at a very slight angle meaning the scan of the tube is not totally along the middle of the tube (cross section). As can be observed in the intensity graphs the red channel emission is the most intense along the length of the tube, backing up the information apparent in the image of predominant emission in the red region. However there does seem to be emission from a broad region across the spectrum indicating that Eu^{3+} may not be the only contributing emitting species.

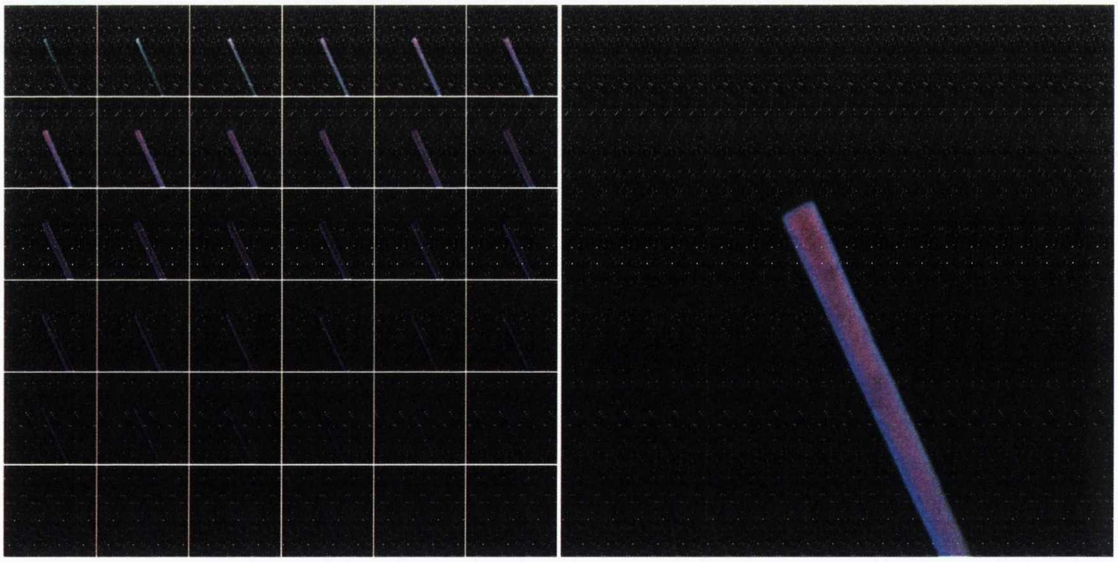

Figure 2.7: Confocal microscope z-scan image Left: Images showing scan through tube (0.45 μm steps) Right: Image of tube showing prominent red emission

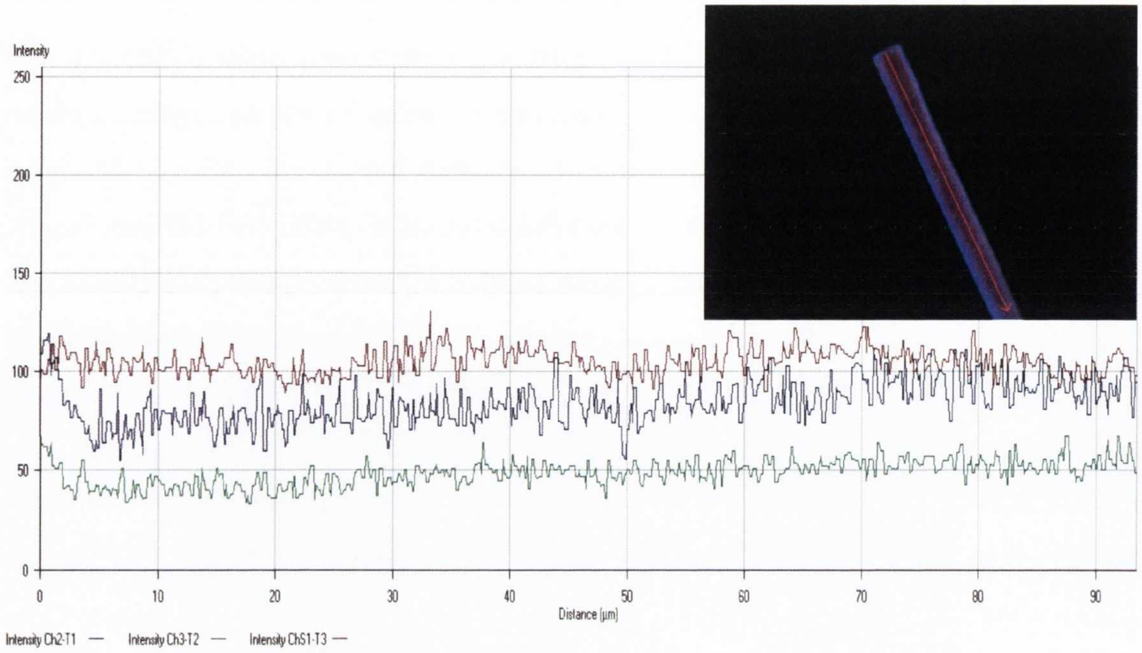

Figure 2.8: Emission intensity curves along the length of the microtube (indicated by red arrow on tube image inset) showing the red, blue and green channels

2.2.2 Photoluminescence spectra of microtubes

Further annealing of tubes released over a Si wafer to 1000 °C was performed in order to burn off carbon impurities and reveal Eu luminescence. Figure 2.9 displays characteristic Eu^{3+} spectra of the annealed samples excited at 457 nm. These peaks correspond to transitions of trivalent Eu (as discussed above in Section 2.2). The bottom curve is from an isolated tube, however the higher intensity curves are taken from different points where two tubes are in contact, the higher intensity is most likely due to the wave-guiding ability of the tubes, resulting in the excitation of multiple tubes which are in contact with one another. This guiding of exciting light from one tube to another, results in an increased intensity from the sample. PL spectra of un-annealed tubes showed no emission upon similar excitation.

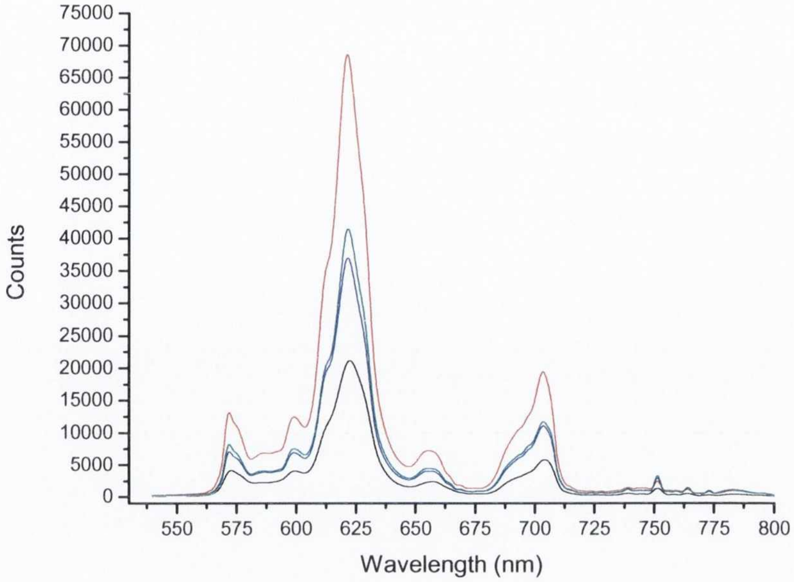

Figure 2.9: Characteristic Eu^{3+} emission from Eu doped aluminosilicate microtubes
— scan of isolated tube — scans of varying position on overlap of tubes

However not all tubes only showed Eu^{3+} peaks, some also displayed a broad intense emission (presumably due to carbon defects) and characteristic europium peaks as shown in Figure 2.10 below. Once again the three higher intensity curves come from the contact area of two tubes and the lower one of an isolated tube again suggesting the excitation of multiple tubes which are in contact with one another as above.

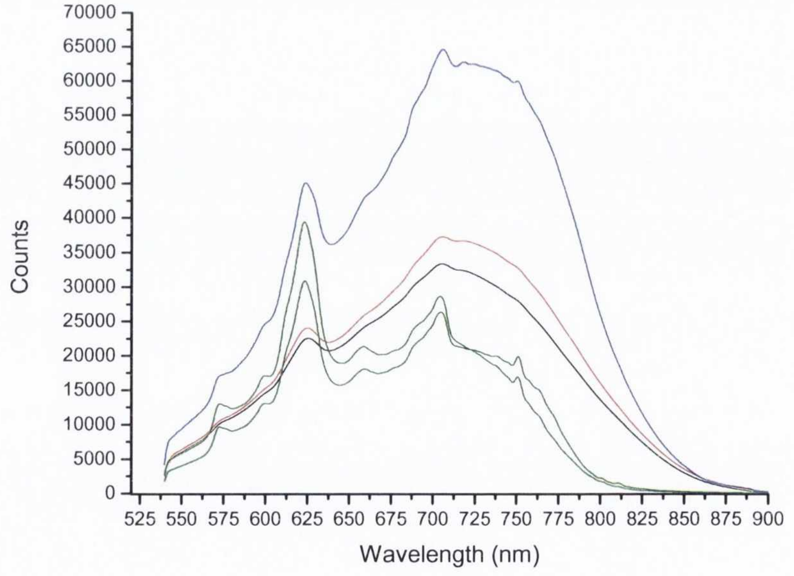

Figure 2.10: Both Eu^{3+} and defect emission shown from doped aluminosilicate tubes excitation at 457 nm — scans of isolated tubes — Scans of tubes overlapping with red scan at optimum position

2.3 Preparation and characterisation of defect luminescent aluminosilicate microtubes

Defect luminescent aluminosilicate microtubes were prepared via a 2 step acid catalysed sol-gel process the same as above. TEOS was partially hydrolysed with a solution of water, ethanol and HCl. Aluminium iso-propoxide was then added to create a Si:Al ratio of 10:1 and co-doped with Europium acetate. The two partially hydrolysed precursors then undergo the second step condensation reaction to achieve a gel. The viscosity is then monitored by eye and when judged to be of the suitable viscosity is infiltrated under vacuum into a MCG membrane. The infiltrated membrane is then left to dry in air for a couple of days and finally annealed at 500 °C for 1 hour to shrink the tubes off the pore wall and activate the defect luminescence. The MCG membrane is then fractured over a suitable substrate for characterisation of the tubes.

2.3.1 Microscopy and photoluminescence characterisation of microtubes

Microtubes with differing diameters were fabricated by infiltration into MCG membranes with different diameters. The microtubes which were produced using 10 μm pore diameter MCG membranes had diameters of ~8 μm and lengths of 70-100 μm, while the use of 25 μm pore diameters MCG membranes resulted in tubes of ~20 μm in diameter and 100-150 μm in length. Optical microscopy images of the tubes on MCG templates are shown below in Figure 2.11.

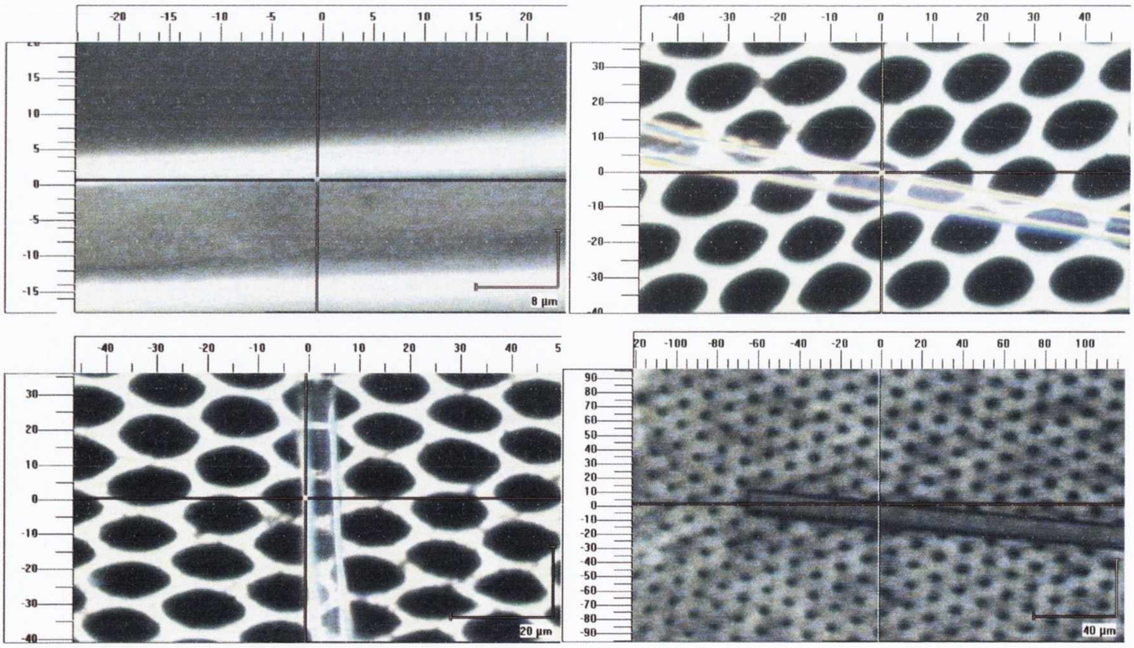

Figure 2.11: Optical microscope images of microtubes on porous MCG templates showing tubes of varying size

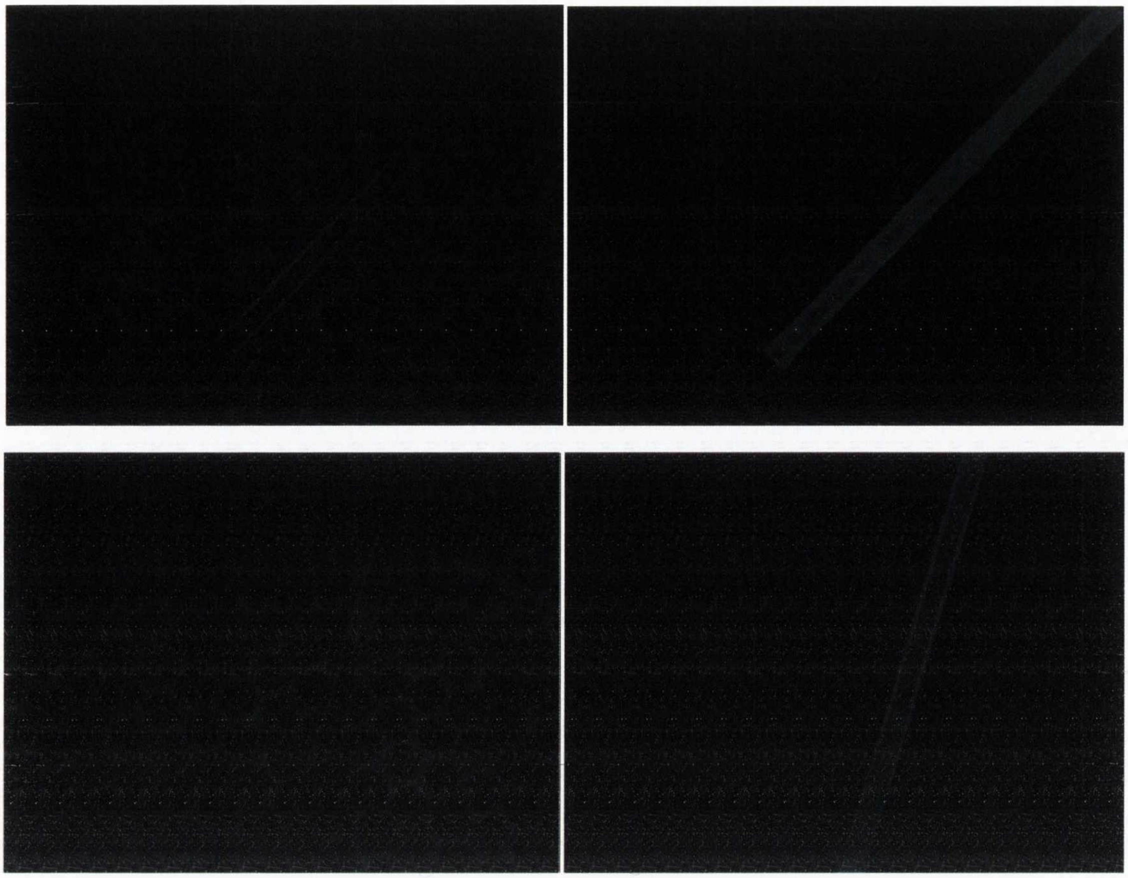

Figure 2.12: Optical and fluorescent (UV excitation) microscope images of microtubes on MCG membrane

Shown above in Figure 2.12 is visible emission from microtubes on MCG membrane under fluorescence microscope showing the uniform emission along length of tube with higher intensity at the edges.

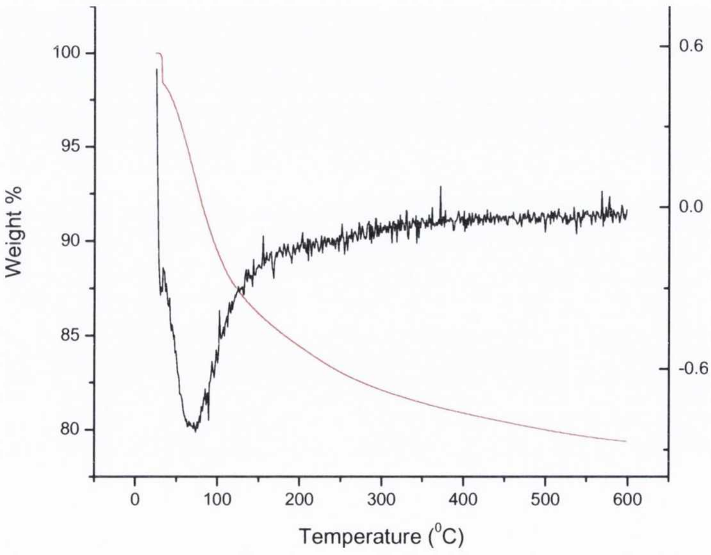

Figure 2.13: TGA (red) and D-TGA (black) curves of xerogel

Thermal analysis of silicates has been widely studied and aptly covered and explained by the seminal text on sol-gel science by Brinker and Scherer[20]. The TGA analysis above (Figure 2.13) shows a weight % decrease of ~20% at 600 °C. This corresponds in the initial region up to 100 °C to the removal of physisorbed water on the surface and in the pores. The next weight loss region from 100-500 °C corresponds to the removal of organics (mainly alkoxide groups) from the xerogel matrix. This happens by carbonization and the oxidation of the organic species where the gel is known to change colour from clear to black to yellow and clear again[20]. This weight loss region is also known to be associated with further condensation of silanols to create siloxane bonds with the production of water; this process is thought to be the largest contributor to the weight loss. This weight loss coincides with a visible shrinkage of the gel with temperature due to structural relaxation with the changing gel structure due to condensation reactions[20]. All microtubes annealed at 500 °C displayed a bright intense visible luminescence. As described in section 1.4 this luminescence is ascribed to luminescent defect centres within the aluminosilicate matrix. Unlike some previous reports on defect emission highlighted in section 1.4 the emission observed from the microtubes showed only an intense broad emission and little or no defined peaks from specific species which points to multiple emission pathways from the defects within the matrix with varying environments. Figure 2.14 shows typical emission spectra from the released annealed aluminosilicate microtubes (very low Eu^{3+} doping concentration) excited at different positions on the tube. As discussed the emission from the microtubes is attributed to defects in the silica matrix due to either oxygen or carbon. Shown in Figure 2.15 is a Raman spectrum of a sample of annealed aluminosilicate xerogel. The spectrum shows peaks in the range 1050 cm^{-1} to 1125 cm^{-1} which are characteristic for Si-O-Si symmetric stretching modes. The 816 cm^{-1} to 950 cm^{-1} range are assigned to Al-O stretching modes while the small peak at 1279 cm^{-1} is thought to be the Si-O-Al stretching mode[26]. The peak at 880 cm^{-1} is attributed to Si-OH groups. The peak at 1455 cm^{-1} (with shoulder) is most likely due to the presence of carbon within the matrix (CH bending) (originated from alkoxy groups during thermal decomposition) in the silica gel, which are expected to be involved in the defect emission. This confirms that the types of groups are present within the xerogel matrix for the formation of emitting defect groups. Although organic groups are present within the aluminosilicate matrix via the alkoxy groups on the precursors removed during the reaction the use of HCl as the acid catalyst during the reaction removes a source of organics which were recognized as a source of the luminescence in previous reports[27]. This does not definitively rule out the possibility of carbon being involved in the emission process but does rule out the source being from the acid. Indeed the acid catalyst seems to be a very important component in producing defect emission as similar attempts using a base catalysed condensation step did not produce any emission upon heat treatment. This is indicates that the acid plays an important role in causing the particular type of defects in the sol-gel reaction that cause the emission.

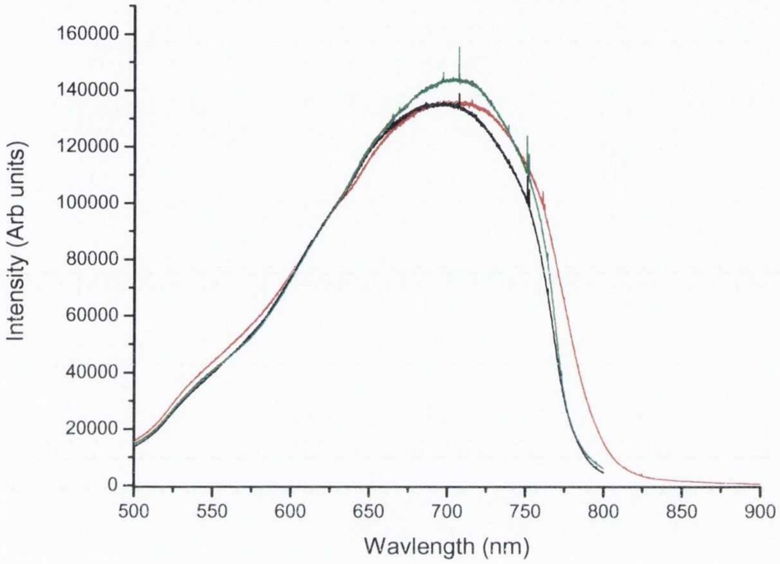

Figure 2.14: *Emission spectra from annealed aluminosilicate microtube (v. low Eu doping) excited at different positions on the tube showing broad emission (ex457 nm)*

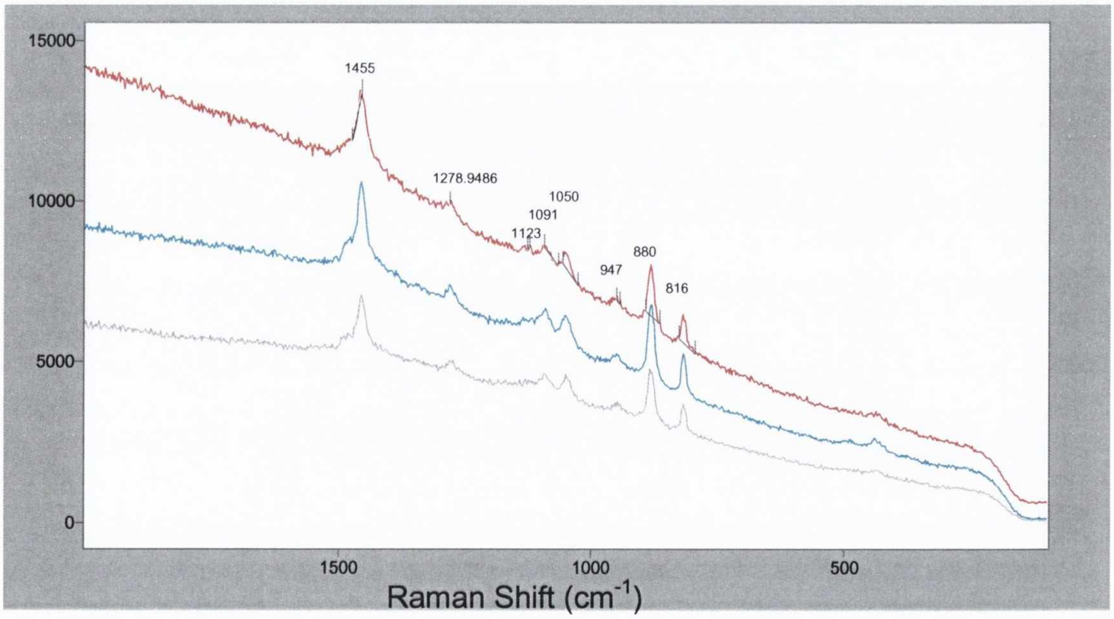

Figure 2.15: *Raman spectra of bulk* Eu^{3+} *doped aluminosilicate xerogel used to fabricate microtubes*

2.3.2 WGM in microtubes

Given the quality of the MCG membranes with their smooth pore walls, if the sol-gel is infiltrated evenly and dries uniformly to create a high quality smooth walled microtube it can be utilised as an optical device by its ability to act as a waveguide. Furthermore when the tube is released from the MCG membrane and placed over a porous substrate the resulting contrast in the refractive index between the tube and the air allows the microtube to demonstrate WGM resonance within the microcavity as described in section 1.2. This WGM resonance was observed in some microtube samples and is displayed below in the PL spectra in Figure 2.16. The spectra show PL scans of a microtube ~20 μm in diameter. As can be observed the spectra show a fine structure of repeating peaks over the emissive range of the microtube. Each one of these peaks represents a resonance mode for that particular wavelength within the microcavity. The observed increase in intensity at the point of modal resonance results from an increased transition probability of the emitting species due to the atom being coupled with the mode of the cavity[3]. The fine structure of the peaks as highlighted in the inset below shows multiple fine peaks. These can be the result of modes mixing and interacting with each other within the cavities walls. The WGM emission is known to be enhanced with the use of polarisers in the right positions due to the nature of the resonances being set up[9].

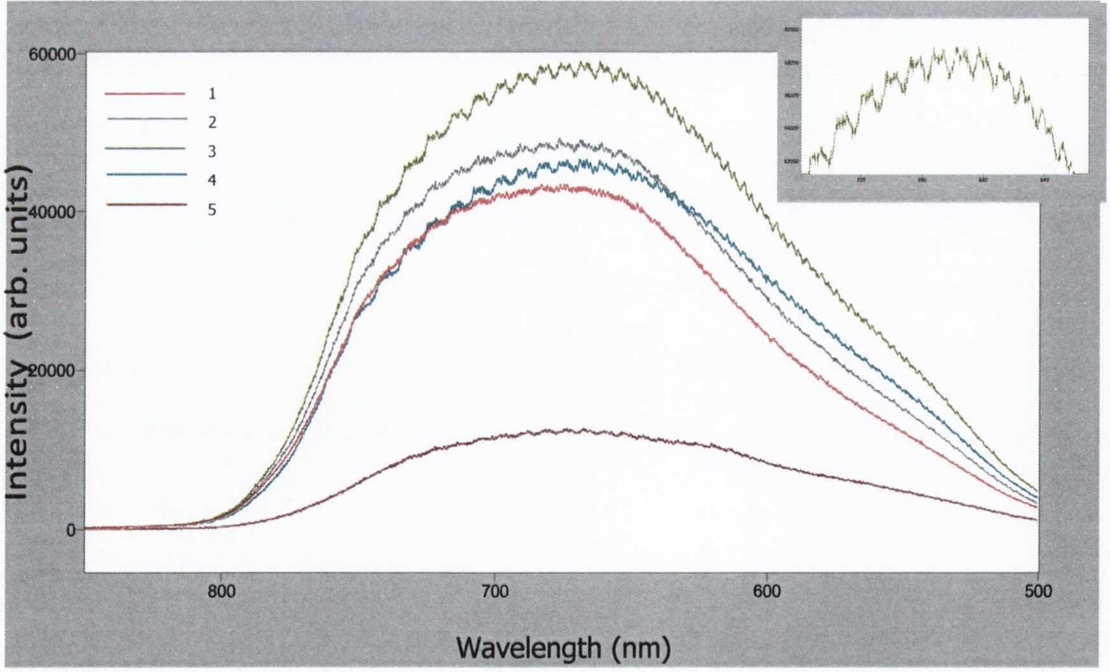

Figure 2.16: PL spectra of Eu doped aluminosilicate microtube showing WGM resonance, 1-5: varying laser focus position, inset: hyperfine structure of curve 3 (630 nm – 720 nm highlighted), excitation at 457 nm

The setting up of WGM resonances is dependent on the efficient placing of the excitation beam on the microtube. The optimum excitation position is one that couples to the evanescent field of the microtube which is achieved by focusing at the edge of the microtube. This is essential so as to excite the microtube so that the emission from the tube walls is set at an optimum angle to undergo total internal reflection for the resonances to set up. This importance is demonstrated in Figure 2.17 which shows the excitation position of the excitation laser (indicated by crosshairs) for the PL spectra above in Figure 2.16. As can be seen as the excitation position moves out from just inside the edge of the tube (position 1) to just outside the edge of the tube (position 3) the increase in intensity of the emission showing the WGM is clearly seen, however it drops again at position 4 as it moves too far out for optimum excitation. At position 5 the excitation point on the tube would seem to be ideal at the opposite side of the tube however since here the tube is more in contact with the underlying membrane the coupling is interrupted and not as efficient which is clearly seen in the PL as spectrum 5 is much reduced in intensity.

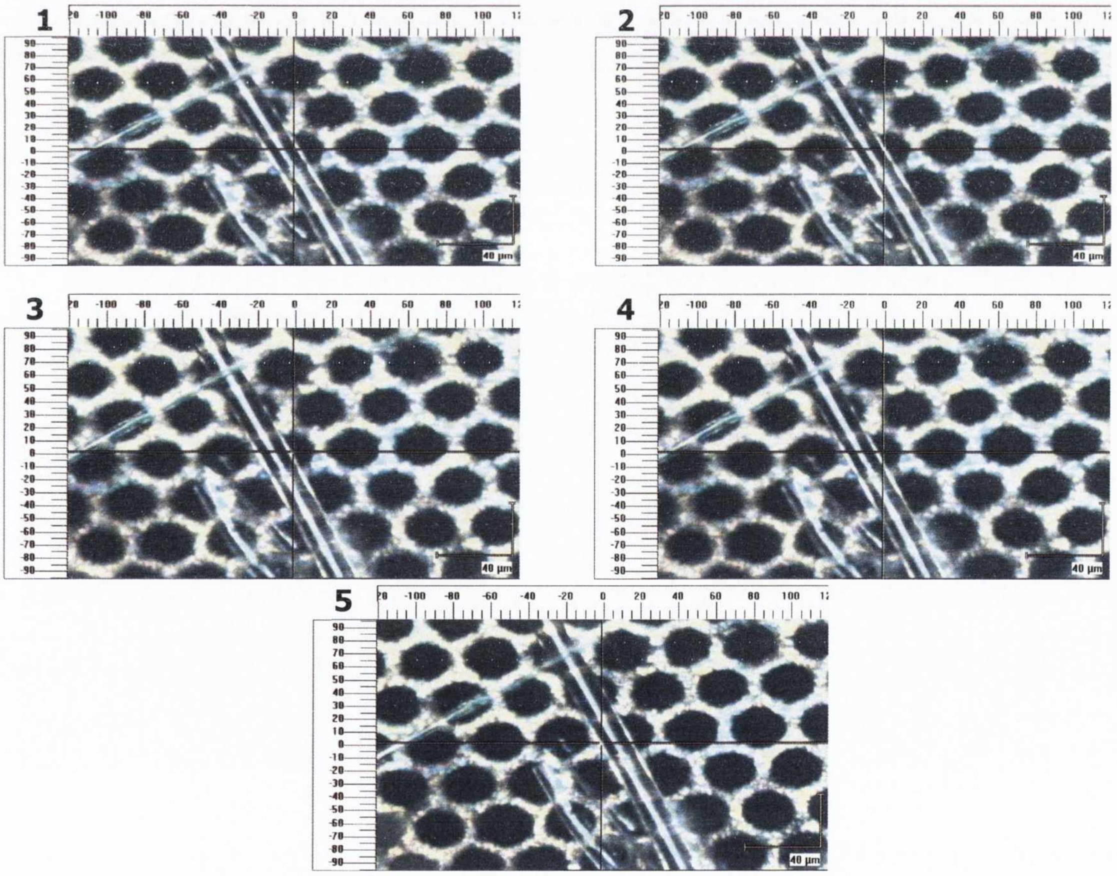

Figure 2.17: Optical images of microtube showing where laser was focused (indicated by the crosshairs)

This effect is also observable in tubes of a smaller diameter as shown in figure 2.17 below. The WGM resonance in this tube is relatively weak and a stronger signal has been observed in similarly fabricated tubes previously[10], this is most likely down to some surface roughness and defects induced during drying and annealing. Also shown in Figure 2.18 is the wave guiding of the excitation light when coupled into the microcavity, this property is very useful for coupling to other devices as will be discussed in the next section. The Q value observed of these types of microtubes (≈ x10^3)[9] is relatively low when compared to other WGM resonators however their size and shape and potential to integrate with other optical devices make them attractive for optical and photonic applications.

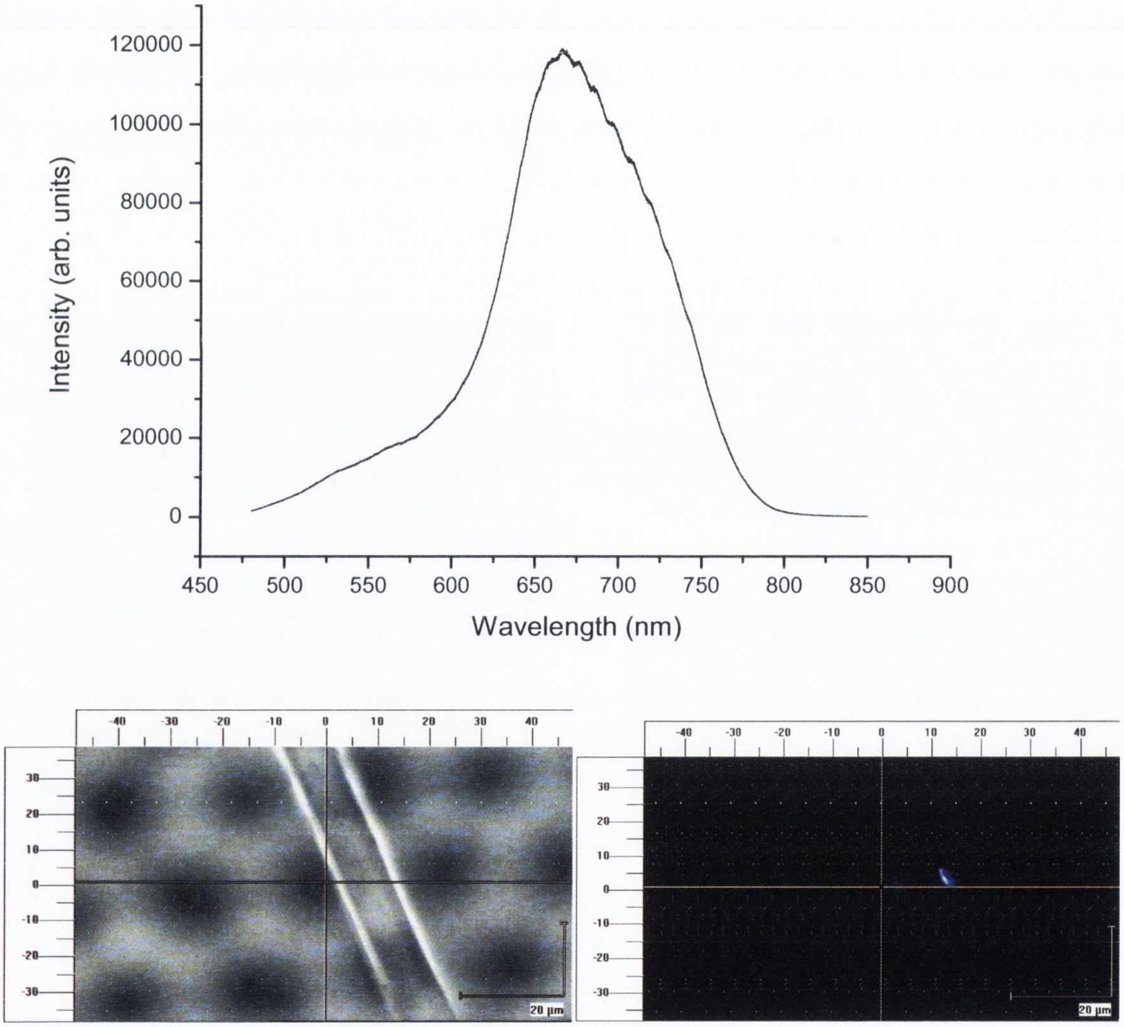

Figure 2.18: Above; PL spectrum of microtube displaying weak WGM emission Below; Microscope images of microtube showing excitation position and laser guiding in tube

2.4 Microtube-microsphere interactions

In the demand for high Q micro resonators, microspheres have received a great deal of attention. Since the process for the fabrication of silica and polymer microspheres with high quality and uniformity they have become a leading article in the field of microcavity optics. Many types of spheres such as polystyrene, melamine and PMMA are available today from commercial sources. These microspheres can be produced by various methods including heating the end of a pure silica fibre which becomes fused and forms a sphere under the influence of surface tension, sol-gel processes or melting process. These spheres have demonstrated very high Q values and the ability to be doped with various emitting materials. Given the size range available for various types of spheres they were considered as an ideal object to examine the interaction potential of the microtubes with other optical devices.

The microtube-microsphere systems are fabricated by infiltration under vacuum of the spheres in aqueous media (diluting the highly concentrated solution of spheres with ethanol to reduce the surface tension and hasten drying) through a MCG membrane containing microtubes. The tubes are then released in the usual manner of breakage of the membrane.

2.4.1 Microscopy and PL characterisation of microtube-microsphere systems

Both fused silica and dye coated (ethidium bromide) melamine microspheres of various sizes were used in the system. The silica spheres used were 3 μm in diameter and non-luminescent (non-emitting). These spheres were used in an attempt to show cooperation of the defect emitting microtubes and the sphere through the observation of optical properties of both. One of the main issues with the infiltration process and characterisation was ascertaining if the spheres were internalised in the tubes. Certainly spheres are residing on the outside of the tube but ones suspected of being on the inside are difficult to say for sure where they are exactly located. This can be observed in the optical microscope images shown in Figure 2.19 below, where clearly it can be seen to have spheres on the outside and seems to contain spheres internally however even trying to focus through the tube did not definitively prove if they are or not. The reason for this accommodation of spheres on the outside of the tubes is that the tubes inside the pores of the MCG membrane are shrunk off the walls upon annealing, therefore this gap between tube and pore walls can be partially filled by the spheres during the vacuum infiltration. This can be observed in the microscope image in Figure 2.20 below of a sample of MCG which has been infiltrated and annealed with microtubes inside and subsequently spheres, the spheres are seen to be trapped around the edges of the tubes in the pores. This observation can also be explained by the surface tension of the liquid which the spheres are supplied in forming over the mouth of the pore and the spheres being pushed to settling around the rim of the pore, although this problem is tackled by breaking the surface tension using the vacuum and the use of a lower surface tension solution such as ethanol the issue is not completely negated. However there was sufficient interaction between microsphere and microtube to be examined using the PL system.

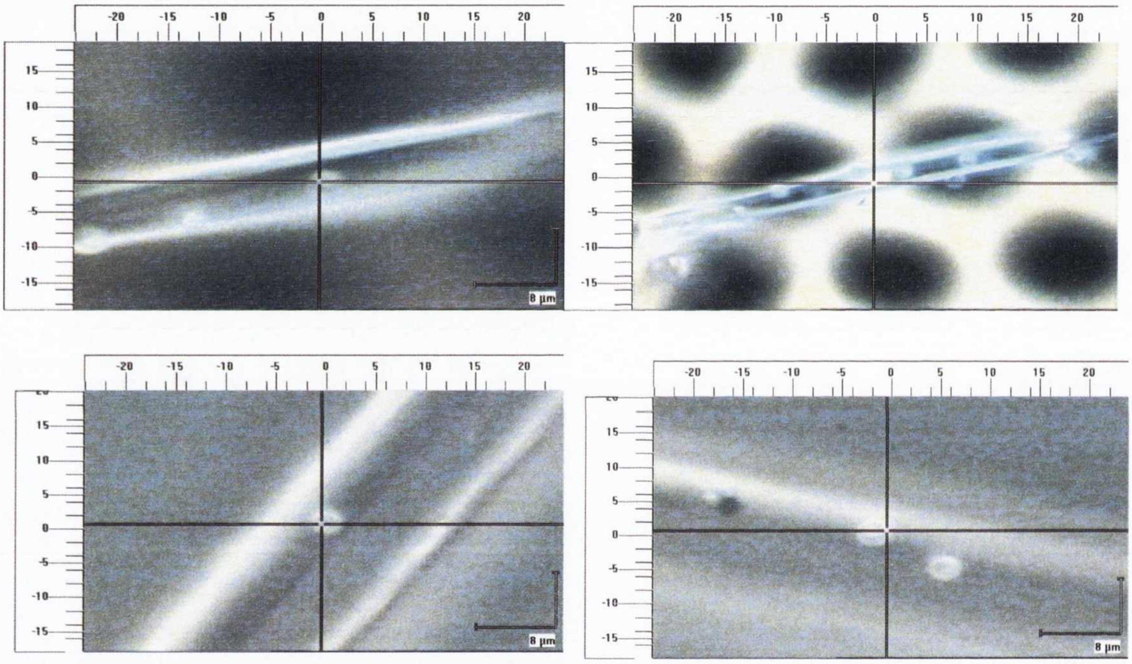

Figure 2.19: Microscope images showing spheres on the side and possibly inside tubes

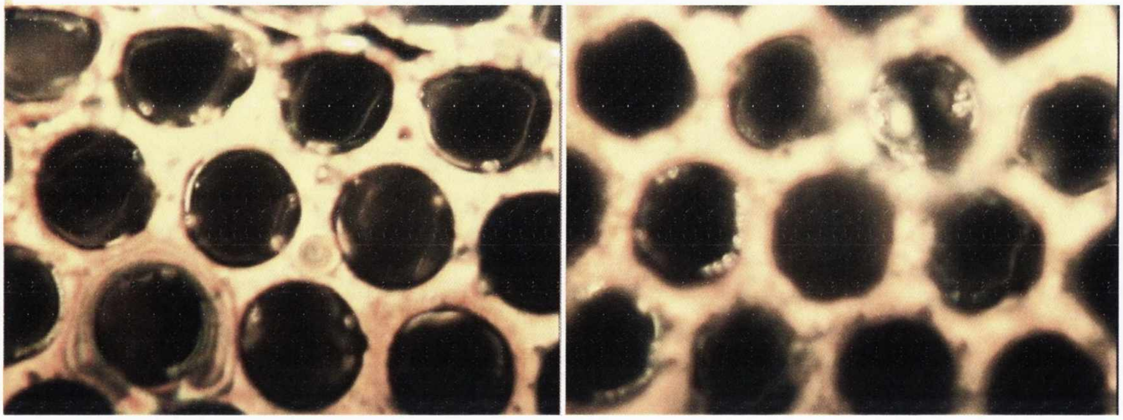

Figure 2.20: Optical microscope images showing microspheres trapped at the edge of microtubes in a MCG membrane

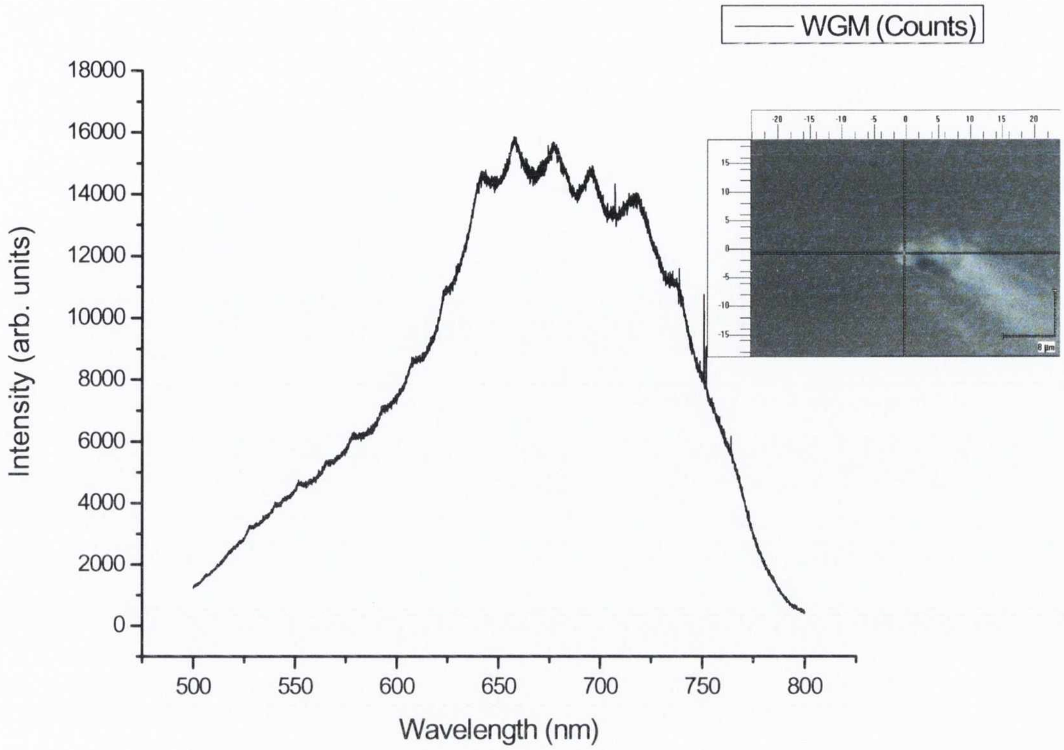

Figure 2.21: Spectra showing WGM from microsphere at end of tube (image of what was scanned shown inset) ex=457 nm

The PL spectrum shown above in Figure 2.21 displays a WGM character over a broad luminescence. This spectrum arises from excitation of a 3 µm silica microsphere which is just on the lip of the end of a defect emitting ~8 µm diameter microtube. The excitation laser is focused on the microsphere (as shown in the inset), however since this sphere is non-emitting the observed luminescence must be coming from the defect emitting microtube which becomes excited via the wave guiding of the sphere upon which the WGM resonance is then set up in the sphere via coupling to it.

As stated previously dye coated melamine microspheres 5 µm in diameter were also used to be incorporated with larger diameter microtubes. These spheres are capable of exhibiting WGM resonance by themselves (Figure 1.3) under external excitation and were incorporated with Eu^{3+} doped aluminosilicate microtubes (as discussed in section 2.1) in an attempt to observe properties of both in cooperation. This was achieved relatively successfully as demonstrated in Figure 2.22. The PL spectrum shown displays an overlaid emission from the Eu^{3+} doped microtube and the WGM from the dye coated microsphere. The origin of the overlap can be seen from the microscope images shown where the excitation laser is focused on the edge of the tube, the tube then guides the light to the other side with maximum intensity where microspheres reside on the outside. The guided laser beam then excites the spheres also resulting in the combined emission from the two devices. This shows good promise of the microtube-microsphere coupling for the potential applications of these two microcavity systems to cooperate in optical devices.

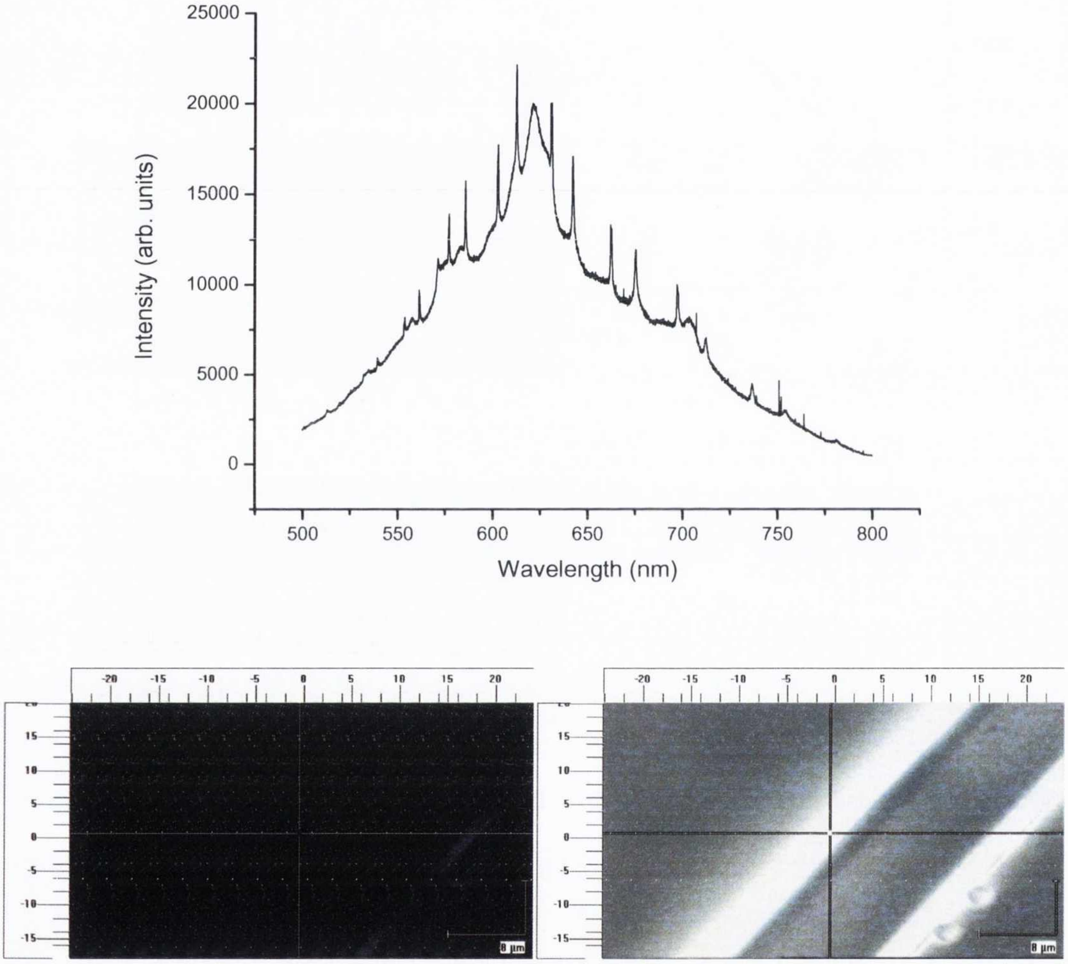

Figure 2.22: Above: PL spectra of aluminosilicate microtube with microsphere on the side showing characteristic Eu^{3+} and WGM luminescence. Below (right): Optical microscope image showing points of laser focus on tube. Below (left): Laser illuminated microscope image with laser focussed at crosshairs

Also observed were emission overlaps from two spheres immobilised on/in the microtube as shown in Figure 2.23. The laser excites one sphere which due to the wave guiding of sphere and tube allows excitation of both. This opens up possibilities of examining comparison of signals from spheres if one had an analyte attached while the other sphere acts as a reference. Such a set up as observed in Figure 2.23 was imaged in SEM below (Figure 2.24). The smooth surfaces of the spheres and tube can be seen which makes them suitable for optics applications.

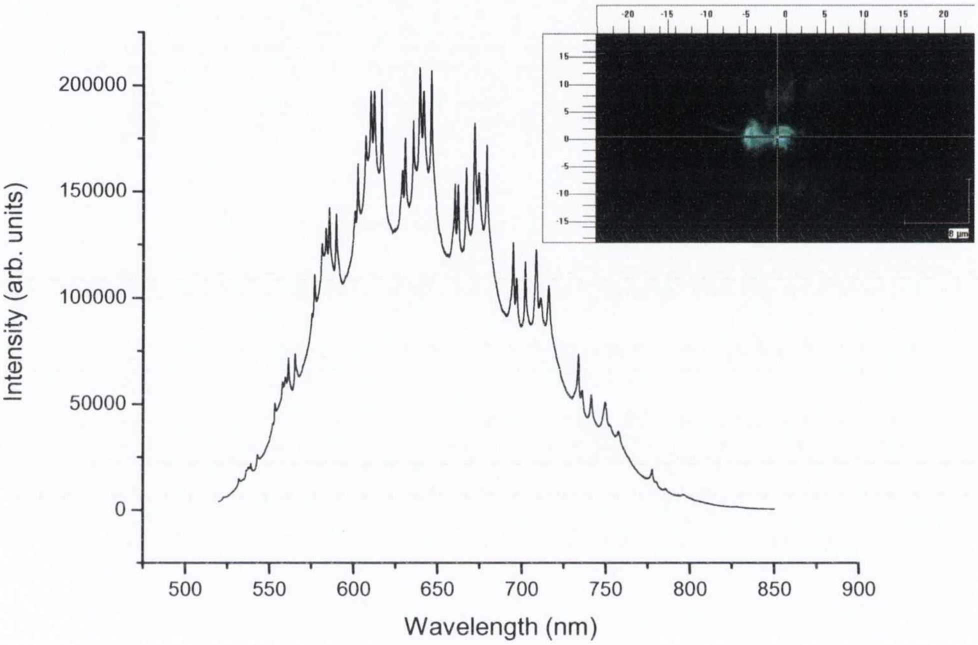

Figure 2.23: Solid state PL spectrum of 2 interacting microspheres in/on tube Inset; Microscope image of laser illumination (ex514 nm)

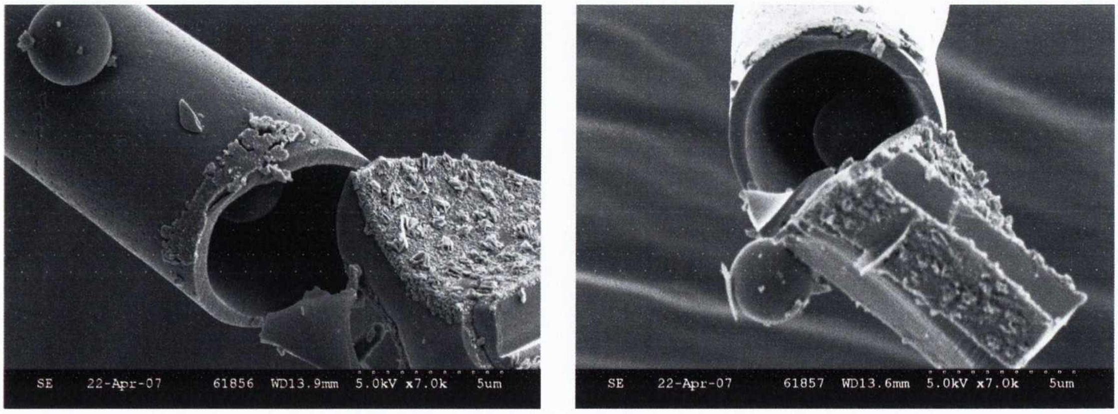

Figure 2.24: SEM images micrograph showing microtube with microsphere inside and outside

2.5 CdTe QD doped Xerogel Microtubes

Preparation of QD loaded sol-gel derived glasses has been investigated previously a number of groups with varying success none more so than Norio Murase et al who has published extensively in the area. Their attempts mainly focussed on doping APS/MPS derived gels (one in conjunction with TEOS) with pre-made CdTe QDs [28-30]. These resulted after a number of days in highly luminescent powders and thin glasses which could be formed to a flat structure. These structures proved to be relatively stable over time however were susceptible to PL degradation with continuous exposure to UV irradiation. They also successfully fabricated CdTe QD embedded in binary silica-zirconia glass via a sol-gel method which showed high PL emission and remained relatively stable over time with only a slight degradation of PL intensity [31]. Work in this area performed by other groups includes CdSe QD loaded glasses via a sol-gel process which resulted in emissive glasses (which again showed a decrease in PL maximum over time before stabilising) [32], also CdSe loaded organic-inorganic gel which retained its luminescence quite well showing little or no degradation [33] and similarly in a commercial organosiloxane spin-on-glass (SOG) product [34]. CdSe QD loaded xerogels and aerogels have also been fabricated from a tetranitromethane precursor and how the QD bandgap varied with gel density [35].

Use of these QD loaded glasses to form some set structures has also been investigated by various groups. Silica coated CdTe QDs have been utilised to form emitting spheres/beads [36-37]. Also so called ‘bristled nano centipedes’ (10-100 nm in diameter and <10 microns in length) have been fabricated which consist of CdTe NWs coated in a bristled silica layer, it is mentioned that the structures are luminescent but no evidence of this is viewed in the paper [38]. Luminescent microtubes based on CdTe QDs have been fabricated previously using silkworm silks as templates after calcination at 500 °C. The microtubes (after calcination) were believed to be made up of various Cd based nanocrystals but still retained luminescent properties under UV excitation [39].

The preparation of the silica coated CdTe QDs was carried according to published procedures [40-42]. Briefly TGA capped CdTe QDs were synthesised in aqueous media and silica coated by surface priming with MPS and building the silica layer with sodium silicate solution (see Figure 2.25). A silica sol-gel was then prepared by partially hydrolysing TEOS with an acid catalyst and then using an excess of base for the condensation step. QDs were added in the 2nd step of the acid-base catalysed silica sol creating a brightly coloured red homogenous sol; QDs were added under basic conditions due to quenching of the dots under acidic pH. The doped silica sol is the infiltrated into microchannel glass under vacuum and left to dry in the darkness in air. Bulk gel was left to dry in air over time and in the dark before examination. Microtubes were released via mechanical breakage of the membrane over suitable substrate and examined.

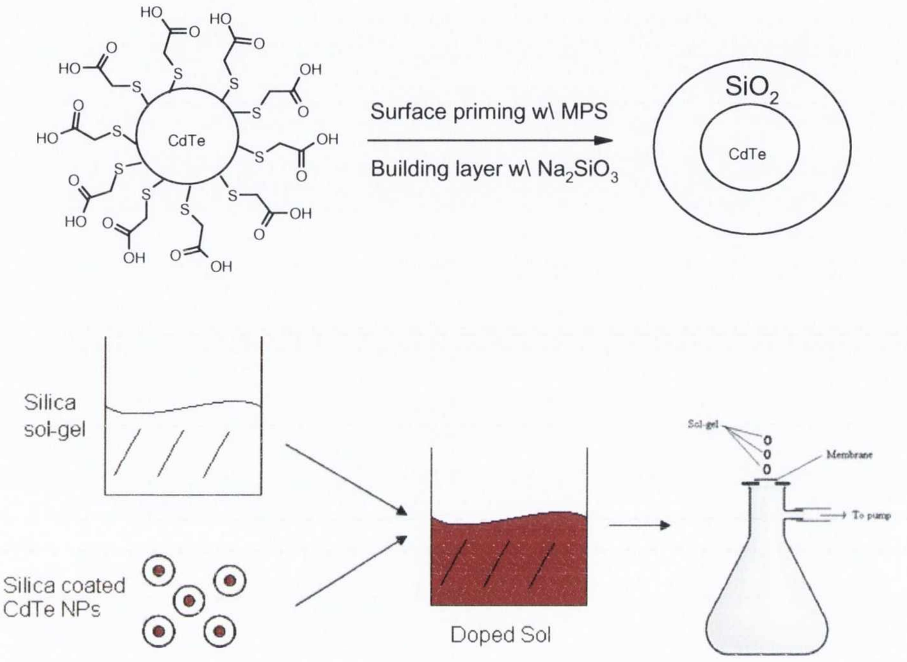

Figure 2.25: Schematic showing coating of QDs and infiltration of MCG membrane

2.5.1 Characterisation of CdTe QD doped bulk xerogels

Preparation of the doped sols provided a number of challenges given the nature of QDs to be very sensitive to their environment. Firstly it involved modifying the sol-gel reaction to have a step in basic conditions while trying to keep the quality of the final xerogel while still catalysing the reaction. This was necessary due to the degradation of the dots and complete quenching of their luminescence under the acidic conditions employed usually in the sol-gel process.

Secondly the QDs required further protection to prevent complete quenching of their luminescence over time in the gel. This was provided by sufficiently silica coating the dots to make them more robust while keeping them relatively stable in the sol and prevent crashing out.

As experiments had previously shown the luminescence of the QDs showed a drop in intensity and a slight red shift in luminescence [37] from 615 nm to 621 nm due to the silica coating (Figure 2.26 – concentration normalised for both samples). At the gelation point of the sol-gel the monolith appeared bright red however showed no emission under UV illumination. The gel dried uniformly over time and gradually the emission increased under UV. Interestingly the emission is blue shifted to 586 nm with respect to the original silica coated QDs added into the sol. This blue shift continued overtime by a further 17 nm as the gel dried and shrank (Figure 2.27). A blue shift in the emission spectrum of QDs shows an increase in the band gap and would usually indicate that the dots had become smaller in size.

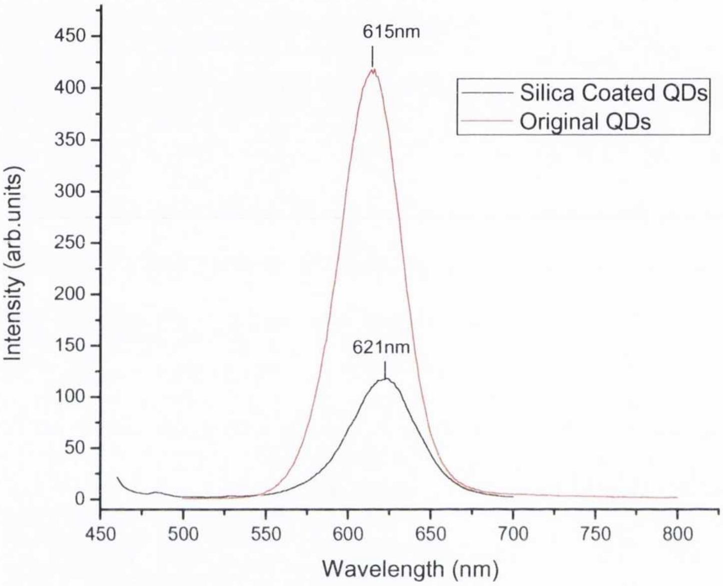

Figure 2.26: PL spectra of TGA capped CdTe QDs and silica coated QDs

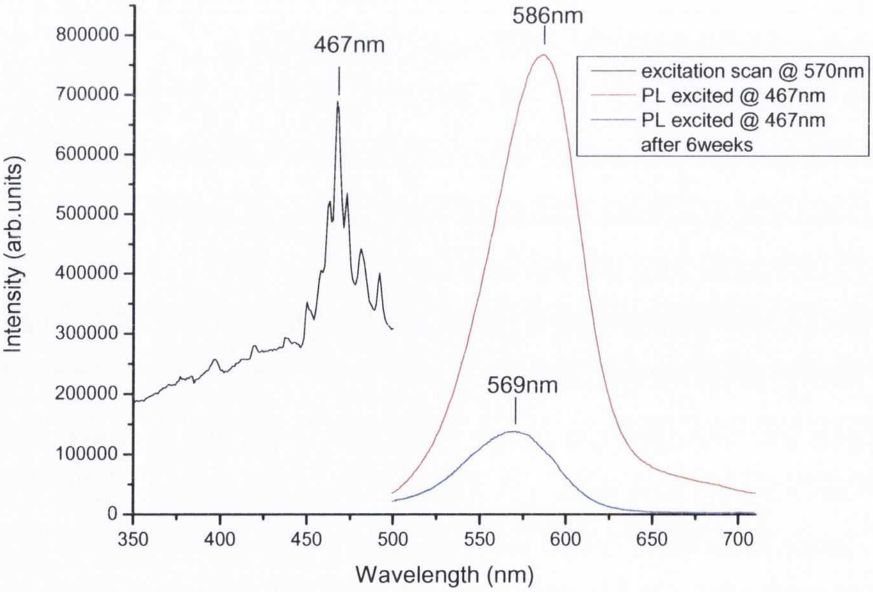

Figure 2.27: Excitation (monitored at 570 nm) and PL spectra of CdTe QD doped silica xerogel showing blue shift over time

In an attempt to find the reason for the blue shift in emission a number of tests were carried out. Firstly the photobleaching effect on the doped xerogel monoliths was examined. This was done by taking a number of PL scans over time while leaving the exciting laser on during each scan whereas a control was carried out turning the laser off between scans. The results shown in Figure 2.28 showed a gradual reduction in emission intensity over time in comparison with the control which remained constant. This shows that the QDs embedded in the silica matrix are susceptible to photobleaching most likely due to photo-oxidation at the surface of the QD. Blinking mechanisms known to occur in QDs (where the emission from individual QDs is seen to turn 'on' and 'off' due to charging of the dots under constant excitation which leads to quenching of the emission) could also be a contributing factor to quenching due to the constant charging of the dots over time causing a permanent reduction in emission intensity[43-45]. Knowing that TGA capped CdTe QDs could be photobleached due to photo oxidation of the surface in an oxygen sufficient environment [46], the question remained what is fuelling this photo-oxidation at the surface within the silica matrix? One hypothesis is that water molecules moving through the silica matrix which during irradiation cause an oxide layer around the QD to form reducing the luminescence intensity and causing a blue shift due to a reduction in the QD size [47]. Similar results of blue shifting have been observed in previous reports of CdTe QD containing silica gels [28,48].

To test this theory of water playing a role further, a piece of the xerogel was placed in water and left in the dark for 5 days (Figure 2.29). The spectra show a further blue shift to 549 nm and increase in intensity of the luminescence. This result shows a contrary result to the photo-bleaching experiment described above in that there is a large increase in emission intensity. This suggests that a different mechanism is at work here and that the immersion of the xerogel in water allows etching of the dot causing a blue shift but not allowing the oxide layer to quench the luminescence.

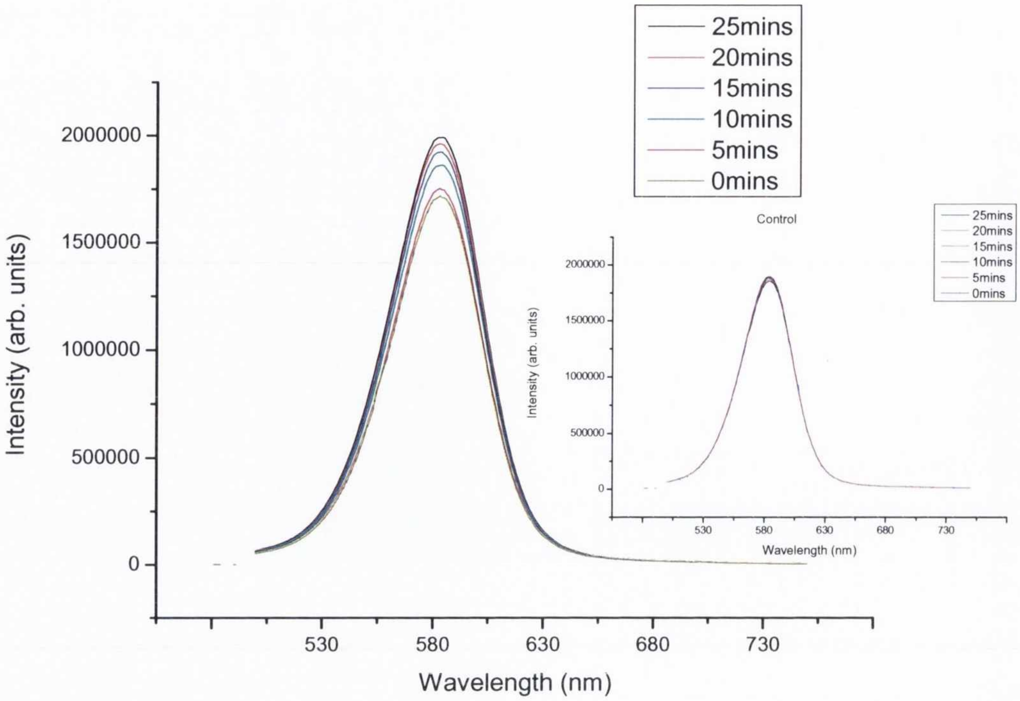

Figure 2.28: PL spectra of CdTe QD doped silica xerogel showing photobleaching over time; Inset: Control spectra of same

To ensure blue shifting and quenching were due to a photo-etching induced effect, two samples of the same initial sol-gel were split up and one kept in darkness and the other exposed to sunlight over a period of days. The results further confirmed the proposed explanation of the observed blue shifting in previous samples. As can be seen in Figure 2.30 below, the sample exposed to the light is less intense and blue shifted in comparison to the sample kept in darkness. Also shown is an image of two bulk QD doped xerogels showing the same result.

The QDs show an increased resistance to etching and associated blue shifting of emission with an increased silica shell around the dot, (the QDs still showed an initial red shift in emission upon silica coating); however this compromises their stability in water and loading level into microtubes.

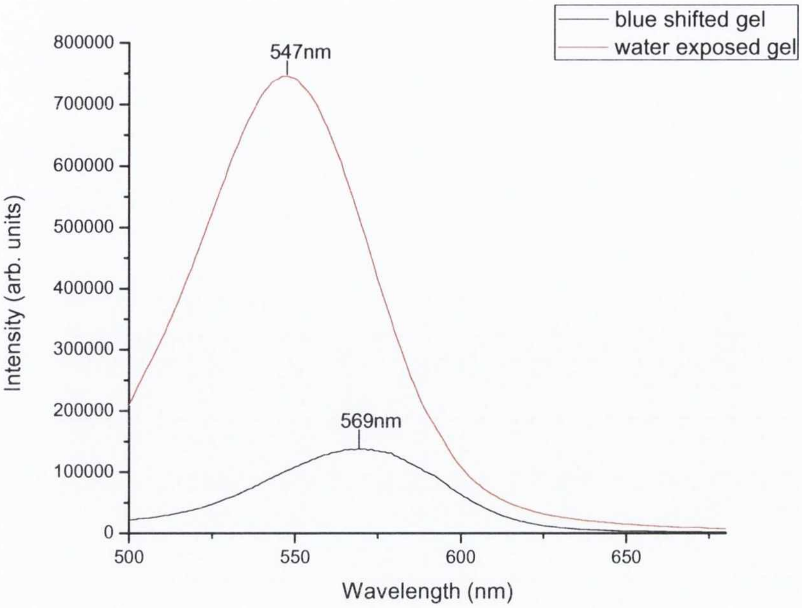

Figure 2.29: PL spectra of water immersed gel (red) and gel (black - shown previously in Figure 2.27)

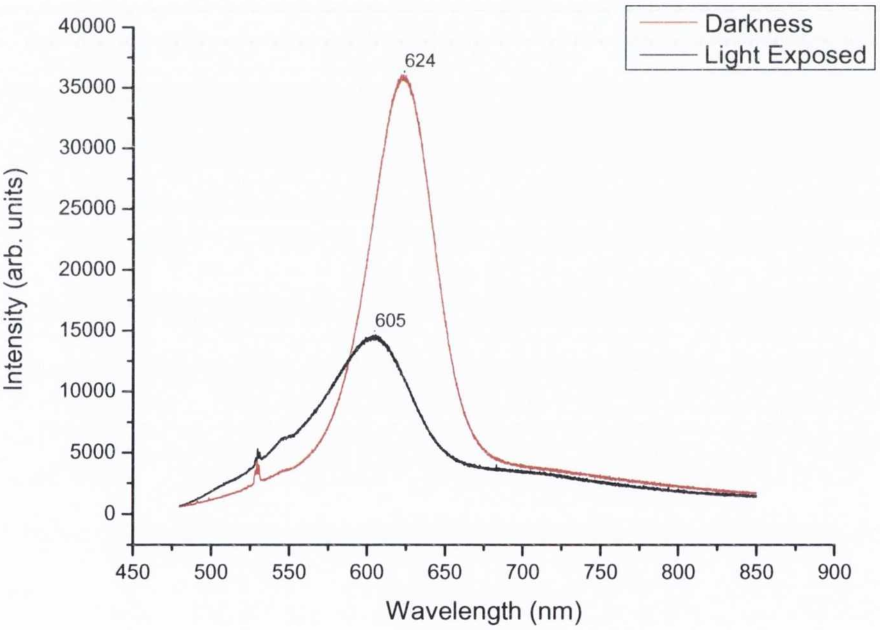

Figure 2.30: PL spectra of 2 doped xerogel samples exposed to light (black) and kept in darkness (red) Inset: Image of QD doped bulk gels under UV radiation

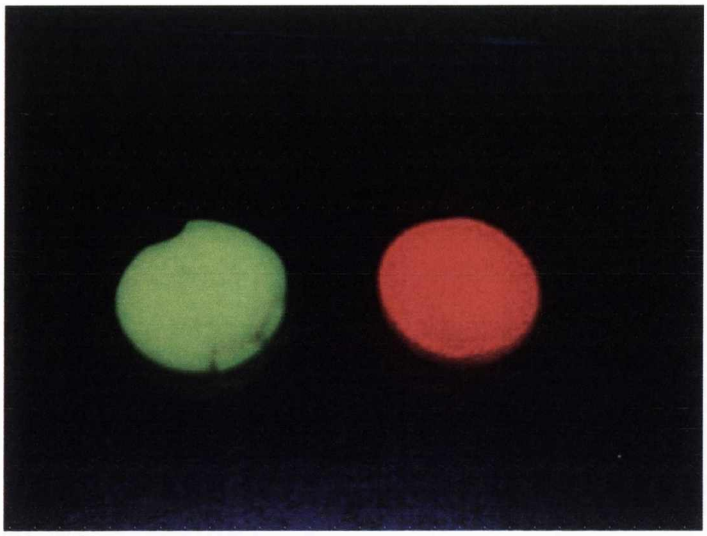

Figure 2.31: Image of CdTe QD loaded silica xerogels under UV lamp; Green emitting gel resulting from a blue shift of emission peak over time, Red emitting gel which has not been exposed to atmosphere for a long period of time

2.5.2 Optical and spectroscopic characterisation of microtubes

The QD doped microtubes are released via mechanical breakage of the microchannel glass over a separate microchannel glass membrane. The microtubes were examined under a 457 nm focussed laser spot and PL spectra taken of the microtubes. Shown below in Figure 2.32 and Figure 2.33 are solid state PL spectra taken of the surface of the infiltrated microchannel glass and of the microtubes themselves respectively. The surface of the infiltrated microchannel glass shows a high intensity peak centred at 630 nm which is a red shift from the original dots. The microtubes display luminescence originating from the QDs however show a marked decrease in emission intensity and a slight blue shift. This is thought to be due to the tubes being inside the pores of the membrane for some time and not being able to dry effectively so the dots are being damaged and severely quenched.

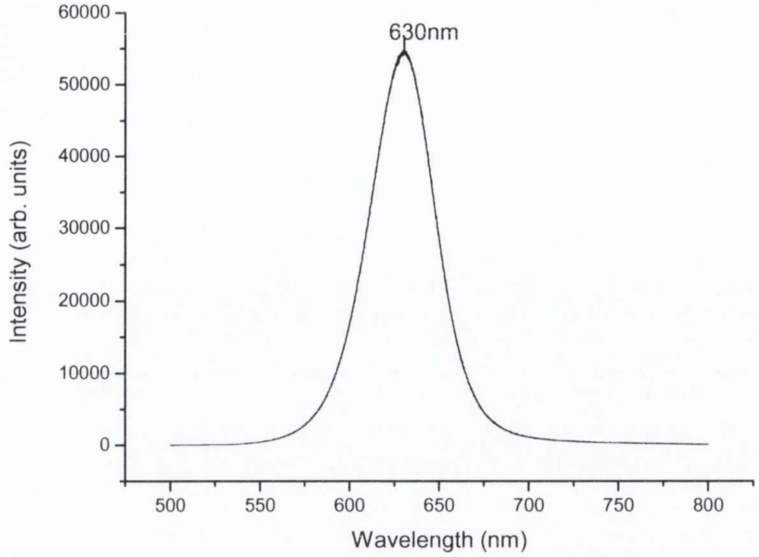

Figure 2.32: PL spectrum of surface of infiltrated microchannel glass

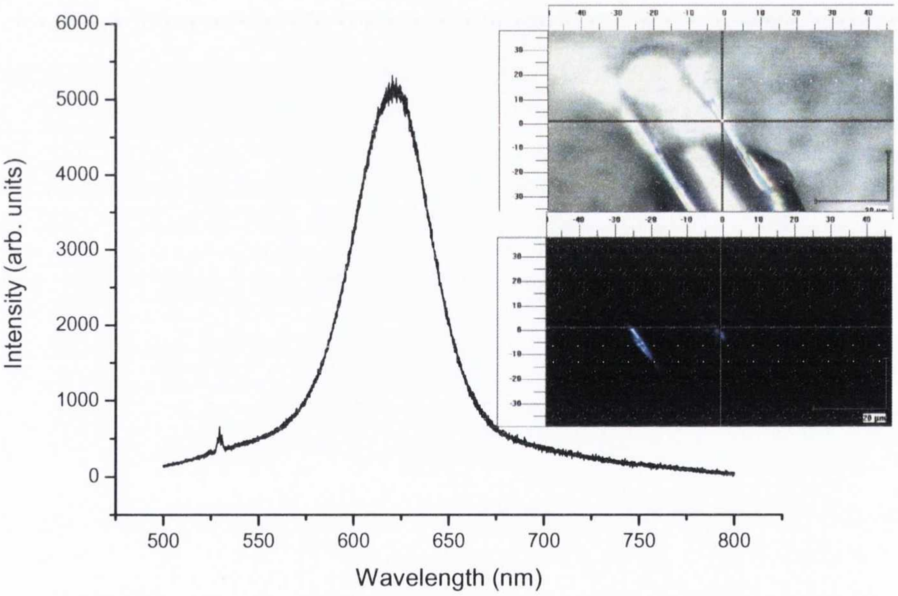

Figure 2.33*: PL spectrum of microtube Inset: Image of excitation point on tube and same showing the incident laser on tube*

2.6 Conclusions:

Microtubes have been successfully fabricated by vacuum assisted sol-gel infiltration into microchannel glass membranes. The microtubes are of high aspect ratio and reasonably good optical quality. The sol-gel reaction process and annealing allowed for the emission properties of the microtubes to be changed depending on the doping and conditions. Silica and aluminosilicate microtubes have been successfully fabricated displaying broad emission originating from carbon and oxygen related defects. Similarly luminescent microtubes doped with Eu^{3+} or CdTe QDs have been obtained and characterised. CdTe doped gels and microtubes demonstrated characteristic blue shifts due to oxidation of QDs inside silica matrix. The quality of selected microtubes enabled them to act as waveguides for light coupling between tubes and other bodies such as microspheres enabling properties of both to be observed in conjunction. The tubes have also displayed some WGM resonance character when excited appropriately. The techniques involved in the production of the tubes allow the creation of robust micro-cylindrical structures with useful potential applications in optical and photonic systems such as micro-cylindrical light emitters, sensors and optical communications devices.

2.7 References:

1 Tonucci, R. J., Justus, B. L., Campillo, A. J. & Ford, C. E. Nanochannel Array Glass. *Science* **258**, 783-785 (1992).

2 Benoit, V. *et al.* Evaluation of Three-Dimensional Microchannel Glass Biochips for Multiplexed Nucleic Acid Fluorescence Hybridization Assays. *Analytical Chemistry* **73**, 2412-2420, doi:10.1021/ac000946r (2001).

3 Vahala, K. J. Optical microcavities. *Nature* **424**, 839-846 (2003).

4 Matinaga, F. M. *et al.* Low-threshold operation of hemispherical microcavity single-quantum-well lasers at 4 K. *Appl. Phys. Lett.* **62**, 443 (1993).

5 Min, B. *et al.* High-Q surface-plasmon-polariton whispering-gallery microcavity. *Nature* **457**, 455-458 (2008).

6 Balistreri, M. L. M. *et al.* Visualizing the whispering gallery modes in a cylindrical optical microcavity. *Opt. Lett.* **24**, 1829-1831 (1999).

7 Dong, C. H. *et al.* High-Q silica microsphere by poly(methyl methacrylate) coating and modifying. *Appl. Phys. Lett.* **96**, 061106-061103 (2010).

8 Lefevre-Seguin, V. Whispering-gallery mode lasers with doped silica microspheres. *Opt. Mat.* **11**, 153-165 (1999).

9 Balakrishnan, S. *et al.* Confined optical modes and amplified spontaneous emission from a microtube cavity formed by vacuum assited filtration. *Appl. Phys. Lett.* **89**, 143113 (2006).

10 Y. P. Rakovich *et al.* The Fabrication, Fluorescence Dynamics, and Whispering Gallery Modes of Aluminosilicate Microtube Resonators. *Adv. Func. Mat.* **17**, 1106-1114 (2007).

11 Steinhart, M. *et al.* Polymer Nanotubes by Wetting of Ordered Porous Templates. *Science* **296**, 1997-, doi:10.1126/science.1071210 (2002).

12 Arai, K. *et al.* Aluminum or phosphorus co-doping effects on the fluorescence and structural properties of neodymium-doped silica glass. *Journal of Applied Physics* **59**, 3430-3436 (1986).

13 Silversmith, A. J. *et al.* Fluorescence yield in rare-earth-doped sol-gel silicate glasses. *Journal of Luminescence* **129**, 1501-1504 (2009).

14 Nogami, M. & Abe, Y. Properties of sol--gel-derived Al2O3---SiO2 glasses using Eu3+ ion fluorescence spectra. *Journal of Non-Crystalline Solids* **197**, 73-78 (1996).

15 Costa, V. C., Lochhead, M. J. & Bray, K. L. Fluorescence Line-Narrowing Study of Eu3+-Doped Sol–Gel Silica: Effect of Modifying Cations on the Clustering of Eu3+. *Chemistry of Materials* **8**, 783-790, doi:10.1021/cm9504910 (1996).

16 Lochhead, M. J. & Bray, K. L. Rare-Earth Clustering and Aluminum Codoping in Sol-Gel Silica: Investigation Using Europium(III) Fluorescence Spectroscopy. *Chemistry of Materials* **7**, 572-577, doi:10.1021/cm00051a019 (1995).

17 De Witte, B. M. & Uytterhoeven, J. B. Acid and Alkaline Sol-Gel Synthesis of Amorphous Aluminosilicates, Dry Gel Properties, and Their Use in Probing Sol Phase Reactions. *Journal of Colloid and Interface Science* **181**, 200-207 (1996).

18 De Witte, B., Aernouts, K. & Uytterhoeven, J. B. Aging of aluminosilicate and silica gels in aqueous solutions of various pH and Al content, a textural and structural evaluation. *Microporous Materials* **7**, 97-108 (1996).

19 Binnemans, K. Lanthanide-Based Luminescent Hybrid Materials. *Chemical Reviews* **109**, 4283-4374, doi:10.1021/cr8003983 (2009).

20 Brinker, J. C. & Scherer, G. W. *The Physics and Chemistry of Sol-Gel Processing.* (Academic Press Limited, 1990).

21 Nogami, M. & Abe, Y. Enhanced emission from Eu2^{+} ions in sol-gel derived Al_2O_3-SiO_2 glasses. *Appl. Phys. Lett.* **69**, 25 (1996).

22 Rakov, N., Maciel, G. S., Lozano, W. B. & de Araujo, C. B. Investigation of Eu^{3+} luminescence intensification in Al_2O_3 powders codoped with Tb^{3+} and prepared by low-temperature direct combustion synthesis. *Appl. Phys. Lett.* **88**, 081908-081903 (2006).

23 Hreniak, D. *et al.* Nature and optical behaviour of heavily europium-doped silica glasses obtained by the sol-gel method. *J. Non. Crys. Sol.* **298**, 146-152 (2002).

24 Biswas, A., Friend, C. S., Maciel, G. S. & Prasad, P. N. Optical properties of Europium doped gels during densification. *J. Non. Crys. Sol.* **261**, 9-14 (2000).

25 Digonnet, M. J. F. *Rare-Earth-Doped Fiber Lasers and Amplifiers.* 2nd edn, (Marcel Dekker, Inc., 2001).

26 Kloprogge, J. T. & Frost, R. L. Raman and infrared microscopy study of zunyite, a natural Al13 silicate. *Spectrochimica Acta Part A: Molecular and Biomolecular Spectroscopy* **55**, 1505-1514 (1999).

27 Green, W. H., Le, K. P., Grey, J., Au, T. T. & Sailor, M. J. White Phosphors from a Silicate-Carboxylate Sol-Gel Precursor That Lack Metal Activator Ions. *Science* **276**, 1826-1828, doi:10.1126/science.276.5320.1826 (1997).

28 Nayak, M., Ando, M. & Murase, N. in *26th Annual Conference on Composites, Advanced Ceramics, Materials, and Structures: B: Ceramic Engineering and Science Proceedings, Volume 23, Issue 4* (ed Mrityunjay Singh Hau-Tay Lin) 695-700 (2008).

29 Li, C. L., Ando, M. & Murase, N. Preparation and characterization of glass embedding photoluminescent CdTe nanocrystals. *Journal of Non-Crystalline Solids* **342**, 32-38 (2004).

30 Li, C. L. & Murase, N. Synthesis of Highly Luminescent Glasses Incorporating CdTe Nanocrystals through Sol-Gel Processing. *Langmuir* **20**, 1-4 (2004).

31 Yang, P. & Murase, N. Intensely emitting CdTe nanocrystals retained initial photoluminescence efficiency in sol–gel derived Si1-xZrxO2 glass. *Applied Physics A: Materials Science & Processing* **89**, 189-193 (2007).

32 Selvan, S. T., Bullen, C., Ashokkumar, M. & Mulvaney, P. Synthesis of Tunable, Highly Luminescent QD-Glasses Through Sol-Gel Processing. *Advanced Materials* **13**, 985-988, doi:10.1002/1521-4095(200107)13:12/13<985::aid-adma985>3.0.co;2-w (2001).

33 Miri Kazes, T. S. R. R. U. B. Organic-Inorganic Sol-Gel Composites Incorporating Semiconductor Nanocrystals for Optical Gain Applications. *Advanced Materials* **9999**, NA (2009).

34 Jeong, S. *et al.* One-Step Preparation of Strongly Luminescent and Highly Loaded CdSe Quantum Dot−Silica Films. *The Journal of Physical Chemistry C* **114**, 14362-14367, doi:10.1021/jp103617m (2010).

35 Yu, H., Liu, Y. & Brock, S. L. Tuning the Optical Band Gap of Quantum Dot Assemblies by Varying Network Density. *ACS Nano* (2009).

36 Yang, P., Ando, M. & Murase, N. Encapsulation of emitting CdTe QDs within silica beads to retain initial photoluminescence efficiency. *Journal of Colloid and Interface Science* **316**, 420-427 (2007).

37 Li, H. & Qu, F. Synthesis of CdTe Quantum Dots in Sol−Gel-Derived Composite Silica Spheres Coated with Calix[4]arene as Luminescent Probes for Pesticides. *Chemistry of Materials* **19**, 4148-4154, doi:10.1021/cm0700089 (2007).

38 Wang, Y., Tang, Z., Liang, X., Liz-Marzán, L. M. & Kotov, N. A. SiO2-Coated CdTe Nanowires: Bristled Nano Centipedes. *Nano Letters* **4**, 225-231, doi:10.1021/nl0349505 (2004).

39 Maoquan, C. & Jiasheng, H. Preparation and characterization of fluorescent microtubes with high length/diameter ratios. *Smart Materials and Structures* **18**, 025013 (2009).

40 Gaponik, N. *et al.* Thiol-Capping of CdTe Nanocrystals: An Alternative to Organometallic Synthetic Routes. *J. Phys. Chem. B* **106**, 7177-7185 (2002).

41 Byrne, S. J. *et al.* Optimisation of the synthesis and modification of CdTe quantum dots for enhanced live cell imaging. *Journal of Materials Chemistry* **16**, 2896-2902 (2006).

42 Wolcott, A. *et al.* Silica-Coated CdTe Quantum Dots Functionalized with Thiols for Bioconjugation to IgG Proteins. *The Journal of Physical Chemistry B* **110**, 5779-5789, doi:10.1021/jp057435z (2006).

43 Jin, S., Song, N. & Lian, T. Suppressed Blinking Dynamics of Single QDs on ITO. *ACS Nano* **4**, 1545-1552, doi:10.1021/nn901808f (2010).

44 Wang, X. *et al.* Non-blinking semiconductor nanocrystals. *Nature* **459**, 686-689, doi:http://www.nature.com/nature/journal/v459/n7247/suppinfo/nature08072_S1.html (2009).

45 Pelton, M., Smith, G., Scherer, N. F. & Marcus, R. A. Evidence for a diffusion-controlled mechanism for fluorescence blinking of colloidal quantum dots. *Proceedings of the National Academy of Sciences* **104**, 14249-14254, doi:10.1073/pnas.0706164104 (2007).

46 Ma, J. *et al.* Photostability of thiol-capped CdTe quantum dots in living cells: the effect of photo-oxidation. *Nanotechnology*, 2083 (2006).

47 Cordero, S. R., Carson, P. J., Estabrook, R. A., Strouse, G. F. & Buratto, S. K. Photo-Activated Luminescence of CdSe Quantum Dot Monolayers. *J. Phys. Chem. B* **104**, 12137-12142 (2000).

48 Murase, N., Yang, P. & Li, C. L. Quantitative Analysis of the Photodegradation of Emitting CdTe Nanocrystals Dispersed in Glass Films. *J. Phys. Chem. B* **109**, 17855-17860 (2005).

Chapter 3

Silica Nanowires

3.1 Introduction

Silica nanowires and nanotubes have many potential applications in areas of bio-medicine, they have shown positive results in gene delivery[1] and their high aspect ratio for bio-detection[2] and even optics where they have been shown to have the capability to be used as low loss waveguiding devices for integrated photonic devices[3]. The fabrication of 1D nanostructures using nano-porous alumina membranes is well known as discussed in section 1.3. This chapter will focus on the preparation of intrinsically defect emitting silica nanowires and magnetically loaded silica nanowires which have been produced via doping using magnetic NPs and their application for bio-sensing and tagging using flow cytometry.

3.2 Defect emitting Silica Nanowires

As discussed in Section 1.4 and 2.2, upon annealing, silica and aluminosilicate xerogels can display bright intense visible luminescence under UV radiation. This phenomenon has been observed in some nanostructures previously fabricated. For example aluminosilicate mesoporous structures displayed bright visible emission at room temperature upon annealing[4]. Nanostructures such as silica nanotubes have been observed to show this emission with fabrication via cellulose whiskers[5] and wetting in porous alumina to create silica nanotubular flakes[6] with the latter even observing a visible PL from unannealed samples which they also attributed to defect emission this would seem an unlikely case given the highly amorphous state of xerogel silica and one wonders whether it was a cause of the unusual method of membrane dissolution with phosphoric and chromic acid. The emitting silica nanowires discussed here were fabricated using the vacuum infiltration method developed for pore filling and release and are the first of the type known that the author is aware[7].

In our work silica nanowires with defect luminescence were fabricated by vacuum infiltration of a silica sol into 200 nm diameter porous alumina membranes. The infiltrated membranes were then polished to remove surface xerogel and annealed at 400 °C for 1hr in air. Release of the wires is achieved via dissolution of the membrane. This is followed by washing of the wires with Millipore water until neutral pH is achieved as schematically demonstrated in Figure 3.1 below.

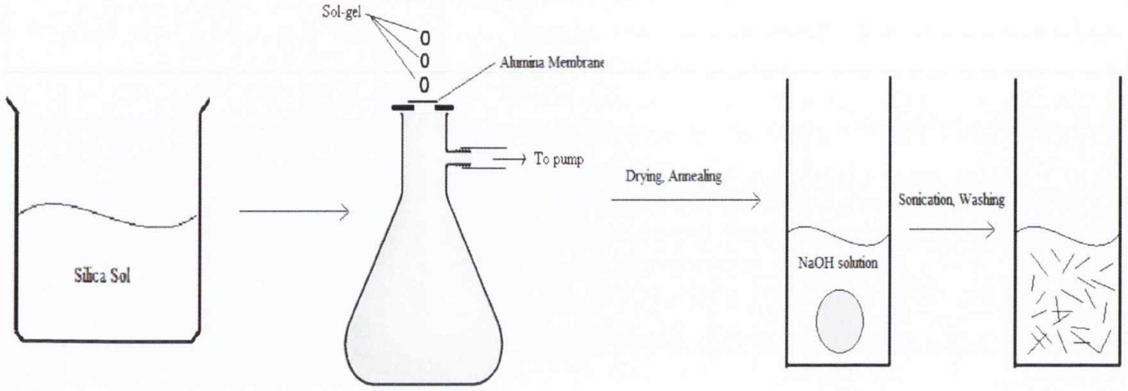

Figure 3.1: Schematic showing silica nanowire fabrication

3.2.1 Optical and fluorescent microscopy characterisation of nanowires

The silica nanowires have been characterised by optical and fluorescence microscopy, TEM and SEM. The microscope images shown below in Figure 3.2 were simply obtained by drying the wires onto glass slides in air.

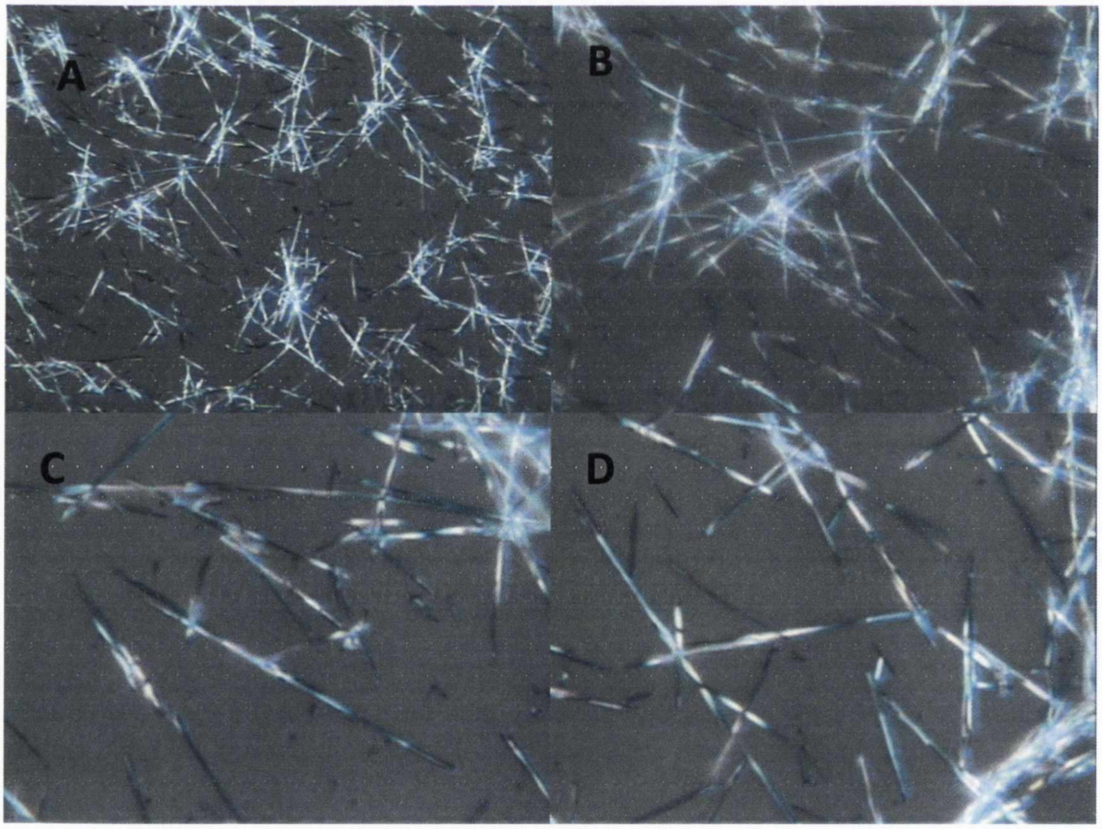

Figure 3.2: Optical Microscope images of silica nanowires A: x50 B: x100 C&D: x150

The images clearly show the high aspect ratio (~50 length/diameter) needle like structure of the wires with a relatively high concentration of wires achieved after the release from the membrane. The optical microscope is reaching the limit of its resolution capability in respect to the diameter of the wires, therefore the images seem blurred as the light reflects around the wires. To demonstrate the fluorescence of the wires they were examined under a fluorescence microscope under UV illumination. The images display the nanowires showing their uniform emission along each wire. The inset in Figure 3.3 below shows the original infiltrated alumina membrane after annealing under a UV lamp, the bright emission is only seen from the infiltrated area and no emission is observed from other areas of the membrane.

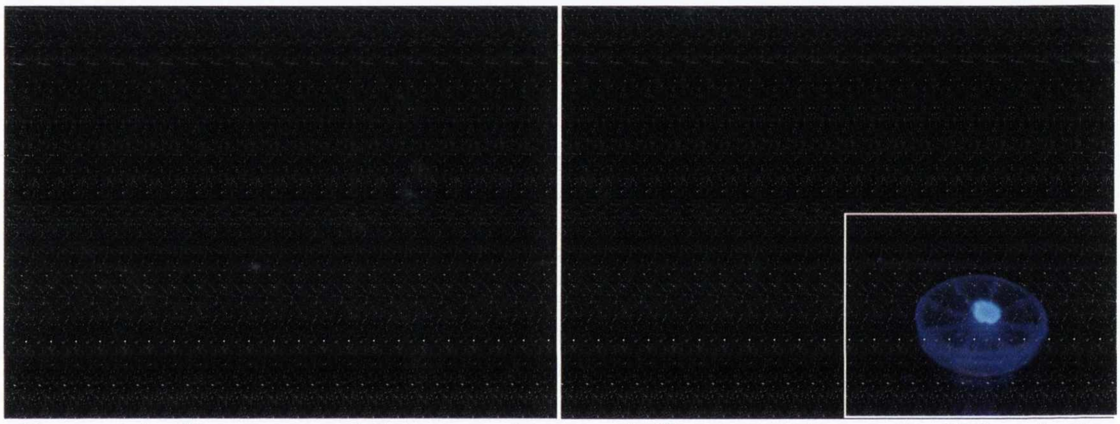

Figure 3.3: Fluorescence Microscope images of silica nanowires under UV excitation (350 nm, x50 magnification) Inset; Photo showing infiltrated alumina membrane after annealing

3.2.2 Electron Microscopy of nanowires

To further characterise the structure and size of the nanowires electron microscopy (SEM and TEM) was carried out. Shown below in Figure 3.4 are SEM images of wires within a porous alumina membrane which has been broken to image the wires within the pores. Upon careful observation it can be seen that some nanowire structures are seen to be merged together where two pores join. This can be more clearly observed in the SEM images in Figure 3.5 of released wires (Note: wires became embedded in the glue and coating and thus it was mainly only bundles that could be imaged). Where the wires branch off or deviate from ideal cylindrical shape can be observed, this is due to the membrane quality used. As the membranes are obtained commercially and whose main purpose is for filtration the pores tend not to be perfectly regular in shape and size. Indeed the inner size of the pores can be larger than the 200 nm quoted and thusly leads to wires whose diameters are larger than expected.

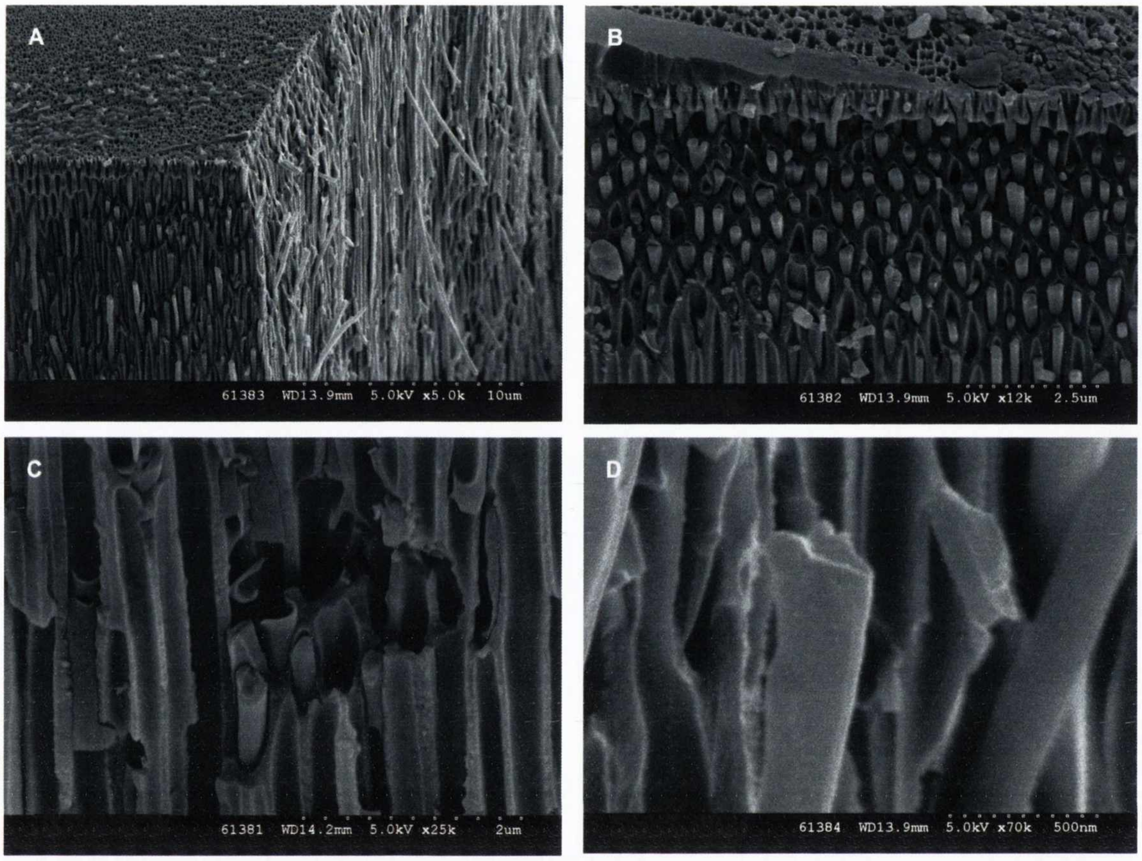

Figure 3.4: SEM images of silica nanowires in pores of alumina membrane

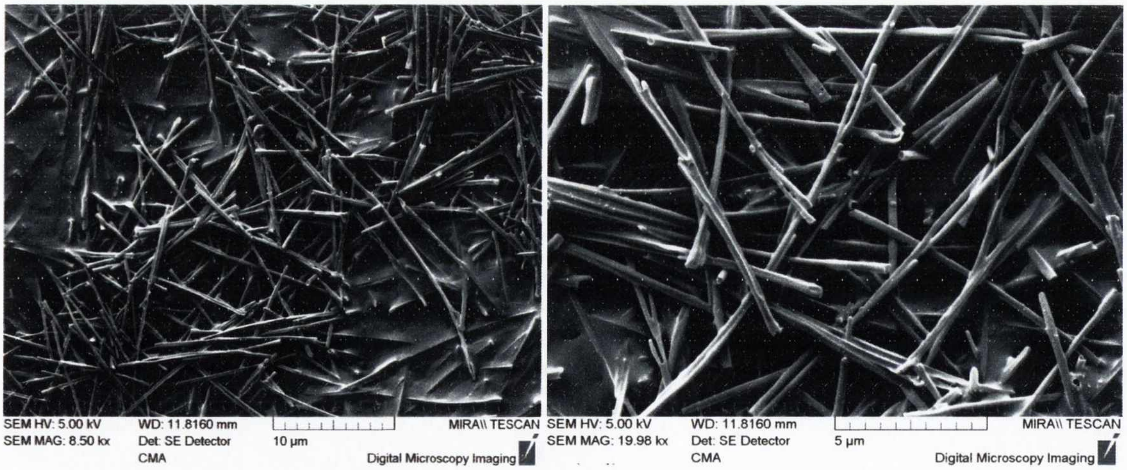

Figure 3.5: SEM images of released silica nanowires

The TEM images shown in Figure 3.6 display in more detail the solid structure of the annealed wires and show the diameter of the wires and how it varies to the quoted size of the pores, with a diameter of 275 nm with a standard deviation of 27 nm. One of the images also shows the effect of the uneven nature of the some pores where they can run into each other which is clearly seen in the bottom left image as the wire curled branches and steps where the pores terminate and branch off.

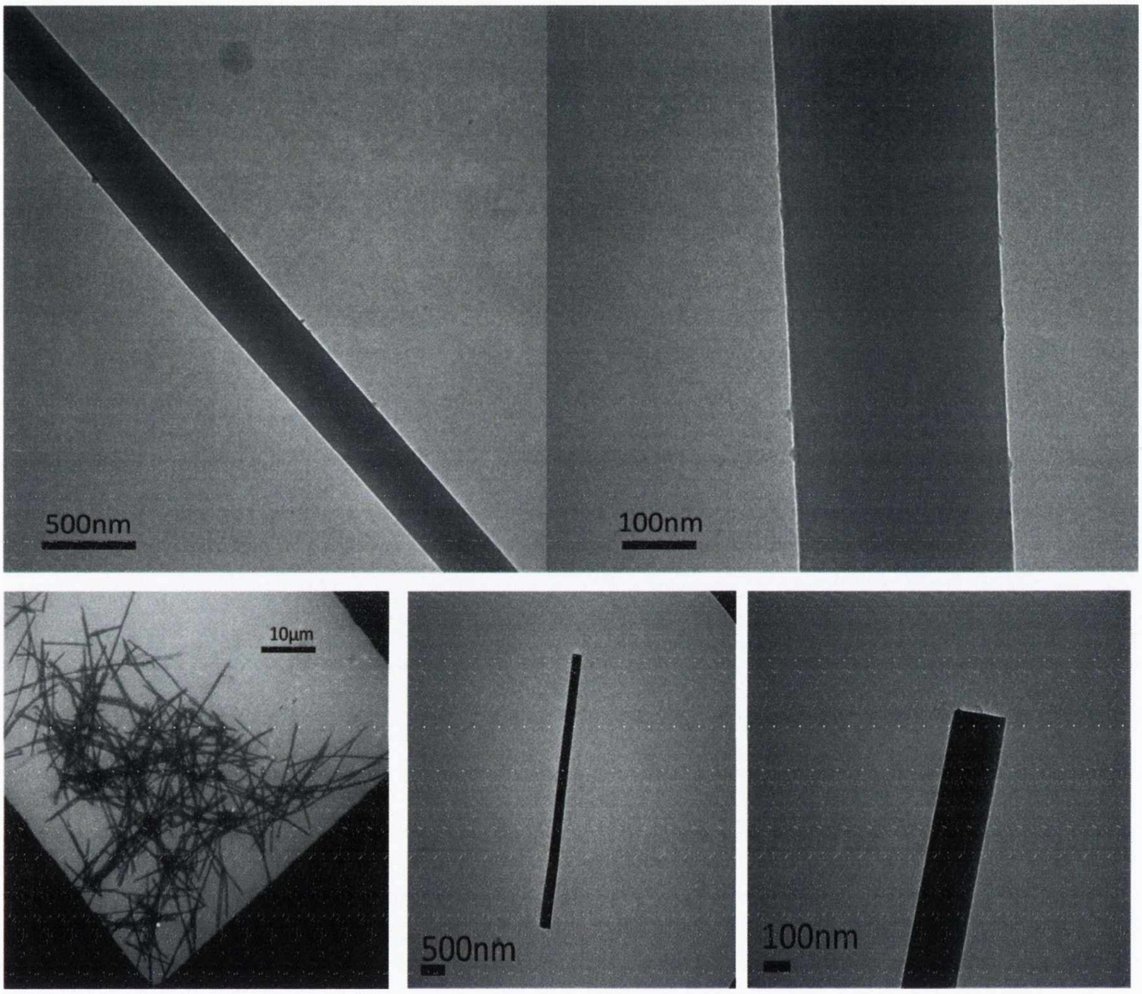

Figure 3.6: TEM images of silica nanowires showing both uniform and membrane altered structures

3.2.3 Emission characterisation of nanowires

Solid state photoluminescence studies were carried out on the wires to determine the nature of the emission. Figure 3.7 displays the spectra taken from several areas on a sample of dried wires on a microscope slide (t2_1-5 representing different focus positions). The spectra demonstrated as expected a broad emission over the visible region of the spectrum. As the different intensities shown in the spectra have the same emission profile the different intensities are considered an increase in intensity due to the different concentration of nanowires on the surface being examined and the number of wires being excited by the laser spot (about 5µm in diameter at the crosshairs) as shown in images accompanying spectra. This emission is again assumed to be from interstitial carbon defects within the silica (again literature points to non-bridging oxygen defects as being responsible for emission mainly in the UV region and bright broad visible emission seems more commonly associated with carbon defects (Section 1.4)) matrix as discussed in previous sections. The emission here seems to differ slightly from that of previous sections concerning microtubes this could be due to the fact that the nanowires were annealed only to 400 °C and not 500 °C resulting in slightly different environments for the emitting species.

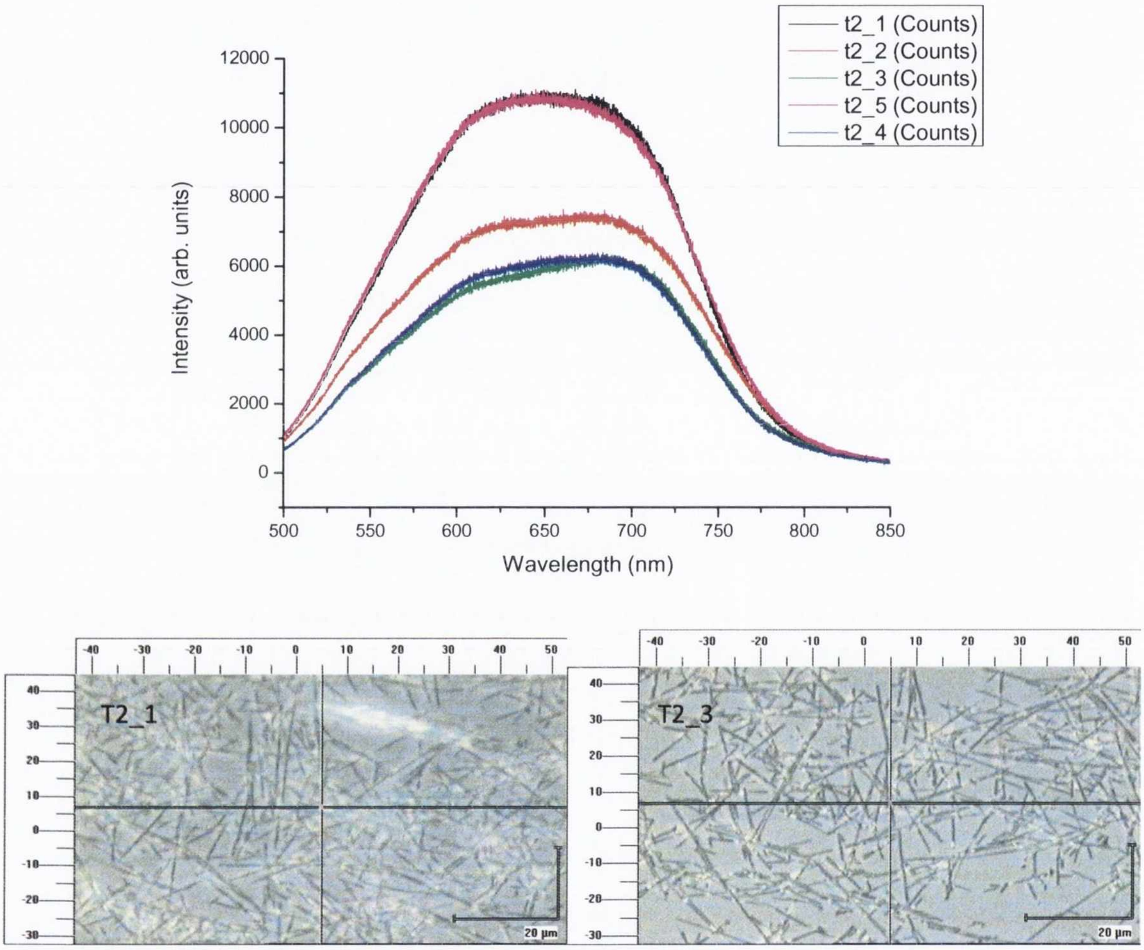

Figure 3.7: Above; Solid state luminescence spectra of nanowires

Below; Sample images of scan positions of spectra

Amplitude 1	22635
Lifetime 1	5.5 ns
Amplitude 2	31879
Lifetime 2	1.1 ns
Background	1659
χ^2	2.573
Average Lifetime	4.5 ns

Table 1: Key values of lifetimes of luminescent species (derived from Figure 3.8)

Fluorescent lifetime studies performed on the nanowires showed them to have an average lifetime of 4.5 ns using a double exponential fitting (see Table 1 and Figure 3.8), which is in the region of that described by Green et al[8] for carbon defect related emission. Thermo-gravimetric analysis (TGA) was performed on the bulk silica xerogel (resulting from the original sol infiltrated into alumina) to determine the weight change in the sample upon annealing and examine if any unique changes are observed. Figure 3.9 shows the results of the TGA which are similar to that of the aluminosilicate xerogels described in Chapter 2, where water loss is observed (up to 100 °C) and accounts for a 20% weight loss (water and organic solvents). There is a brief interval of no weight loss between 100 °C-200 °C until 200 °C-300 °C whereupon there is a gradual further weight loss of 5%, which corresponds the removal of water and OH groups within the matrix coinciding with condensation of silanol bonds to form siloxane bonds[9] plus the beginning of the thermal decomposition of residual organic groups (e.g. ethoxy groups). Tellingly there is a distinct decrease in weight beginning at ~385 °C (clearly visible in the D-TGA) which could indicate the onset of formation of the luminescence species within the silica matrix. Weight loss continues down to around 70% of the original weight.

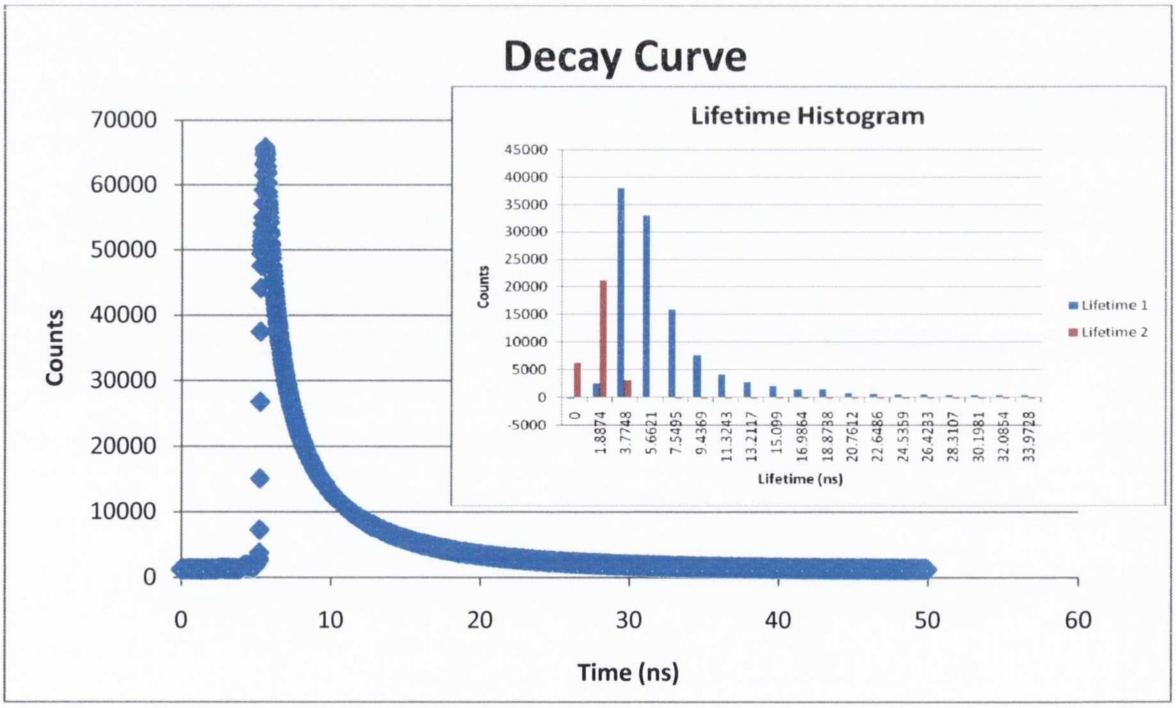

Figure 3.8: Decay Curve and fluorescent lifetime histogram of nanowires

Raman scans of the bulk xerogel annealed at 400 °C (Figure 3.10) shows evidence of organic groups with prominent peaks at 1445 cm^{-1} and 1596 cm^{-1} which are typical of carbon-carbon single and double bonds, also in the 1100-1200 cm^{-1} region is thought to show the Si-O-C vibration[10] along with numerous peaks related top Si-O-Si, Si-O and Si-O-H vibrations and stretching. This is not to say that the emission is caused definitively by the carbon defects but strongly indicates their presence in the system and most likely contribution in some form.

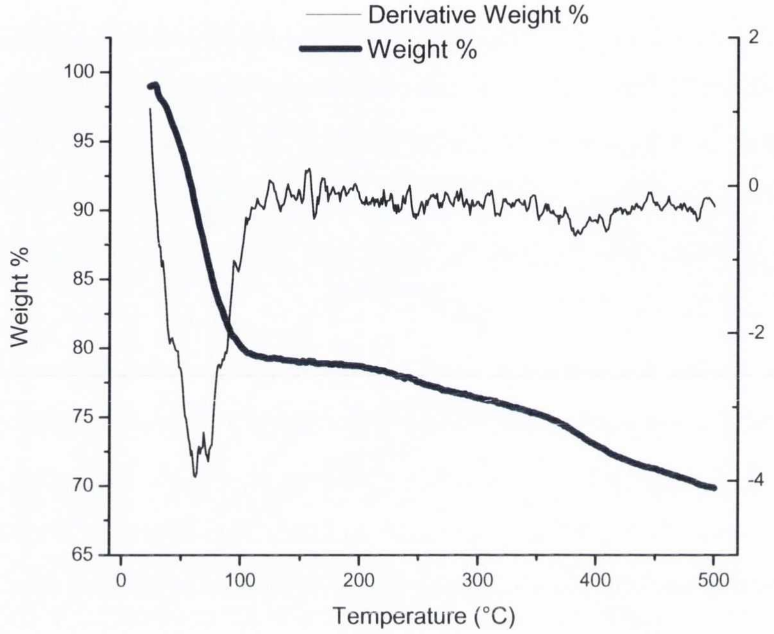

Figure 3.9: TGA and D-TGA curves of bulk silica xerogel

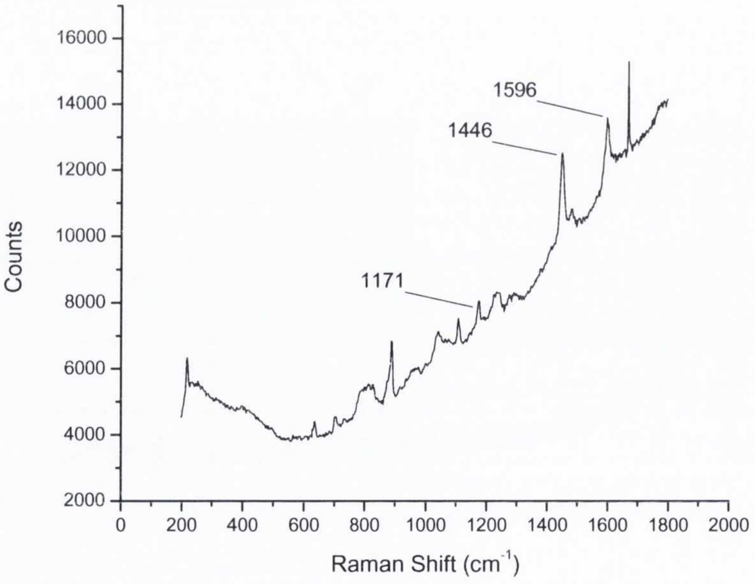

Figure 3.10: Raman spectrum of bulk xerogel sample

3.3 Gold Nanoparticle (AuNP) coating of Silica Nanowires

As discussed in more detail in section 1.5.2, the properties of AuNPs in relation to their plasmonic features can provide a valuable tool in areas of sensing, catalysis and energy transfer mechanisms. With this in mind it was undertaken to functionalise silica nanowires and attach AuNPs to their surface to obtain nanowires with the potential to utilise the plasmonic properties of the AuNPs.

3.3.1 AuNP fabrication and characterisation

Briefly (fully explained in Section 6.3.4) the AuNPs were fabricated by the phase transfer of $AuCl_3$ from chloroform to the aqueous phase by stabilisation with DMAP and reduction with $NaBH_4$ to create spherical AuNPs with a weak DMAP ligand shell which remained stable in water over long periods of time[11]. Their size range varies from ~10-20 nm, with some larger particles resulting from flocculation over time (Figure 3.11).

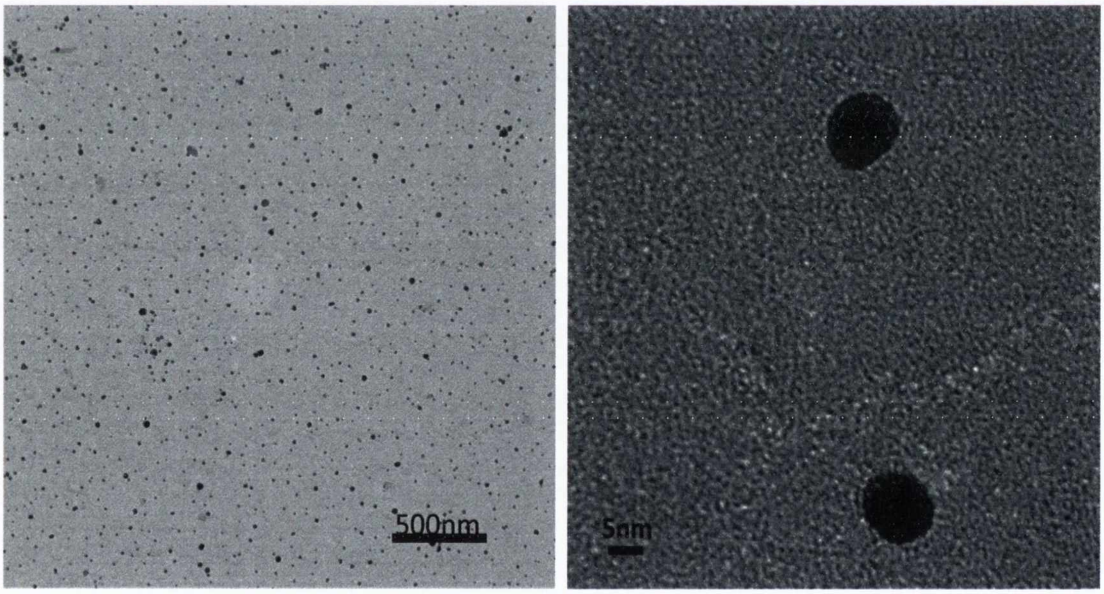

Figure 3.11: TEM images of DMAP stabilised AuNPs

The surface plasmon band of the AuNPs was monitored with UV-vis as shown below in Figure 3.12 and found to be centred at 520 nm as expected for NPs in the 5-20 nm size range[12].

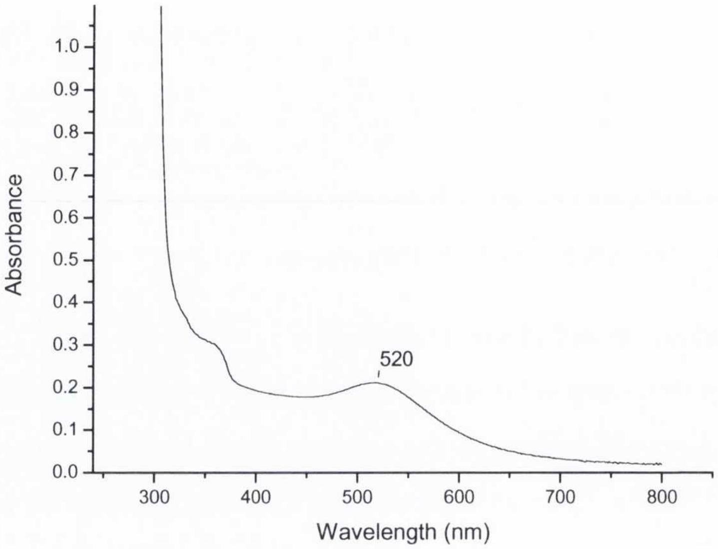

Figure 3.12: UV-vis absorption spectrum of AuNPs

3.3.2 Surface functionalisation and AuNP coverage

To attach the AuNPs to the silica nanowires functional groups on the surface of the wire are required for the NP to bind to. Given the nature of production of the silica wires by sol-gel processing, surface binding sites in the form of silanol groups are known to readily exist on the surface (in the region of 3-5 OH/nm^2) [9]. However for a higher degree of surface coverage with AuNPs, surface functionalisation of the wire is desired. We performed AuNP attachment with and without specific functionalisation which is described here for comparison.

Firstly the attempted NP attachment to unfunctionalised wires was performed by diluting the original AuNP solution (estimated to be ~17.6 μM) x200 times and adding 0.5 ml of this to a 1ml suspension of the wires and vortexed for 2 hours to stimulate attachment. The wires were examined under TEM before and after washing (via filtration to remove excess AuNPs) to determine the coverage by AuNPs. As demonstrated in the images shown in Figure 3.13 (top), the unwashed samples show a reasonably high degree of coverage before washing, however this may be partly due to free AuNPs in solution depositing on the wires upon drying on the TEM grid. As can be seen there is also a large number of AuNPs deposited around the wires. The wires washed via filtration shown in Figure 3.13 (bottom) show the effect of the treatment (both the filtration process and sonication treatment during it) on the wires with AuNPs attached when unfunctionalised, with the wires showing less coverage in general and even patchy areas of coverage most likely due to certain areas being cleaned of particles during sonication.

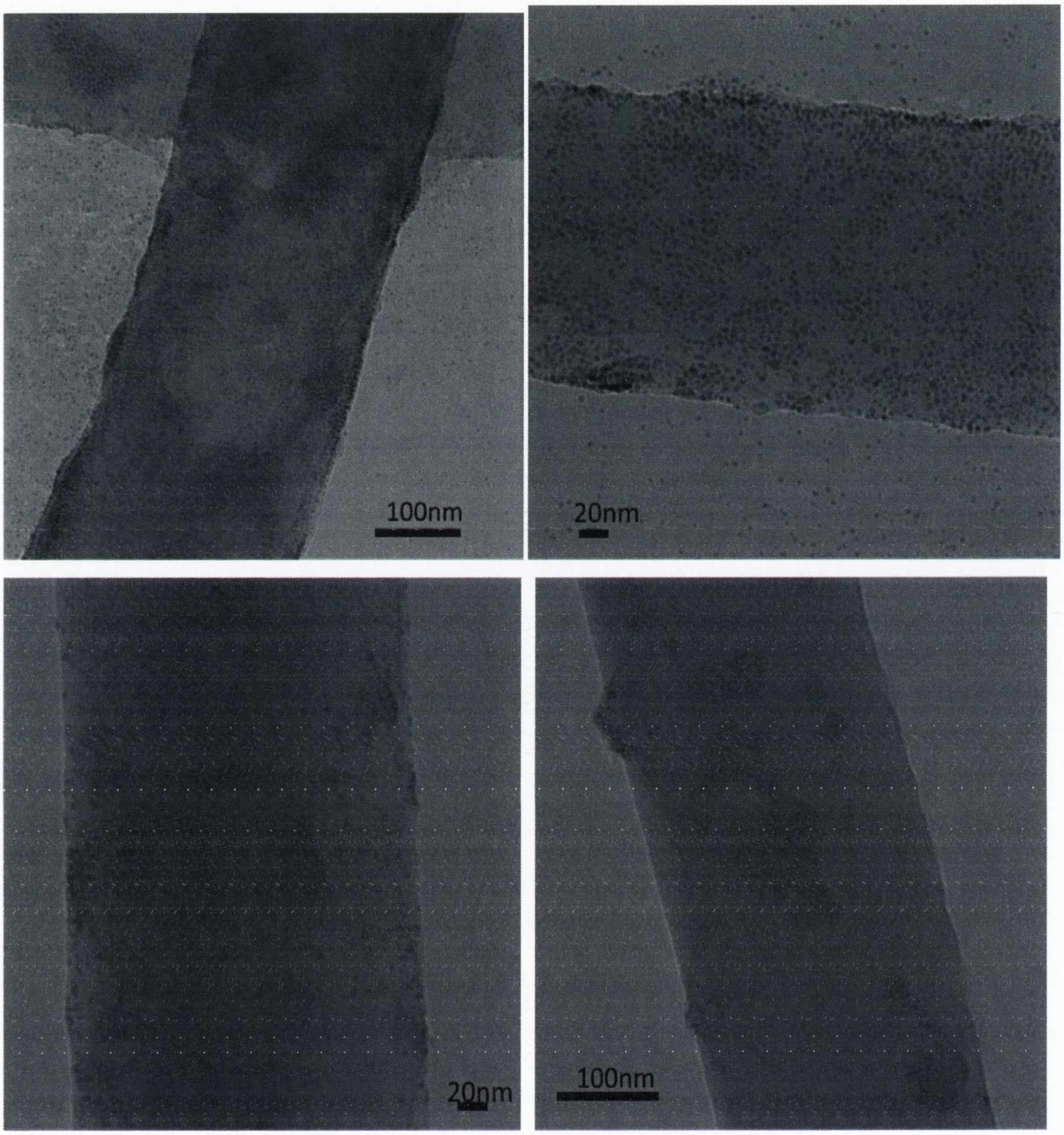

Figure 3.13: TEM images of AuNP coated unfunctionalised silica nanowires (top; unwashed, bottom; washed)

In an attempt to achieve stronger bonded and higher particle coverage the nanowires were functionalised using 3-mercaptopropyltrimethoxysilane (MPS) as shown in Figure 3.14 in several ways. Initial experiments using solutions of MPS in iso-propanol (IPO) and conc. ammonia and adding it to a dispersion of nanowires in water and vortexing, however this caused formation of polyhedral oligomeric silsesquioxanes (POSS) NPs by polymerisation of the MPS and subsequent attachment of AuNPs upon their addition to these particles resulting in little or no AuNPs on the wires. To prevent this, the wires were washed and redispersed in IPO, with the addition of the MPS in IPO solution and conc. ammonia to this and subsequent vortexing and washing (to remove excess MPS). The wires were washed and redispersed in water to allow for the addition of the aqueous phase AuNPs to the wires which with vortexing were chemisorbed onto the surface of the nanowires displacing the weak DMAP ligand stabiliser and bonding via the thiol group as demonstrated in Figure 3.14 below.

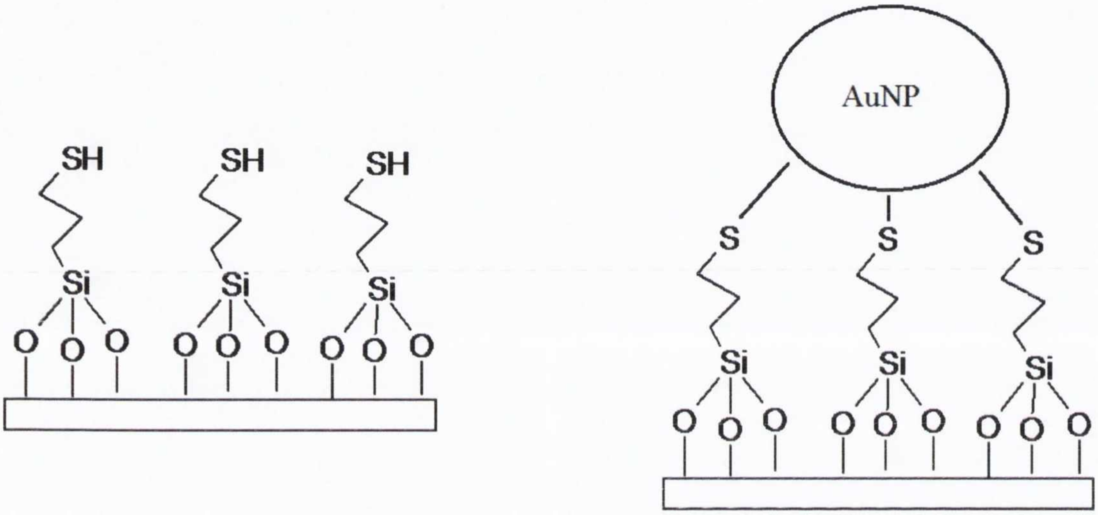

Figure 3.14: Diagrams representing surface functionalisation with MPS and attachment of AuNP to functionalised wire

The results are outlined in Figure 3.15 below with TEM images showing the higher level of AuNP coverage on the wires compared to the unfunctionalised wires. The larger AuNPs observed in the pure sample above in Figure 3.11 don't seem to bind to the wires, possibly due to their large size and tendency to be more easily removed during sample preparation. A small amount of aggregation and POSS NP formation is also observed in the samples most likely due to the inevitable small amounts of water existing in the ammonia and on the surface of the wires even after washing with IPO, but even more so with the redispersion of the wires into water and some residual MPS remaining which was not completely removed during washing of the samples causing the POSS NP formation.

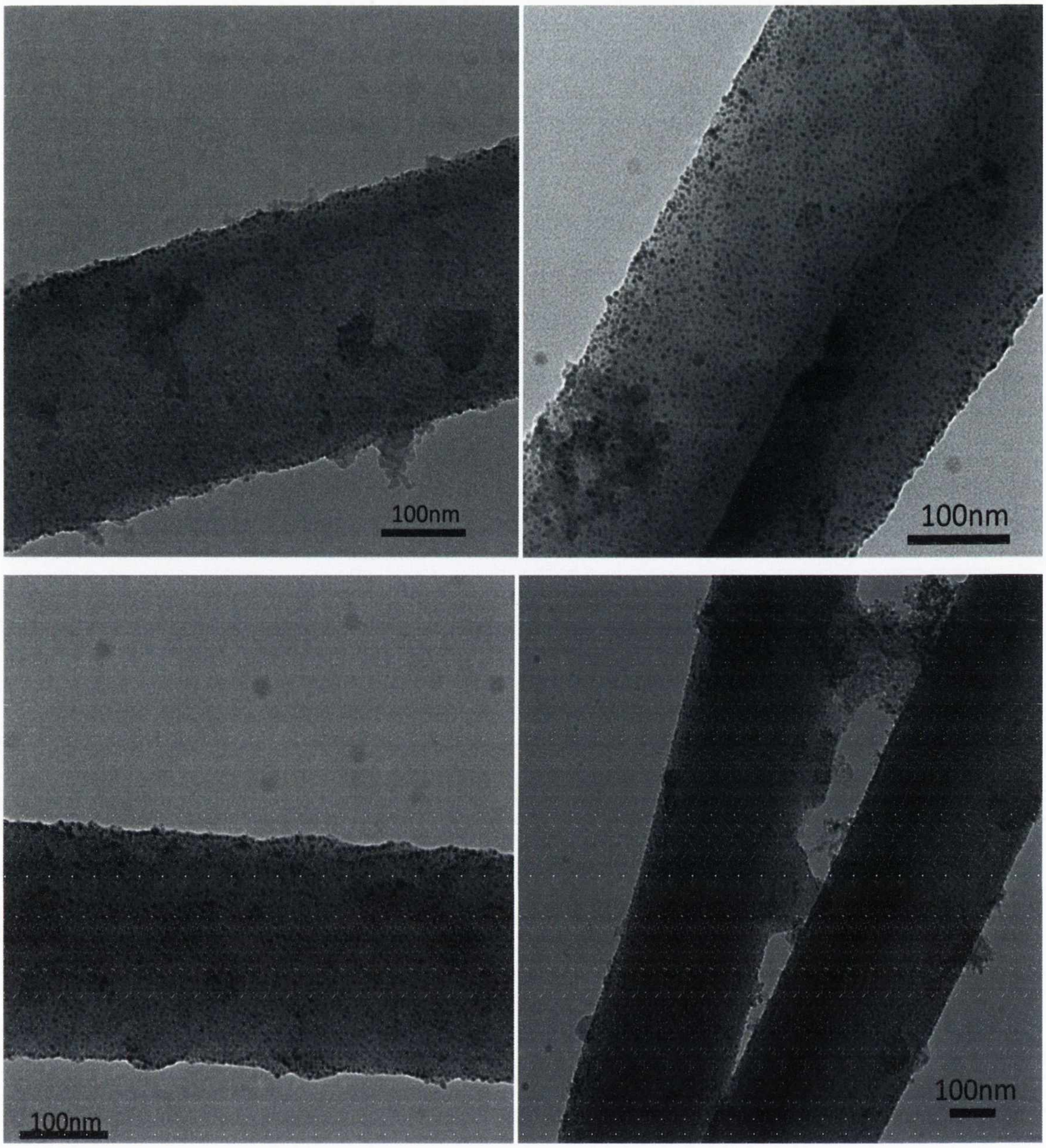

Figure 3.15: TEM images of functionalised silica nanowires showing high coverage of AuNPs on their surface

Samples of the functionalised nanowires were examined using fluorescence confocal microscopy (as described in section 6.2.11) to get an optical characterisation of the wires. The functionalised wires show a high level of reflectance from their surface upon irradiation with green light (488 nm) as seen from the bundle of irradiated wires in Figure 3.16 (right). This effect is commonly seen from metallic nanowires and is due to the SPB of the metallic AuNPs on the surface of the wires[13]. In comparison with the plain silica nanowires which show no interaction upon exposure as shown below in Figure 3.16 (left).

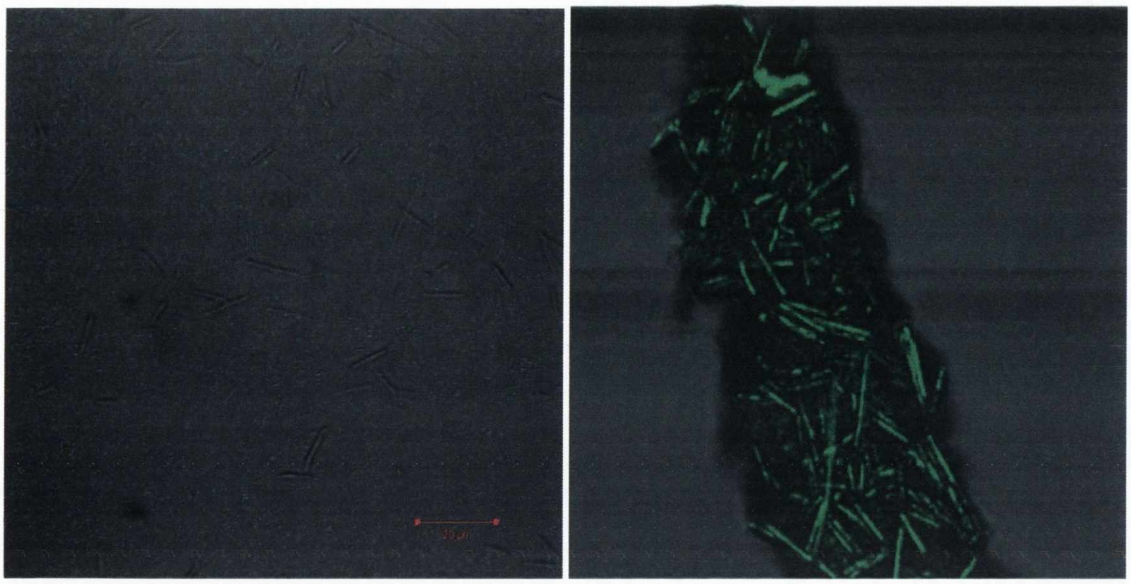

Figure 3.16: Fluorescence confocal microscope images of plain (left) and AuNP coated (right) under green light (488 nm) irradiation

The coverage of these wires with AuNPs opens up the possibility of their use for photonic and sensing applications due to their plasmonic properties. In particular it is hoped these structures could prove useful in the area of FRET to work in conjunction with other bodies.

3.4 Magnetic nanoparticle loaded silica nanowires

Magnetic nanoparticles and nanowires have received a lot of attention in recent years in various bio-medical applications including biosensing, magnetic sorting and delivery. Pure metallic magnetic nanowires have been fabricated with the use of alumina templates via elctro-deposition[14-15] and atomic layer deposition to fabricate iron oxide nanotubes[16]. Silica encapsulated nanoparticulate magnetite[17-19] and sol-gel derived magnetite particle doped silica monoliths[20] have been developed along with magnetic silica nanotubes utilising magnetic nanoparticles[21]. These various types of magnetic nanotube/nanowire structures have shown great potential to be used in bio-medical applications such as cell internalisation[22], cell manipulation and separation[23-24], drug delivery[21] and cell constructs and microarrays[25].

Our project was focused on the fabrication of magnetic nanoparticle loaded silica nanowires for potential bio-medical applications was developed and tested using flow cytometry in comparison to particles. This section explores the fabrication and characterisation of such structures.

3.4.1 Magnetite nanoparticle doped silica nanowires

As discussed in section 1.5.3 magnetite displays superparamagnetic behaviour when nanoparticulate (<20 nm) in nature. The goal was therefore to incorporate these superparamagnetic particles into a silica nanowire allowing the nanoparticle properties to be utilised while encapsulated in the silica nanowire frame. This allows a biocompatible, high surface area structure which is easily coated and functionalised for analysis while also keeping the magnetic properties for future possible separation upon application of a magnetic field.

Preparing magnetite nanoparticle doped sol-gels required altering of the sol-gel process and the nanoparticles to protect the properties of the particles during the reaction. Firstly the magnetite nanoparticles prepared via a co-precipitation of iron II and III chlorides with subsequent stabilisation of the nanoparticles with CTAB to aid suspension. Secondly the sol-gel process was modified to a two step acid-base catalysed reaction to prevent etching of the nanoparticles by adding them into a basic media (immediately after the base catalysed condensation step), this resulted in a homogenous brown solution which was then infiltrated into 200 nm porous alumina membranes and released after drying and surface polishing via membrane dissolution as demonstrated in the schematic in Figure 3.17.

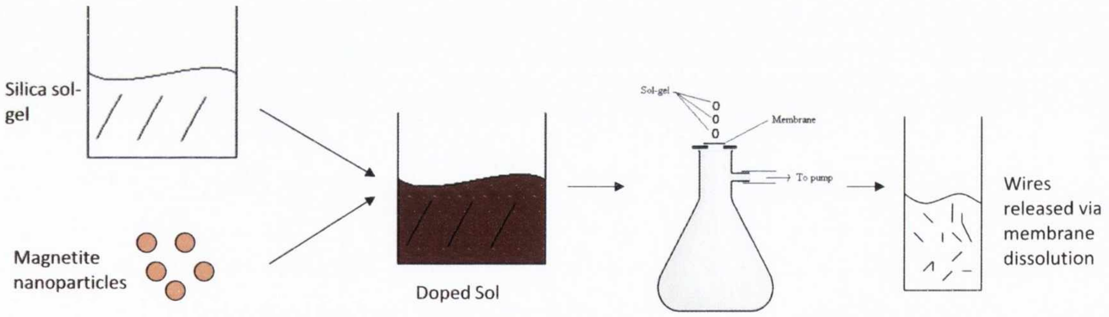

Figure 3.17: Schematic representation of fabrication of magnetite doped silica nanowires

3.4.1.1 Microscopy characterisation of nanowires

The loaded nanowires were visually characterised using optical and electron microscopy to examine their aspect ratio, size and structure. Shown below in Figure

3.18 are optical microscope and TEM images of the loaded nanowires. The images clearly show the high aspect ratio and needle like structure of the wires (again ~50 similar to the pure silica wires given the fact that the same type of membrane is used). TEM images of the wires showed them to have good structure and lengths of tens of microns with a wide distribution due to fracturing of the wires during processing most likely during sonication to assist template dissolution; diameters as discussed previously were all between 200-250 nm varying between samples in reflection of the variation of internal template diameters.

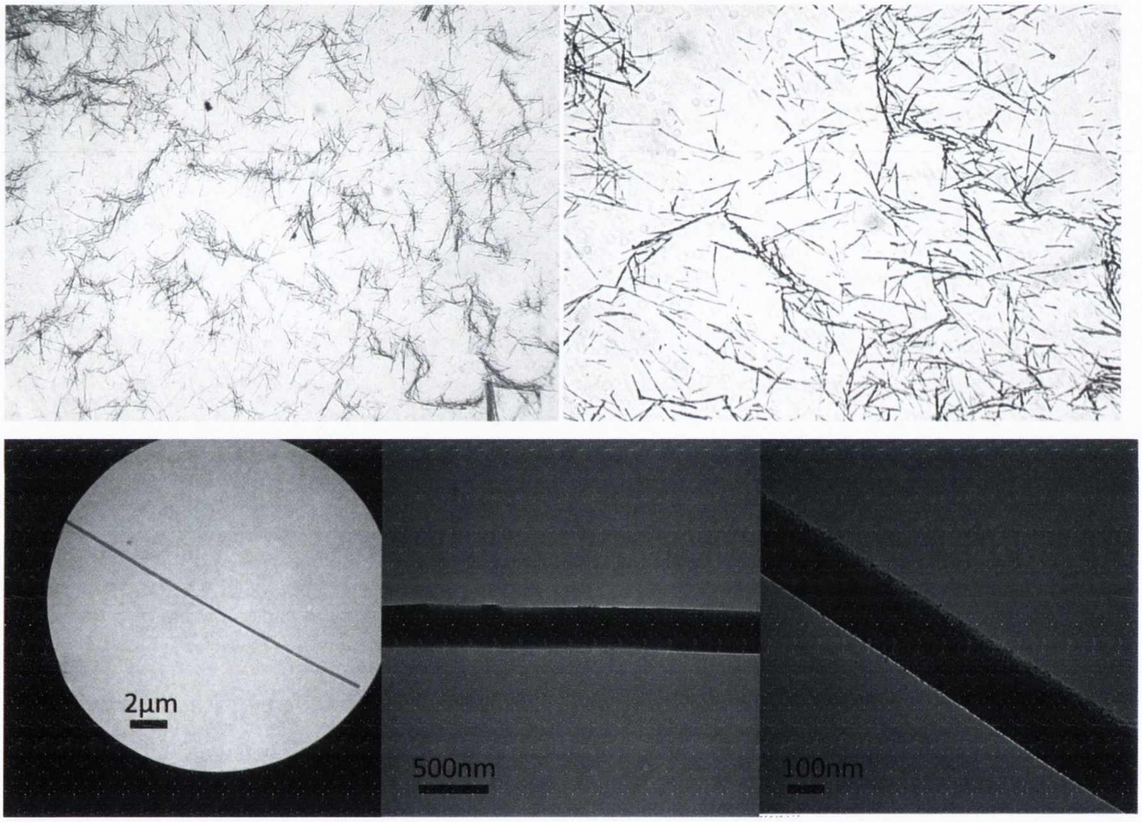

Figure 3.18: Optical microscope and TEM images of magnetite loaded silica nanowires

The wires were dried in the presence of a magnetic field to observe a possible response and alignment to the field. Figure 3.19 shows the response with a majority of the wires showing alignment with the field, the wires pointing in other directions is assumed to be due to the drying and clustering effects causing them to orient randomly.

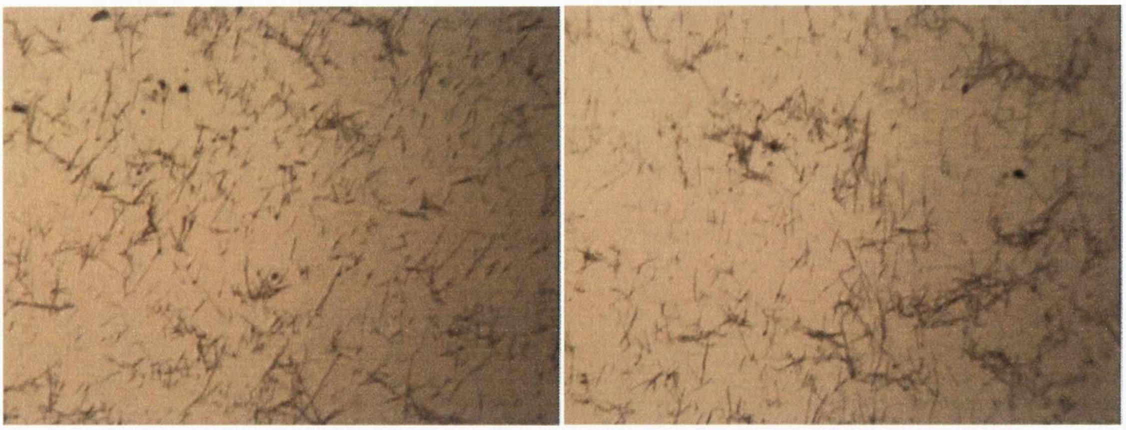

Figure 3.19: Optical microscope images showing wires in magnetic field

3.4.1.2 Magnetic characterisation of nanowires

Magnetic characterisation of the wires was carried out using vibrational sample magnetometer (VSM) and superconducting quantum interface device (SQUID) magnetometer. Initial experiments into fabrication of the wires relied on a purely acid catalysed sol-gel reaction. However, acid had a damaging effect on the magnetite nanoparticles in solution and thus reducing the magnetism of the particles and thusly the nanowires. This was demonstrated in a test experiment shown in Figure 3.20 with a reduction in magnetisation of 65 Am^2/Kg to 45 Am^2/Kg where the nanoparticles were placed in dilute HCl (approximating to concentration in sol-gel reaction) for a similar period of time as in the sol-gel reaction. The oxidising nature of the xerogel matrix causes the conversion of magnetite to maghemite and hematite (γ-Fe_2O_3 and α-Fe_2O_3) which have a lower magnetisation than magnetite. The wires also had a relatively low loading of particles within the wires further contributing to their low magnetisation; therefore the first samples (the samples used in the flow cytometry testing) were of a lower magnetic quality showing a magnetisation saturation (determined by SQUID) of only 0.04 Am^2/Kg (see Figure 3.20), also the structural quality of the wires was slightly compromised by the early washing procedures used to remove excess NaOH and other alumina hydroxides in solution, the prolonged exposure to the basic media caused the wires to suffer surface damage. These results were improved slightly by adding a more concentrated magnetite nanoparticle solution during the sol-gel reaction however degradation of the nanoparticles still occurred and a VSM measurement on the bulk material (hence somewhat more scattered) showed a higher magnetism of ~0.2 Am^2/Kg but the magnetic character is quite poor (Figure 3.21). The washing procedures were also perfected during this time which resulted in more structurally sound wires in ‘cleaner’ environments (i.e. much less excess material due to membrane dissolution). To combat the degradation of the magnetite nanoparticles during the reaction, the process was modified to a 2-step acid-base catalysed reaction with the nanoparticles being added into basic media after the second step. This reaction modification had the desired effect to reduce the degradation of the nanoparticles during the reaction and subsequent drying. The bulk gel showed a magnetisation saturation of ~0.4 Am^2/Kg (Figure 3.22) and retained its quality much more as a xerogel over time in comparison to purely acid catalysed xerogels.

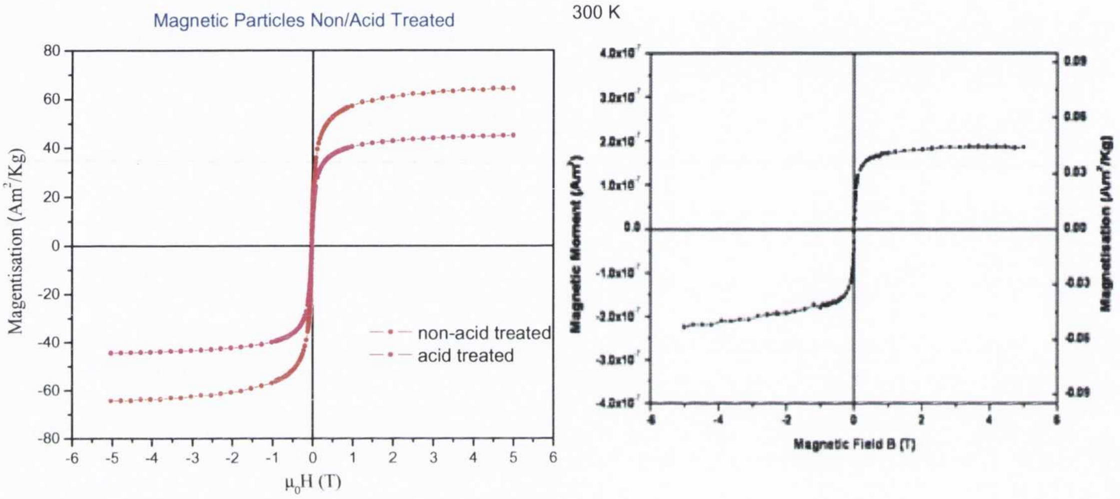

Figure 3.20: Magnetisation curves: Left; showing effect of acid on magnetite nanoparticles Right; SQUID measurement of loaded nanowires

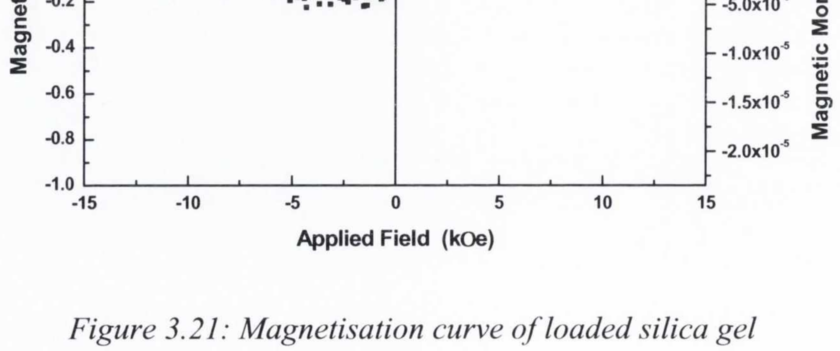

Figure 3.21: Magnetisation curve of loaded silica gel

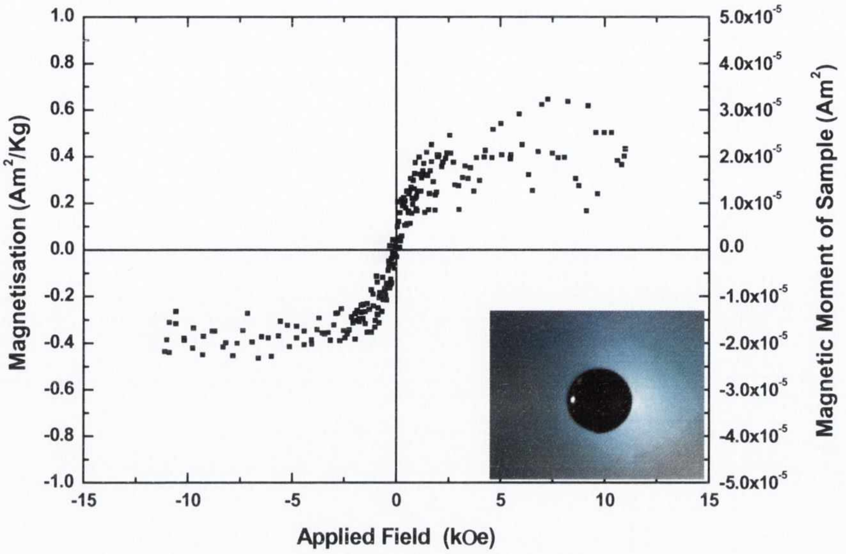

Figure 3.22: Magnetisation curve of loaded silica xerogel fabricated with acid-base catalysed sol-gel reaction Inset: Photo of loaded silica xerogel

Furthermore the magnetisation scans show that the nanowires retain a superparamagnetic properties from the nanoparticles which is important so as to ensure that the nanowires do not form bundles and aggregate in solution via magnetic interaction which allows them to be a much more viable candidate for flow cytometry studies which operates on a single body detection parameter (see section 3.2.1.3).

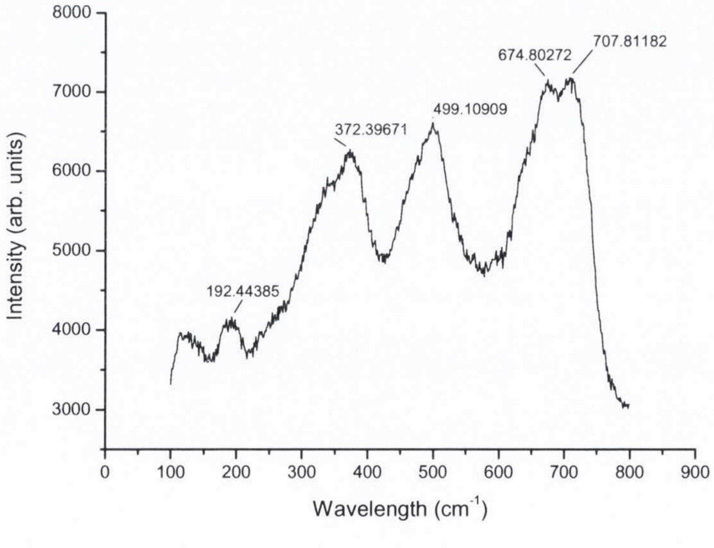

Figure 3.23: Raman scan of magnetite NP loaded silica xerogel

A Raman scan of the magnetite loaded silica monolith (acid-base catalysed sample) shown in Figure 3.23 reveals the two phases of magnetite and maghemite. Two distinct peaks located around 192 cm^{-1} and 674 cm^{-1} are characteristic of magnetite (T_{2g} – (Fe^{II} and O ions involved) and A_{1g} – (O ions) modes respectively). Peaks at 372 cm^{-1} (with shoulder at ~340 cm^{-1}), 499 cm^{-1} and 707 cm^{-1} are thought to be maghemite peaks corresponding to the T_1, E and A_1 modes[26]. It is well known that laser induced heating effects during Raman gathering can cause oxidation of magnetite to maghemite[27], however with care taken here the effect is thought to be minimal in this instance and maghemite is previously present in the sample.

3.4.1.3 Biological conjugation and flow cytometry application

The magnetite/maghemite loaded silica nanowires were investigated by functionalisation of the nanowire surface and bio-conjugation to be analysed by flow cytometry. Flow cytometry is a standard technique for quantitative immunoassays whereby cells are flowed through a micro-channel one by one and detected using a laser by forward and side scattered light from the cell and also detects fluorescence from labelled antibodies bound to it. This analysis gives information about the size and structure of the cell travelling through the detection area, while the fluorescence detection can determine different markers indicating if there has been an antibody-antigen interaction for example. It was hoped that the high aspect ratio of the nanowires would give a clearer read out signal of the scattered light from the flow cytometry.

The nanowires showed the capacity for a high degree of functionalisation with varying concentrations of 3-aminopropyltriethoxysilane (APTES) due to its surface chemistry and high number of preferential surface binding sites. Figure 3.24 shows how the fluorescence intensity from the antibody (x-axis; FL1-H) on the surface of the nanowire varies with the amount of APTES used in the functionalisation step. As can be seen 80 and 120 μL result in the broadest intensity signal observed from 10^1 to 10^3. This corresponds to the best (widest) range in which to detect a signal during flow cytometry in comparison to the narrower signals seen from lower amounts of APTES used.

This propensity for surface functionalisation allowed efficient binding to antibodies via 1-ethyl-3-(3-dimethylaminopropyl) carbodiimide hydrochloride (EDC) coupling. The binding of the fluorescently labelled antibodies onto the nanowires is displayed in Figure 3.25. This clearly shows the high luminescence from the antibodies on the wire surface under fluorescence microscopy.

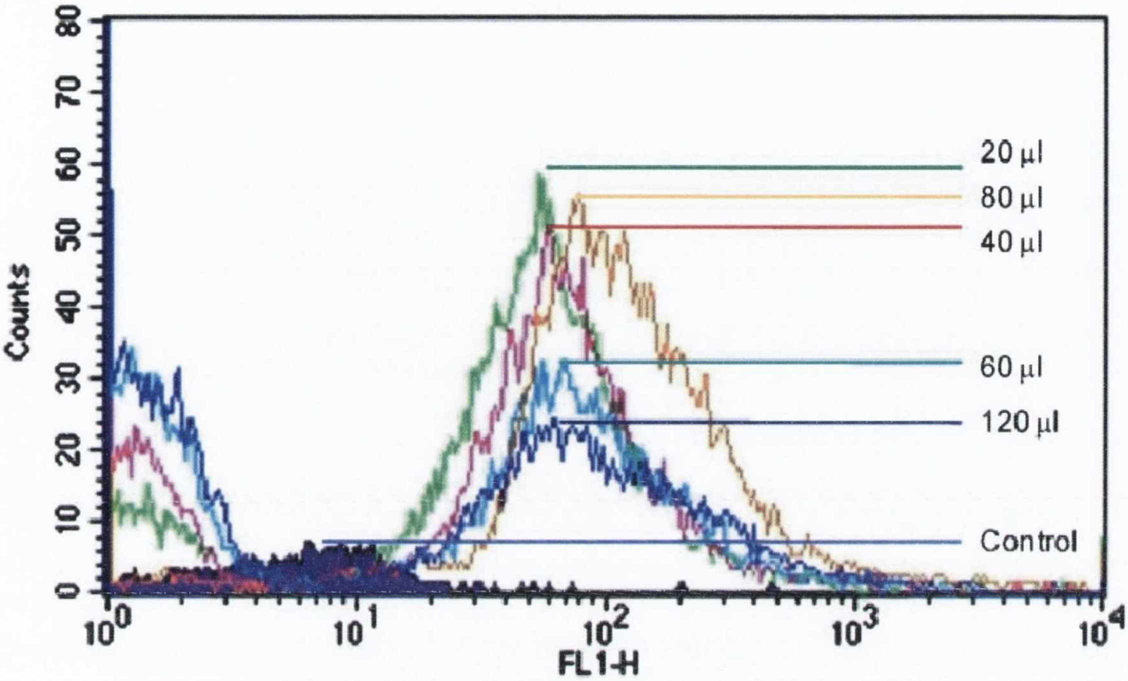

Figure 3.24: Effect of APTES addition on the fluorescence intensity (FL1-H response of the antibody functionalisation[2]

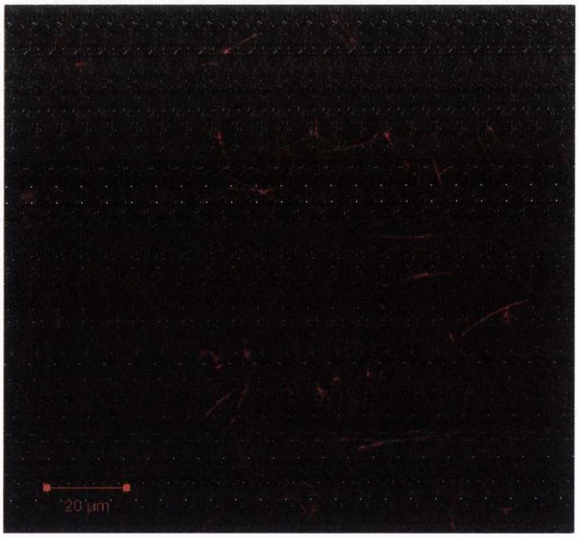

Figure 3.25: Fluorescent microscope image showing nanowires functionalised with fluorescently labelled antibodies

The functionalised nanowires were analysed using flow cytometry to analyse the signal detection from bound cells to nanowires. The antibody functionalised nanowires were incubated with THP-1 cells (nuclear stained with DAPI) for 1hr. Flow cytometry studies on the functionalised nanowires with intracellular adhesion molecule 1 (ICAM-1) secondary antibody showed that they had the ability to bind to THP-1 cells as demonstrated schematically in Figure 3.26 where the FITC fluorescence is expressed due to the binding of cells to the nanomaterials.

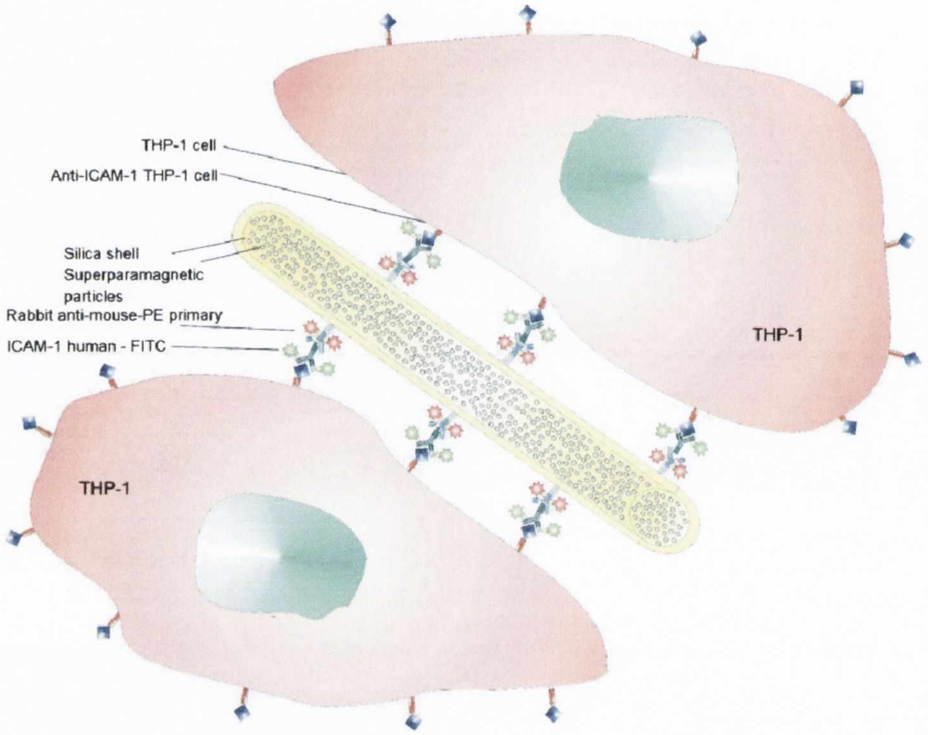

Figure 3.26: Schematic demonstrating nanowire functionality and binding to THP-1 cells[2]

The study was carried out in comparison to nanoparticles; the wires were shown to have a unique detection fingerprint in the flow cytometry output (Figure 3.27) which gives a much clearer readout of nanomaterials bound to cells[2]. The plots show the detection of the FITC conjugated fluorescence (only observed in the event of a nanoparticle/wire binding to the cell) of the cells and particles or wires. In section R5 (gate R5) of the plot shows that 62% of the NPs specifically bind to viable cells where as the nanowires show 17% specific binding. Even though the NPs show a higher binding percentage the nanowires display a much clearer reading of bound and unbound to THP-1 cells due to their unique scattering profile (Figure 3.27, right), also the nanowires bind more efficiently to the cells as their concentration in the experiment 65 times less than that of the particles[2].

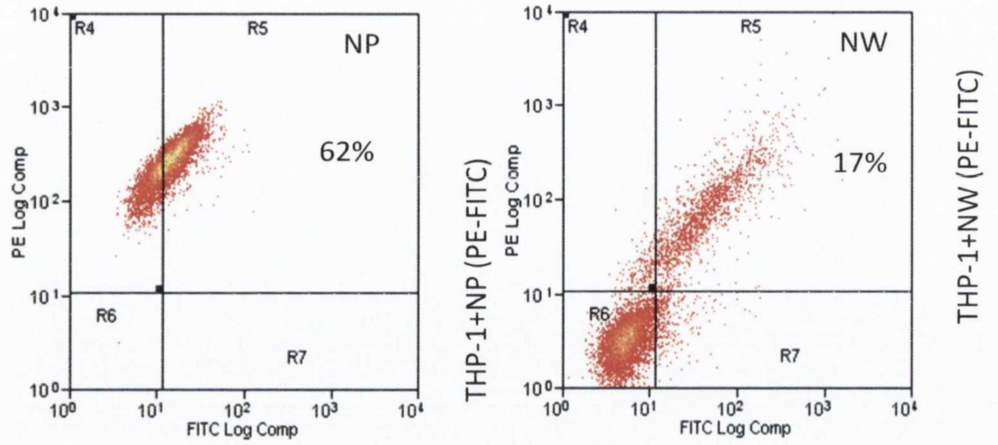

Figure 3.27: Flow cytometry results showing different scattering profiles[2]

3.4.2 Cobalt Ferrite NP doped Silica and Aluminosilicate nanowires

Metal ferrite nanoparticles have (as with the likes of magnetite) gained a large amount of interest due to their unique size induced magnetic properties as well as other potential applications in magnetic data storage and bio-medical technology. Cobalt Ferrite NPs in particular have received attention due their stability, reasonable magnetic saturation and greater wear resistance to environment and temperature increases (in comparison to typical iron oxide NPs such as magnetite or maghemite)[28-34]. They have also demonstrated good potential applications in hypothermic treatments as well as magnetic sorting applications[35-37].

Briefly the doped silica and aluminosilicate composites and nanowires were fabricated using a 2 step acid catalysed (HCl) sol-gel process using TEOS and aluminium iso-propoxide (for aluminosilicate gel) as precursors. Polystyrene sulfonate (PSS) coated $CoFe_2O_4$ NPs were added after the second step and the resulting sol was sonicated to aid dispersion of the NPs into the sol and to keep reaction going without the aid of magnetic stirring (for obvious reasons). The sol is infiltrated into porous alumina membranes (200 nm diameter pores) under vacuum assistance and allowed to dry, nanowires were released by membrane dissolution using NaOH solution and subsequent washing.

3.4.2.1 Characterisation of Nanowires

The $CoFe_2O_4$ loaded nanowires were characterised by optical microscopy, TEM and magnetisation measurements. Shown below in Figure 3.28 are optical microscope images of both silica and aluminosilicate loaded nanowires. The images show the high aspect ratio and needle like structure of the wires with a high yield during harvesting (colour difference of background in images due to use of different microscopes).

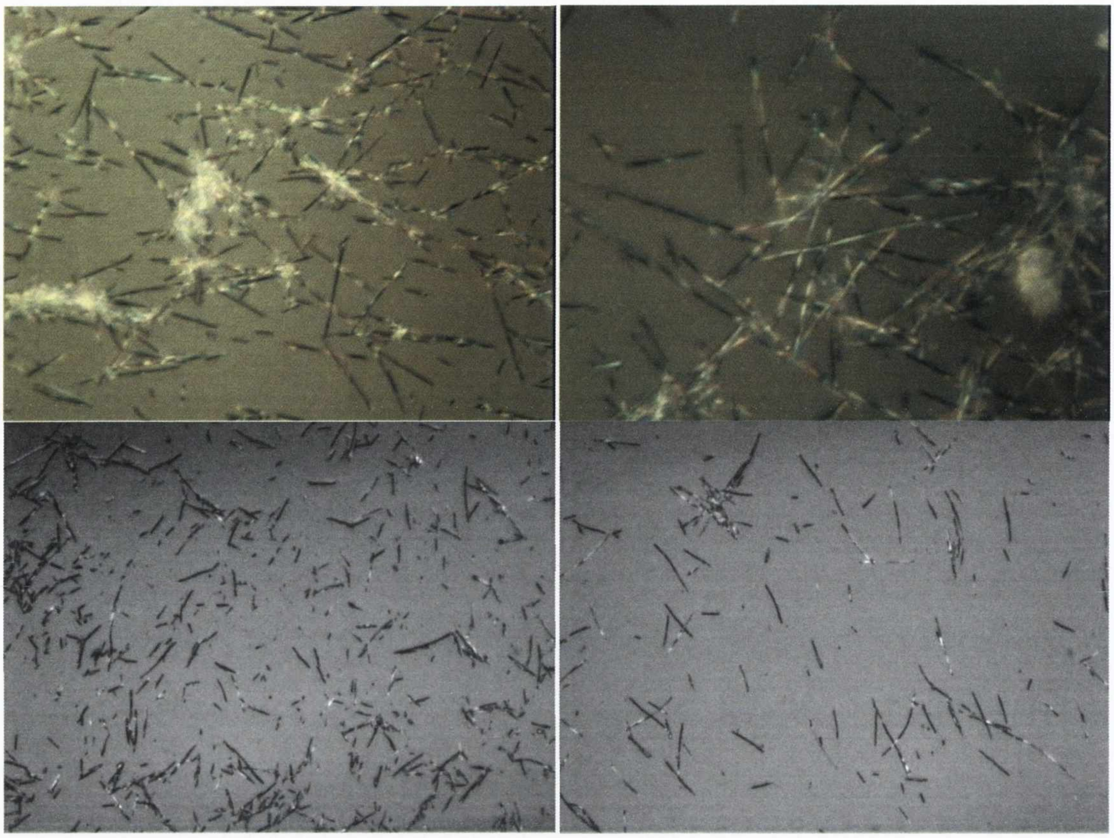

Figure 3.28: Optical microscope images of loaded silica (above) and aluminosilicate (below) nanowires

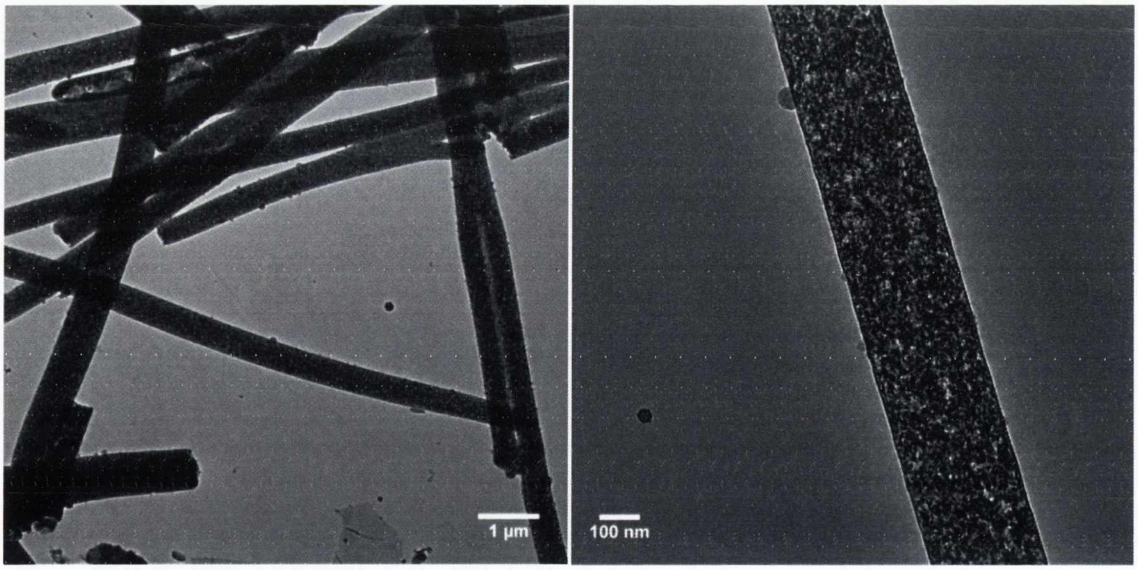

Figure 3.29: TEM images of $CoFe_2O_4$ NP loaded aluminosilicate nanowires

A closer examination of the nanowires was undertaken using TEM, shown in Figure 3.29. The images show the high-quality structure of the wires with diameters of

~270 nm. The images also seem to show nanoparticles uniformly embedded in the surface structure of the wire demonstrating their distributed loading.

Figure 3.30 (A-right) shows a TEM image of the original PSS coated $CoFe_2O_4$ NPs. It shows that they have a large size distribution from ~20-100 nm. However given the nature of the nanowire fabrication technique employed, only the smaller size range of the NPs can enter the pores and hence nanowire given the tendency of the larger particles to aggregate due to magnetic interaction and become trapped as such at the pore openings of the alumina membrane. It is therefore expected that the smaller NPs tend to make up the loading in the nanowires. VSM measurements were carried out on the xerogels to ascertain the magnetic quality of the samples is shown below in Figure 3.30. The first scan (A) shows the hysteresis loop for the original PSS coated (added to enable dispersion in solution and assist protection of NP) $CoFe_2O_4$ NPs displaying a saturation magnetisation of ~65.5 Am^2/Kg at 300 K and some small hysteresis, this value is quite characteristic of NPs[32] which is below the typical bulk value of ~80 Am^2/Kg due to their nanoparticulate nature taking into account size and coating effects. In (B) the magnetisation curve is shown for the loaded silica xerogel, as can be clearly seen the magnetic characteristics are quite poor and shows a large decrease in saturation magnetisation from the original particles to only 0.2 Am^2/Kg. This was visually observed in the drying of the gel where the initial colour turned from black/brown to a yellowish xerogel demonstrating the complete degradation of the NPs and loss of magnetism. This result was mirrored as the nanowires also showed poor response to applied magnetic field when attempting to pull through solution. The degradation of the NPs is assumed to be a result of the acidic conditions involved in the sol-gel process over the time taken for it to gel and dry. This result is in stark contrast to the aluminosilicate loaded xerogel which displays a saturation magnetisation of ~24 Am^2/Kg which taking into account the added weight of the bulk aluminosilicate xerogel shows that the NPs show little or no degradation. The nanowires also showed much greater ability to be manipulated in solution by an applied magnetic field. The greater retention of the NP magnetic quality in the xerogel over time is thought to be due to the fact that the addition of alumina species to the sol-gel reaction can assist in gelation time with better nucleation and form a better quality gel with a smaller pore structure[38-39]. Furthermore the alumina ions could coordinate to the surface of the NPs helping to stabilize and further passivate the surface especially if there is any Co^{2+} or Fe^{3+} ions on the surface of the particle[31,40].

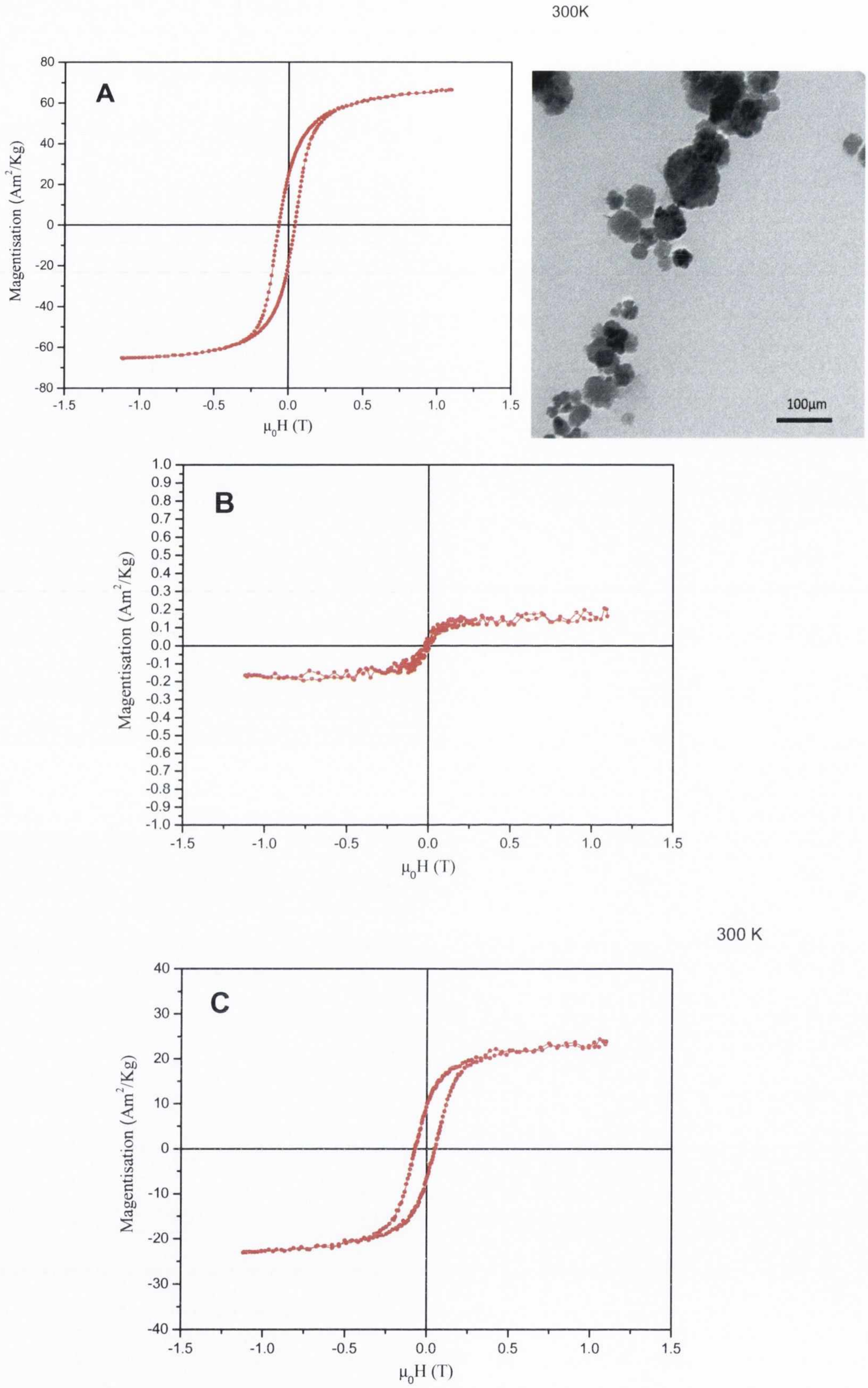

Figure 3.30: From top; Magnetisation curves of original PSS coated NPs (A), loaded silica xerogel (B) and loaded aluminosilicate xerogel (C)

3.5 Conclusions

We have demonstrated that various functional silica and aluminosilicate 1D nanostructures can be fabricated using sol-gel technology and the use of appropriate porous templates. The silica based nanostructures have been worked to develop intrinsic luminescent nanowires based on defect related emissive species within the silica matrix brought upon via annealing treatment. The work has also shown the development of surface functionalisation and AuNP attachment to create nanowires with plasmonic properties of the attached NPs. The attachment of these particles to the sol-gel derived silica nanowires opens up the possibility of multimodal structures with the particles working in conjunction with dopants incorporated into the silica matrix via sol-gel doping. The fabrication of magnetic nanowires via loading of magnetite and cobalt ferrite NPs into the silica/aluminosilicate nanowire has also been demonstrated. These nanowires have demonstrated great potential for magnetic manipulation in solution allowing ease of working during washing steps and through this showed potential for bio-separation in their incorporation into cells. The wires have also been used for novel detection agents after bio-conjugation to antibodies and analysis through a flow cytometry system. We have demonstrated that the loaded silica nanowires have intrinsic advantages when compared to similar particles due to their unique "flow cytometric fingerprint", which allow them to be clearly distinguished when utilized as carriers for immunodetection applications. We believe that the nanowire high aspect ratio could be used as an analytical tool in flow cytometry for the multiplexed immunoassay detection.

Overall this work has contributed to the further development of the fabrication and application of oxide based nanowires, opening possibilities in this area of research.

3.6 References:

1 Chen, C. C. *et al.* Preparation of fluorescent silica nanotubes and their application in gene delivery. *Advanced Materials* **17**, 404-+, doi:10.1002/adma.20040966 (2005).

2 Prina-Mello, A. *et al.* Comparative Flow Cytometric Analysis of Immunofunctionalized Nanowire and Nanoparticle Signatures. *Small* **6**, 247-255 (2010).

3 Tong, L. *et al.* Subwavelength-diameter silica wires for low-loss optical wave guiding. *Nature* **426**, 816-819 (2003).

4 Chang, H. J., Chen, Y. F., Lin, H. P. & Mou, C. Y. Strong visible photoluminescence from SiO2 nanotubes at room temperature. *Appl. Phys. Lett.* **78**, 3791 (2001).

5 Scheel, H., Zollfrank, C. & Greil, P. Luminescent silica nanotubes and nanowires: Preparation from cellulose whisker templates and investigation of irradiation-induced luminescence. *Journal of Materials Research* **24**, 1709-1715, doi:10.1557/jmr.2009.0224 (2009).

6 Ming, Z. *et al.* Bright visible photoluminescence from silica nanotube flakes prepared by the sol--gel template method. *Appl. Phys. Lett.* **80**, 491-493 (2002).

7 McCarthy, J. *et al.* in *Nanophotonic Materials V.*1 edn 703019-703016 (SPIE).

8 Green, W. H., Le, K. P., Grey, J., Au, T. T. & Sailor, M. J. White Phosphors from a Silicate-Carboxylate Sol-Gel Precursor That Lack Metal Activator Ions. *Science* **276**, 1826-1828, doi:10.1126/science.276.5320.1826 (1997).

9 Brinker, J. C. & Scherer, G. W. *The Physics and Chemistry of Sol-Gel Processing*. (Academic Press Limited, 1990).

10 Smith, E. & Dent, G. *Modern Raman Spectroscopy: A practical approach*. (Wiley, 2005).

11 Gittins, D. I. & Caruso, F. Spontaneous Phase Transfer of Nanoparticulate Metals from Organic to Aqueous Media. *Angewandte Chemie International Edition* **40**, 3001-3004 doi:10.1002/1521-3773(20010817)40:16<3001::aid-anie3001>3.0.co;2-5 (2001).

12 Daniel, M.-C. & Astruc, D. Gold Nanoparticles: Assembly, Supramolecular Chemistry, Quantum-Size-Related Properties, and Applications toward Biology, Catalysis, and Nanotechnology. *Chemical Reviews* **104**, 293-346, doi:10.1021/cr030698+ (2003).

13 Du, C. L. *et al.* Confocal white light reflection imaging for characterization of metal nanostructures. *Optics Communications* **281**, 5360-5363 (2008).

14 Chaure, N. B., Stamenov, P., Rhen, F. M. F. & Coey, J. M. D. Oriented cobalt nanowires prepared by electrodeposition in a porous membrane. *J Magn Magn Mater* **290**, 1210 - 1213 (2005).

15 Chiriac, H., Moga, A. E., Urse, M. & Ovari, T. A. Preparation and magnetic properties of electrodeposited magnetic nanowires. *Sensor Actuat A-Phys* **106**, 348 - 351 (2003).

16 Pitzschel, K. *et al.* Controlled Introduction of Diameter Modulations in Arrayed Magnetic Iron Oxide Nanotubes. *ACS Nano*, doi:10.1021/nn900909q (2009).

17 Zhang, M. & et al. Synthesis and characterization of monodisperse ultra-thin silica-coated magnetic nanoparticles. *Nanotechnology* **19**, 085601 (2008).

18 Santra, S. *et al.* Synthesis and Characterization of Silica-Coated Iron Oxide Nanoparticles in Microemulsion: The Effect of Nonionic Surfactants. *Langmuir* **17**, 2900-2906, doi:10.1021/la0008636 (2001).

19 Philipse, A. P., van Bruggen, M. P. B. & Pathmamanoharan, C. Magnetic silica dispersions: preparation and stability of surface-modified silica particles with a magnetic core. *Langmuir* **10**, 92-99, doi:10.1021/la00013a014 (1994).

20 Yasumori, A., Matsumoto, H., Hayashi, S. & Okada, K. Magneto-Optical Properties of Silica Gel Containing Magnetite Fine Particles. *Journal of Sol-Gel Science and Technology* **18**, 249-258 (2000).

21 Son, S. J., Reichel, J., He, B., Schuchman, M. & Lee, S. B. Magnetic Nanotubes for Magnetic-Field-Assisted Bioseparation, Biointeraction, and Drug Delivery. *J. Am. Chem. Soc.* **127**, 7316-7317 (2005).

22 Prina-Mello, A., Diao, Z. & Coey, J. Internalization of ferromagnetic nanowires by different living cells. *Journal of Nanobiotechnology* **4**, 9 (2006).

23 Hultgren, A. *et al.* Optimization of Yield in Magnetic Cell Separations Using Nickel Nanowires of Different Lengths. *Biotechnol Prog* **21**, 509 - 515 (2005).

24 Hultgren, A., Tanase, M., Chen, C. S., Meyer, G. J. & Reich, D. H. Cell manipulation using magnetic nanowires. *J Appl Phys* **93**, 7554 - 7556 (2003).

25 Tanase, M. *et al.* Assembly of multicellular constructs and microarrays of cells using magnetic nanowires. *Lab Chip* **5**, 598 - 605 (2005).

26 Chamritski, I. & Burns, G. Infrared- and Raman-Active Phonons of Magnetite, Maghemite, and Hematite: A Computer Simulation and Spectroscopic Study. *J. Phys. Chem. B* **109**, 4965-4968 (2005).

27 Shebanova, O. N. & Lazor, P. Raman study of magnetite Fe_2O_3: laser-induced thermal effects and oxidation. *Journal of Raman Spectroscopy* **34**, 845-852 (2003).

28 Hanh, N., Quy, O. K., Thuy, N. P., Tung, L. D. & Spinu, L. Synthesis of cobalt ferrite nanocrystallites by the forced hydrolysis method and investigation of their magnetic properties. *Physica B: Condensed Matter* **327**, 382-384 (2003).

29 da Silva, S. W. *et al.* Stability of citrate-coated magnetite and cobalt-ferrite nanoparticles under laser irradiation: a Raman spectroscopy investigation. *Magnetics, IEEE Transactions on* **39**, 2645-2647 (2003).

30 Franco, J. A. & C. e Silva, F. High temperature magnetic properties of cobalt ferrite nanoparticles. *Appl. Phys. Lett.* **96**, 172505-172503 (2010).

31 Soler, M. A. G. *et al.* Aging Investigation of Cobalt Ferrite Nanoparticles in Low pH Magnetic Fluid. *Langmuir* **23**, 9611-9617, doi:10.1021/la701358g (2007).

32 Tung, L. D. *et al.* Magnetic properties of ultrafine cobalt ferrite particles. *Journal of Applied Physics* **93**, 7486 (2003).

33 Templeton, T. L. *et al.* Magnetic properties of CoxFe3-xO4 during conversion from normal to inverse spinel particles. *Journal of Applied Physics* **73**, 6728 (1993).

34 Liu, C., Zou, B., Rondinone, A. J. & Zhang, Z. J. Chemical Control of Superparamagnetic Properties of Magnesium and Cobalt Spinel Ferrite Nanoparticles through Atomic Level Magnetic Couplings. *Journal of the American Chemical Society* **122**, 6263-6267, doi:10.1021/ja000784g (2000).

35 Kückelhaus, S. *et al.* In vivo investigation of cobalt ferrite-based magnetic fluid and magnetoliposomes using morphological tests. *Journal of Magnetism and Magnetic Materials* **272-276**, 2402-2403 (2004).

36 Fortin, J.-P., Gazeau, F. & Wilhelm, C. Intracellular heating of living cells through Néel relaxation of magnetic nanoparticles. *European Biophysics Journal* **37**, 223-228 (2008).

37 Baldi, G. *et al.* Synthesis and Coating of Cobalt Ferrite Nanoparticles: A First Step toward the Obtainment of New Magnetic Nanocarriers. *Langmuir* **23**, 4026-4028, doi:10.1021/la063255k (2007).

38 De Witte, B. M. & Uytterhoeven, J. B. Acid and Alkaline Sol-Gel Synthesis of Amorphous Aluminosilicates, Dry Gel Properties, and Their Use in Probing Sol Phase Reactions. *Journal of Colloid and Interface Science* **181**, 200-207 (1996).

39 De Witte, B., Aernouts, K. & Uytterhoeven, J. B. Aging of aluminosilicate and silica gels in aqueous solutions of various pH and Al content, a textural and structural evaluation. *Microporous Materials* **7**, 97-108 (1996).

40 Radwan, N. R. E. & El-Shobaky, H. G. Solid-solid interactions between ferric and cobalt oxides as influenced by Al2O3-doping. *Thermochimica Acta* **360**, 147-156 (2000).

Chapter 4

Polystyrene Nanowires

Polymer nanocomposites have attracted a lot of attention during the last few years due to their unique properties and potential industrial applications. Polymer composites are relatively easy to process. For example during the initial polymerisation it is possible to incorporate substituent's during the reaction[1]. Subsequent loading of nanomaterials into polymers can also be achieved via dissolution in appropriate solvent[2], polymer swelling to and incorporation of materials into surface sites[3-4].

Many polymer composites (e.g. polystyrene based) are known to be bio-compatible and therefore they have found a range of application in bio-medical reagents and devices [5-6]. For example Dynabeads®, is a commercially available product, which consists of superparamagnetic nanoparticle loaded PS microparticles. These beads have found numerous uses in bio-separation and analysis in various areas of research. However this area of research has shown some promising potential for 1-dimensional nanostructures

This chapter will explore the fabrication of polystyrene nanowires using template synthesis and subsequent doping to create multimodal fluorescent and magnetic PS nanowires. The functionalisation of these nanowires for bio-conjugation will then be investigated and their interaction with cells. PS nanowires will also be developed displaying QD emission.

4.1 Fabrication of Polystyrene Nanowires

Polymer 1D nanostructures have been prepared in porous alumina membranes by modified wetting procedures, which have been used in the past by various groups[7-8], also the use of vacuum assisted infiltration into alumina membranes has achieved nanotube arrays of PS[9]. The general procedure involved in the optimisation and production of dispersed solid nanowires is as follows. Solutions of PS (M_w=350,000, M_n=170,000) in THF were made up with varying concentrations (~1-10 wt%) and infiltrated under vacuum into 200 nm diameter alumina membranes. These different weight percentages produced (or failed to produce) 1D nanostructures with varying properties. The higher weight percentages were generally too viscous to enter efficiently into the pores of the membrane. Even with further vacuum assistance the membranes fractured or broke under the strain of vacuum trying to pull the viscous solution through the membrane. The lower weight percentage solutions tended to form hollow tubular structures which were not desirable given the required function to load and protect magnetic and fluorescent components within the nanostructures for potential bio-medical applications. A ~3.4 wt% solution was found to be most appropriate for infiltration and formation of nanowires within the pores. The formation of the wires within the porous membrane is thought to proceed via continuous coating of the pore walls with addition of solution to membrane with constant quick evaporation of the THF solvent with the flow of air through the pores until the pore is filled. The wires within the pores will still contain some solvent clearly but with drying and ageing the solvent evaporates fully and the wires densify. Initial results yielded arrays of wires from partially dissolved membranes and released wires of poor quality (Figure 4.1).

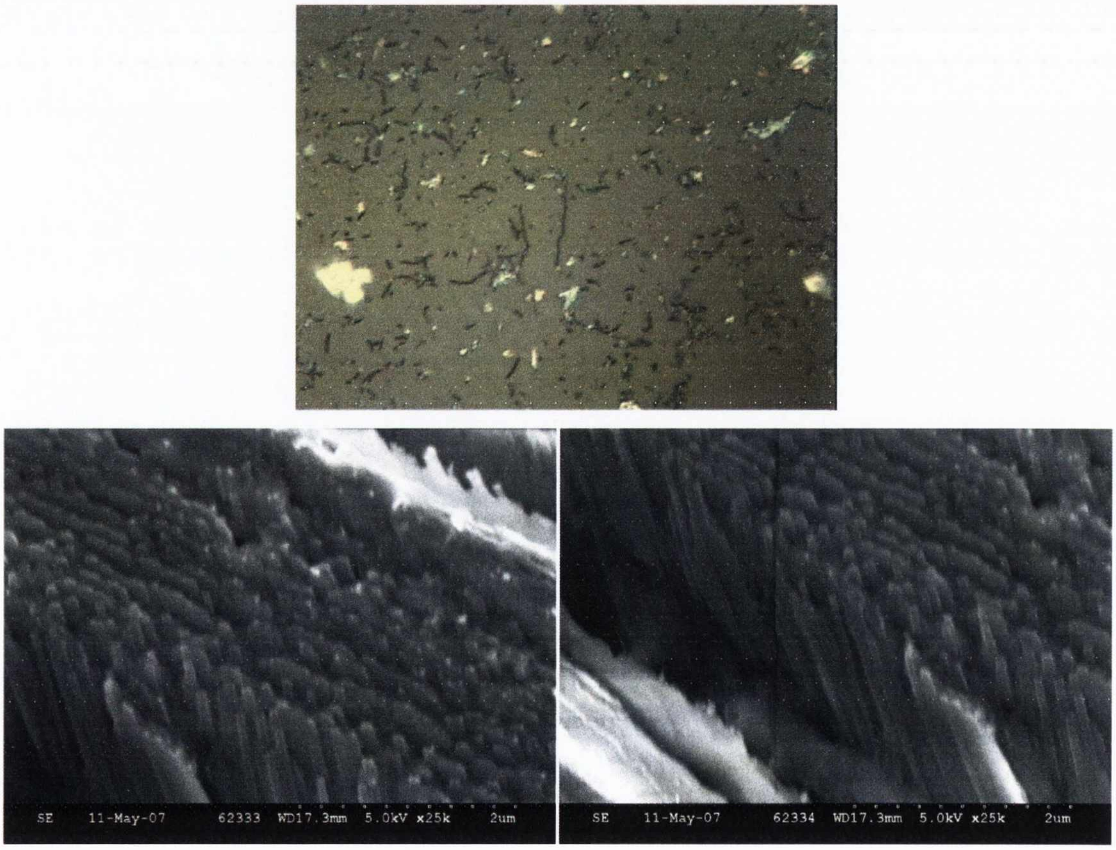

Figure 4.1: Optical Microscope (top) and SEM images (bottom) of polystyrene nanowires

Polishing of the infiltrated membrane to remove surface polymer and dissolution in NaOH with the aid of sonication (to break up and expedite membrane dissolution) resulted in the release of the wires into solution. Subsequent washing via centrifugation and/or filtration yields dispersed nanowires in a desired medium. These preliminary studies in PS nanowire formation and properties allowed for the next step in the loading of the nanostructures to create multimodal PS nanowires.

4.2 Multimodal Magnetic - Fluorescent Polystyrene Nanowires

Nanowires and more specifically magnetic nanowires have attracted a reasonable amount of attention due to their potential bio-medical as outlined in chapter 2 with reference to silica nanowires. Biocompatible polymers have been used to fabricate magnetic nanorods and nanofibers previously by an electrostatic assembly of aggregates of PAA and γ-Fe_2O_3 nanoparticles[10] and infiltration into alumina membranes of PVC and magnetitie[11] respectively. Also there is a desire for nanostructures with fluorescent properties to aid detection within and attached to biological bodies[12]. With this in mind our main aim was to fabricate multimodal (fluorescent and magnetic) PS nanowires.

4.2.1 Fabrication of Multimodal PS Nanowires

Briefly magnetite nanoparticles have been prepared according to established methods[13] by the co-precipitation of iron II and III chloride in the presence of water and ammonia and oleic acid. The as prepared magnetite nanoparticles were then transferred from the aqueous to the organic phase by separation of phases by addition of chloroform and phase transfer of the magnetic nanoparticles by placing sample on magnet. With subsequent removal of upper water layer the result was a highly stable dispersion of magnetite nanoparticles in chloroform. As schematically demonstrated in Figure 4.2, 0.6-1 ml of this dispersion was added to a stable solution of 300 mg of PS in 9.4 ml THF and ~2.5 mg of commercial dye coumarin-153 creating a green tinged brown lightly viscous homogenous solution. This solution was infiltrated into 200 nm porous alumina membranes and left to dry in air for ~ 24 hr. The wires were released via membrane dissolution in NaOH solution and washed with water via filtration. Then the wires were re-dispersed in water giving relatively stable suspensions, which crashed out over a number of hours but could be re-dispersed out again via a short sonication.

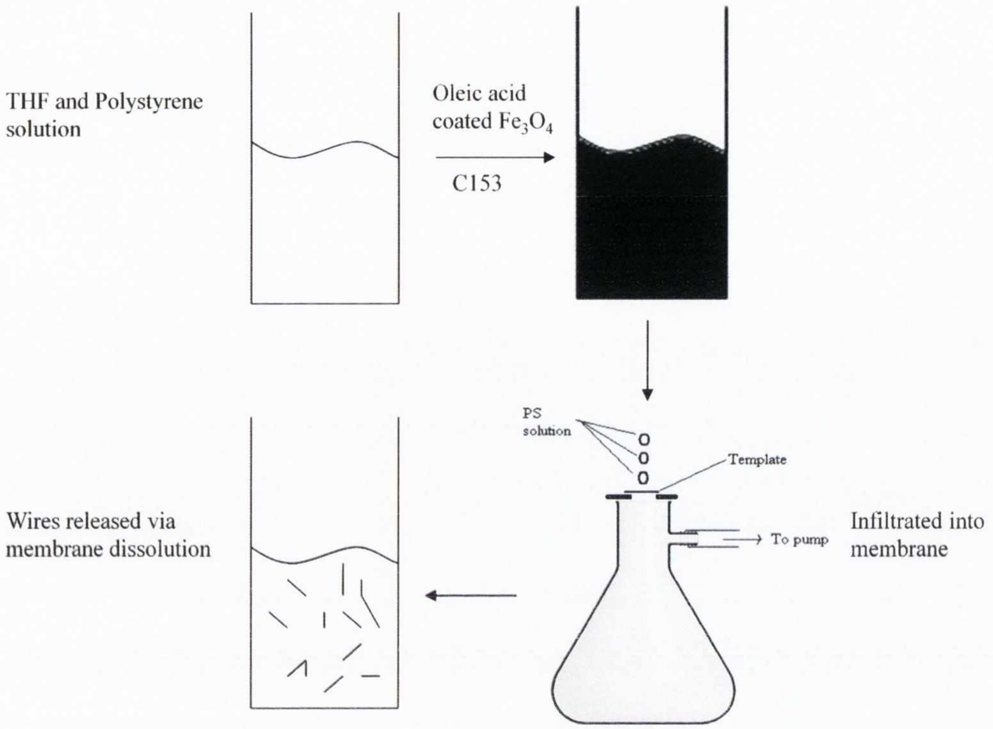

Figure 4.2: Schematic demonstrating the fabrication of multimodal PS nanowires

4.2.2 Characterisation of PS-Magnetite Nanowires

The magnetite NPs were characterised by TEM and VSM (Figure 4.3), the TEM images showed that the particles were nanoparticulate in nature and had a size of 11.5 nm ± 2.2 nm. VSM on the nanoparticles showed them to have a magnetisation saturisation of 48.5 Am^2/Kg and to be superparamagnetic in nature which is ideal for the desired magnetic properties of the nanowires. The value of the magnetisation is lower than that of other pure magnetite NPs but is comparable to other reported values for oleic acid coated magnetite at room temperature[13-14].

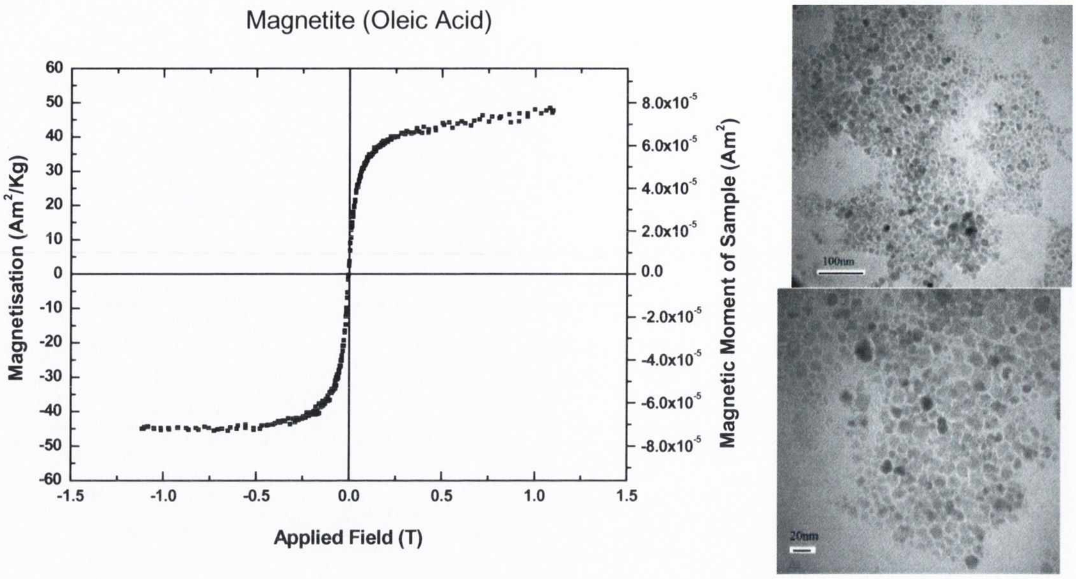

Figure 4.3: Magnetisation curve and TEM images magnetite NPs

The nanowires have been characterised by optical and fluorescence microscopy, TEM and quantatively by VSM and solid state PL. Initially the nanowires showed some interesting features upon examination by optical microscopy (Figure 4.4).

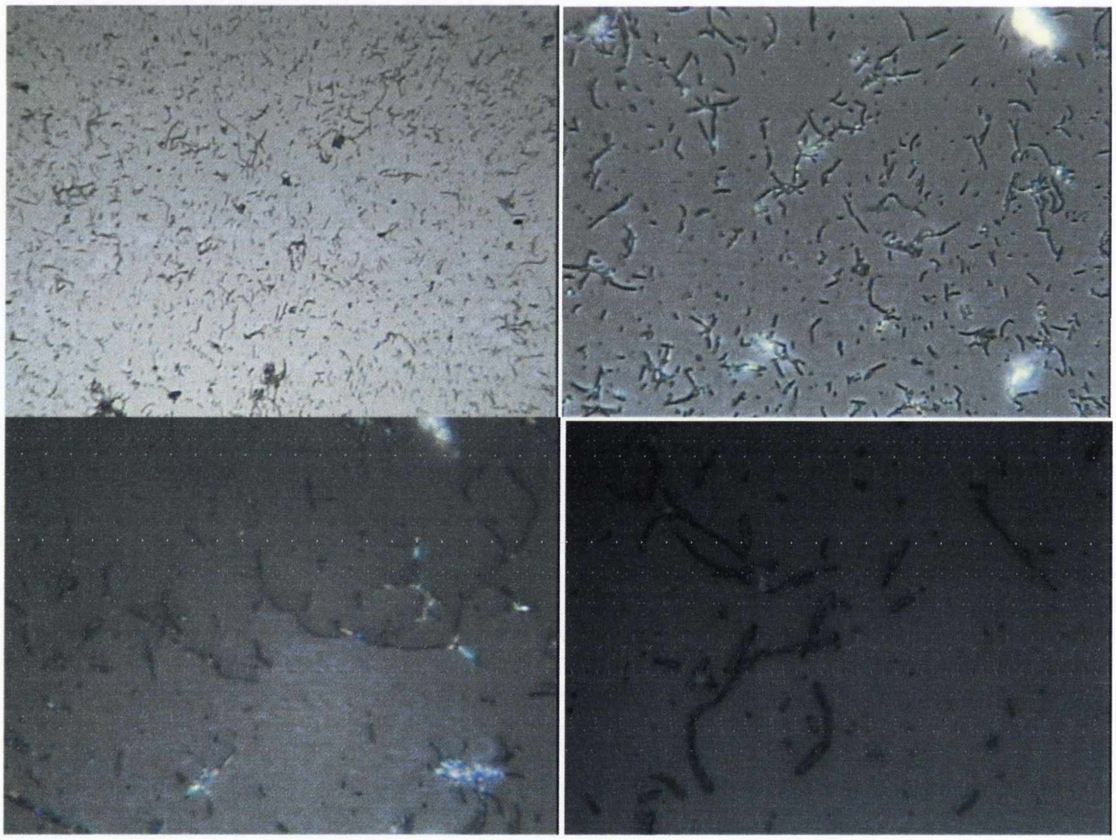

Figure 4.4: Optical microscope images of doped nanowires

The images revealed that the nanowires were bent and curled at a number of kink points along the wire, this is attributed to the nature of the polymer to curl under stress after membrane dissolution. The deformation of polymer nanowires can also be caused by the heating of the sample during the processing and sonication procedures. TEM (Figure 4.5) images have demonstrated that many of the wires have a type of 'bamboo' structure to them in that there are near break sites along the wires where the connection is quite weak which could account for the large distribution of lengths observed in the samples. The severity of the breaks shown in the TEM images may however be accentuated by the TEM beam causing some damage to the polymer which is known to happen. Nevertheless the wires still show a high aspect ratio however with a diameter of 270 nm (8 nm SD) and lengths of several microns (which as indicated previously is down to the membrane used).

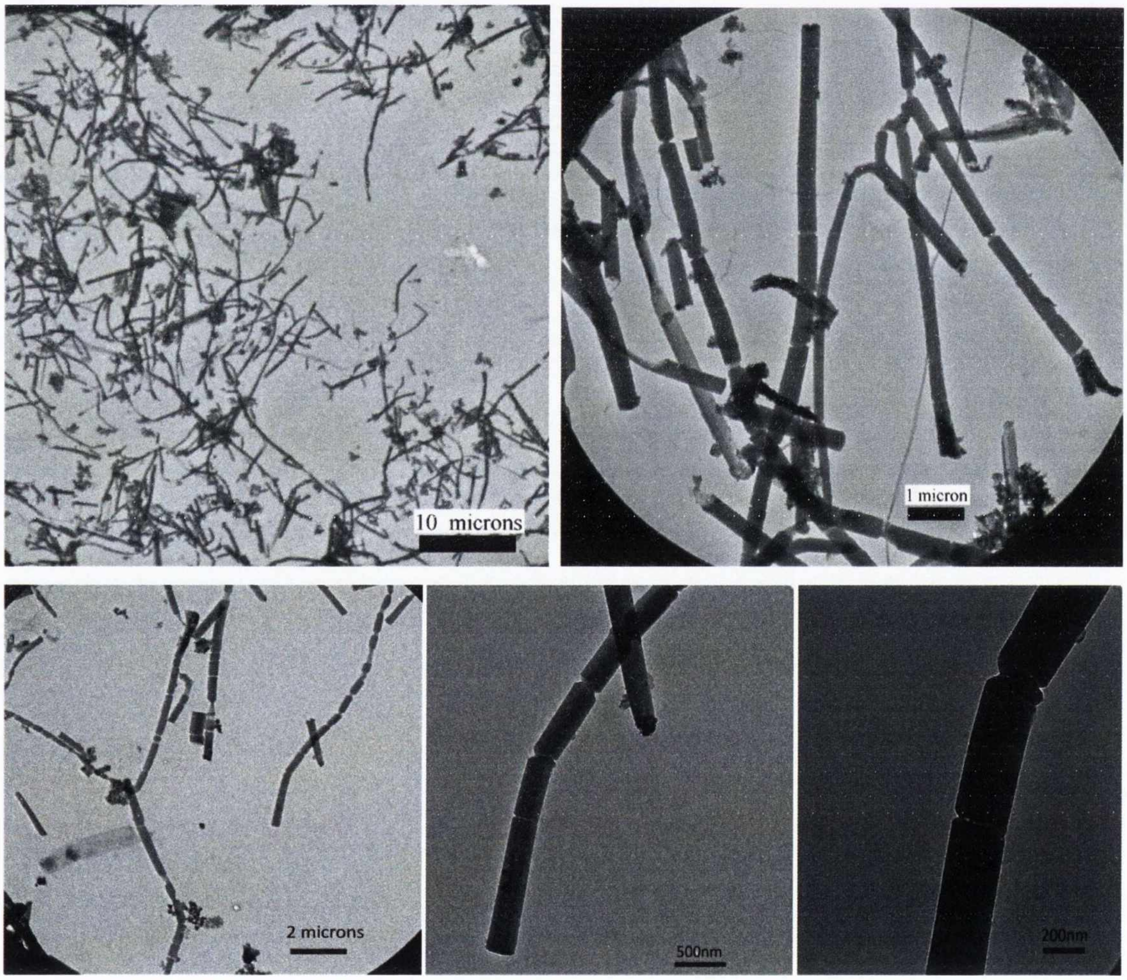

Figure 4.5: TEM images of nanowires

Solid state PL (Figure 4.6) was carried out on a thin film of the doped polystyrene to ascertain the emission profile of the sample; this showed a strong peak at 534 nm which is the typical emission region of coumarin 153 dye.

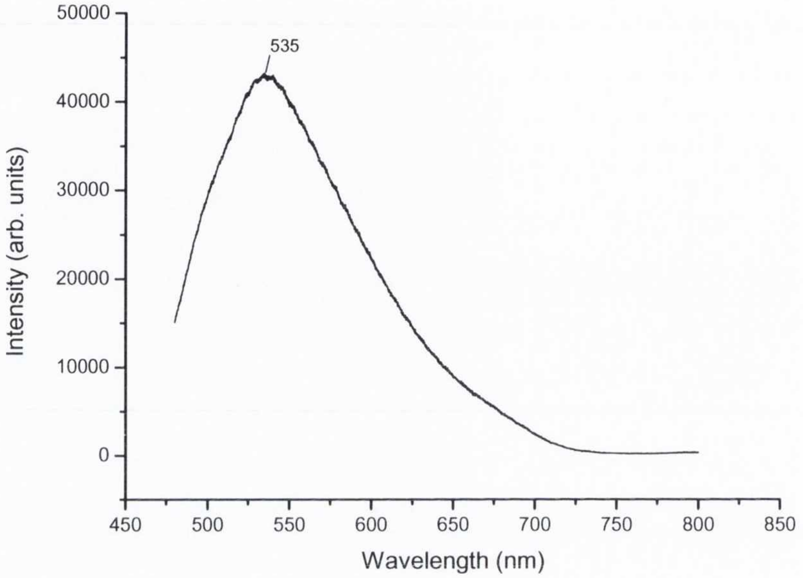

Figure 4.6: Solid state PL of doped PS thin film (ex 457 nm)

Magnetisation characterisation was also carried out on a doped thin film of the sample. The magnetisation curves shown below in Figure 4.7 are of two different concentrations of magnetite loading initially in the PS solution. The trade off between higher magnetism is the result that the wires are not as luminescent and further loading could end up compromising the structure of the wires by overloading them. The higher loaded sample showed a magnetisation saturisation of 5.2 Am^2/Kg.

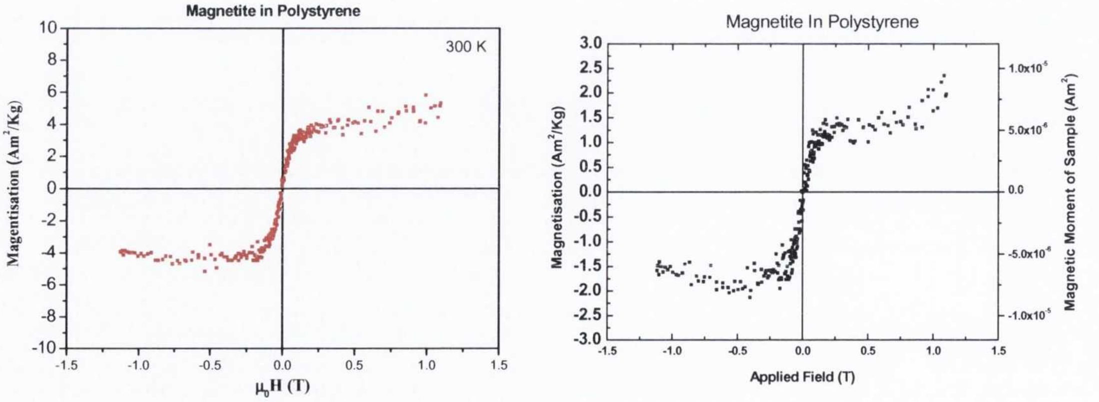

Figure 4.7: Magnetisation curves for different loadings of magnetite in PS

To further display the magnetic and fluorescent quality of the wires they were dried on a glass slide in a magnetic field and examined under a fluorescent microscope (Figure 4.8). The wires show strong emission under UV radiation and good alignment to the applied field under drying. The wires align in bundles most likely due to individual attraction the wires feel in the field and the fact that they are curled causes them to bundle under drying. The image in Figure 4.9 shows the wires having been pulled by a magnet through solution. This ability to be orientated by an external magnetic field is vital for potential applications in magnetic separation in biological applications and very useful for purification (e.g. washing) of the sample during subsequent workings.

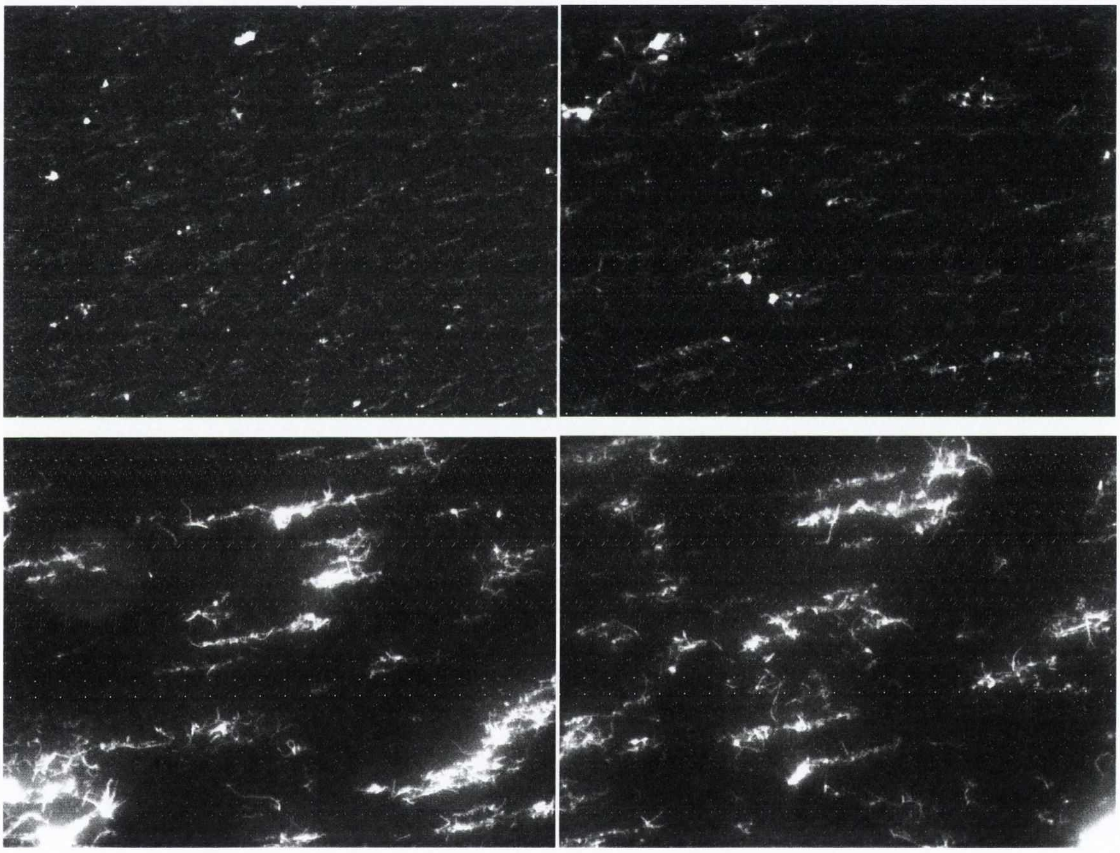

Figure 4.8: Fluorescent microscope images of aligned nanowires (emission max at 334/365 nm)

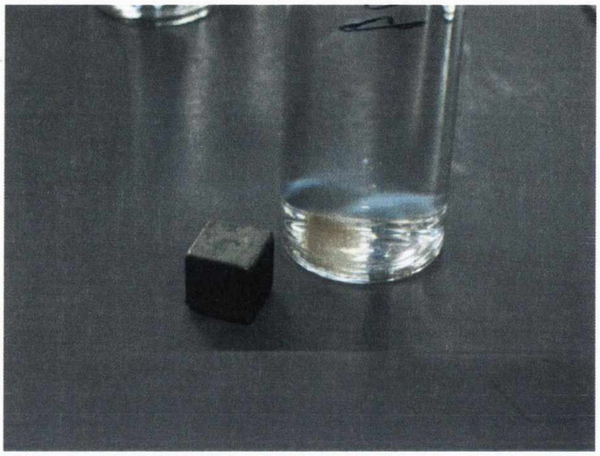

Figure 4.9: Image showing wires having been pulled through solution by magnet

4.2.3 Sulfonation of PS surface for bio-conjugation

To functionalise the surface of the PS nanowires the sulfonation of PS films using highly concentrated sulfuric acid was investigated. Briefly PS thin films were placed in stirring conc. sulfuric acid at 60 °C for 2-4 hr. This resulted in the aromatic sulfonation of the PS surface. The films were characterised by FTIR spectroscopy to observe peaks due to the presence of sulfate groups. New peaks at 668 cm^{-1} and a large increase in the peak around 1130 cm^{-1} (Figure 4.10 and Figure 4.11) are believed to be attributed to sulfate groups[15] The increase in the peak at ~834 cm^{-1} is caused by the para substitution of the benzene ring suggesting that the sulfate group is in this position [15-16].

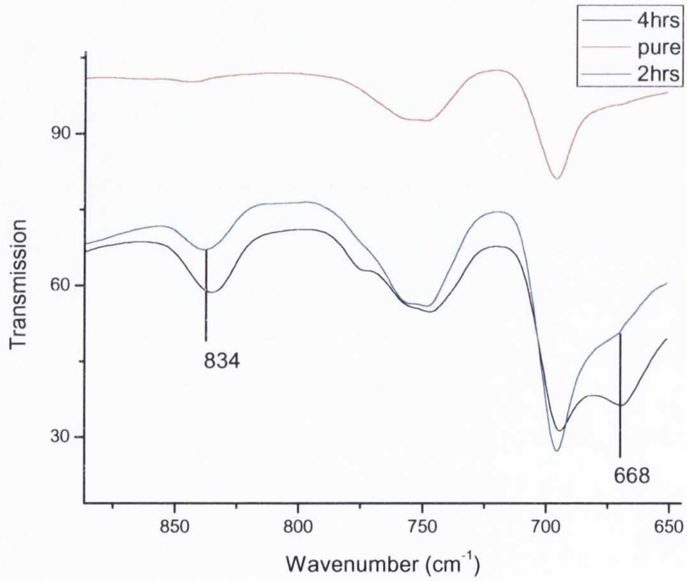

Figure 4.10: FTIR spectrum of sulfonated PS films (650-900 cm^{-1})

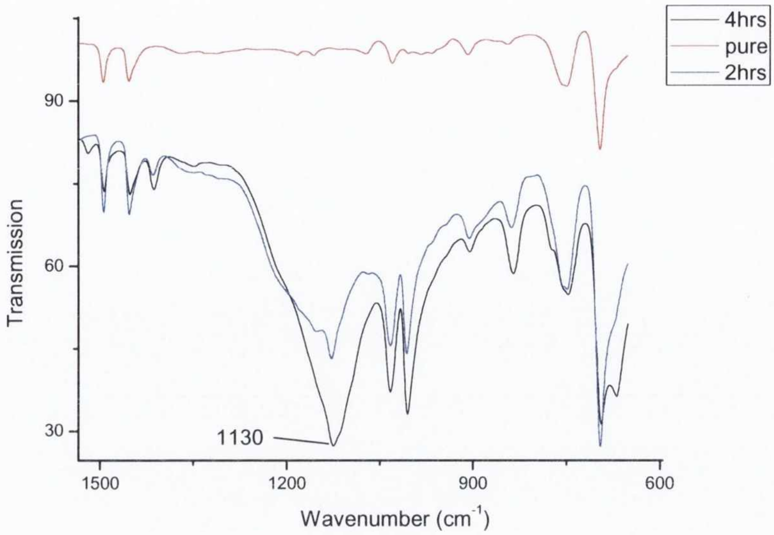

Figure 4.11: FTIR spectrum of sulfonated PS films (600-1500 cm^{-1})

This procedure was then performed similarly on the nanowires (with an immersion time of 1 hr) to functionalise their surface. The wires still showed strong emission under the fluorescence microscope after the sulfonation procedure.

4.2.4 Bio-conjugation of functionalised PS nanowires

The interaction of the surface functionalised nanowires with live cells was examined by further functionalising the wire with fluorescently labelled primary and secondary antibodies. Firstly the wires were functionalised via EDC to a conjugated Immunoglobulin-G antibody (TRITC or PE, according to application targeted). The sample was then washed and functionalised with a second Inter-Cellular Adhesion Molecule 1 (ICAM-1) antibody conjugated with FITC.

Figure 4.12 shows a representative confocal image (confocal image acquisition and set up described in Section 6.2.11) of a PS nanowire functionalised with primary (TRITC labelled) and secondary antibodies (FITC labelled). The image clearly shows the emission from the coumarin-153 doping of the nanowire (blue) and of the TRITC from the primary antibody (red).

Figure 4.12: Confocal image of functionalised PS nanowire

In vitro exposure of PS nanowires to cellular model: wires were then incubated for 24 hr at 37 °C, 5% CO_2 and 95% humidity with a suitably chosen cellular model: A549 (epithelial lung cancer cells). Exposed cells were then 'fixed' using paraformaldehyde (PFA), permeabilised (with Triton X) and stained using Hoechst dye (nucleus, DAPI-blue), Mito-tracker dye (Mitochondria, TRITC-Red) and F-Actin dye (cytoskeletal actin filaments (or cell scaffolding filaments), FITC-Green). These were imaged using confocal microscopy to investigate the interaction between both. Figure 4.13 shows a confocal image of a representative stained cellular nucleus and nanowire with emission in blue (primary antibody tagged with PE and is not excited here); cell cytoskeletal staining in green. Cellular mitochondrial activity stained in red, followed by a bright field image showing the whole cell and nanowire localization. Finally a fuse image of all the four previous layers is shown as a comprehensive overlay of the confocal imaging. It is interesting to see, that the blue image clearly shows two nanowires in/on the cell. The larger curved nanowire resides on the surface of cell while the shorter straight wire appears to have been taken up by the cell into the cytoplasm, as explained below. The nanowire uptake is associated with an increase in mitochondrial activity in the cell (indicated by the enhanced red emission). Confocal imaging was repeated on several fields and samples in order to confirm the here reported cell-wire interactions in vitro.

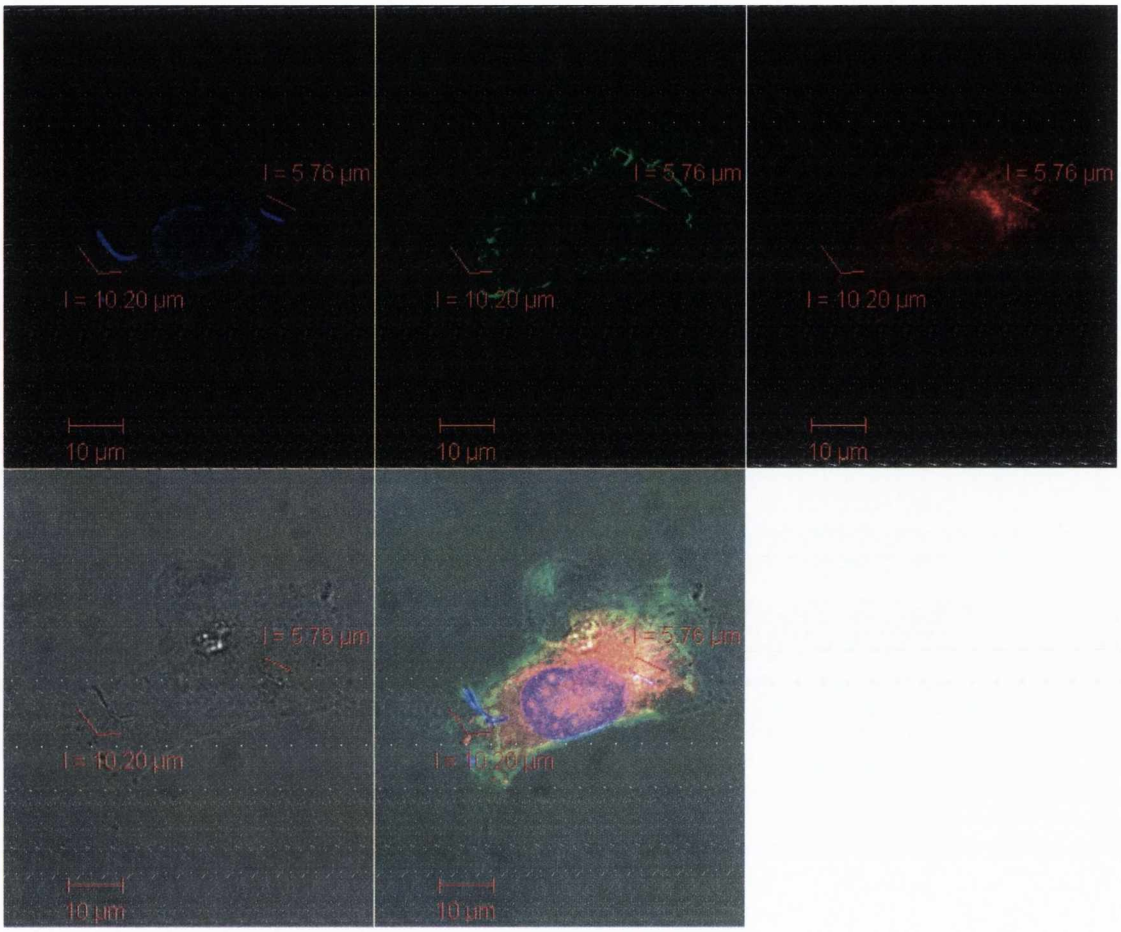

Figure 4.13: Confocal image of cell-nanowire interaction

To confirm the location of the wires within/outside the cell, z-plane confocal slice acquisition was carried out with fix optical slide of 0.46 microns gap between sections. Over a full cell height of approximately 10 microns the z-stack imaging clearly showed that the longer wire is positioned in contact with the cell membrane surface while the shorter wire is most likely internalised into the cell. In order to confirm the latter, Figure 4.14 gives a clear representation using orthogonal view of both imaged wires in the YZ and XZ planes. Crosshairs reference is situated at a point along each wire showing their position within the cell (bright field and mitochondria staining omitted for ease of viewing).

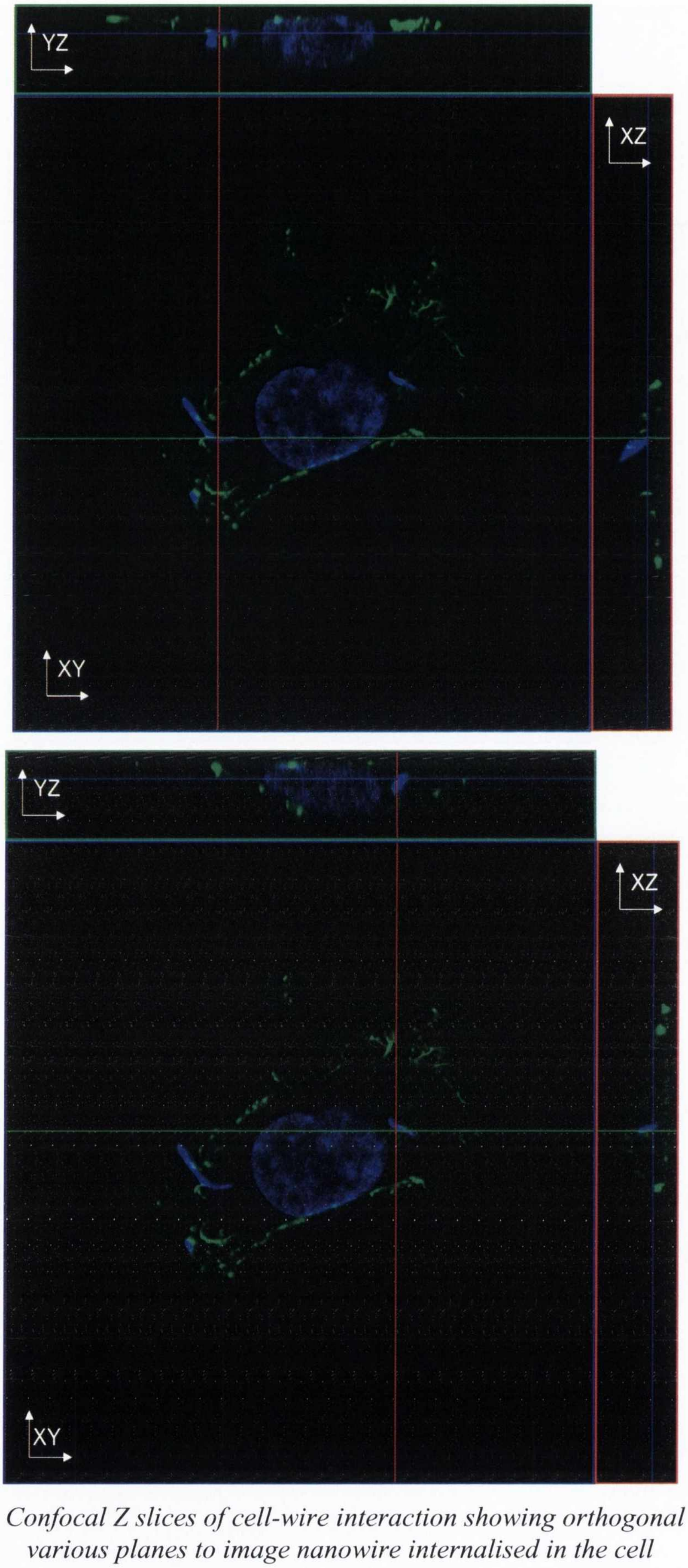

Figure 4.14: Confocal Z slices of cell-wire interaction showing orthogonal views of the various planes to image nanowire internalised in the cell

4.3 QD doped PS nanowires

As highlighted in section 1.5.4, QDs have unique advantages over commercial dyes in so much as their high fluorescence quantum yield, high degree of optical tuning for absorption and emission[17]. However problems in QDs toxicity have led to the need for their encapsulation in more bio-friendly materials. QD doped polymeric nanostructures have been reported by other groups, which have used various types of QD and differing methods to create the composites such as microemulsion, electro-spinning and an in situ formation of the QDs within the nanostructure casing at times involving comparatively complex fabrication processing and heat treatment[18-20]. Recently alloyed core-shell CdZnSe/ZnSe QDs have shown been shown to have very high quantum yield and photoluminescence properties[21]. The main aim of this part of our work was to produce PS nanowires by the infiltration method into porous alumina membranes incorporating this type of QD to create luminescent PS nanowires suitable for bio-medical applications.

4.3.1 Fabrication and characterisation of doped nanowires

The fabrication of the nanowires proceeded by preparation of a solution of 64 mg of PS (350,000 Mw) in 2 ml of toluene + 300μL of the QD solution in toluene shook up to create a stable solution. 2-3 drops of this solution was infiltrated as before into 200 nm diameter AAO membranes under vacuum assistance and left to dry in the dark for 2 days. Although the infiltrated membranes and thin films of the doped polymer showed strong emission from the dots under UV radiation, release of the nanowires via membrane dissolution with NaOH (as described in previous sections) resulted in the wires showing no emission under examination. This was most likely caused by the NaOH being able to penetrate the slightly porous polymer matrix when undergoing dissolution due to use of sonication and the resulting heating associated therewith and causing the dots to degrade and loose fluorescence. A number of tests using different concentrations of NaOH and varying the sonication usage (not allowing it to heat up to much for example) to dissolve the membrane were tested and found that 0.025 M was sufficient to dissolve the membrane and weak enough not to damage the QDs in the wire. Fluorescent microscope images shown below in Figure 4.15 show the luminescent wires under UV radiation. The images only show a black and white representation of the emission; however the wires under physical observation demonstrate green-orange emission. This is indicated in the PL spectra of a thin film of the loaded PS showing emission peaking at 605 nm (Figure 4.16).

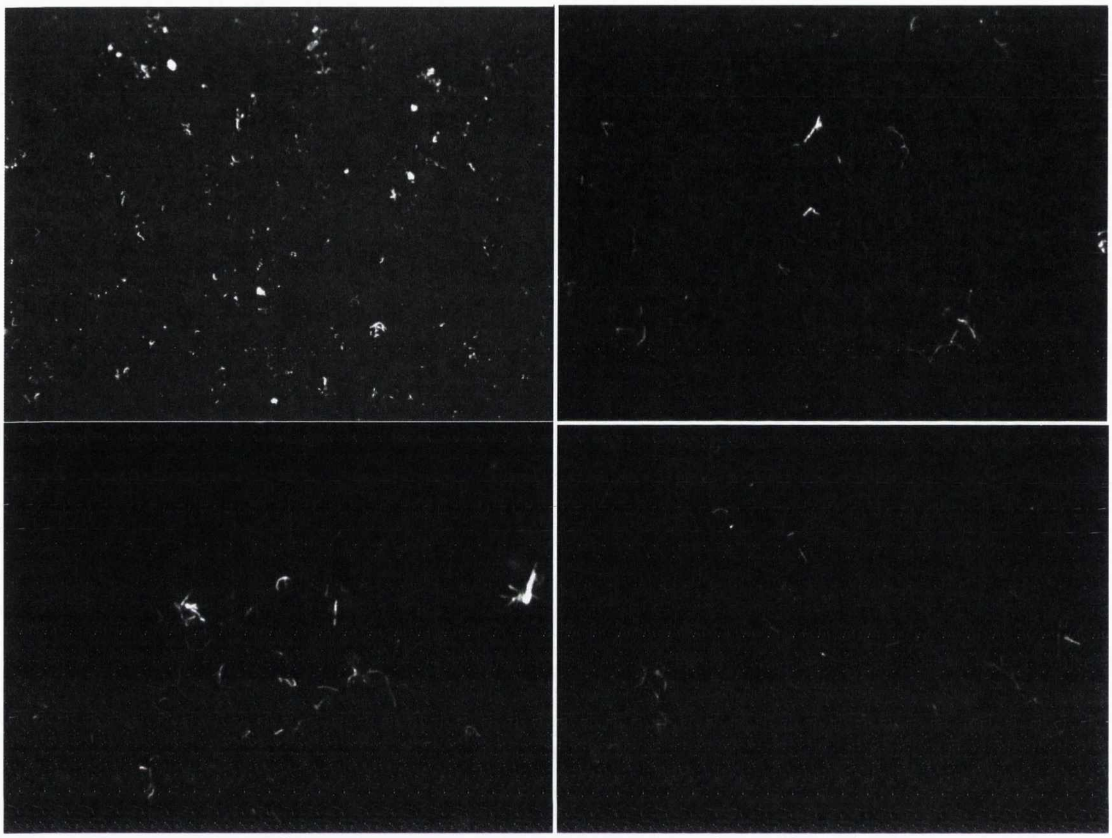

Figure 4.15: Fluorescence microscope images of QD doped PS nanowires

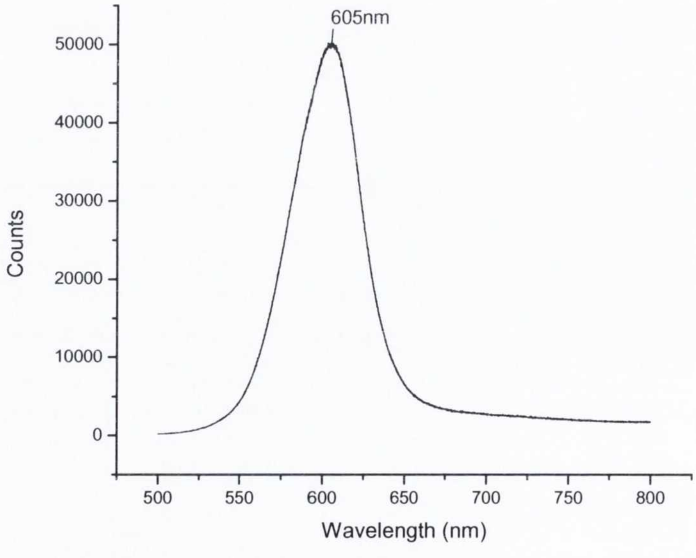

Figure 4.16: Solid state PL spectrum of QD loaded PS

TEM (Figure 4.17) showed the wires to have diameters of 255 nm with high aspect ratios. A similar structure is observed in the wires as described in the previous section with regards to its bamboo like links.

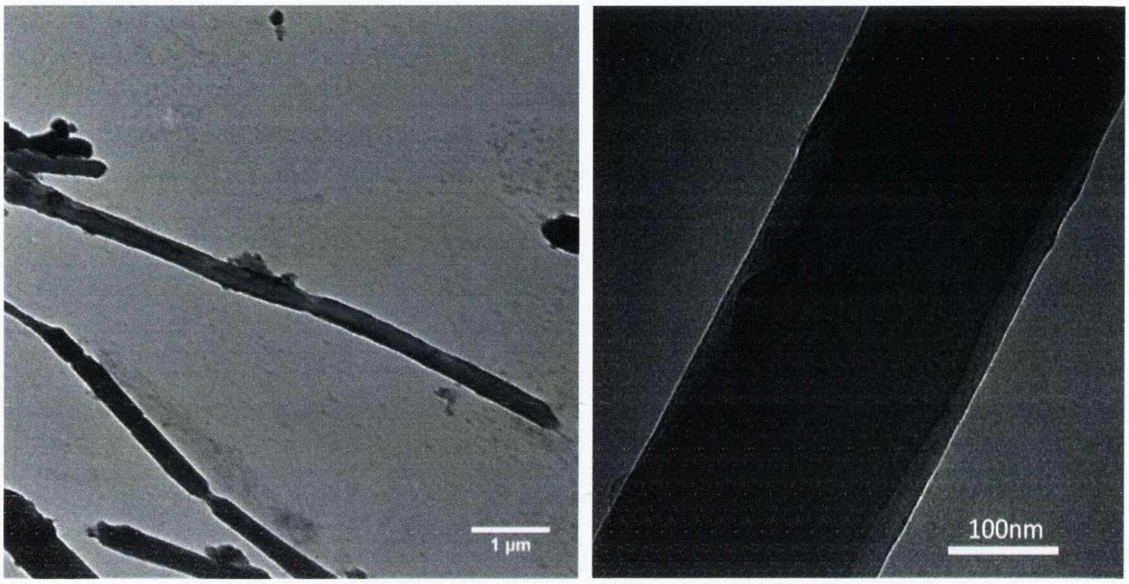

Figure 4.17: TEM images of QD doped PS nanowires

4.4 Conclusions

Thus we have developed the preparation of new high aspect ratio PS multimodal (magnetic and fluorescent) nanowires by vacuum infiltration into 200 nm diameter porous alumina membranes. In our procedure superparamagnetic magnetite nanoparticles of ~12 nm were fabricated and coated with oleic acid to stabilise them in organic media. These were used to create a doped PS solution along with coumarin-153 dye which was infiltrated and dried to create multimodal (fluorescent and magnetic) PS nanowires. The wires displayed good magnetic character and ability to be manipulated by magnetic field. The wires showed strong emission under UV excitation and their magnetic properties eased their manipulation for washing steps. Sulfonation of the PS nanowires surface was performed to aide in their functionalisation and conjugation to antibodies. This antibody functionalisation was successfully carried out on the fluorescent magnetic PS nanowires and interaction with epithelial lung cancer cells examined showing that the nanowires do bind to the surface of the cells and in some cases are internalised into the cell cytoplasm with some indication that shorter straight nanowires are more likely to be internalised than longer curled ones. Their functionalisation, multimodal character and PS makeup open them up to be used for magnetic separation applications in bio-medical systems. Secondly, CdZnSe/ZnSe QD loaded PS nanowires have been developed without damaging the QDs and characterised resulting in luminescent wires.

4.5 References:

1 Jiang, J. & Thayumanavan, S. Synthesis and Characterization of Amine-Functionalized Polystyrene Nanoparticles. *Macromolecules* **38**, 5886-5891, doi:10.1021/ma0507286 (2005).

2 TAMILVANAN, S. & SA*, B. Effect of production variables on the physical characteristics of ibuprofen-loaded polystyrene microparticles. *Journal of Microencapsulation* **16**, 411-418, doi:doi:10.1080/026520499288870 (1999).

3 O'Connor, I., Hayden, H., Coleman, J. N. & Gun'ko, Y. K. High-Strength, High-Toughness Composite Fibers by Swelling Kevlar in Nanotube Suspensions. *Small* **5**, 466-469, doi:10.1002/smll.200801102 (2009).

4 Erdogan, M., Hizal, G., Tunca, Ü., Hayrabetyan, D. & Pekcan, Ö. Molecular weight effect on swelling of polymer gels in homopolymer solutions: a fluorescence study. *Polymer* **43**, 1925-1931 (2002).

5 Vaquette, C. *et al.* In vitro biocompatibility of different polyester membranes. *Bio-Medical Materials & Engineering* **16**, S131-S136 (2006).

6 El Fray, M., Prowans, P., Puskas, J. E. & Altstädt, V. Biocompatibility and Fatigue Properties of Polystyrene−Polyisobutylene−Polystyrene, an Emerging Thermoplastic Elastomeric Biomaterial. *Biomacromolecules* **7**, 844-850, doi:10.1021/bm050971c (2006).

7 Li, X. *et al.* Fabrication of Patterned Polystyrene Nanotube Arrays in an Anodic Aluminum Oxide Template by Photolithography and the Multiwetting Mechanism. *The Journal of Physical Chemistry B* **113**, 12227-12230, doi:10.1021/jp904254s (2009).

8 Steinhart, M. *et al.* Polymer Nanotubes by Wetting of Ordered Porous Templates. *Science* **296**, 1997-, doi:10.1126/science.1071210 (2002).

9 Song, G., She, X., Fu, Z. & Li, J. Preparation of good mechanical property polystyrene nanotubes with array structure in anodic aluminum oxide template using simple physical techniques. *J. Mat. Res.* **19**, 3324-3328 (2004).

10 J. Fresnais, Berret, J. F., Frka-Petesic, B., Sandre, O. & Perzynski, R. Electrostatic Co-Assembly of Iron Oxide Nanoparticles and Polymers: Towards the Generation of Highly Persistent Superparamagnetic Nanorods. *Advanced Materials* **20**, 3877-3881 (2008).

11 Martin, J., Vazquez, M., Hernandez-Velez, M. & Mijangos, C. One-dimensional magnetopolymeric nanostructures with tailored sizes. *Nanotechnology*, 175304 (2008).

12 Corr, S. A. *et al.* Magnetic-fluorescent nanocomposites for biomedical multitasking. *Chemical Communications*, 4474-4476 (2006).

13 Liu, X. *et al.* Preparation and characterization of hydrophobic superparamagnetic magnetite gel. *Journal of Magnetism and Magnetic Materials* **306**, 248-253 (2006).

14 Roca, A. G., Marco, J. F., Morales, M. D. & Serna, C. J. Effect of nature and particle size on properties of uniform magnetite and maghemite nanoparticles. *J. Phys. Chem. C* **111**, 18577-18584, doi:10.1021/jp075133m (2007).

15 Yang, J. C., Jablonsky, M. J. & Mays, J. W. NMR and FT-IR studies of sulfonated styrene-based homopolymers and copolymers. *Polymer* **43**, 5125-5132 (2002).

16 Gibson, H. W. & Bailey, F. C. Chemical Modification of Polymers. 13. Sulfonation of Polystyrene Surfaces. *Macromolecules* **13**, 34-41, doi:10.1021/ma60073a007 (1980).

17 Resch-Genger, U., Grabolle, M., Cavaliere-Jaricot, S., Nitschke, R. & Nann, T. Quantum dots versus organic dyes as fluorescent labels. *Nat Meth* **5**, 763-775, doi:http://www.nature.com/nmeth/journal/v5/n9/suppinfo/nmeth.1248_S1.html (2008).

18 Li, S. *et al.* Bulk Synthesis of Transparent and Homogeneous Polymeric Hybrid Materials with ZnO Quantum Dots and PMMA. *Advanced Materials* **19**, 4347-4352, doi:10.1002/adma.200700736 (2007).

19 Wang, C. *et al.* Tunable photoluminescence of poly(phenylene vinylene) nanofibers by doping of semiconductor quantum dots and polymer. *Synthetic Metals* **160**, 1382-1386 (2010).

20 Yunhua Yang, Z. W. Y. D. M. G. Incorporating CdTe Nanocrystals into Polystyrene Microspheres: Towards Robust Fluorescent Beads13. *Small* **2**, 898-901 (2006).

21 Wang, X. *et al.* Non-blinking semiconductor nanocrystals. *Nature* **459**, 686-689, doi:http://www.nature.com/nature/journal/v459/n7247/suppinfo/nature08072_S1.html (2009).

Chapter 5

TiO_2 Based Composite Materials

5.1 Introduction

TiO_2 is one of the most widely worked on materials in research due to its wide range of applications most notably in the area of photo induced processes such as photovoltaics and photocatalysis. TiO_2 exists primarily in three different phases; anatase (tetrahedral), rutile (tetrahedral) and brookite (orthorhombic) (with TiO_2-B also able to occur naturally). Rutile is known to be the most thermodynamically stable of the phases however the difference in free energy between the phases means that solids will remain stable in either phase once transformed. Both rutile and anatase show photocatalytic activity however anatase phase TiO_2 shows higher activity than rutile in most tests which is attributed to its higher Fermi level and higher surface hydroxylation, however it has been shown that in some cases a mixture of rutile and anatase phases can perform better[1-2]. For this reason it is then desirable to obtain and explore the conversion to primarily anatase phase materials. The conversion of phases depends on a number of parameters, primarily the number and type of defects in the material, particle size and method of material synthesis. The most common method of phase transformation is to anneal the material at a suitable temperature which can also help to crystallise the phases. The photocatalytic properties of TiO_2 are like most photo induced phenomena in semiconductors caused by the absorption of light greater than the active bandgap of the material thus causing the promotion of an electron to the conduction band of the material and leaving 'hole' in the valence and thus creating an electron-hole pair. It is this photo excitation that is responsible for the activity of TiO_2 in areas of photocatalysis. The most common application for materials in photocatalysis is that of the degradation of organic/inorganic pollutants and microorganism to inert or less harmful substances by the oxidation of the absorbed pollutant. However the effectiveness and quality of a good photo-catalyst is judged on a number of factors such as for it to be chemically and biologically inert, its ease and cost effective production, reusability, active in sunlight conditions and photo-catalytically stable. For the material to be photocatalyticly stable it must overcome a number of competing processes so as to be effective, these processes are highlight below in Figure 5.1 showing the main process the system undergoes upon successful excitation.

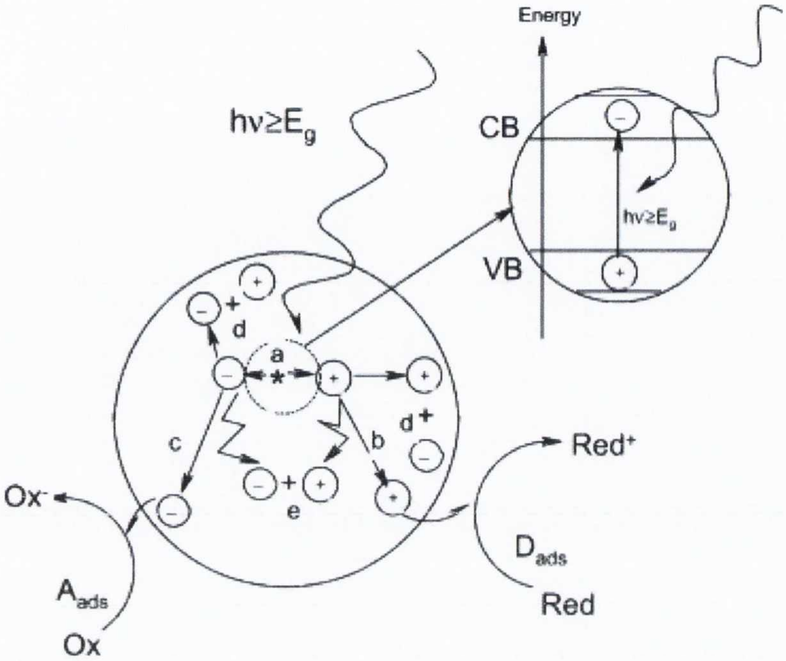

Figure 5.1: Schematic of the main process of a semiconductor particle after excitation; (a) electron-hole formation (b) oxidation of donor (c) reduction of acceptor (d) & (e) electron-hole recombination at surface and in bulk[2]

One of the main drawbacks of TiO_2 however is that it does not absorb in the visible region of the spectrum with typical bandgaps of 3.05 eV for rutile and 3.26 for anatase. This can be addressed by doping the semiconductor so as to alter the bandgap structure or by the use of sensitizer molecules in devices such as dyes or QDs[2-4] which result in the greater activity in the visible region of the spectrum. Another important factor in the effectiveness of photocatalysis is there surface area or more specifically their active surface area, which is important for the obvious reason of the greater area available for adsorption of the target species and thus reaction. However the activity of the catalyst is related to its ability to avoid electron-hole recombination, a large surface area can sometimes inhibit the effectiveness of the catalyst for example when you get down to the low nanoscale environment the small size means a large number of defects which can act as traps for the excited pair and result in reduced activity but at the small size the quantum yield of electron-hole formation increases so therefore there is a degree of trade off between the two. The crystallinity of the sample also plays an important role as the activity of TiO_2 is higher for crystalline samples than amorphous.

The role of the fabrication method of TiO_2 is clearly important in creating and altering the aspects important to the photocatalytic activity mentioned above. There are many ways in which to synthesize TiO_2 however for this work only alkoxide based sol-gel synthesis will be discussed and explored. As discussed in Section 1.1 one of the unique advantages of sol-gel processing is the relative ease of doping to create homogeneous materials with good stoichiometric control, with the requirements of improving TiO_2 as a photocatalyst this is very much a desirable advantage. The method also helps create a high degree of hydroxylation on the surface which is vital for the creation of hydroxyl radicals (HO·) and adsorption of molecules onto the surface. However often the prepared gels must be annealed to remove residual organic groups and induce crystallinity, which causes shrinkage and a reduction of surface area and can cause the removal of surface hydroxyl groups. Again a balance between these advantages and disadvantages must be struck by altering the sol-gel process to suit the goals of the researcher.

One such system of a mixed TiO_2 structure achieved by sol-gel processing which will be investigated in the present work is that of silica-titania mixed glasses. Silica-titania systems have attracted interest in areas of anti fogging coatings[5], ultra low expansion glass (ULE®), improved storage and release of substances in its porous structure[6] and photocatalysis in the forms of aerogels and a hydrosol[7-9]. This type of missed oxide glass displays interesting properties when changing the content of TiO_2 due to the complex nature of homogeneous mixing in glasses when the mol% of one goes past a certain point and the nature of the phase change upon annealing differing from that of the pure substance. Their production also requires knowledge of sol-gel processing so as to achieve a good mixture of the components and not have the TiO_2 precipitate out due to its precursors higher reaction rates (See Section 1.1.1)[10]. The concentration of part of this project was to fabricate and characterise with the aim to explore the photocatalytic potential of SiO_2-TiO_2 xerogels. The main goal of this part of the project was to fabricate, characterise and explore the photocatalytic potential of various SiO_2-TiO_2 and TiO_2 based materials and nanostructures.

5.2 Preparation and characterisation of SiO_2-TiO_2 sol-gels

Silica-titania xerogels were prepared with the goal of fabricating clear glassy composites displaying photo-catalytic activity for possible future applications in mircrotube production or clear photoactive coatings. The composites have been prepared by combination of a partially hydrolysed silica and titania sol using an acid catalyst. A condensation step with water-ethanol solution was then performed to induce gelation to the system. The gels were allowed to dry in air and annealed at various temperatures for characterisation. Gels were made up with titania compositions of 10-50 mol% and tested at different temperatures; majority of samples had a clear glassy complexion to the naked eye.

Annealing experiments were carried out on xerogels with a 1:1 Si:Ti atomic ratio at temperatures of 200, 400 and 600 °C. The samples were annealed by heating at 5°C/min up to the desired temperature and holding for 1 hr before allowing to cool naturally to room temperature.

Figure 5.2 demonstrates the Raman spectra of the silica-titania samples showing the emergence of anatase phase TiO_2 after annealing at a temperature of 600 °C. The spectrum of the 600 °C annealed sample displays distinct broad peaks at 404, 511, and 621 cm^{-1} which are indicative of anatase phase TiO_2 [11-12] while still displaying some weak rutile character. The lower end of the spectra ($<150\ cm^{-1}$) is not shown due to detection limit of the set up used. The original thermally untreated xerogel (bulk) and samples which were annealed at 400 °C showed very weak and broad rutile related peaks at 240 cm^{-1}, ~450 cm^{-1} and 610 cm^{-1}, sample at 200 °C shows no distinct peaks and a high background signal indicative of the fact that at this temperature we have only amorphous material with impurities still present. Complete conversion to anatase phase was observed with annealing at 900 °C, Figure 5.3 shows characteristic anatase peaks with no rutile observed in the sample. Also shown in scan 'b' is gel fabricated very similar but with an instant gelation instead of a stepped one, this gel when annealed showed a more intense anatase phase signal and conversion to anatase phase at a lower temperature than previous prepared samples.

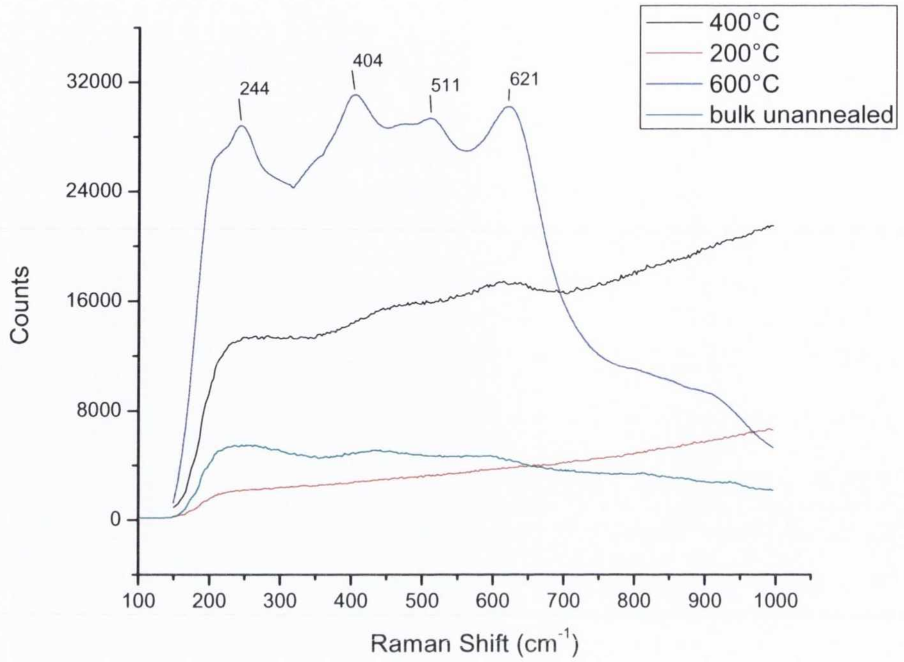

Figure 5.2: Raman spectra of 1:1(Si:Ti) xerogel annealed at different temperatures

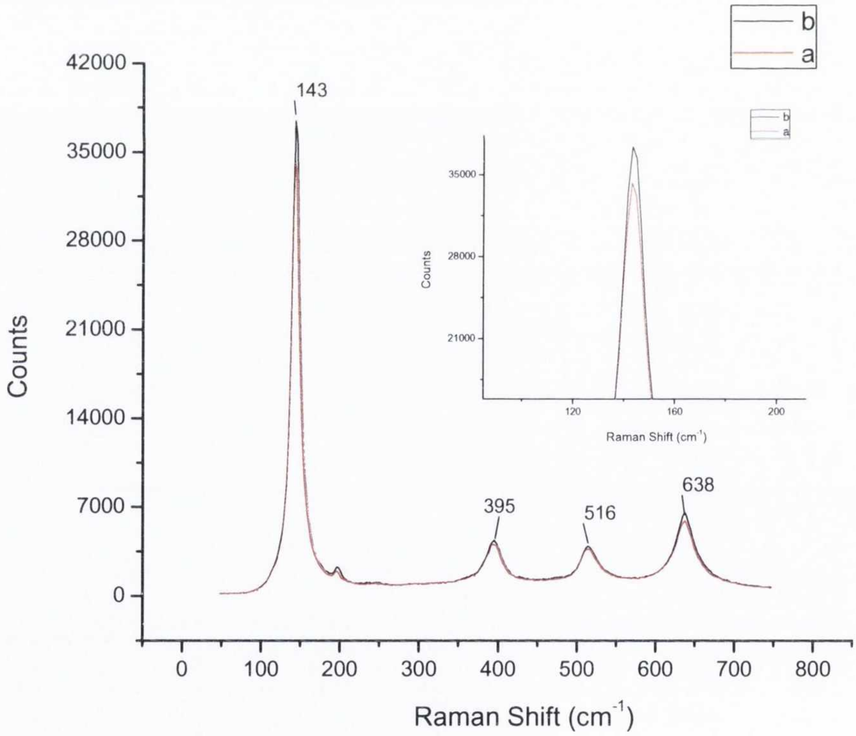

Figure 5.3: Raman spectra of 1:1 (Si:Ti) gels annealed at 900°C; 'a' and 'b' are two gels made very similarly with the 'b' gel made with an instant gelation step

After established the annealing conditions for samples with a 1:1 Si:Ti ratio, gels containing different mol% of TiO_2 were also fabricated and annealed at 600 °C and

900 °C to examine their properties with annealing. The Raman spectra (Figure 5.4) of gels containing 30 and 40 mol% TiO_2 and annealed at 600 °C and 900 °C clearly demonstrated the disappearance of the amorphous phase with some rutile character to the emergence of anatase phase at 600 °C and showing only anatase phase after annealing at 900 °C.

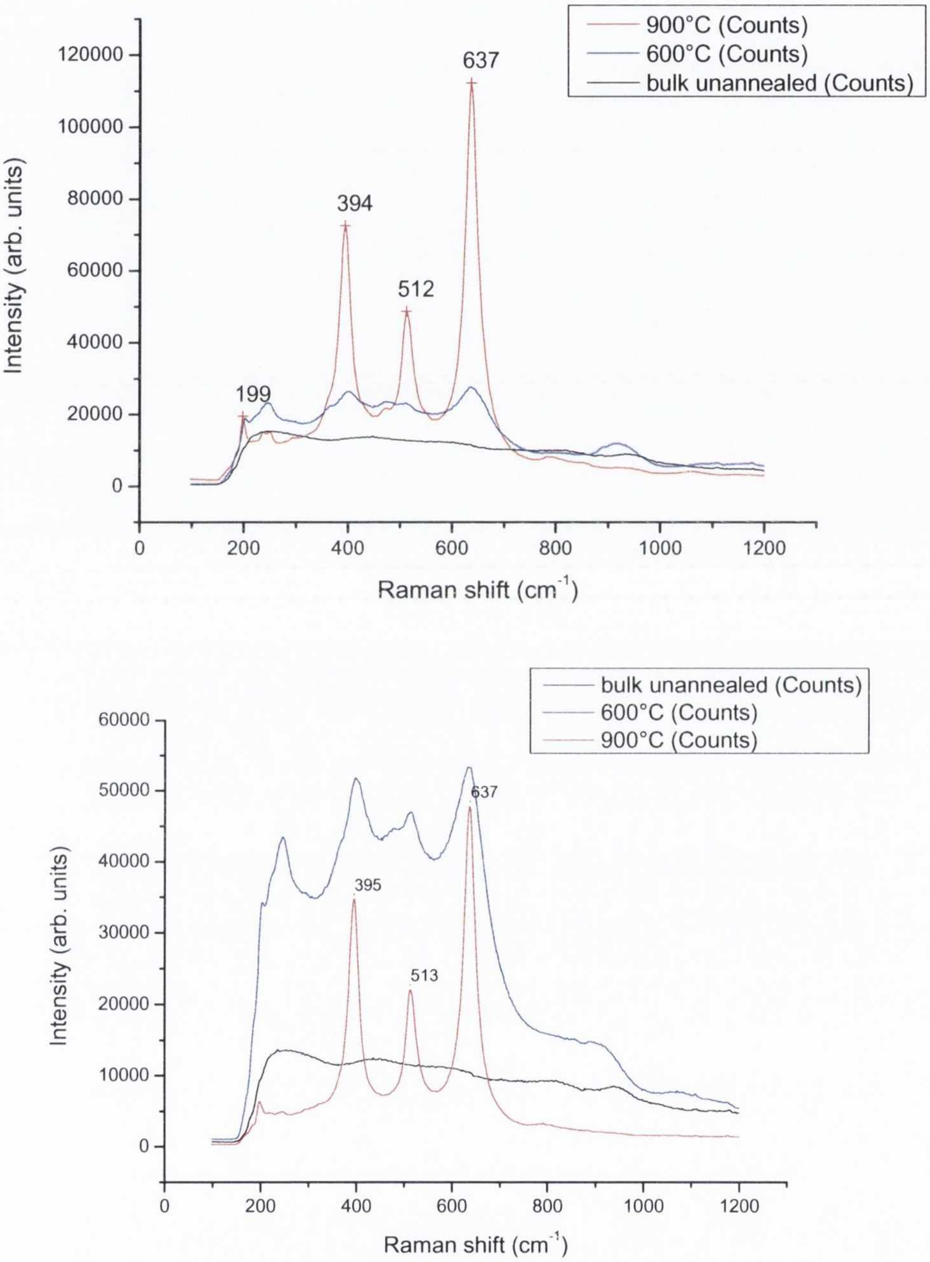

Figure 5.4: Raman spectra of annealed gels containing 30mol% (top) and 40mol% (bottom) TiO_2

Gels were also prepared with lower TiO_2 content (10 & 20 mol%). These gels again showed weak rutile character in the amorphous phase similar to the higher % gels but also noticeably a more distinct peak at ~943 cm^{-1} (Figure 5.5 (top)) is observed especially in the 10 mol% gel, this is thought to be due to the Ti-O-Si bond formation[13-14]. For comparison the spectra of the gels containing 30 and 40 mol% of TiO_2 are shown in Figure 5.5 (top). These spectra have a seriously diminished peak at ~943 cm^{-1}, this is due to phase separation of the SiO_2 and TiO_2 phases in higher % gels where the titanate species bond to each other more forming clusters of TiO_2 [10].

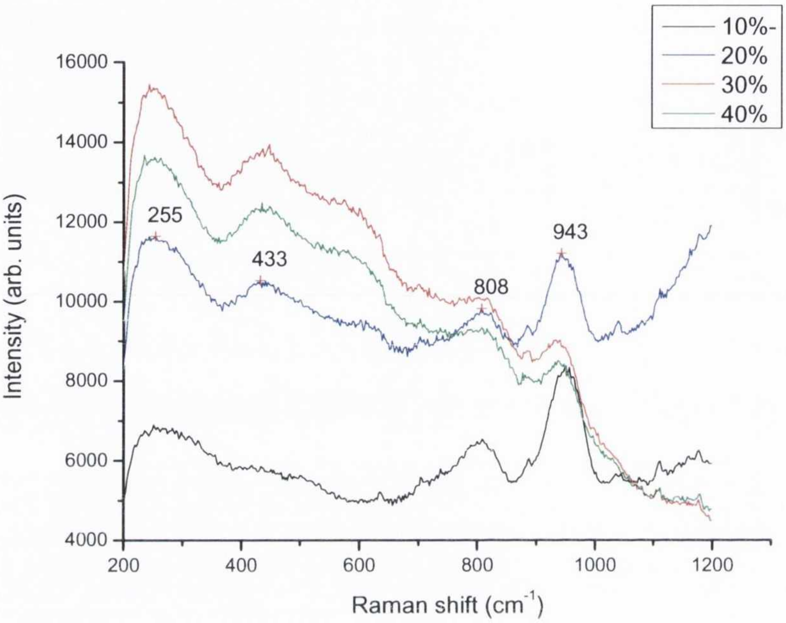

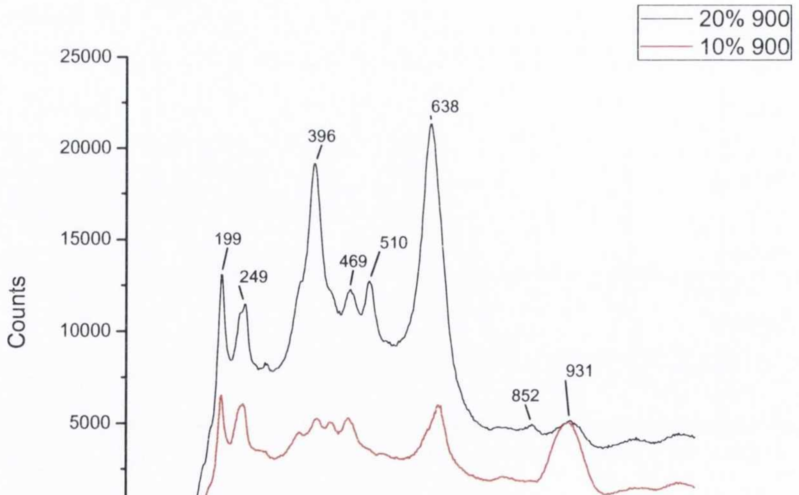

Figure 5.5: Raman spectra of (top) amorphous bulk gels of TiO_2 content 10-40 mol% and (lower) 10&20 mol% gels annealed at 900 °C

However the gels with lower TiO_2 % gels showed a relatively poor conversion to pure anatase phase with annealing temperature (Figure 5.5 (lower)) compared with the higher % gels annealed at the same temperature. This is seen in the fact that both the 10 and 20 mol% gels display a mixture of anatase and rutile phase peaks after annealing at 900 °C whereas the gels with a greater amount of TiO_2 showed only anatase phase present in Raman spectroscopy.

The 1:1 Si:Ti gel was selected for further study and testing due to its higher content of anatase phase TiO_2 (anatase phase is known to more active photocatalytic applications). The TGA scan shown in Figure 5.6 below shows a weight loss of 28% due to the evaporation of water and burning off of the alkoxy groups from the gel matrix. It can be seen that at 200 and 400 °C the gel is still losing weight due to continued burning off of impurities, this may account for the amorphous phase at 200°C and only the emergence of other phases at 400°C (where the weight loss is almost complete) observed in the Raman spectra in Figure 5.2. As can be seen at 600 and 900 °C the gel has reached a plateau in its weight loss profile. Similar findings have been made with regard to silica-titania composites [15].

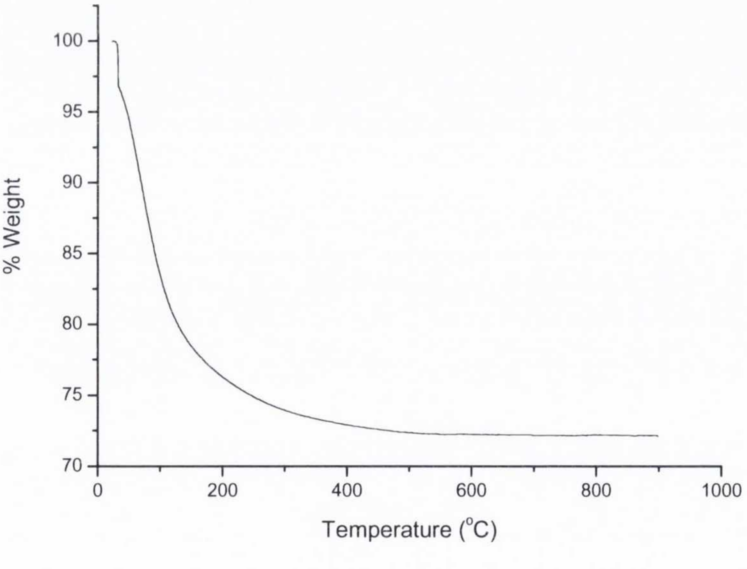

Figure 5.6: TGA of 1:1 SiO_2-TiO_2 gel

The XRD pattern of the 1:1 SiO_2-TiO_2 gel annealed at 900 °C is shown in Figure 5.7, this was fitted to known anatase phase TiO_2 peak positions which matched up within an acceptable degree accuracy from the diffraction pattern database and the pattern is quite characteristic for anatase phase TiO_2[16-17]. The peaks at 25.1°, 37.7°, 48°, 54.1°, 55° and 62.6° correspond to the (101), (004), (200), (105), (211) and (204) planes of anatase phase respectively.

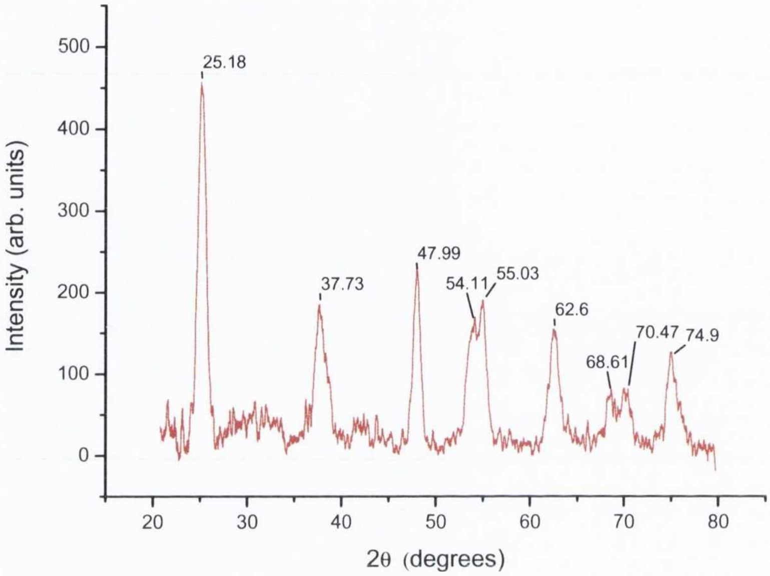

Figure 5.7: XRD pattern of 1:1 SiO_2-TiO_2 gel annealed at 900 °C

5.2.1 Photocatalytic Testing of SiO_2-TiO_2 composite

Photocatalytic tests were carried out for gels with a 1:1 ratio of SiO_2 to TiO_2 prepared as described above. The SiO_2-TiO_2 samples were tested as photo-catalysts for the degradation of methylene blue (MB-Figure 5.8), which is a standard dye to perform PC tests on [4,18]. The absorption of MB onto the surface of TiO_2 is through the cationic sulfur group. The photo-degradation of methylene blue proceeds by the oxidation of the sulfur heteroatom from -2 to 0 oxidation state due to the production of photo holes and OH radicals [18]. The importance of the pH of the solution on the photo-reactivity of MB is important. Since MB is cationic it adsorbs more efficiently onto a positively charged surface. Thus in a low pH environment (< 3 below the point of zero charge (PZC) of TiO_2 of about 6-7) TiO_2 is positively charged ($TiOH_2^+$) while in a high pH environment TiO_2 has a negative surface charge (TiO^-). Therefore MB absorbs more readily onto the surface of TiO_2 in a high pH environment [18]. While in a neutral solution (such as water) the surface of the TiO_2 should have both positive, negative and neutral (TiOH) surface sites.

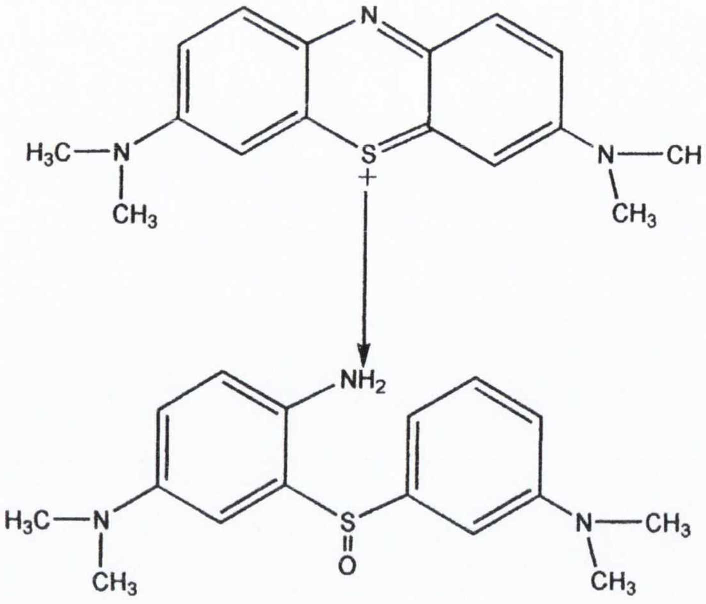

Figure 5.8: Degradation step of Methylene Blue[18]

Tests were carried out by placing 120 mg of the crushed sample annealed at 900 °C into a 1 cm quartz cuvette and adding 3.67 ml of 0.25×10^{-4} M solution of methylene blue in neutral water. The mixture was stirred under UV lamp radiation emitting at 365 nm for 4 hours. Solution was examined using UV-vis absorption spectroscopy to monitor the decrease in absorbance of MB. Control tests were also performed using the same concentration of MB solution and subjected to the same conditions. A test to determine the amount of surface adsorption of MB occurring onto the sample was performed by repeating PC tests in the absence of light. Results of this test showed a large degree of adsorption onto the surface of the sample showing a decrease of 27% absorbance in the main absorption peak at 662 nm from the initial scan (Figure 5.9), with the control sample showing no decrease in absorbance. Most reports on photocatalytic testing using MB show initial adsorption onto the catalyst surface is complete within 1 hour and considered sufficient to stir in dark for this length of time [9,18-19] indicating that adsorption onto the surface is almost certainly fully complete at this point.

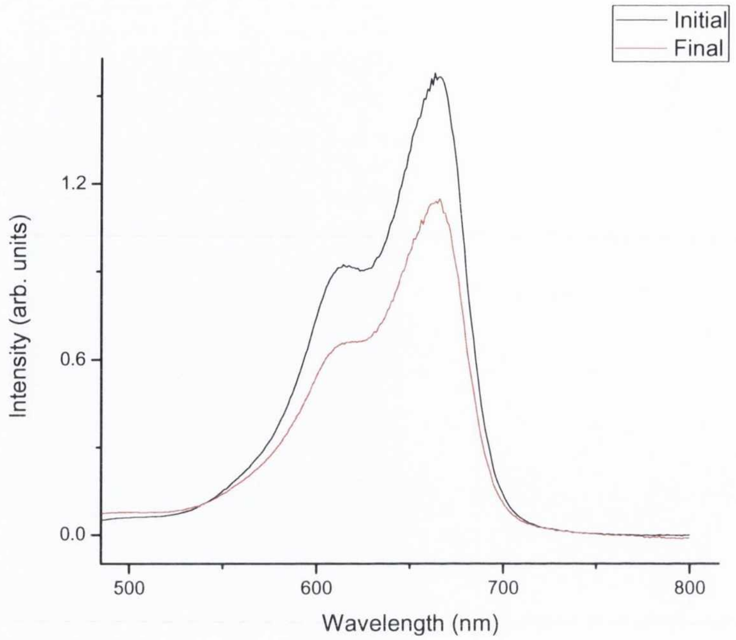

Figure 5.9: Absorbance scans of sample + MB after stirring in dark

This sample was then stirred under UV radiation @365 nm for 4 hr to examine any PC activity. The results are shown in Figure 5.10 below demonstrated a decrease of 11.3% in the absorbance due to the photo-degradation of MB. The relatively low activity of the sample is most likely due to the low surface area when compared to nano-materials of similar composition and the fact that not all surface sites will be anatase titania given the percentage of silica present. Another possible reason for the low activity is the suggestion that the PZC of silica-titania (in the region of pH = 2) [20] composites is lower than that of titania (~7) however another report suggests that it is quite similar to that of titania [8]. No change in the pH of the neutral water was observed with the addition of the solid catalyst. If the PZC is lowered the composite surface would be negatively charged and thus the MB would bind efficiently to the surface of the catalyst and might account for the large decrease in absorbance of the MB when stirred in the dark due to a large adsorption of the dye on to the catalyst surface. Also the degradation of the absorbance of MB shows no hypsochromic shift it suggests that photo-degradation proceeds by direct attack on the chromophore and not demethylation processes [20-21]. Despite the low activity the material does show the potential for development of clear glassy materials showing PC activity that can be shaped and worked to fit a particular design with the advantages of sol-gel processing (such as microtubes described previously). The fact that the gels are clear opens up the potential for their application for transparent coatings.

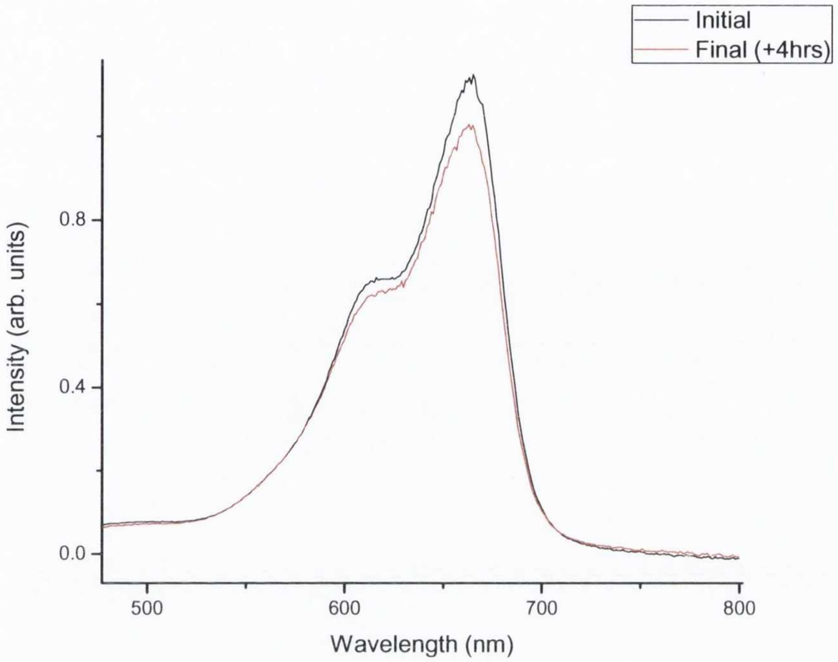

Figure 5.10: Absorbance scans of sample + MB after UV radiation exposure

5.3 Fabrication and characterisation of TiO_2 nanowires

TiO_2 1D nanostructures have attracted a great deal of attention over recent years, due to their potential in photocatalysis applications. There are several effective methods of production of these nanostructures (nanowires and nanotubes) such as hydrothermal synthesis[22], electrophoresis[23], wet corrosion method of Ti plate[24] and sol-gel template formation[25-26]. In our work, TiO_2 nanowires were fabricated using our established vacuum assisted infiltration method into porous alumina membranes to form solid nanowires and tested for photocatalytic activity.

Initially titanium isopropoxide has been hydrolysed using a water, ethanol, HCl solution and allowing stirring overnight to obtain a milky white sol. This was infiltrated into 200 nm pore diameter alumina membranes and allowed to dry in air. The infiltrated membrane was then annealed at 400 °C for 1 hour to partially crystallise the titania to anatase phase and the wires released with membrane dissolution using NaOH. The annealing temperature was chosen as above this temperature the membrane begins to degrade and the nanowires obtained are not of high quality. The bulk and nanowire sample was characterised by TGA, Raman, TEM and UV-vis absorption while photocatalytic activity was examined by degradation of MB solution using UV irradiation.

Shown below in Figure 5.11 is a Raman spectrum of the xerogel used to fabricate the nanowires annealed at 400 °C. The spectrum displays characteristic peaks for anatase phase TiO_2, confirming the disappearance of amorphous phase which showed a slight rutile character. The TGA scan (Figure 5.12) demonstrates a weight loss of 30% on annealing to 900 °C, the scan also shows the weight loss levelling out between 400-500 °C where the titania fully condenses and begins to crystallise and change phase [27].

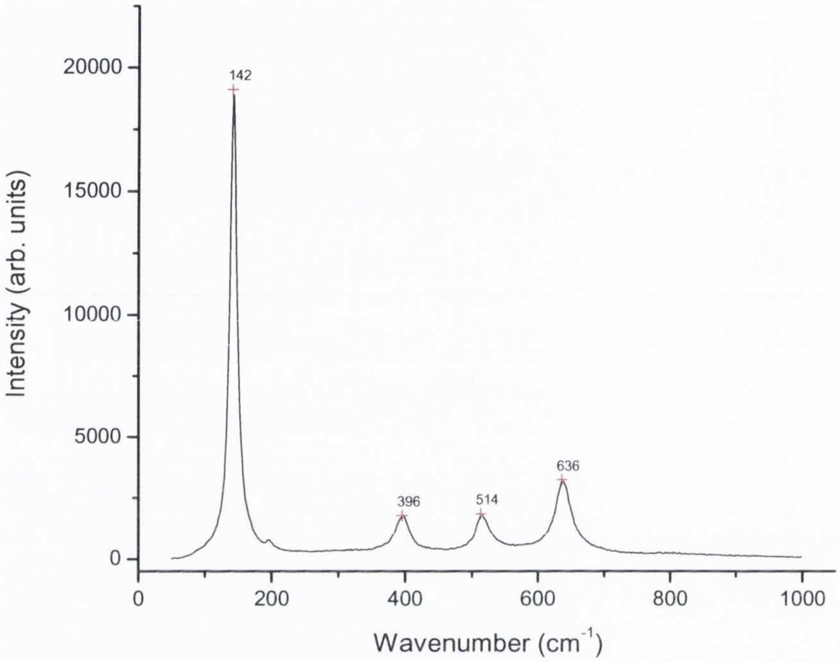

Figure 5.11: Raman spectra TiO_2 annealed at 400 °C

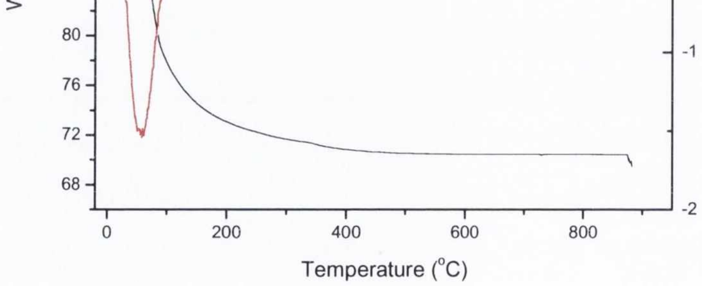

Figure 5.12: TGA and D-TGA scan of TiO_2 xerogel

The annealed nanowires were examined with optical microscopy and TEM to investigate their size and examine their surface structure. The wires demonstrated high aspect ratio and excellent yield after the membrane dissolution process to release the wires. TEM characterisation showed them to have a diameter of 236 nm ± 8 nm and lengths of 2-10 μm.

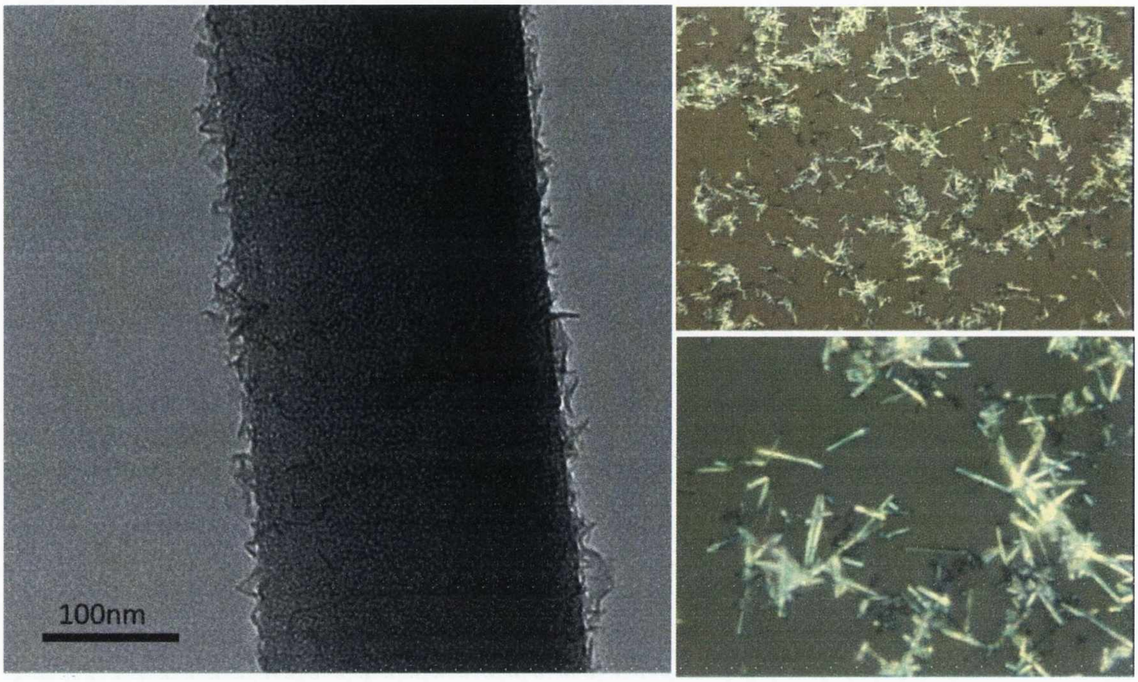

Figure 5.13: TEM and optical microscope images of TiO_2 nanowires annealed at 400 °C

UV-vis absorption spectroscopy of the wires (Figure 5.14) shows them to have a large increase in absorbance from the blue region of visible light into the deep UV, typical of TiO_2 absorbance scans. Given the high absorbance of the sample in the deep UV, the photocatalytic activity of the sample was investigated using a UV lamp emitting primarily at 254 nm. The spectra (Figure 5.15) demonstrate the results of exposing the nanowires mixed with a MB solution in neutral water (no observed change in pH of wires in water) after stirring in the dark (tests carried out showed little or no surface absorbance of MB by the sample) to 254 nm radiation for 4 hours under constant stirring and that of the control experiment with no sample added. The scans showed a decrease of 11.3% in the main absorbance band of MB over 4.25 hours. The apparently low activity can be explained by the very low weight of nanowires used (approx 1mg (very upper limit)) to a 4 ml MB solution of 0.25×10^{-4} M (1 mg:3.2×10^{-2} mg TiO_2:MB).

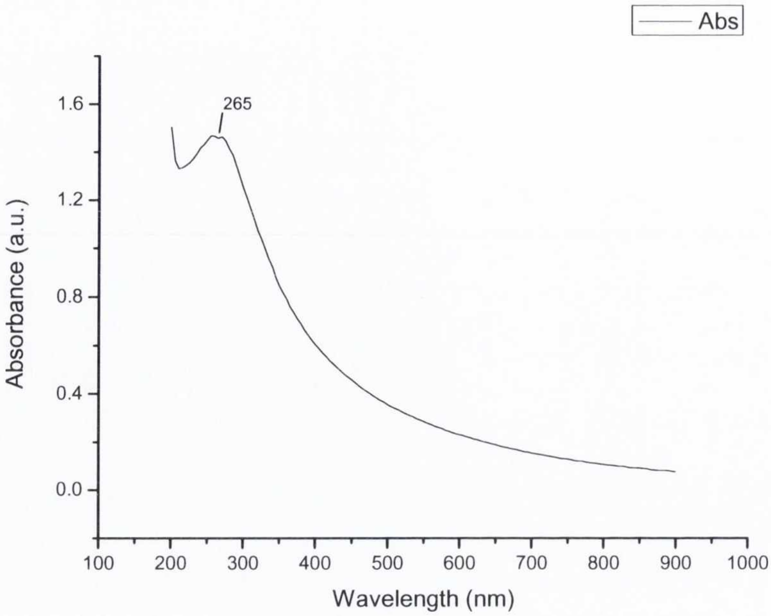

Figure 5.14: UV-vis absorbance scan of TiO_2 nanowires in water

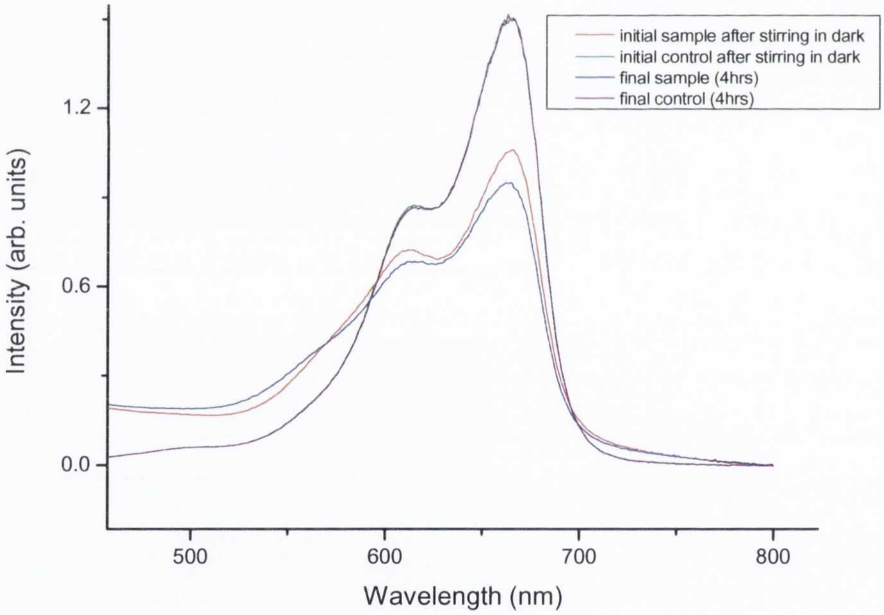

Figure 5.15: Absorption scans showing degradation of MB after UV irradiation @ 254 nm

5.4 AuNP loaded TiO_2 Nanowires

Metal NP-TiO_2 composites have previously been employed enabling the decrease of electron-hole recombination by creating an improved charge separation between the two by formation of a schottky barrier between the metal and semiconductor[2-3]. AuNPs have also been investigated due to their SPB centred at ~520 nm (see Section 1.5.2), which makes them an attractive sensitizer for TiO_2 allowing it to be active in the visible light region[28]. Au/TiO_2 systems have been tested for photocatalytic activity fabricated by sputtering AuNPs on to sol-gel derived TiO_2 films and shown to increase the photocatalytic activity for the degradation of organic molecules[29]. It was therefore undertaken in this project to fabricate AuNP loaded TiO_2 nanowires using our established sol-gel vacuum infiltration method into nano-porous alumina templates.

5.4.1 Fabrication and Characterisation of AuNP loaded TiO_2 Nanowires

The loaded sol-gel was based on a modified version of a previously reported process[30]. A titania sol was formed by adding 2.4 ml acac and 1.02ml EtOH to 5 ml of Ti-$(OBt)_4$ and leaving to stir for 2 hr. A solution of 1ml DMAP coated AuNPs (prepared as described previously in Section 6.3.4) and 2.55 ml EtOH was then added under stirring. This solution was then infiltrated into 200 nm diameter porous alumina membranes with vacuum assistance after 30 sec, 2, 4 and 10 min, with a thin film being made after 5 min by deposition of sol onto a clean glass slide. The quick infiltration and deposition of the sol is important as the AuNPs will aggregate and grow in the sol-gel conditions and is evident in the membrane infiltrated at 10 min and the sol over time due to the shift in colour from red to deep purple. The sol gelled after 2 days and was a deep purple coloured (reflecting larger Au particles present) powder. The nanowires were released by membranes dissolution with 0.1 M NaOH and washing via filtration with water. The nanowires characterised herein were obtained from the sample infiltrated after 30 sec of addition of AuNPs to sol. This sample will have AuNPs of the smallest size incorporated into it as the AuNPs will not have aggregated after this time. The nanowires were not annealed to prevent melting and aggregation of the AuNPs [30].

The nanowires and thin film were characterised using Raman, TEM and UV-vis absorption. Raman spectroscopy of the thin film and dried nanowires are shown in Figure 5.16. The Raman spectrum of the thin film shows clear anatase phase peaks at 149, 198, 399, 514 and 628 cm^{-1}. The spectrum of the nanowires however shows a more amorphous character to the TiO_2 with broad rutile and anatase peaks present. However the spectrum of the nanowires may be distorted by the glass slide upon which they are dried since the wires do not have a dense coverage over the slide and are relatively dispersed in comparison to a thin film, this could account for the weak signal of the wires resulting in an unclear spectrum (peak at 915 cm^{-1} for example is likely attributable to the glass slide beneath).

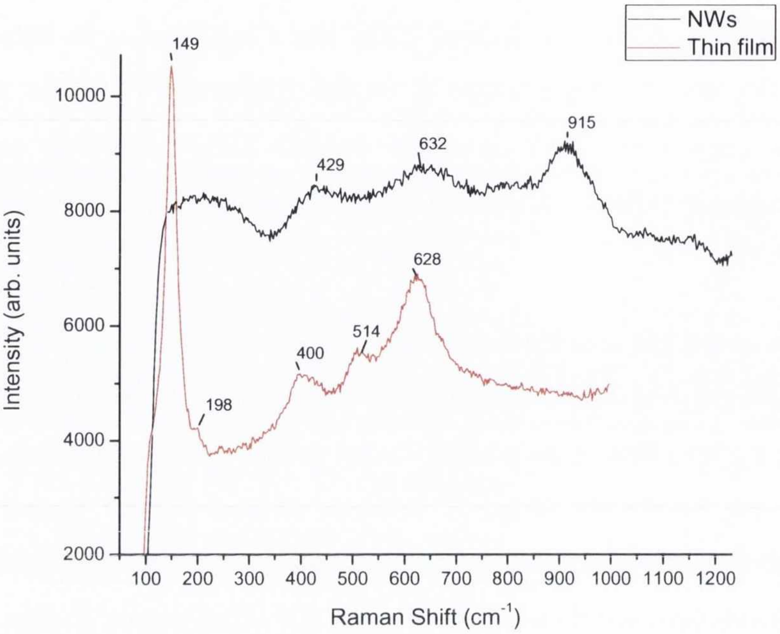

Figure 5.16: Raman spectra of AuNP loaded TiO_2 (thin film and nanowires)

TEM on the nanowires was performed to determine the size and structure of the wires. Shown in Figure 5.17 are several TEM images of the wires. The top two images show the wires to have a high aspect ratio with varying lengths between 3-10 μm. Size measurements on the diameter of the wires showed them to have a mean diameter of 235 nm (with a standard deviation of 27 nm). It was difficult to observe AuNPs in the nanowires, this is primarily due to the small size of the AuNPs, which are dispersed in quite thick TiO_2 nanowire matrix. However if the images are examined carefully, dark areas on the wire can be observed possibly due to the presence of the AuNPs. Also in the bottom right image, when the TEM beam was over focussed into the wire, dark patches and spots can be observed more clearly. Since the AuNP are metallic and conducting they would show up darker under TEM (as seen in Section 3.3.2). However neither of these observations conclusively shows the presence and distribution of the AuNPs but given the high loading and clear presence of the particles in the bulk gel the author is in no doubt that they are indeed present.

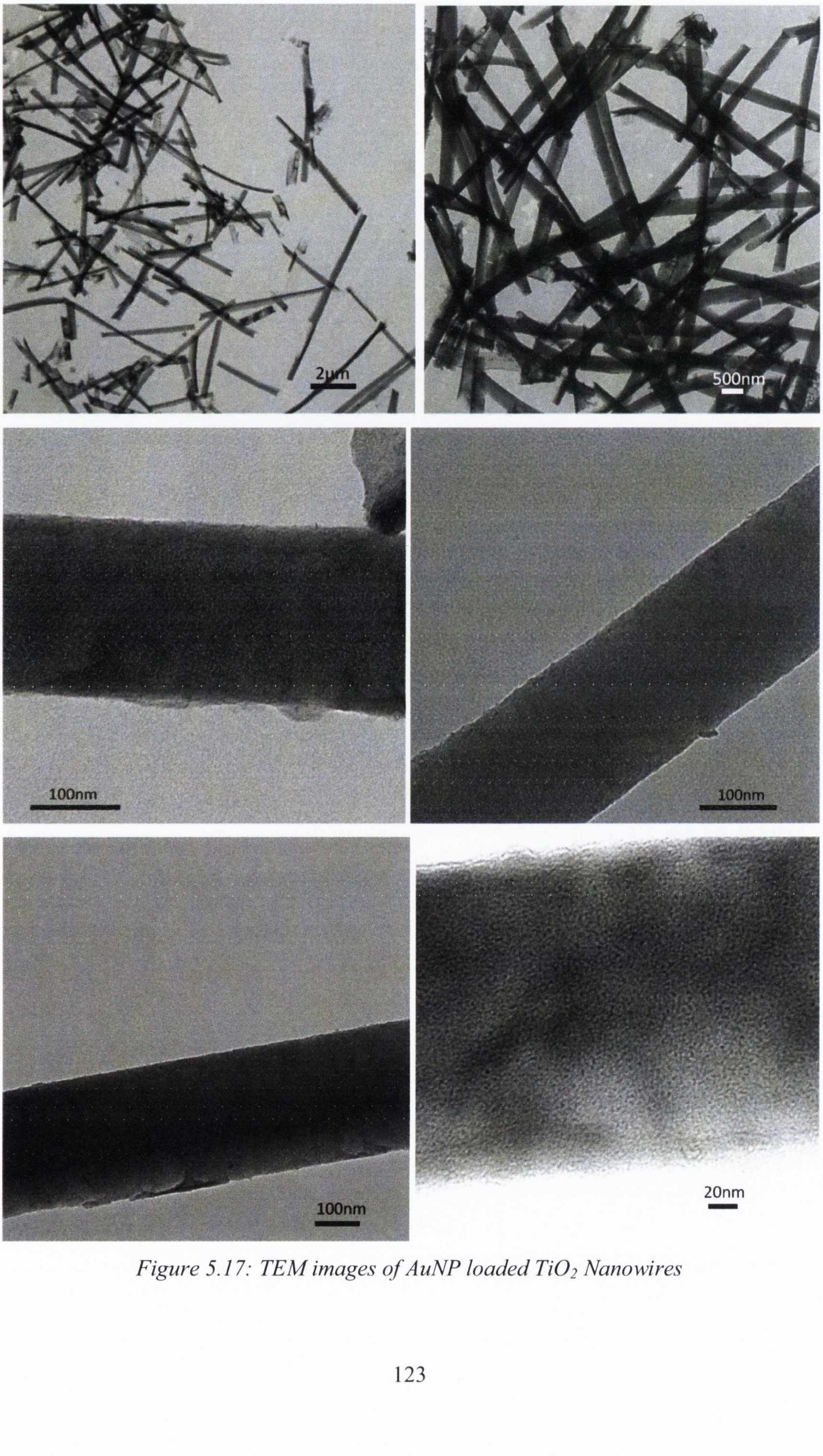

Figure 5.17: TEM images of AuNP loaded TiO_2 Nanowires

UV-vis of the wires dispersed (nanowires only remain dispersed for short period of time before crashing out) in water was taken to observe the absorption properties (Figure 5.18). The spectra (shown for two different concentrations) show a large increase in absorbance entering the UV region peaking at ~300 nm as is characteristic for TiO_2 materials.

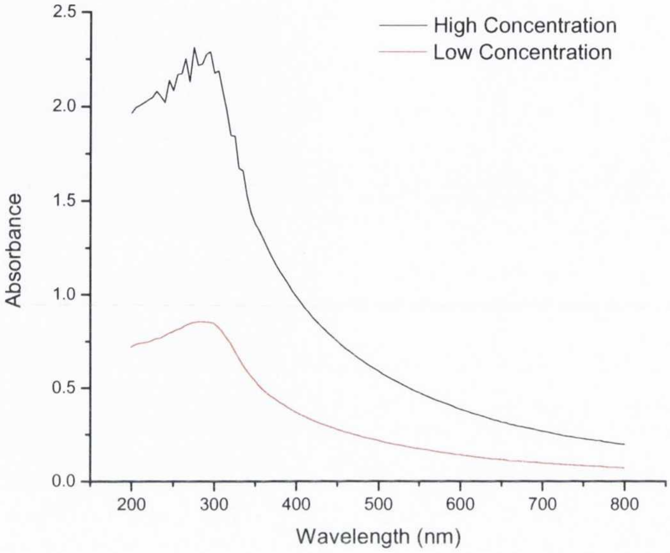

Figure 5.18: UV-vis absorbance spectra of AuNP loaded TiO_2 Nanowires in water with different concentrations

5.4.2 Photocatalytic testing of AuNP loaded TiO_2 Nanowires

Photocatalytic testing of the nanowires was carried by observing the degradation in absorbance of MB organic dye (as described above in 5.4.2). 2.75 ml of the nanowires in water (after dispersion with sonication) was added to 0.92 ml of 1×10^{-4} M MB solution. An identical control solution was also prepared (minus the sample) to ensure no dye degradation (or correct any occurring) due to other factors. Initial absorbances were taken after stirring in the dark for 50 min to negate absorbance of dye onto sample. This was based on tests done that showed after stirring in the dark for 50 min the decrease in absorbance of MB due to adsorption onto surface of nanowires was the same of that when left in the dark to stir for 4 hours. Sample then placed under UV lamp emitting primarily at 254 nm and left vigorously stirring for 4 hr, with final absorbance then taken after exposure.

The results of the test are displayed in Figure 5.19, the control sample shown in the graph demonstrated no degradation after the test, indicating that there is no other factors but that of the nanowires causing the dye's absorbance to diminish. The spectra relating to the nanowire sample show a 40.4% decrease in absorbance over the 4hrs. However testing the full level of absorbance of MB onto the wires and allowing for complete crashing out of sample in the dark over 18 hr showed a slight decrease in absorbance not due to PC activity however since all scans are taken with wires in a dispersed state the effect on the results is thought to be quite small however a degree of error here has to be taken into account. The mass of nanowires in solution was estimated by drying 3 ml of solution onto a previously accurately weighed glass slide and reweighing the total mass of both and subtracting the initial weight of glass slide. This showed the mass to be 0.24 mg ± 0.05 mg in 3 ml. That corresponds to a weight ratio of 0.22 mg:0.03 mg; NWs:MB in solution.

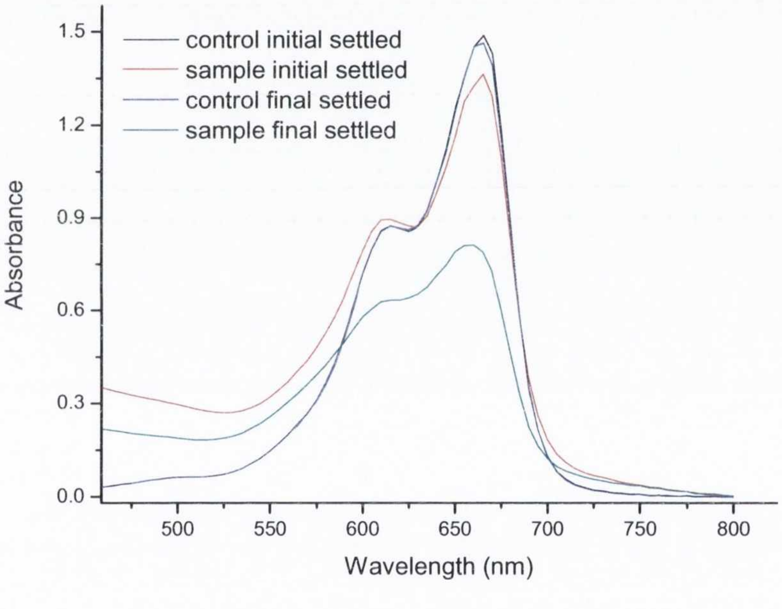

Figure 5.19: UV-vis absorbance spectra showing the degradation in the absorbance of MB due to AuNP loaded TiO_2 nanowires after 254 nm exposure for 4 hr

Figure 5.20 shows the decrease in absorbance of MB over a time of 300 min. This was done by removing the cuvette which the solution was in from UV radiation and running an absorbance scan at the indicated time (±1min) and then replacing the cuvette back stirring under the UV lamp to continue the test. Figure 5.21 shows the trend of the degradation with time. The rate of decay tends to follow a pseudo first order reaction kinetics (see Figure 5.21-inset plot of $\ln A_t$ (where A_t is absorbance after time t) vs time) with an associated rate constant of 0.0018 s^{-1}. The actual kinetics for photo-mineralisation of organic species tends to be somewhat complicated but is generally well described by the Langmuir-Hinshelwood law which is widely used in reaction rates of heterogeneous catalysis. This describes the kinetics of reactions with two adsorbed species (radical on the surface and a free substrate and a free radical and an adsorbed substrate) [2]. In circumstances where the dilution is low (which it is in our case; the MB solution is ~2.5×10^{-5} M) the rate reaction is generally seen to be first order and for higher concentrated solutions (in the region of 10^{-3} M) it is judged to be zero order [2]. The trend of degradation of MB also shows no hypsochromic shift as mentioned previously indicating that degradation proceeds via attack on the chromophore and not by demethylation. In the latter region of the PC tests, error associated with the evaporation of solvent over time due to heating can cause the solution to become more concentrated and affect the trend of degradation as the experiment continues.

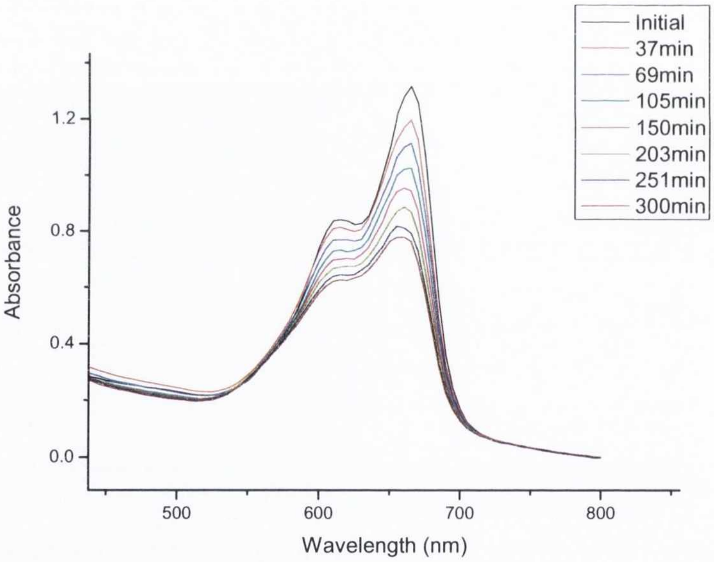

Figure 5.20: UV-vis absorbance spectra showing the degradation in the absorbance of MB over time due to AuNP loaded TiO_2 nanowires under 254 nm radiation

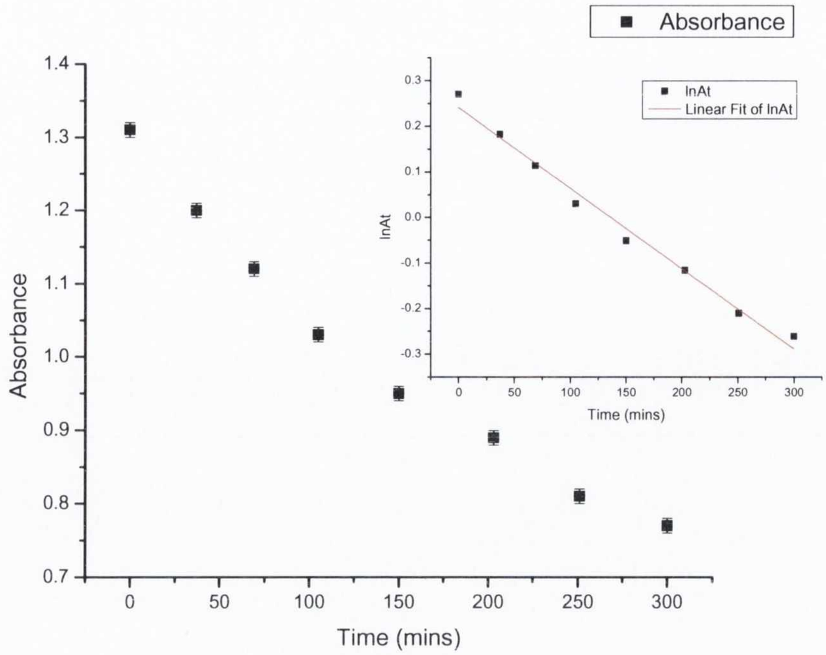

Figure 5.21: Change in absorbance of MB vs time; Inset: Plot of lnA_t *vs time with linear fit*

5.5 TiO_2 coated CdTe QDs

The luminescent properties of QDs and photocatalytic properties of TiO_2 highlighted in previous sections leads to the expectation that the combination of these two materials could have potential in the field of photocatalysis and photovoltaic's. Most of the previous work has been focused on the fabrication of differing layers of TiO_2 and nano-crystalline layers of II-VI semiconductors (CdTe, CdS etc) [31-35]. Other systems include aqueous solutions of TiO_2 NPs and QD working in conjunction in a photovoltaic cell[36]. The basictheory is that the semiconductor QDs act as a sensitizer to the TiO_2 so to expand its absorption range as demonstrated for a CdSe QD and TiO_2 system in Figure 5.22, where the QD absorbs light an becomes excited whereby energy transfer to the more stably excited conduction band of the TiO_2 particle occurs allowing current flow to the electrode. It was thus undertaken to explore coating CdTe QDs with a TiO_2 coating and examine its optical properties.

In our work coating of the CdTe QDs with TiO_2 was attempted by adding a solution of titanium ethoxide in dry iso-propanol and acetyl acetone (acac) (Ti:acac 1:1) drop-wise to a suspension of D-cysteine stabilised CdTe QDs in water (2:1 ratio of Cd^{2+}:Ti) under constant stirring. It was expected that the titanium ethoxide solution should hydrolyse and condense on contact with the water and form a coating around the QDs with the aid of the acac stabiliser helping the titanium ethoxide to remain stable for longer and not form NPs immediately. Samples were taken at 5mins, 2hrs and 20hrs (stopped stirring reaction assumed complete) to monitor the changes in emission and absorbance of the sample.

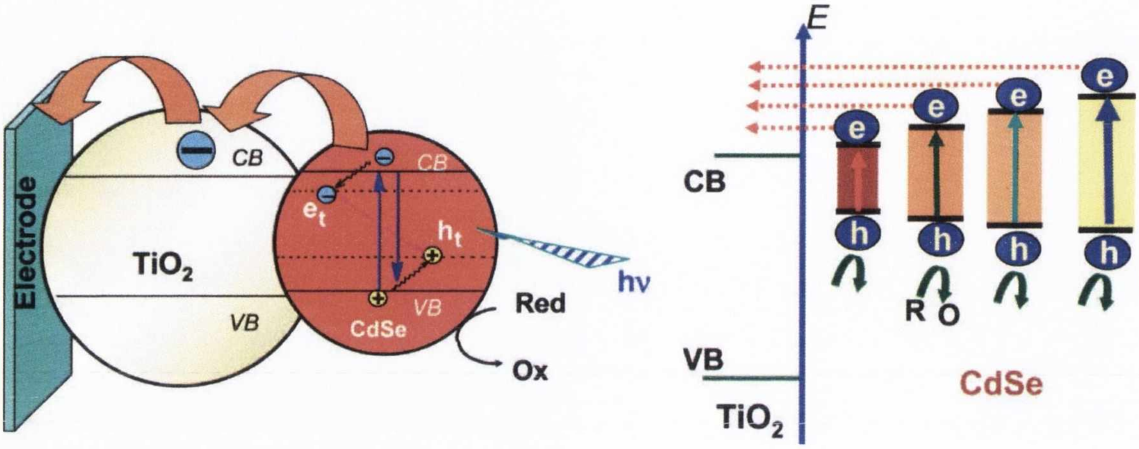

Figure 5.22: Schematic showing absorption and energy transfer of light to TiO_2 with CdSe acting as a sensitizer in a photovoltaic device [36](reproduced with permission from reference and ACS; License Number: 2634781251412)

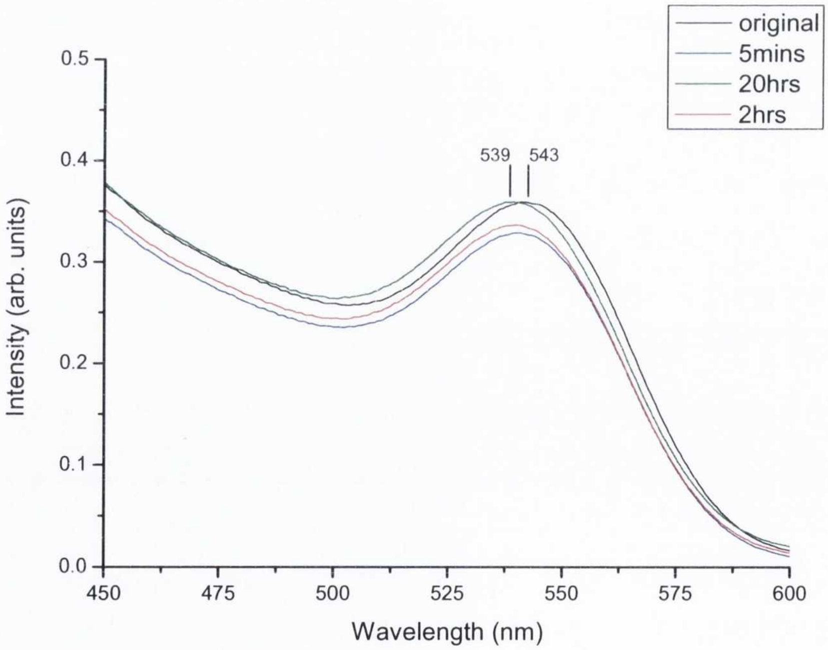

Figure 5.23: UV-vis absorbance spectra of TiO_2 coating on CdTe QDs over time

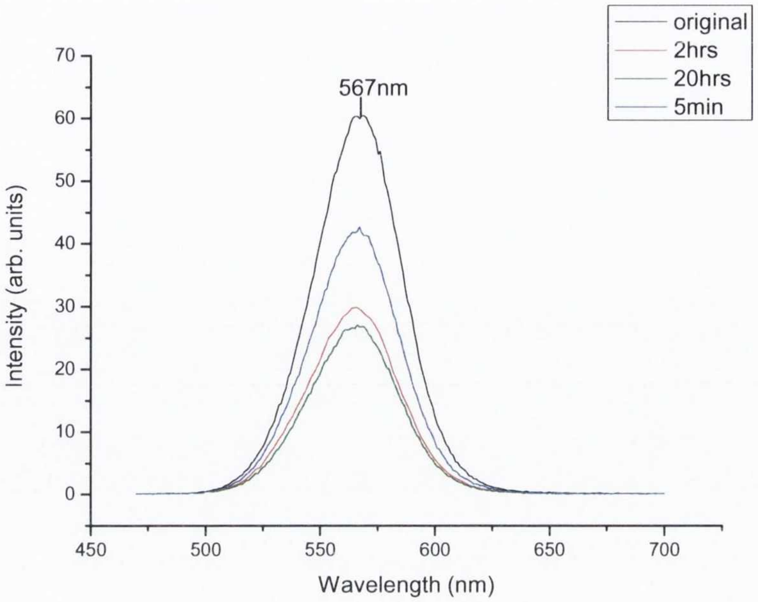

Figure 5.24: PL spectra of TiO_2 coating on CdTe QDs over time

The absorbance scans shown in Figure 5.23 show a very slight blue shift and slight decrease in absorbance (when baseline is taken into account) of the QDs, while also a large increase in absorbance in the deep UV region of the spectrum typical of TiO_2. The PL spectra of the reaction over time (Figure 5.24) revealed a decrease in the luminescence intensity of ~56% at the 20 hr end point. This decrease in emission intensity is expected if the dots are coated with oxide shell (TiO_2).

The sample was examined using a zetasizer to get an idea of the size range of the sample changing over time. The zetasizer which measures the hydrodynamic radius of particles in solution by dynamic light scattering (DLS) and therefore shows them to be quite a bit larger than that observed in TEM for example. The results (see Table 1) showed an increase in particle size with reaction time from 66.5 nm to 79.9 nm. The PdI is high suggesting that there is a large distribution of sizes in the sample.

Rxn Time	Size av	PdI
5mins	66.5nm	0.274
2hrs	71.8nm	0.347
20hrs	79.9nm	0.264

Table 1: Zetsizer DLS results for CdTe QD-TiO_2 nanocomposite

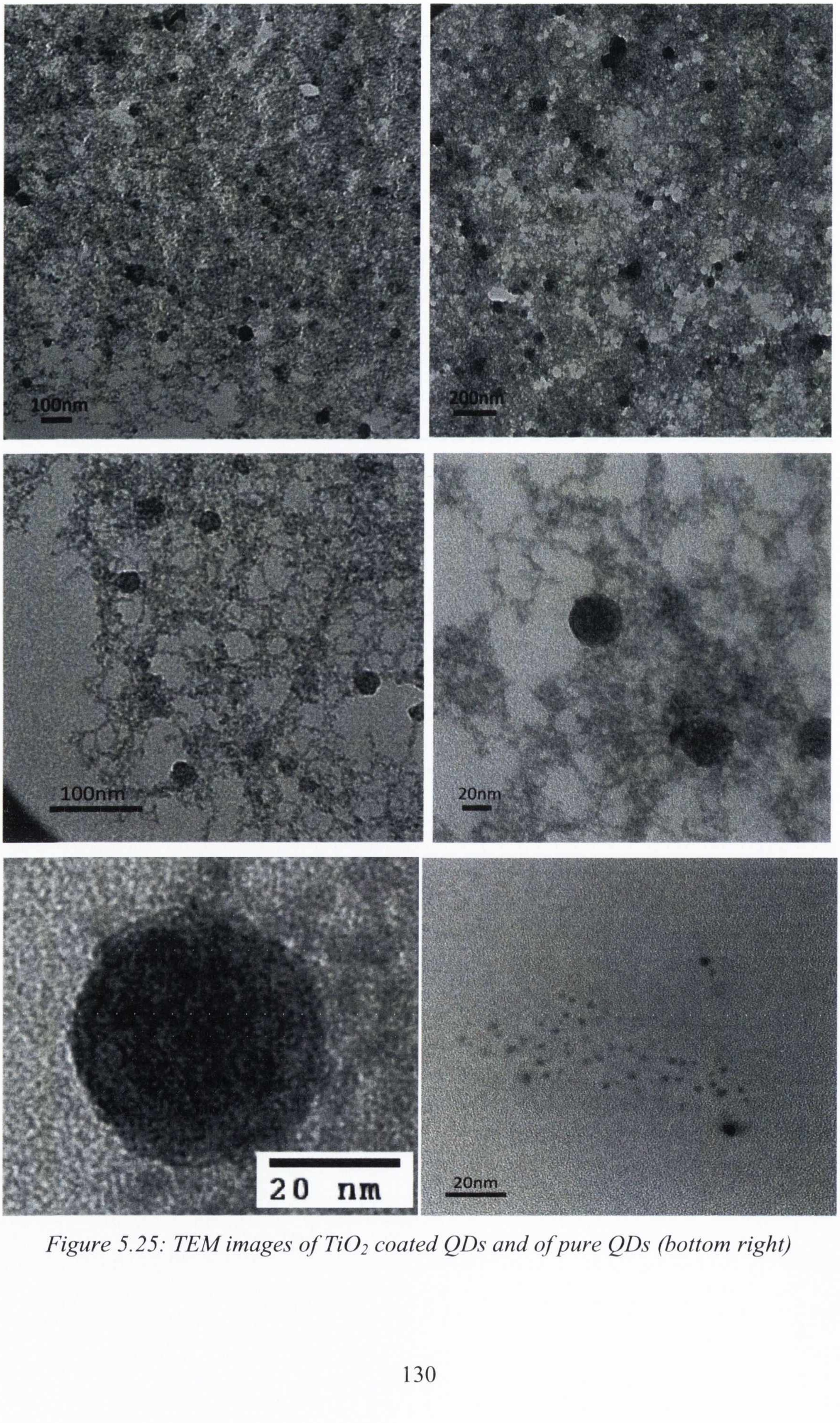

Figure 5.25: TEM images of TiO_2 coated QDs and of pure QDs (bottom right)

TEM images of the CdTe-TiO_2 sample after the purification using a sephadex column are shown in Figure 5.25. The images show a number of large particles of about 20 nm in size doted in amongst a lot of excess of aggregated CdTe QDs. The close up of one of the particles seems to show dark spots on/in the particle, however it is difficult to definitively say if these are CdTe QDs. These particles are most likely mixed aggregates of QD and titania. The bottom right image shows the original QDs used in the reaction for comparison, it cannot be ruled that initial free dots and/or QD/TiO_2 nanostructures are present also.

The particles however were not stable in when exposed to light for a period of time and degraded over time losing all luminescence, eventually turning black due to the presence of tellurium. This is assumed to be caused by the photo-oxidation of the QD catalysed by the presence of the TiO_2. This was also observed in previous samples fabricated under gentle heating and without the use of acac as a stabiliser.

Raman studies (Figure 5.26) of the dried sample were performed (using 785 nm laser to avoid the excitation and luminescence of the QDs) to ascertain the phase of the TiO_2. The spectrum displays a high noise background and broad peaks, this is to be expected from highly luminescent materials and the broad peaks due to the low laser power used to ensure the sample is not damaged and to prevent the background from being too high. The amount of TiO_2 present will also hinder obtaining a clear signal. However weak peaks were observed at 125, 232 and 447 cm^{-1}. These would indicate a rutile phase character to the TiO_2 present however a peaks at around 366 and 560 cm^{-1} might indicate the presence of anatase. The broad peaks make it difficult to accurately assign peaks and interference from the glass substrate may also interfere with the spectrum. It does indicate that the TiO_2 coating is most likely amorphous in nature.

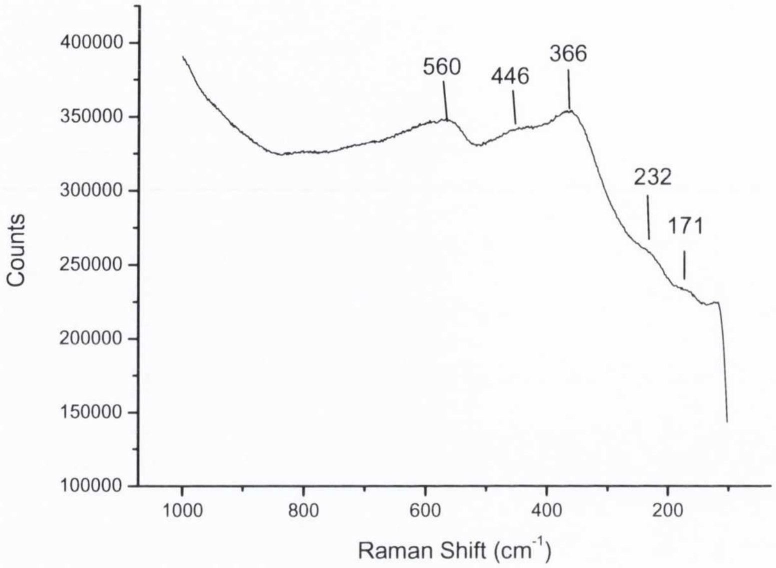

Figure 5.26: Raman spectrum of dried TiO_2 coated CdTe QDs

5.6 Conclusions

Thus we have developed and investigated a range of TiO_2 based materials for potential in photocatalysis applications. Initially SiO_2-TiO_2 composite glass fabrication was optimised to obtain clear transparent materials which contain anatase phase TiO_2 by characterising gels with differing TiO_2 content and the effect of different annealing temperature on the composites. The sample showing the highest quantity of anatase phase TiO_2 was then tested for photocatalytic activity using the degradation of MB under UV radiation as the examination for its potential, showing some activity with a decrease of 11.3% in absorbance.

We have also demonstrated that TiO_2 based nanowires can be fabricated using infiltration into porous templates resulting in easily producible 1D nanostructures with high surface areas and good photocatalytic activity. Pure TiO_2 nanowires were investigated firstly using a Ti-$(OPr^i)_4$ derived sol-gel infiltrated into porous alumina membranes and sintered to induce phase change to anatase and partial crystallisation. The testing of photocatalytic activity of the nanowires in the degradation of MB demonstrated a decrease of 11.3% in absorbance of MB.

We have also developed a new approach in the preparation of AuNP loaded TiO_2 nanowires by doping the acac stabilised Ti-(OBt) derived sol-gel with DMAP stabilised

AuNPs and infiltrating into porous alumina membranes resulting in high aspect ratio nanowires loaded with AuNPs. These composite nanowires demonstrated the highest photocatalytic activity aamong our samples resulting in a decrease of 40% in the absorbance of MB. These results demonstrate the high potential of Au-TiO_2 nanostructures in photocatalysis.

Finally we prepared new QD-TiO_2 composites by the coating of CdTe QDs with TiO_2 and investigated their interaction and luminescent properties. The absorption and PL of the QD-TiO_2 nanocomposites showed a decrease in emission with reaction time and coating, due to the degradation (oxidation by TiO_2) of QDs. We believe that new approaches are necessary to further develop QD-TiO_2 composite area.

5.7 References

1 Linsebigler, A. L., Lu, G. & Yates, J. T. Photocatalysis on TiO2 Surfaces: Principles, Mechanisms, and Selected Results. *Chemical Reviews* **95**, 735-758, doi:10.1021/cr00035a013 (1995).

2 Carp, O., Huisman, C. L. & Reller, A. Photoinduced reactivity of titanium dioxide. *Progress in Solid State Chemistry* **32**, 33-177 (2004).

3 Kim, Y., Kim, C.-H., Lee, Y. & Kim, K.-J. Enhanced Performance of Dye-Sensitized TiO2 Solar Cells Incorporating COOH-Functionalized Si Nanoparticles. *Chemistry of Materials* **22**, 207-211, doi:10.1021/cm902907e (2009).

4 Chen, X., Lou, Y. B., Samia, A., Burda, C. & Gole, J. Formation of Oxynitride as the Photocatalytic Enhancing Site in Nitrogen-Doped Titania Nanocatalysts: Comparison to a Commercial Nanopowder. *Advanced Functional Materials* **15**, 41-49, doi:10.1002/adfm.200400184 (2005).

5 Tricoli, A., Righettoni, M. & Pratsinis, S. E. Anti-Fogging Nanofibrous SiO2 and Nanostructured SiO2-TiO2 Films Made by Rapid Flame Deposition and In Situ Annealing. *Langmuir* **25**, 12578-12584, doi:10.1021/la901759p (2009).

6 Chou, T., Zhou, X. & Cao, G. SiO2–TiO2 xerogels for tailoring the release of brilliant blue FCF. *Journal of Sol-Gel Science and Technology* **50**, 301-307 (2009).

7 Akly, C., Chadik, P. A. & Mazyck, D. W. Photocatalysis of gas-phase toluene using silica-titania composites: Performance of a novel catalyst immobilization technique suitable for large-scale applications. *Applied Catalysis B: Environmental* **99**, 329-335 (2010).

8 Malinowska, B., Walendziewski, J., Robert, D., Weber, J. V. & Stolarski, M. The study of photocatalytic activities of titania and titania-silica aerogels. *Applied Catalysis B: Environmental* **46**, 441-451 (2003).

9 Zhang, M., Shi, L., Yuan, S., Zhao, Y. & Fang, J. Synthesis and photocatalytic properties of highly stable and neutral TiO2/SiO2 hydrosol. *Journal of Colloid and Interface Science* **330**, 113-118 (2009).

10 Brinker, J. C. & Scherer, G. W. *The Physics and Chemistry of Sol-Gel Processing*. (Academic Press Limited, 1990).

11 Ma, H. L. *et al.* Raman study of phase transformation of TiO2 rutile single crystal irradiated by infrared femtosecond laser. *Applied Surface Science* **253**, 7497-7500 (2007).

12 Zhang, W. F. & et al. Raman scattering study on anatase TiO 2 nanocrystals. *Journal of Physics D: Applied Physics* **33**, 912 (2000).

13 Smith, D. Y., Black, C. E., Homes, C. C. & Shiles, E. Optical properties of TiO2–SiO2 glass over a wide spectral range. *physica status solidi (c)* **4**, 838-842, doi:10.1002/pssc.200673847 (2007).

14 Marques, A. C. & Almeida, R. M. in *13th International Workshop on Sol-Gel Science and Technology (Sol-Gel 2005).* 371-378 (Springer).

15 Lee, H. J., Hahn, S. H., Kim, E. J. & You, Y. Z. Influence of calcination temperature on structural and optical properties of TiO2-SiO2 thin films prepared by sol-gel dip coating. *Journal of Materials Science* **39**, 3683-3688 (2004).

16 Viswanath, R. N. & Ramasamy, S. Study of TiO2 nanocrystallites in TiO2---SiO2 composites. *Colloids and Surfaces A: Physicochemical and Engineering Aspects* **133**, 49-56 (1998).

17 Bi-Tao, X. *et al.* Preparation of nanocrystalline anatase TiO_2; using basic sol-gel method. *Chemical Papers* **62**, 382-387, doi:10.2478/s11696-008-0040-0 (2008).

18 Houas, A. *et al.* Photocatalytic degradation pathway of methylene blue in water. *Applied Catalysis B: Environmental* **31**, 145-157 (2001).

19 Periyat, P., McCormack, D. E., Hinder, S. J. & Pillai, S. C. One-Pot Synthesis of Anionic (Nitrogen) and Cationic (Sulfur) Codoped High-Temperature Stable, Visible Light Active, Anatase Photocatalysts. *The Journal of Physical Chemistry C* **113**, 3246-3253, doi:10.1021/jp808444y (2009).

20 Feng Chen, Jincai Zhao & Hidaka, H. Highly selective deethylation of rhodamine B: Adsorption and photooxidation pathways of the dye on the TiO2/SiO2 composite photocatalyst. *International Journal of Photoenergy* **5**, 209-217, doi:doi:10.1155/S1110662X03000345 (2003).

21 Zhang, T. *et al.* Photooxidative N-demethylation of methylene blue in aqueous TiO2 dispersions under UV irradiation. *Journal of Photochemistry and Photobiology A: Chemistry* **140**, 163-172 (2001).

22 Jitputti, J., Suzuki, Y. & Yoshikawa, S. Synthesis of TiO2 nanowires and their photocatalytic activity for hydrogen evolution. *Catalysis Communications* **9**, 1265-1271 (2008).

23 Lin, Y. & et al. Fabrication and optical properties of TiO 2 nanowire arrays made by sol–gel electrophoresis deposition into anodic alumina membranes. *Journal of Physics: Condensed Matter* **15**, 2917 (2003).

24 Kim, J.-I., Lee, S.-Y. & Pyun, J.-C. Characterization of photocatalytic activity of TiO2 nanowire synthesized from Ti-plate by wet corrosion process. *Current Applied Physics* **9**, e252-e255 (2009).

25 Attar, A. S. *et al.* Sol-gel template synthesis and characterization of aligned anatase-TiO2 nanorod arrays with different diameter. *Materials Chemistry and Physics* **113**, 856-860 (2009).

26 Lee, S., Jeon, C. & Park, Y. Fabrication of TiO2 Tubules by Template Synthesis and Hydrolysis with Water Vapor. *Chemistry of Materials* **16**, 4292-4295, doi:10.1021/cm049466x (2004).

27 Nobuaki Negishi & Takeuchi, K. TiO_2 photocatalytic coatings deposited on soda lime glass. *2nd Internatinoal Conference on Coatings on Glass* **Coatings on glass**, 144-147 (1998).

28 Daniel, M.-C. & Astruc, D. Gold Nanoparticles: Assembly, Supramolecular Chemistry, Quantum-Size-Related Properties, and Applications toward Biology, Catalysis, and Nanotechnology. *Chemical Reviews* **104**, 293-346, doi:10.1021/cr030698+ (2003).

29 Lidia, A. & et al. Photocatalytic and antibacterial activity of TiO 2 and Au/TiO 2 nanosystems. *Nanotechnology* **18**, 375709 (2007).

30 Buso, D., Pacifico, J., Martucci, A. & Mulvaney, P. Gold-Nanoparticle-Doped TiO_2 Semiconductor Thin Films: Optical Characterization. *Advanced Functional Materials* **17**, 347-354 (2007).

31 Ernst, K. *et al.* Contacts to a solar cell with extremely thin CdTe absorber. *Thin Solid Films* **387**, 26-28 (2001).

32 Larramona, G. *et al.* Nanostructured Photovoltaic Cell of the Type Titanium Dioxide, Cadmium Sulfide Thin Coating, and Copper Thiocyanate Showing High Quantum Efficiency. *Chem. Mater.* **18**, 1688-1696 (2006).

33 Seabold, J. A. *et al.* Photoelectrochemical Properties of Heterojunction CdTe/TiO2 Electrodes Constructed Using Highly Ordered TiO2 Nanotube Arrays. *Chem. Mater.* **20**, 5266-5273 (2008).

34 Singh, R. S. *et al.* Nano-structured CdTe, CdS and TiO2 for thin film solar cell applications. *Solar Energy Materials and Solar Cells* **82**, 315-330 (2004).

35 Bang, J. H. & Kamat, P. V. Solar Cells by Design: Photoelectrochemistry of TiO_2 Nanorod Arrays Decorated with CdSe. *Advanced Functional Materials* **9999**, NA (2010).

36 Kamat, P. V. Quantum Dot Solar Cells. Semiconductor Nanocrystals as Light Harvesters†. *The Journal of Physical Chemistry C* **112**, 18737-18753, doi:10.1021/jp806791s (2008).

Chapter 6

Experimental

6.1 Starting Materials and General Procedures

All precursor chemicals were purchased from Sigma-Aldrich unless otherwise stated. Microspheres were purchased from microParticles GmbH in Germany, dye coated spheres are made of melamine formaldehyde and dye is Ethidium Bromide (ex/em = 302(505)/602 nm). Alumina membranes (Anodisc) were purchased from Whatman®. Millipore water was used throughout in all experiments. All micro-channel glass templates were provided by the State Optical Institute, St. Petersburg, Russia.

Sol-gel reactions were carried out in a standard 150ml beaker in air with a Parafilm™ cover. The ultra sonic bath used was an Ultrawave, the shaker used is an IKA KS130 with variable time and frequency. The centrifuges used are a Hettich Universal 33 Centrifuge with variable time and rpm and an Eppendorf 5410 centrifuge with variable time. The ultra sonic tip used was a model CV33 with tapered tip. Samples annealed in a Nabertherm S27 furnace with heating rate control. Some bright field images were taken using the Leica microscope on the Raman system and some with the ERGOPLAN microscope.

6.2 Characterisation Techniques

Below is described in brief the main details of the various characterisation techniques, which have been used in this project.

6.2.1 Raman Spectroscopy

Raman measurements were performed using a Renishaw 1000 micro-Raman system equipped with a Leica microscope attachment. The system is equipped with one multi-line Ar^+ ion laser system (Laser physics relient 150 select multi-line) with operating wavelengths of 457 nm, 488 nm and 514 nm operated nominally between 1-10mW also a red line HeNe laser with an emission wavelength of 633 nm and a 785 nm diode laser with max power output of 200mW. The wavelength and laser power (altered by changing the emission power of the laser and/or applying a power filter) used during spectra gathering was altered depending on the type and nature of sample used. For example magnetite based nanoparticles required a low power excitation with the 633 nm line while other samples such as the xerogels can be examined under higher power and lower wavelengths. The spectra are collected by focusing a laser spot of ~1μm in diameter using a x50 objective onto a dry sample and running the collection process in the dark with the appropriate collection protocols. Calibration of the instrument was carried out before every session using a Si standard reference.

6.2.2 Solid State PL Spectroscopy

Solid state PL measurements are also carried out using the micro-raman system described above in 6.2.1. The protocols are changed to read in nm and the laser line used is mainly the blue 457 nm line or though the 488 and 514 nm lines were also employed. The detection range of the instrument is from just after the excitation wavelength (depending) up to 800 nm. The beam is focused on the sample via objective lens' (x5, x10, x50, x100) at a specific appropriate point of excitation. The output power of the laser can be altered as desired, and also polarisers in some instances can be inserted for polarised light detection. The sample is laid flat on a glass slide for example (or any desired flat substrate) and focused using optical microscope with a crosshair to pinpoint the excitation spot, the beam is then focussed separately (if visible depending on power) and all external light noise removed via closed chamber attached on machine and turning off room lights the spectrum can then be recorded.

6.2.3 Transmission Electron Microscopy (TEM)

TEM images were taken with on a JEOL 2100 TEM in the Centre for Microscopy Analysis with the assistance of Mr. Neal Leddy. The beam was operated at 100kV. Samples for TEM were prepared by placing a drop of the sample to be analysed on a formvar 400 mesh copper grid (grid mainly used however carbon and lacey carbon grids were used at times) to evaporate fully or in some cases for enough time so the sample deposits on the grid and the excess is removed.

6.2.4 Scanning Electron Microscopy (SEM)

SEM measurements were performed using a Tescan MIra Variable Pressure Field Emission Scanning Electron Microscope and a Hitachi S-4300 Field Emission Scanning Electron Microscope at room temperature with the assistance of Mr. Neal Leddy. Samples were placed on a adhesive label and coated with a thin layer of gold (as required) to aid conductivity to the sample for non-conducting samples (e.g. SiO_2 based samples).

6.2.5 Thermal Gravimetric Analysis (TGA)

TGA was carried out on a Pyris-1 TGA machine under air by setting the balance with an empty ceramic crucible boat and then placing between 4-6mgs of the sample to set the weight. Heating is commenced by setting the machine to heat at 5°C/min up to the desired temperature. The change in weight of the sample during heating is accurately monitored by the software giving information on weight change during heating and thusly constituents being 'burned off' during the heating process.

6.2.6 UV-vis Absorption Spectra

UV-vis spectra were recorded using SHIMADZU UV2101 PC UV-Vis scanning spectrometer operated at room temperature. Samples were examined in a 4ml quartz cuvette over the appropriate wavelength range for the sample (200-800 nm) after a baseline of the solvent was run.

6.2.7 Vibrating Sample Magnetometry (VSM)

VSM measurements were performed at room temperature using a LakeShore 7300 vibrating sample magnetometer by Ms. Fiona Byrne (School of Physics), which operates by placing a small amount of sample (~20-30mg) in a magnetic field (up to 1T) and making it undergo mechanical motion and thus a changing magnetic field which induces a voltage which can be read and converted to magnetic moment via a simple equation.

6.2.8 X-Ray Diffraction (XRD)

XRD was carried out on a Siemans D500 XRD, with the assistance of Dr. Karsten Rode. Sample preparation involved placing a powdered or crushed sample over a 3x2 cm square with a gel used for adhesion on a glass plate and loading the sample at a known angle for measurement. Scan time can be varied to increase signal gain.

6.2.9 UV source for Photocatalytic tests

Photocatalytic tests were carried using a Spectroline ENF-260C UV lamp capable of operating at 254 or 365 nm. The typical peak intensity @365 nm is 350 $\mu W/cm^2$ and @254 nm is 390350 $\mu W/cm^2$ at the cabinet floor. The cabinet used is a Spectroline model CM-10 with dimensions 22.8 cmW x 30 cmL x 16.5 cmH.

6.2.10 FTIR Spectroscopy

FTIR was carried out on a Perkin Elmer spectrum 100 with a diamond tip attachment. A background signal is taken before each scan and automatically subtracted from the final collection. The diamond tip is screwed down in contact with the sample at an appropriate pressure (indicated by the software) before the scan is taken.

6.2.11 Confocal Microscopy

All confocal images were captured using a Zeiss 510 confocal microscope at the Institute of Molecular Medicine in St. James's hospital with the assistance of Jennifer Conroy and Dr. Adriele Prina-Mello. The 3 exciting lasers operating were 405 nm (Ch1 blue BP filter: 420 nm – 480 nm), 488 nm (Ch2 green BP filter: 505 nm – 550 nm) and 561 nm (Ch3 red LP filter: 650 nm). Images can be collected in each channel or only certain selected ones; these separate images from each channel can then be overlaid or split into separate images. A z-scan mode is operated by taking a set XY image in various focal planes in the z direction (for example a 0.5 μm slice through a sample might be typical). Slit size and exposure can be altered to remove background and capture images.

6.3 Experimental procedures for Chapter 2

6.3.1 Preparation of aluminosilicate gels (with and without europium doping)

A mixture of 0.66 g water, 1.76 g ethanol (EtOH) and 1 drop 8.77M HCl was added to 8.2 ml of TEOS (98% pure or Reagent plus ≥ 99.9% depending on application). This mixture was left to stir for ~1hour at ambient temperature and then 0.75 g (this is for a 10:1 Si:Al ratio but can vary depending on required ratio) of aluminium iso-propoxide was added and heated at ~70 °C for 10-15 min to allow solid to dissolve. This is allowed to cool to room temperature. To create a europium co-doped gel, 0.133g of europium acetate hydrate is added at this point (again amount can vary depending on required mole%) and allowed stir for one hour. A solution of 2.6ml water, 2.25ml of ethanol and 3 drops 8.77M HCl is added under stirring to achieve gelation in either system. This process generally takes about 1 hour (generally slightly longer for the europium doped gel) depending on ambient conditions such as lab temperature. The gels are allowed to dry in air for a number of days until complete drying and shrinkage has occurred and a xerogel formed. Annealing of the bulk gels, microtubes within the MCG template and microtubes released from membranes were annealed using furnace described in 6.1 above. All heating rates were at 5°C/min, annealing microtubes to higher temperatures of 1000°C an annealing procedure of firstly heating to 500°C and holding for 1 hour before proceeding to 1000°C and holding at this for 2 hours, cooling took place naturally over a number of hours to nearly room temperature in the furnace.

6.3.2 Silica Coating of CdTe QDs

Silica coating CdTe QDs was performed according to a modified procedure by Wolcott et al[1]. Thioglycolic acid stabilised CdTe QDs were obtained from Wei-Yu Chen at an estimated concentration of 4×10^{-4} mol/L. 500μL of the QDs were placed in a 1.5ml eppendorf container and 75μL of a 48mM solution of iso-propanol and (3-Mercaptopropyl)trimethoxysilane (MPS) and then vortexed for 2hrs. This was then placed in dialysis tubing dialysed against basified Millipore water (pH 11) for 2hrs. QDs were then once again transferred to an eppendorf and 50μL of sodium silicate (27%) was added, sample was vortexed once again for 72hrs this time. A final addition 50μL of the 48mM MPS solution was added and vortexed finally for a further 24hrs.

6.3.3 Preparation of CdTe QD doped silica gels

Firstly TEOS was partially hydrolysed with a solution of 0.66ml H_2O, 2.25ml EtOH and 1 drop of conc. HCl under stirring for 1hr. Than a solution of 2ml H_2O, 2.25ml EtOH, and 3 drops of conc. NH_3 solution was added under stirring. After 1 minute 0.6ml of the silica coated QDs described above in 6.3.2 were added creating a homogeneous red (due to dots) sol. This gelled after ~6 min and was allowed to dry and shrink over ~ 5days in darkness.

6.3.4 Infiltration of sol into MCG membranes to create microtubes

The infiltration and release method of the microtubes is based on published method[2]. The MCG membranes are placed on a piece of flat hardened plastic with a bored hole in it (diameter 1.2cm) secured on top of a Buchner flask which is attached to a vacuum pump. When the 'sol' was at a sufficient viscosity estimated by eye (often not long before gelation) it was poured on the MCG membrane at the position above the hole while the vacuum was on. This resulted in microtube formation within the pores of the porous MCG. This was then allowed to dry for ~24hrs and annealed as described above.

6.4 Experimental procedures for Chapter 3

6.4.1 General procedures for release and washing of nanowires

The general procedure for the release of all nanowires samples from porous alumina membranes is to polish the infiltrated membrane lightly with a fine grade sand paper to remove surface gel or polymer and place it in dilute NaOH (usually 0.1M) with the aid sonication to dissolve the alumina and release the wires into solution. The excess NaOH and alumina is removed by washing using either or a combination of (depending on the sample) centrifugation by removing the supernatant and redispersion multiple times in 'clean' solvent (usually water) to achieve neutral pH and filtration using PVDF filters and washing with copies amount of solvent and redispersion into desired media.

6.4.2 Preparation of silica gel for defect emitting silica nanowires

The sol-gel processing was performed as described above with partially hydrolysing TEOS (>99%) with a solution of 0.66ml H_2O, 2.25ml EtOH and 1 drop of conc. HCl under stirring for 1hr. Added condensation solution of solution of 2.6ml water, 2.25ml of ethanol and 3 drops of conc. HCl. This sol was infiltrated under vacuum assist into 200 nm diameter porous alumina membranes and allowed to dry in air for 48hrs. The infiltrated membrane was lightly polished with fine grade sand paper and the polymer support ring removed from edge of membrane to allow for annealing at 400°C for 1hr.

6.4.3 Preparation of DMAP stabilised AuNPs

DMAP coated AuNPs have been prepared according to a modified published procedure[3]. A solution of 0.25g DMAP in 12ml $CHCl_3$ was added to 0.15g $AuCl_3.3H_2O$ in 12ml H_2O in a 50ml round bottom flask and left to stir vigorously for 1hr. The process resulted in an aqueous (bright orange) and organic phase separating out, the lower organic phase was removed leaving the DMAP coated gold ions. 0.7ml of a solution of $NaBH_4$ (0.1g in 10ml H_2O) was added drop-wise (1 drop every 10 seconds) to the gold solution under vigorous stirring. This was then left to stir for 2hrs, turning deep red colour indicating the formation of AuNPs which were highly stable in solution (prolonged stability was achieved by storing in a fridge). Concentration is ~17.6μM.

6.4.4 Surface functionalisation and AuNP attachment to silica nanowires

Took 500μL (conc. ~$1x10^7$ NWs/ml) of silica wires have been centrifuged and then redispersed them in 500μL iso-propanol (performed 3 times to ensure complete washing). 500μL of a MPS in iso-propanol (48mM) solution and 25μL conc. NH_3 solution to the wires. This mixture was vortexed for 2hrs and washed via centrifugation with iso-propanol and then water. A concentrated solution of DMAP coated AuNPs was added and once again vortexed for 2hrs. The sample was then washed via filtration with a 200 nm porous alumina membrane to remove excess AuNPs and redispersed in water by quickly sonicating the membrane to remove the functionalised wires from the surface.

6.4.5 Preparation of Magnetite doped Silica Nanowires

CTAB stabilised magnetite nanoparticles were obtained from Dr. Áine Whelan. A silica sol-gel was prepared by partially hydrolysing TEOS (>98%) with a solution of

0.66ml H_2O, 2.25ml EtOH and 1 drop of conc. HCl under stirring for 1hr. A condensation solution of 0.6-2ml H_2O, 2.25ml EtOH and 3 drops HCl or NH_3 solution depending on the sample, this was then placed on a shaker and magnetic stirrer removed. 0.6-2ml of the stabilised magnetite solution was then added again depending on the sample creating a homogeneous brown sol and left to shake while 200 nm diameter alumina membranes were infiltrated with the sol at various times (1-10 min). The samples were left to dry in air for 24hrs and the wires released by membrane dissolution described above.

6.4.6 Nanowire Surface Functionalisation with APTES

The magnetite loaded nanowires (500 μL, conc. ~$1x10^7$ NWs/ml) were centrifuged down and the supernatant removed and redispersed in 500μL iso-propanol and 100 μL H_2O. 125 μL of a 0.42M APTES in iso-propanol solution was added plus 50 μL of conc. NH_3 solution. This was vortexed for 24hr to react and once again washed using centrifugation and the wires redispersed in water.

Biological tagging with antibodies and flow cytometry work was carried out in St. James' Hospital by Dr. Áine Whelan, Dr. Adriele Prina-Mello and Ann Atzberger.

6.4.7 Preparation of $CoFe_2O_4$ NP loaded Aluminosilicate Nanowires

PSS stabilised $CoFe_2O_4$ NPs were obtained from Gemma-Louise Davies. A sol-gel was prepared by partially hydrolysing TEOS (>99%) with a solution of 0.66ml H_2O, 2.25ml EtOH and 1 drop of conc. HCl under stirring for 1hr. 0.75g of aluminium iso-propoxide was then added and left to stir for 15 min at 70°C and then let cool to room temperature. A condensation solution of 2.6ml H_2O, 2.25ml EtOH and 3 drop of conc. HCl was added. This was then taken off the magnetic stirrer where 5.1mg of the PSS stabilised $CoFe_2O_4$ NPs were added, this was then placed in a sonic bath for 2hrs which kept the NPs stable in solution. The sol was then infiltrated into 200 nm porous alumina membranes and left to dry for 24hrs. The wires were released by membrane dissolution in 0.1M NaOH.

6.5 Experimental procedures for Chapter 4

6.5.1 Preparation of Oleic acid coated Magnetite NPs

Oleic acid coated magnetite NPs were prepared by dissolving 2.35g of Iron (III) chloride in 40ml of degassed water under argon atmosphere and left to stir. 0.5ml of oleic acid in 5ml acetone was then added followed by 0.86g of Iron (II) chloride. 20ml of conc. ammonia solution was added in 4ml aliquots, resulting in a viscous black mixture. This was then left to stir for 2hrs. 100ml of $CHCl_3$ was then added and the whole solution placed on a magnet for 2 days to allow the coated magnetite to settle into the $CHCl_3$ layer. This layer was then removed to obtain highly stable oleic acid coated magnetite NPs in $CHCl_3$.

6.5.2 Preparation of Multimodal PS Nanowires

A solution of ~300mg of PS (M_w=350,000) was dissolved in 9.4ml of THF with the aid of sonication. To this ~2.5mg of commercial dye coumarin-153 and 0.6-1ml of the oleic acid coated magnetite NPs was added depending on the sample. This resulted in a green tinted brown homogeneous solution with the appropriate viscosity for infiltration into 200 nm porous alumina membranes. 3 drops of the solution was used to infiltrate with vacuum assist and samples left to dry in air for 24hrs. Thin films were also made by placing ~1ml of the solution on a clean glass slide and allowing to dry in air. Nanowires were released by membrane dissolution and washed as described above.

6.5.3 Surface sulfonation of PS

The sulfonation of the surface of PS was carried out by placing the PS sample stirring in 40mls of conc. H_2SO_4 (95-97%) at 60°C. This was left to stir for 1-4hrs before being removed and thoroughly washed with water.

6.5.4 Preparation of CdZnSe/ZnSe QD doped PS Nanowires

CdZnSe/ZnSe QDs in toluene were obtained from Cormac Hanley. 64mg of PS (M_w=350,000) was dissolved in 2ml of toluene with the aid of sonication. To this 300μL of the QD solution was added and shaken to obtain a homogeneous solution. This solution was infiltrated with vacuum assistance into 200 nm diameter alumina membranes using 3 drops of solution. These samples were allowed to dry in air in darkness for 48hrs. Thin film was made by dropping ~1ml of solution onto clean glass slide and drying under same conditions. Nanowires were released by membrane dissolution using 0.025M NaOH with careful sonication and washed using regular procedure.

6.6 Experimental procedures for Chapter 5

6.6.1 Preparation of SiO_2-TiO_2 composite gels

SiO_2-TiO_2 composite gels (50:50 for example) were prepared by hydrolysing Ti-$(OPr^i)_4$ for 30 min with stirring with a EtOH and HCl solution; molar ratio 1:4:1.4x10^{-4} Ti:EtOH:HCl. Separately TEOS was initially hydrolysed with a water, EtOH, HCl solution for 1hr under stirring; molar ratio 1:4:1:1x10^{-4} Si:EtOH:H_2O:HCl. These solutions were combined and allowed stir for 15 min. A condensation solution of EtOH, water and HCl; molar ratio 1.08:1:1x10^{-5} EtOH:H_2O:HCl (resulting in a total H_2O:metal alkoxide ratio of 7:1). This resulted in a gelation within 1 min to a clear gel. The product was allowed to completely dry in air for ~5days, showing considerable shrinkage but remaining clear. The xerogel samples were annealed at various temperatures heating at 5°C/min and allowing to cool naturally to room temperature. Gels of other TiO_2 percentages were prepared in a similar fashion altering the ratios of the hydrolysis and condensation solutions reflecting the changing precursor ratios.

6.6.2 Preparation of TiO_2 Nanowires

TiO_2 nanowires were prepared by taking 5ml Ti-$(OPr^i)_4$ and adding 7.87ml EtOH and 50μL HCl, and allowing to stir for 20 min. A solution of 150μL H_2O and 1.96ml EtOH was added to this and allowed to stir for ~24hrs to obtain a white milky viscous sol. The sol was infiltrated under vacuum into 200 nm diameter alumina membranes and allowed to dry in air overnight. Samples were annealed by heating at 5°C/min to 400°C and holding for 1hr before allowing cooling to room temperature. Wires were released by membrane dissolution and washed as previously described.

6.6.3 Preparation of AuNP loaded TiO_2 Nanowires

DMAP stabilised AuNPs were fabricated as described in Section 6.4.3. A titania sol was prepared by adding 2.4ml acac and 1.02ml EtOH to 5ml Ti-$(OBt)_4$ and stirred for 2hrs. A solution of 1ml DMAP stabilised AuNPs in water and 2.55ml EtOH was added to the sol. 200 nm diameter alumina membranes were infiltrated with this sol very quickly after AuNP addition (30secs to 10 min) and allowed to dry overnight. The sol was left stir for 24hrs and turned from an initial red colour to deep purple upon gelation. Wires were released by membrane dissolution and washed as previously described.

6.6.4 Procedure for photocatalytic tests of samples using methylene blue (MB)

Testing samples for photocatalytic activity was performed in a quartz cuvette with a 10mm path length. A typical test is carried out by adding 0.92ml of $1x10^{-4}$M MB solution to 2.75ml of nanowires in water (similarly the control tests were carried out using 2.75ml of pure water, also in the case of the SiO_2-TiO_2 crushed samples were added to this same solution make up). A small magnetic stirring bar was added and the samples left to stir in the dark for 45-50 min. An initial absorbance scan was taken and the cuvette placed stirring under a UV lamp (emitting at 254 or 365 nm as described in Section **Error! Reference source not found.**) shielded from ambient light. The exposure time was generally in the region of 4hrs after which a final absorbance was taken.

6.6.5 Preparation of TiO_2 coated CdTe QDs

Cysteine stabilised CdTe QDs were obtained from Mícheál Moloney and their UV-vis absorption and PL have been recorded. Separately 0.43ml of dry acac was added to a $14x10^{-2}$M solution of Ti-$(OEt)_4$ in dry iso-propanol (1:1 Ti:acac atomic ratio). 0.143 of this solution was added to 25ml of the QDs (having a 2:1 Cd:Ti atomic ratio). This was allowed to stir for 20hrs with samples taken at 5 min and 2hrs and UV and PL taken of these. Purification of the final sample was performed using a sephadex column. A sample for Raman spectroscopy was prepared by drying solution on a glass slide in the dark.

6.7 References

1 Wolcott, A. *et al.* Silica-Coated CdTe Quantum Dots Functionalized with Thiols for Bioconjugation to IgG Proteins. *The Journal of Physical Chemistry B* **110**, 5779-5789, doi:10.1021/jp057435z (2006).

2 Y. P. Rakovich *et al.* The Fabrication, Fluorescence Dynamics, and Whispering Gallery Modes of Aluminosilicate Microtube Resonators. *Adv. Func. Mat.* **17**, 1106-1114 (2007).

3 Gittins, D. I. & Caruso, F. Spontaneous Phase Transfer of Nanoparticulate Metals from Organic to Aqueous Media. *Angewandte Chemie International Edition* **40**, 3001-3004, doi:10.1002/1521-3773(20010817)40:16<3001::aid-anie3001>3.0.co;2-5 (2001).

Chapter 7

Conclusions and Future Work

7.1 Conclusions

Over the course of this work we have developed and investigated a range of micro- and nano- structures with high aspect ratio.

Firstly new hollow cylindrical microstructures have been prepared by vacuum assisted infiltration of silica/aluminosilicate sol-gels into highly ordered microchannel glass membranes have been fabricated. These structures showed a strong broad luminescence under UV radiation upon annealing treatment. The origin of the broad white luminescence can be explained by interstitial carbon defects, which are generated during the thermal treatment. Some of the microtubes demonstrated good optical quality in displaying WGM resonance. It has also been shown that the luminescent properties of the microtubes can be altered by using doped and loaded sol-gels, namely europium and CdTe QD doped sols. This enables us to produce microtubes with controlled desired emission profiles. The interaction of the microtubes with optically active microspheres was also investigated showing energy transfer between these two microstructures. This work demonstrates the potential approach to create robust microtube structures with a range of luminescent properties. These materials could find important applications as micro-cylindrical light emitters, resonators, sensors and components of optical communications devices.

This project has also resulted in the development of various 1D silica and aluminosilicate nanowires. The nanowires, prepared by infiltration of sol-gels into nano-porous alumina templates, show a high aspect ratio needle like structure. These have been successfully developed by the doping and loading of sol-gels to create luminescent and magnetic nanowires. The functionalisation of the wires to accommodate AuNPs on their surface has also been investigated and developed. The magnetic nanoparticle loaded wires have demonstrated high surface functionality for bio-conjugation to antibody markers. Investigation by flow cytometry showed the wires to have superior detection properties due to their "flow cytometric fingerprint" and higher binding percentage when compared to particles of similar make up. Polystyrene has also been utilised to create nanowires using infiltration into alumina templates. The doping of the PS solution with superparamagnetic NPs and dye allowed the creation of new multimodal nanowires. QD loaded nanowires have also been fabricated and show good emission from the dots under UV excitation. These wires have shown the potential to be used as multiplexed immunoassays and have definite potential to be used in areas such as bio-separation and magnetic sorting applications.

Another area of research, which was developed in the project is TiO_2 based materials with high aspect ratio for potential in photocatalytic applications. One of the areas researched was that of SiO_2-TiO_2 composite gels and their optimisation to obtain a clear glass material which contains anatase phase TiO_2. This was done successfully and shown to be photocatalytically active. Nanowires consisting of pure TiO_2 and AuNP loaded TiO_2 were also fabricated by the vacuum assisted infiltration into alumina templates. These structures were characterised and tested for photocatalytic activity. They both showed some activity with the AuNP loaded wires showing the greater activity. Both of these materials showed some photocatalytic activity, which was greater for AuNP loaded wires. This work demonstrates a great potential for developing novel nano-wire based materials with potential photocatalytic properties. The coating of CdTe QDs with TiO_2 was also investigated resulting in the formation of nanoparticle conjugates of the two which maintained the luminescence of the dots and showed an increase in absorbance in the deep UV region due to the TiO_2 coating.

The work has contributed overall to the development of functional template synthesised microtubes and nanowires by the doping and loading of polymer solutions and sol-gels with various materials and nanoparticles allowing the utilisation of their unique properties in a structure shown to be applicable to modern technologies.

7.2 Future Work

The work performed throughout the various projects and some of our feasibility studies have led to new avenues of work opening up for future consideration.

The successful doping of microtubes with europium showing strong characteristic emission opens up the possibility of further of further development of microtubes containing rare earth metal systems. For example combining different RE metals in the silica matrix can give rise to cooperative up-conversion (e.g. erbium-ytterbium, europium-ytterbium systems etc). Preliminary results show this to be promising with the occurrence of second harmonic generation within the silica monolith.

In our preliminary studies we have fabricated new microstructured arrays by infiltration of polymer (polystyrene, PMMA) and silica into pre-fabricated Ni template (sieves). This processing resulted in a range of microstructures of different shapes (Figure 7.1). We have also shown that these structures can be doped and loaded with quantum dots resulting in light emitting arrays. The Ni templates can also be fabricated with various pore sizes and shape to suit application. We believe that these microstructures have great potential for microfluidics and potential photonics applications.

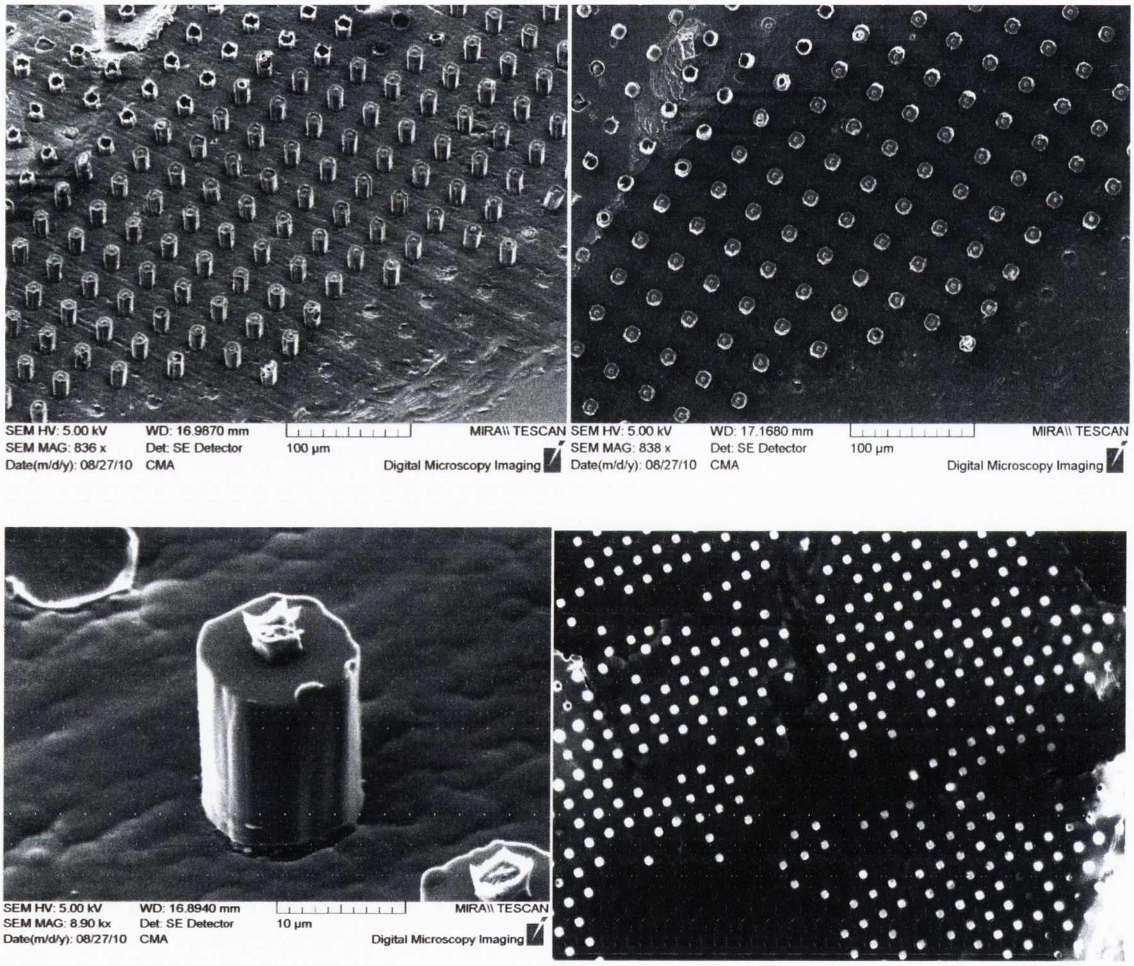

Figure 7.1: SEM images of arrays of dye doped PS microstructures and (bottom right) fluorescence microscope image of same

The successful loading of silica nanowires on the surface with AuNPs opens up new possibilities for energy transfer through the SPB of the particles in 1D nanostructures. Further research will involve the optimisation of nanoparticle loading on the surface of silica nanowires and detailed investigation of their optical and sensing properties.

Our research has also demonstrate that magnetically loaded silica nanowires have intrinsic advantages when compared to similar particles due to their unique flow cytometry fingerprint. Therefore, the nanowire aspect ratio could be of advantage for multiplexed immunoassay detection. Future efforts will be focused on their multimodal use as an analytical tool in flow cytometry for rapid assaying of selected antibodies, cytokines, and nucleic acids. In addition similar multimodal polymer (PS) nanowires have also been targeted for testing in bio-medical applications such as flow cytometry and cell internalisation as possible new devices for magnetic separation of biological species. Preliminary work has already been carried out in this area with some promising results.

We believe that there are also a lot of new opportunities in the area of the TiO2 based micro- and nano- composites. The SiO_2-TiO_2 composites can be further optimised to improve their photocatalytic activity by doping the sols, also the formation of micro and nano structures to improve the surface area of the materials. Both the pure and AuNP loaded TiO_2 nanowires have shown good potential as nanoscale photo-catalysts. We plan to perform their further development by investigating the effect of changing parameters in the sol-gel reaction on the formation and properties of the wires. The coating of CdTe QDs with TiO_2 resulted in a novel luminescent and potentially very active material for photovoltaic and photocatalytic devices. Further work on their stability and protection from degradation possibly involving placing a protective layer on the QDs and testing their potential for photo-induced applications will be necessary. Then we plan to study both the photovoltaic and photocatalytic properties of the QD-TiO_2 nanocomposites.

All this future work should result in new micro/nano structures of high aspect ratio with a range of potential applications.

Appendices

Appendix 1: Additional information and results to accompany Chapter 2

Shown in Figure 1.1 are PL spectra of various SiO_2 microtubes annealed at 400°C for 1hr. The tubes displayed relatively weak WGM (the small 'humps' in the spectra) however showed very good uniformity across many tubes.

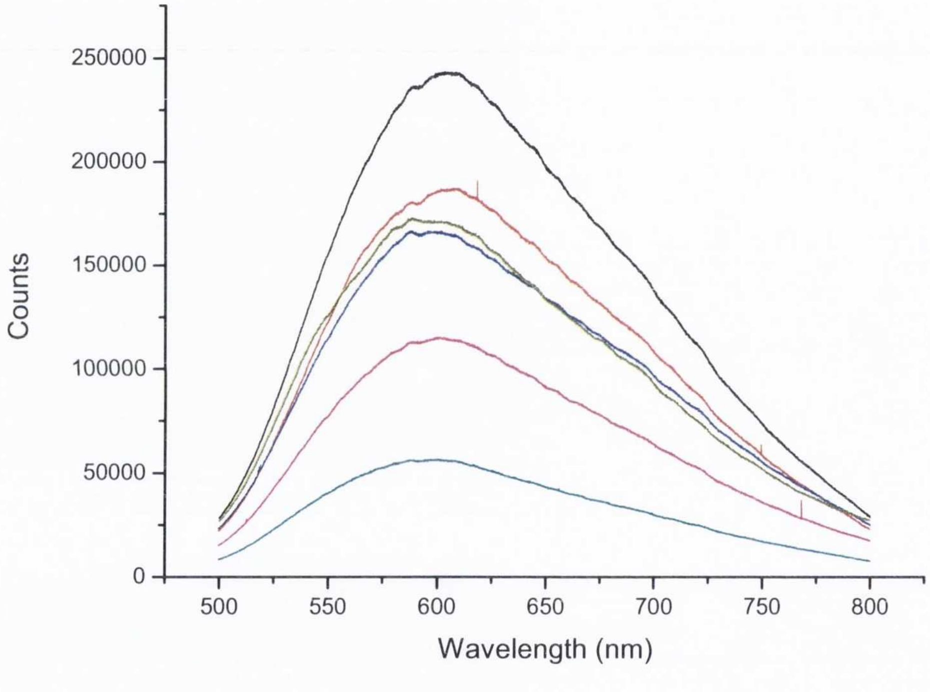

Figure 1.1: PL spectra of SiO_2 microtubes annealed at 400°C displaying weak WGM

The coating of silica microtubes with CdSe QDs by vacuum assisted infiltration of the QD solution through a MCG membrane containing tubes was also investigated. Some results from these experiments are shown in Figure 1.2 and Figure 1.3. The coated tubes showed a high PL at 561nm.

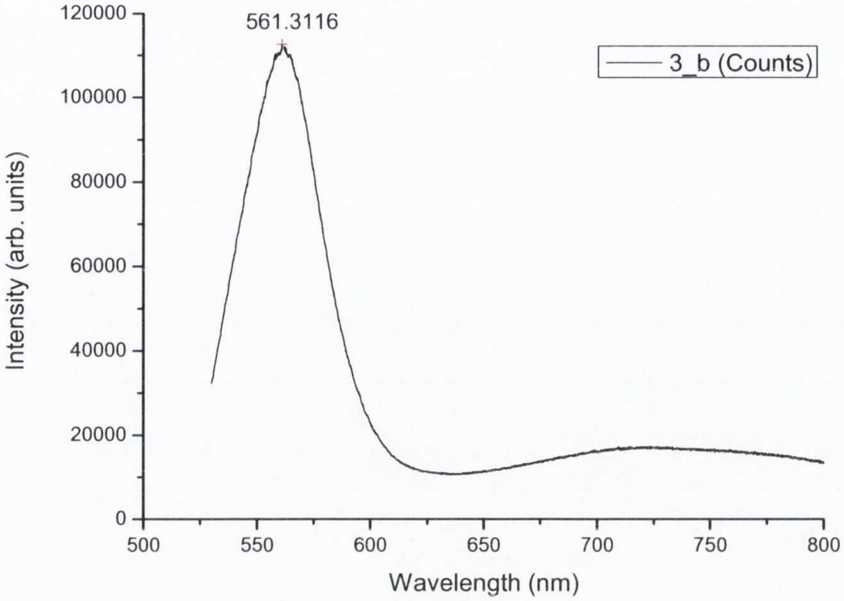

Figure 1.2: PL spectra of CdSe QD coated SiO_2 microtubes

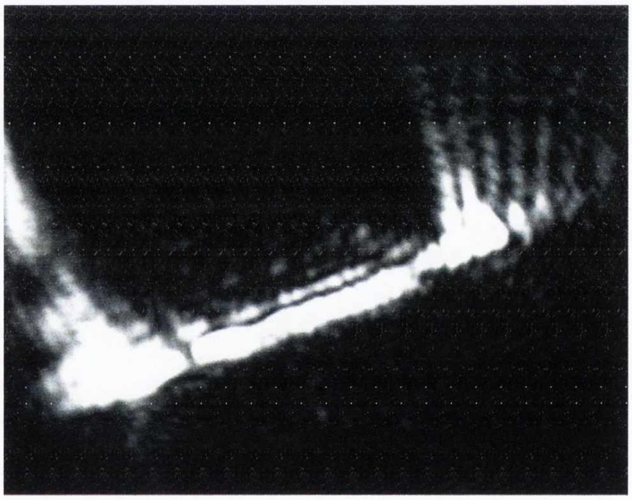

Figure 1.3: Microscope image of laser light circulating in microtube

Appendix 2: Additional information and results to accompany Chapter 3

During the course of the work aluminosilicate nanowires were also fabricated, samples of these wires are shown in Figure 2.1. Also shown are two TEM images of the

AuNP decorated POSS NPs created unintentionally when attempting to functionalise the silica nanowires for AuNP attachment (Figure 2.2).

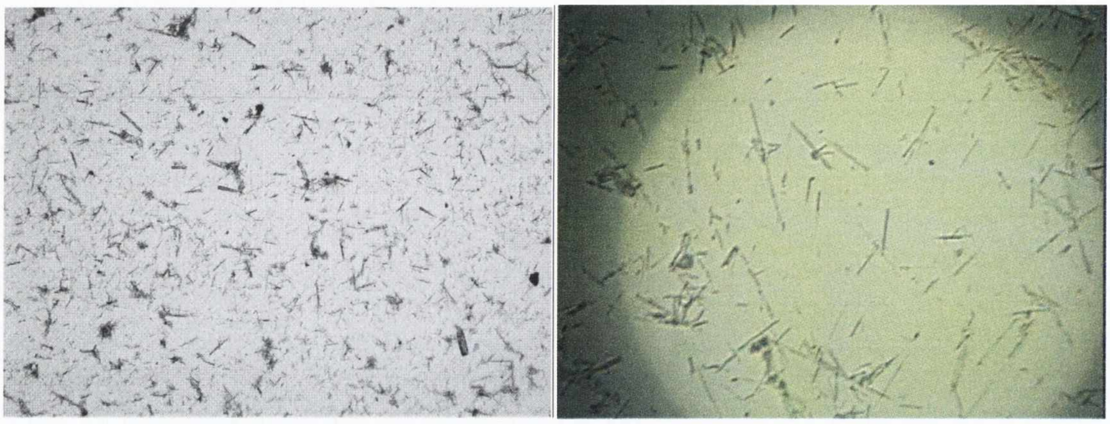

Figure 2.1: Microscope images of aluminosilicate nanowires

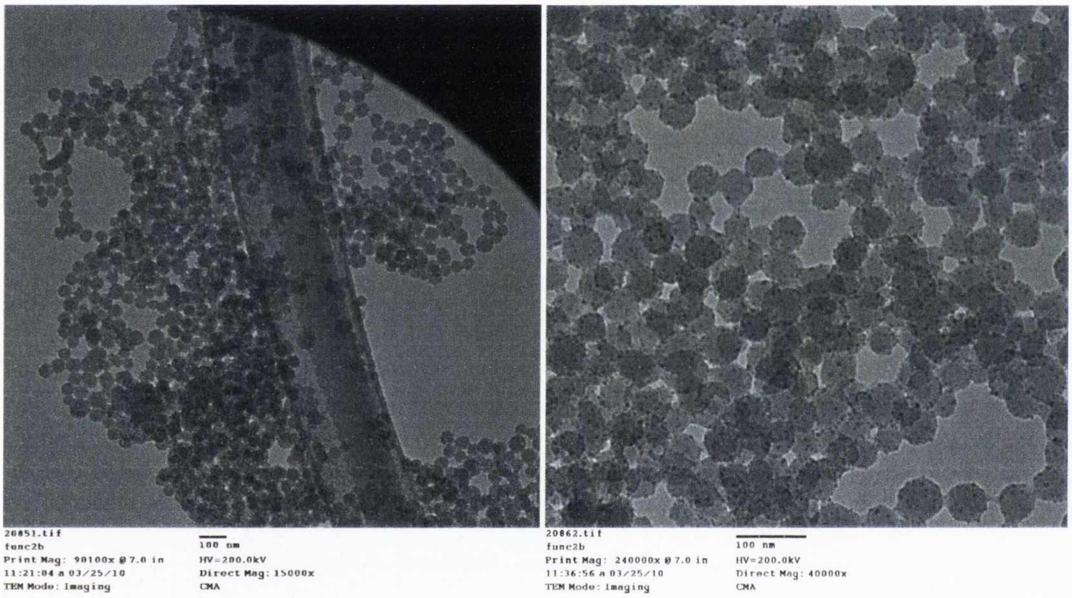

Figure 2.2: TEM images of AuNP decorated POSS NPs

The dependence of gelation time with volume of conc. NH_3 solution in the condensation step was studied for a standard acid hydrolysed sol-gel used in our experiments (See Table 1).

Volume of conc. NH_3 solution added (μL)	Gelation time (secs) ± 5secs
25	N/A
50	1350
100	394
150	160

Table 1: Relation of gelation time to volume of ammonia in condensation step

Appendix 3: Additional information and results to accompany Chapter 4

Shown in are additional confocal microscope images of PS nanowires interacting with epithelial lung cancer cells.

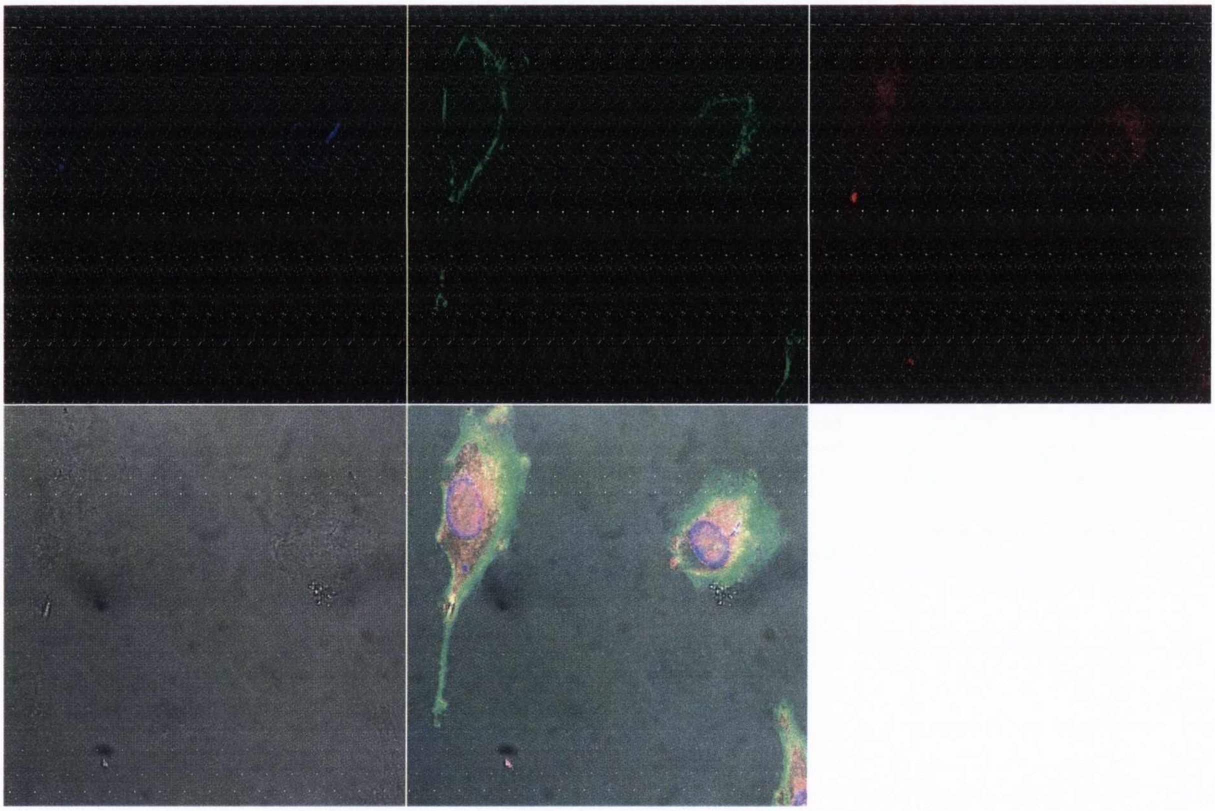

Figure 3.1: Confocal image of nanowire interacting with cell

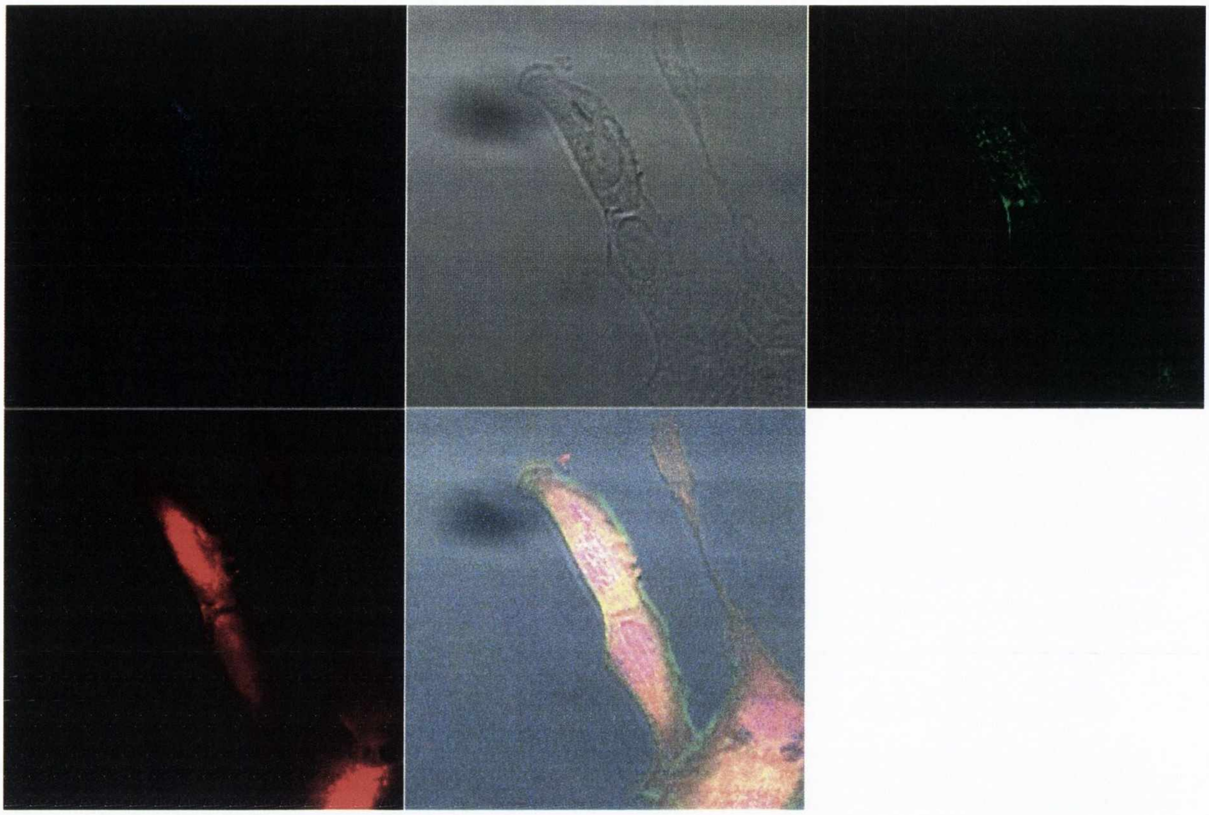

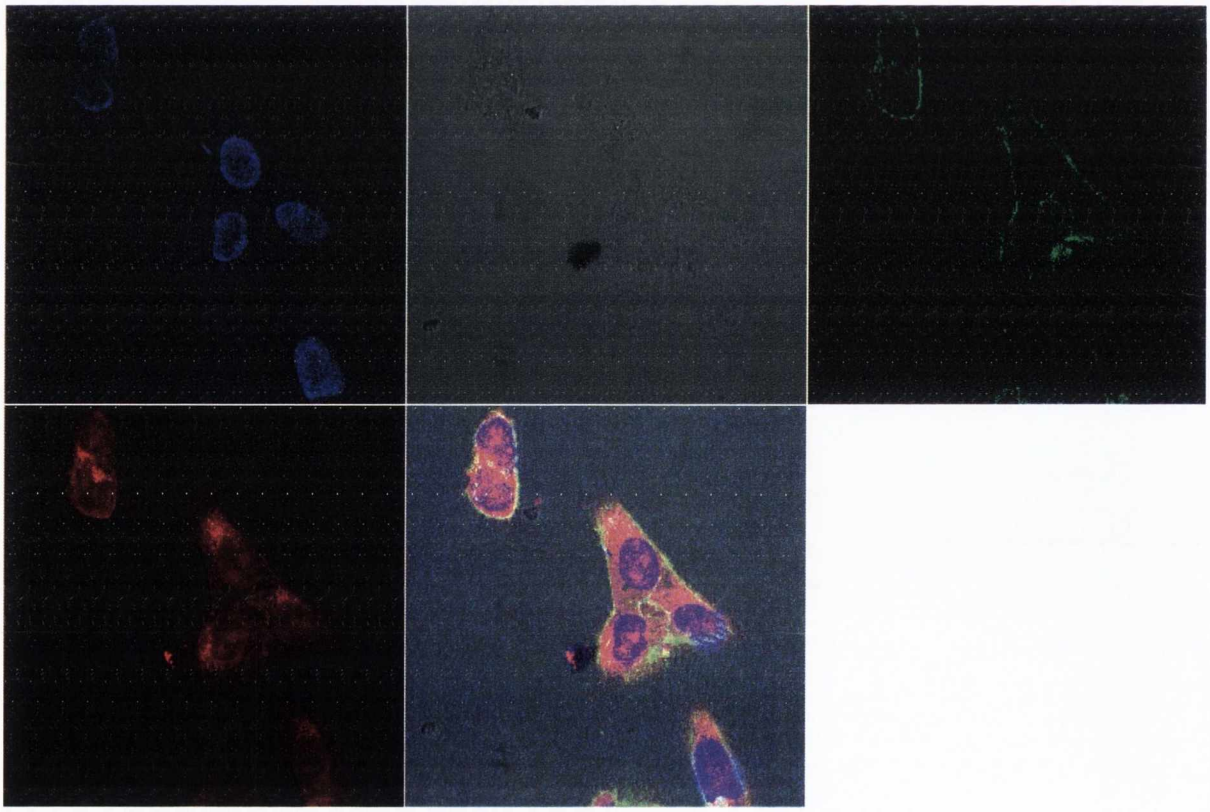

Figure 3.2: Confocal images of nanowire interacting with cells

Appendix 4: Additional information and results to accompany Chapter 5

Figure 4.1 shows additional TEM images of TiO_2 nanowires.

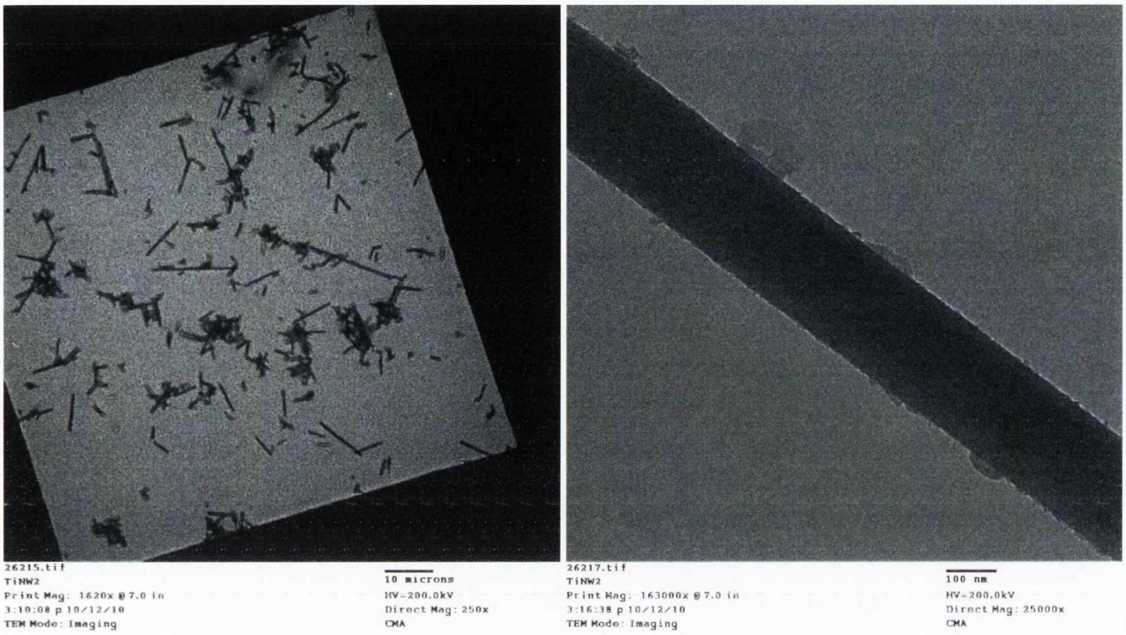

Figure 4.1: TEM images of TiO_2 nanowires

Appendix 5: List of Presentations and Publications

‘Fabrication and Characterisation of Photonic Nanowires’ – Poster, SPIE Optics and Photonics Conference, San Diego, August 2008

‘Fabrication of luminescent optical quality Aluminosilicate Microtubes’ – Poster, ICAM Conference, Rio de Janeiro, September 2009

‘Fabrication and Characterisation of 1D Micro- and Nano- Structures’ Departmental Seminar, May 2009

‘Reinforcement of poly(vinyl chloride) and polystyrene using chlorinated polypropylene grafted carbon nanotubes’ Rowan Blake, Jonathan N. Coleman, Michele T. Byrne, Joseph E. McCarthy, Tatiana S. Perova, Werner J. Blau, Antonio Fonseca, Janos B. Nagy and Yurii K. Gun’ko* - J. Mater. Chem., 2006, **16**, 4206–4213

'Chemical functionalisation of titania nanotubes and their utilisation for the fabrication of reinforced polystyrene composites' Michele T. Byrne, Joseph E. McCarthy, Mathew Bent, Rowan Blake, Yurii K. Gun'ko,* Endre Horvath, Zoltan Konya, Akos Kukovecz, Imre Kiricsi and Jonathan N. Coleman - J. Mater. Chem., 2007, **17**, 2351–2358

'New optical cylindrical microresonators' Yurii K. Gun'ko*, Sivakumar Balakrishnan, Joseph E. McCarthy, Yuri P. Rakovich, John F. Donegan, Tatiana S. Perova, Vasily Melnikov - Proc. of SPIE Vol. 6739, 67391F, (2007)

'Fabrication and characterisation of photonic nanowires' Joseph E McCarthy, Áine M Whelan, Gemma-Louise Davies, Fiona Byrne, Jennifer Conroy, Yuri Volkov, Yurii Gun'ko - Proc. of SPIE Vol. 7030, 703019, (2008)

'Comparative Flow Cytometric Analysis of Immunofunctionalized Nanowire and Nanoparticle Signatures' Adriele Prina-Mello,* Aine M. Whelan,* Ann Atzberger, Joseph E. McCarthy, Fiona Byrne, Gemma-Louise Davies, J. M. D. Coey, Yuri Volkov and Yurii K. Gun'ko*

'Covalent crosslinking of single-walled carbon nanotubes with poly(allylamine)' Amro Satti, Anouk Perret, Joseph E. McCarthy and Yurii K. Gun'ko* - J. Mater. Chem., 2010, 20, 7941–7943